RADIATION DOSIMETRY OF CONVENTIONAL AND LASER-DRIVEN PARTICLE BEAMS

by

DANIEL KIRBY

A thesis submitted to
The University of Birmingham
for the degree of
DOCTOR OF PHILOSOPHY

School of Physics and Astronomy
College of Engineering and Physical Sciences
The University of Birmingham
April 2011

Abstract

The measurement of radiation dose in radiotherapy is vital in ensuring the accuracy of treatments. As more advanced techniques using protons and ions emerge, they pose challenges to ensure the same level of accuracy of dosimetry is achieved as for conventional X-ray radiotherapy. A relatively new method of particle acceleration using ultra-high intensity lasers and thin metallic targets has sparked a large effort to investigate the possible application of this technology in radiotherapy, which in turn requires accurate methods of dosimetry to be carried out and is the main motivation for this work. Accurate dosimetry was initially performed here using an air ionisation chamber, various models of GafChromic film and a PMMA phantom in 15 and 29 MeV protons and 38 MeV α-particles from the Birmingham cyclotron. In developing an accurate protocol for absorbed dose-to-water at these relatively low proton energies, new data was generated on the proton energy response of GafChromic films. This enabled accurate dosimetry of a prototype laser-particle source, and provided improvements to a method of spectroscopic measurement in the resultant mixed field of multi-energy protons, electrons and X-rays. Monte Carlo simulations using MCNPX but mainly FLUKA were performed throughout to support and verify experimental measurements.

This thesis is dedicated to my ever supportive wife Heidi, and baby daughter Eva Grace for making my life richer beyond imagination.

ACKNOWLEDGEMENTS

Seldom is any real work achieved without the significant contribution of others. At the top of the list is my supervisor Dr. Stuart Green for his hard work and dedication in supervising not only myself but all of his students. His enthusiasm in the development of novel radiotherapy technologies has been a true inspiration. The vast majority of my work was performed using the Birmingham cyclotron, run by Prof. David Parker and his team Mike Smith, Greg Wood and John Lowe who showed great patience and extreme helpfulness for which I am eternally grateful. I would also like to thank Dr. Hugo Palmans for sharing his great knowledge of particle dosimetry and providing further support whenever I needed it and my fellow student and friend Francesca Fiorini for all her help, especially with FLUKA, and keeping me company on many trips to Belfast and other meetings and conferences.

Others who have played a significant role in my work and deserve many thanks are Cecile Wojnecki, Richard Hugtenburg, Marco Borghesi and the group at Queens University Belast, and many people at International Specialty Products Corp. for going to great lengths to support my research with GafChromic film. I also wish to thank the School of Physics and Astronomy for providing my doctoral stipend.

Lastly, I want to thank my wonderful wife Heidi and all my family for their support during not only my doctoral studies but also for a patience-testing total of nine years at University.

CONTENTS

LIST OF FIGURES

LIST OF TABLES

LIST OF ACRONYMS

AAPM American Association of Physicists in Medicine

B-G Bragg-Gray

BASH Bourne-again shell, a UNIX command shell

CoP Code of practice

CPA Chirped pulse amplification

CSDA Continuous slowing down approximation

IAEA International Atomic Energy Agency

IBT Ion beam therapy

ICRU International Commission on Radiation Units and Measurements

IMRT Intensity modulated radiotherapy

LET Linear energy transfer

LiPCDA Lithium pentacosa-10,12-dyinoate; the lithium salt of PCDA

MC Monte Carlo

NIST National Institute of Standards and Technology

OD Optical density

PCDA Pentacosa-10,12-dyinoic acid

PET Polyethylene terephthalate, also known as polyester, Mylar or Melinex

PMMA Polymethyl methacralate, also known as Perspex or Plexiglas

PSDL Primary Standard Dosimetry Laboratory

PT Proton therapy

RCF Radiochromic film; film whose colour properties are sensitive to radiation

RPA Radiation pressure acceleration

RT Radiotherapy

TNSA Target-normal sheath acceleration

TPS Treatment planning system

CHAPTER 1

INTRODUCTION TO PARTICLE ENERGY LOSS, ACCELERATION AND RADIOTHERAPY

This chapter firstly describes the main physical interactions of protons and ions in matter within the energy ranges of interest to radiotherapy, and how these interactions contribute to absorbed dose in a medium. The typical dose distribution of ions is compared to that of X-rays which are used most widely in radiotherapy, and the benefits of using ions are discussed. A short technical section follows describing conventional methods of acceleration, and introduces current research technologies. Following on from this, laser-plasma acceleration (which this work focusses on) is described in more detail: the theory behind the physics, and its potential to one day supersede conventional methods resulting in significant cost and footprint reduction for ion beam therapy.

Finally a brief summary of the scope of work contained in this thesis is given.

1.1 Principles of ion beam therapy

1.1.1 Interactions of heavy charged particles

The term *heavy* charged particles (HCPs) is inclusive of all ions from the proton (z=1) upwards as they are heavy with respect to electrons. In general, the nature of interactions of all ions in matter are similar and can be scaled from the corresponding proton interaction and so the proton recieves the preferred treatment. As ions travel through matter, they can either interact with both nuclei and electrons that come within close proximity to their path, and undergo continuous interactions until they have lost all of their energy and stop. This is in contrast to uncharged particles such as photons or neutrons, which interact much less frequently and do not ever *stop* unless they are absorbed in an interaction. As the mass of any ion is much greater than atomic electrons, the deflection angle after an electronic interaction is extremely small and to a good approximation, ions travel in fairly straight paths through matter. The main deflections of protons are due to the much rarer elastic interactions with nuclei.

1.1.1.1 Stopping power and range

HCPs interact with electrons so frequently, that they appear to lose energy continuously along their path. Depending on the proximity of the interaction, the energy transferred by the incident ion will either raise the electron to a higher shell, exciting the atom, or provide it with sufficient energy to leave the atom and contain some kinetic energy of its own. If the latter occurs, then the electron may have received enough energy to cause further ionization along its path. The maximum energy that can be transferred in a single interaction from an ion with mass m and kinetic energy E, to an electron with mass m_0 (in the non-relativistic limit) is:

$$W_m = 4Em_0/m \tag{1.1}$$

or roughly 1/500 of the incident particle energy per nucleon. These secondary electrons are sometimes referred to as δ-rays and are responsible for the microscopic structure of energy deposition around the primary ion track. On the macropscopic scale however, the range of these δ-rays is insignificant compared to the range of the primary ion, and an often used approximation in dosimetry and Monte Carlo transport simulations is that the energy is deposited at the site of interaction, or ‘on the spot’. This simplification allows the use of the average rate of energy loss, called the stopping power, S:

$$S = -\frac{\mathrm{d}E}{\mathrm{d}x}$$

This general form is also known as the *unrestricted* stopping power, as opposed to *restricted* which is explained later. The units of S are usually in MeV cm^{-1}, but more commonly the total mass stopping power, S/ρ, is given in reference materials so that the values are independent of density variations[1] from one material sample to another. The most comprehensive set of stopping power data is in ICRU report 49 (ICRU, 1993), and from here onwards will just be referred to as ICRU49. The total mass stopping power is a sum of energy losses due to electronic collisions (S_{col}/ρ) as well as Coulomb interactions with atomic nuclei (S_{nuc}/ρ), however for the vast majority of proton energies the electronic losses dominate substantially. For protons in water as an example, S_{nuc}/ρ becomes larger than 1% of S_{col}/ρ only at energies below about 20 keV, and at 10 MeV the ratio is less than 0.1% . The nuclear interactions referred to in the stopping power are elastic and result in recoil energy being imparted to atoms, and are separate to the non-elastic nuclear interactions discussed in section 1.1.1.2 which have much greater implications for dosimetry at therapeutic energies (i.e above 50 MeV).

The full expression which describes S_{col}/ρ for any ion with atomic number z and velocity v, is based on the Bethe theory and its refinements or 'corrections'. The expression may vary in detail depending on the source and the extent to which various corrections are appropriate in the context. Shown below is the expression from ICRU 49:

$$S_{col} = \frac{4\pi e^4 z^2}{m_0 c^2 \beta^2} \frac{1}{u} \frac{Z}{A} z^2 L(\beta) \tag{1.2}$$

where m_0c^2 is the rest mass energy of an electron, A and Z are the mass and atomic numbers of the absorber material respectively, u is the atomic mass unit and β is the particle velocity in units of the velocity of light.

---

[1] However there is a very small dependence on material polarisation, called the density effect which is described later.

The L factor is called the stopping number, and is an essential part of the Bethe theory expression. It is a collection of refinements to the gross definition of energy loss in the factors which precede it. There is a large amount of information required to derive them all, and including it here would be beyond the necessary scope and the reader is advised to refer to ICRU49 for further information. The stopping number is expressed as the sum of three terms:

$$L(\beta) = L_0(\beta) + zL_1(\beta) + z^2L_2(\beta) \tag{1.3}$$

The first term is defined as

$$L_0(\beta) = \frac{1}{2}\ln\left(\frac{2m_0c^2\beta^2W_m}{1-\beta^2}\right) - \beta^2 - \ln I - \frac{C}{Z} - \frac{\delta}{2} \tag{1.4}$$

where C/Z is the shell correction and $\delta/2$ is the density effect (Sternheimer) correction. The parameter I represents the average excitation and ionization potential of the absorber material and is usually determined experimentally or calculated from oscillator strength distributions. For radiotherapy, the I-value for water is of utmost significance but is relatively uncertain due to molecular effects (Gottschalk, 2010). The value used for the stopping power tables in ICRU49 was 75.0 ± 3 eV, but after the work was completed new values of 80 ± 2, 81.8 and 77 eV were reported by Bischel and Hiraoka (1992), Dingfelder et al. (1999) and Krämer et al. (2000) respectively. Values for I differing from 75–80 eV result in stopping power differences of 0.8–1.2% in the energy region of 10–250 MeV for protons (Kumazaki et al., 2007) which consequently has the same impact on the determined dose and range. The maximum energy transfer, W_m, is used as given in equation 1.1 in order to yield the unrestricted stopping power, but sometimes in track structure calculations or precise dosimetry the restricted stopping power is used. This includes only collisions with energy transfers smaller than some fixed cut-off value, and 10 keV is typically used following the recommendation of Spencer-Attix cavity theory (Spencer and Attix, 1955) that it should equal the electron energy required to traverse the cavity of an ionization chamber (10 keV yields a $R_{csda} \approx 2.4$ mm in dry air). This differentiates between the energy lost by a charged particle, and the energy deposited (absorbed dose) as δ-rays above this cut-off can remove energy from the cavity. More discussion on cavity theory is included in section 2.2.1.

The shell correction is only relevant when the velocity of the particle is no longer large compared to the velocities of the bound atomic electrons. As the velocity decreases, the contribution to the stopping power from interactions with K-shell electrons decreases, and this trend continues with the higher shells as the particle's velocity gets ever closer to zero. The density effect correction accounts for the reduction of stopping power due to the polarization of the medium caused by the passage of the particle. It was proposed by Sternheimer (1952), and is only large when the kinetic energy of the particle is of the order of its rest mass energy. For protons, it becomes a 1% level correction only above 500 MeV.

The second and third terms in 1.4 are the Barkas and Bloch corrections, respectively. The Barkas correction is proportional to an odd power of z and accounts for the smaller stopping power experienced by a particle with negative as opposed to positive charge but having the same mass and velocity. The Bloch correction is to correct for the discrepancy between the classical and quantum mechanical treatment of the Bethe formula, and is proportional to z^4 and is only important at low energies.

An approximate way to find the range of a heavy charged particle is to simply assume that the particle loses energy continuously at a rate determined by the stopping power, and that angular deflections due to multiple Coulomb scattering can be neglected. This approach is called the continous-slowing-down-approximation (csda) range, and is expressed as

$$R_{csda} = \int_{E=0}^{E_{max}} \frac{1}{\mathrm{d}E/\mathrm{d}x} \, \mathrm{d}E \tag{1.5}$$

For energies above a few MeV, this is quite a close approximation to the average path length traversed by a charged particle as it comes to rest. However, a more accurate calculation of range needs to account for the departure from linearity near the end of the particle track. ICRU49 provides tabulated values of both the csda ranges and the more useful ‘projected’ range, which does take this into account and gives the average projected depth along a single axis. Both of these are theoretical estimates of range, in contrast to the ‘practical’ range, R_p, which is governed by a measured depth-dose distribution and is described in section 2.1.

As mentioned before, stopping powers and ranges describe the average behaviour of charged particles, but there needs to be appreciation for the random nature of particle transport. The description of the full population of particles in radiation beams is governed by the energy and range ‘straggling’, which means the magnitude of the deviation of energy losses and range from the mean values. In non-thin absorbers, the transmitted energy distribution of an initially monoenergetic beam can be very well approximated by a Gaussian distribution, and a rigorous solution was found by Vavilov (1957). This takes into account the statistical nature of the energy losses by charged particles. This in part contributes to differences in path lengths between individual particles, but also the statistical nature of multiple Coloumb scattering means that every particle takes a different random path through an absorber and this is the other, much smaller, contributor to range straggling. For practical purposes, Molière’s theory (Bethe, 1953) is used. The distribution of particle ranges also follows a Gaussian distribution, although this neglects the minority of particles which either undergo large-angle nuclear (Rutherford) scattering or non-elastic nuclear interactions which substantially reduces the apparent projected range of these particles.

1.1.1.2 Non-elastic nuclear collisions

Non-elastic nuclear collisions refer to those where the incident particle overcomes the Coulomb potential surrounding the target nucleus and has some interaction with via the strong force. As the name suggests, kinetic energy is not conserved in these collisions. The main interactions of note are inelastic scattering, direct reactions, transfer reactions and compound-nucleus reactions. Inelastic scattering involves only an energy and momentum transfer and the original particle continues on its way with no change to the make up of the nucleus. A direct reaction is a ‘grazing’ collision where either the primary particle emerges with less energy or another nucleon(s) is kicked out and this interaction happens on a much shorter timescale. The momentum transfer is usually quite small and so any resultant particles usually depart in the forward-peaked direction. A transfer reaction is where one or more nucleons are transferred between the projectile and target and generally happens at lower energies than direct reactions. A compound-nucleus reaction results in a ‘re-shuffling’ of the nucleus and a nucelon (usually a neutron) is ‘boiled off’. Of concern in particle therapy are the loss of primary particles (which reduces fluence with depth) and the dose characteristics of the secondary particles and their contribution to the total absorbed dose.

Typical reactions of interest for protons in RT are (p,xp$'$), (p,xp$'$n) and (p,xα) reactions, but a wide variety of products exist depending on the target nuclei and proton energy. Secondary charged particles do not stray too far from the primary proton track and so they contribute to the primary dose component. Reactions yielding neutrons or photons lead to energy being carried away from the primary field and contribute to (undesired) whole body dose to a patient. The total cross-section for non-elastic nuclear interactions peaks around 20–30 MeV, suggesting that the contribution to total dose from non-elastic secondaries should be maximum nearer to the BP of a therapeutic beam. However, the energy lost in non-elastic reactions increases almost linearly with proton energy (Paganetti, 2002) and so the maximum dose due to inelastic secondaries occurs further upstream (at higher proton energies). The ‘heavier’ products such as deuterons, tritons, ^{3}He and ^{4}He nuclei contribute the least to the total dose of all the inelastic products. A good illustration of all the dose components for a 150 MeV proton beam can be seen in figure 1.1.

For the case of heavier ions, the repertoire of secondary particles is more diverse as 1 or more nucleons can be transferred to target nuclei or knocked out of the projectile.

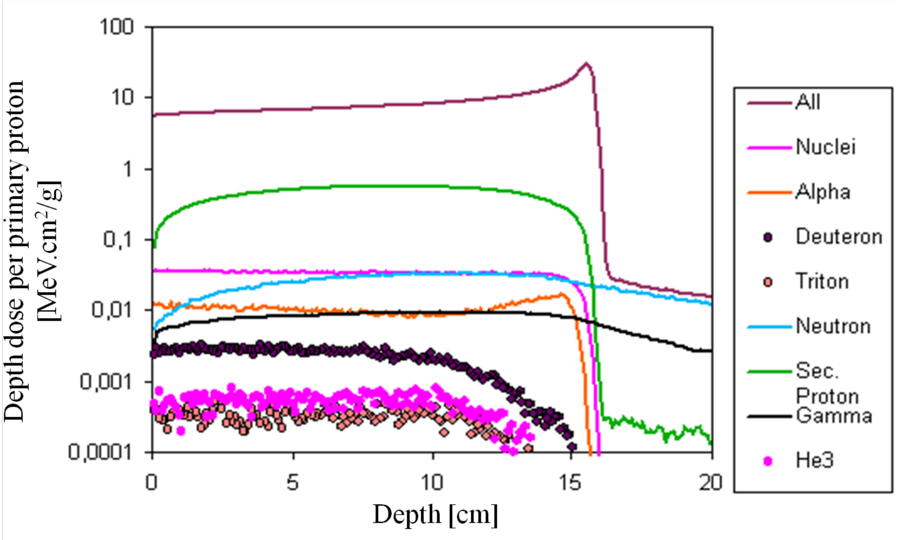

Figure 1.1: Dose components due to inelastic products in a simulated 150 MeV pencil proton beam in water. Note the log scale on the vertical axis. (Reprinted from Soukup et al. (2003) with permission from the author.)

This leads to what is called *ion fragmentation* and is the cause of the significant 'dose tail' beyond the range of the primary particle, as seen for carbon ions in figure 1.3. As these fragments can retain a significant amount of kinetic energy and are lighter, they can have a significant range.

1.1.2 Dose distributions of protons and ions

RT with external proton and ion beams, or ion beam therapy (IBT) has many advantages over more established RT modalities using X-rays or electrons. Unlike X-rays, ions are slowed and stopped in matter, depositing the majority of their energy at the end of their range. To treat deep-seated tumours, proton energies of 200–250 MeV ($\sim$ 400 MeV/n for C^{6+} ions) are required to obtain ranges of the order of 20–30 cm in tissue. The superior dose distributions available with IBT mean that healthy organs in the vicinity of a tumour are more readily spared than with other modalities. This is demonstrated by the Bragg peak (BP) at the end of the proton dose-depth curve, shown in figure 1.2. Two possible configurations for treatment are, i) using passive scattering foils to create a large, uniform radiation field; and ii) scanning with pencil beams, to effectively 'paint' the dose onto the tumour, which are discussed in section 1.1.4. Both scenarios require some form of beam modulation, for passive scattering with a cyclotron source this is usually achieved with a plastic, rotating wheel of stepped thickness to shape the effective particle energy spectrum so that the overall depth-dose distribution within the patient is a spread-out BP (SOBP). Synchrotron beams can instead change the output particle energy directly. This enables maximum dose to be deposited over a volume consistent with the dimensions of the tumour.

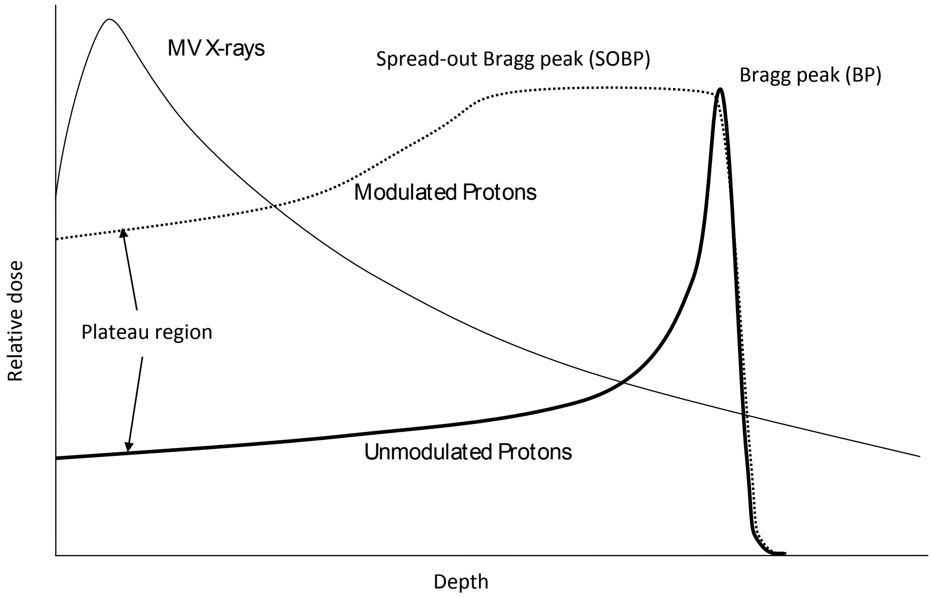

Figure 1.2: Comparison of relative depth-dose curves for megavoltage X-rays, unmodulated and modulated protons (arbitrary energies).

The higher cost of the facilities required is the main drawback of IBT, hence why it is taking longer to establish itself as a widely-available treatment option. Carbon ions as an alternative to protons are also being realised, as they can potentially more readily spare healthy tissue and better treat radio-resistant tumours and those with a poor blood supply leading to lower oxygen levels. The main drawback however is the side production of secondary contaminant particles in the treatment field when passive scattering and/or beam modulation are used.

There are approximately 30 proton therapy (PT) centres worldwide with 2 providing carbon ion therapy in addition, with another 4 carbon ion only centres. By the end of

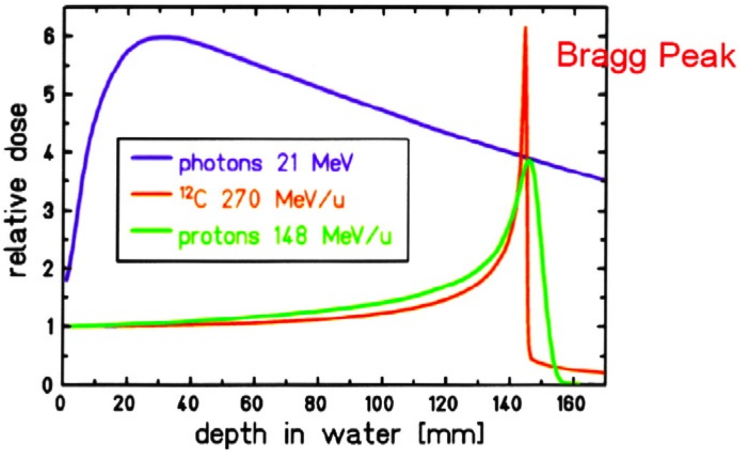

Figure 1.3: Comparison of measured Bragg curves for 148 MeV/n protons, 270 MeV/n carbon ions and 21 MV photons. (Reproduced from Fokas et al. (2009) via Rightslink license 2473741071127).

2009, in total over 67,000 patients had been treated with protons and 7000 with carbon ions according to the Particle Therapy Co-Operative Group (PTCOG, 2010) and these numbers will increase exponentially as the number of centres proposed or under construction at any time continues to rise. Of the existing PT centres, 7 are limited to lower proton energies between 60–72 MeV (effective range of ≈30 mm) and used exclusively for ocular tumours. One such example is the Clatterbridge Centre for Oncology (CCO) in Wirral, UK. Clinical scientists there have been collaborating with the National Physical Laboratory (NPL), the UK's National Measurement Institute to develop a primary standard for absolute dosimetry in PT, as no such standard currently exists for any form of IBT.

1.1.3 Radiobiological benefit of ions

In RT terms, the effect of radiation on biological cells is usually characterised by the likelihood of cell death. Whilst radiation can cause ionization in any part of a cell, most consequences are minor chemical changes and hydroxyl free radical formation in non-critical cell structures. The terminal damage can only occur when the strands of DNA contained within the cell nucleus are broken to the degree that upon the repair period of the cell cycle, if the strands cannot be correctly repaired then the cell will undergo apoptosis, i.e. programmed cell death. Usually, single-strand breaks (SSB) alone are not sufficient to kill a cell as enough information is retained on the other side of the DNA double helix for the base-pair to be correctly re-established. If a double-strand break (DSB) occurs, then apoptosis is a much more likely outcome.

There are two possible mechanisms for DNA damage, *direct* and *indirect*. *Direct* damage occurs when ionizing radiation interacts with DNA molecules, and *indirect* damage is when radiation induces formation of highly reactive hydroxyl free radicals in the surrounding cell medium which then attack the DNA. For lower LET radiation such as X-rays and electrons, the *direct* damage almost always results in SSBs and so cell death relies on nearby *indirect* damage contributing to DSBs. The likelihood of this occuring has significant dependence on the oxygenation of the tissue containing the cells. Higher LET radiation such as heavy ions, or low energy protons ($\lesssim 5$ MeV) cause such a higher density of ionization around their tracks that direct DSBs are much more likely when passing through the cell nucleus and the reliance on *indirect* damage (and sufficient oxygenation) is reduced. This has two benefits, in that cells can be killed more efficiently than with lower LET radiation but for the same total absorbed dose, and that hypoxic tumours resistive to (for example) X-rays can be more effectively treated. The quanitification of this effect is the relative biological effectiveness (RBE) which is the dose of reference radiation divided by the dose of user radiation required to give the same biological effect.

RBE depends on many factors, such as radiation type and energy (or *quality*), absorbed dose, the type of cell, oxygenation, cell cycle repair and the cell endpoint of interest. Over the last 40 years or so, a lot of effort has been expended in measuring RBE for a wide number of these factors and biological models are ever becoming more successful in predicting cell response in different conditions. Table 1.1 lists typical RBE values for different radiation types used in RT. By definition, the RBE of (250 kV) X-rays = 1 as it is the reference radiation quality.

The relationship between S, the fraction of cells surviving a radiation dose, D, can

Table 1.1: Typical RBE values for different radiation qualities.

Radiation quality	typical RBE
250 kV X-rays	1.0
MV X-rays	1.0
electrons	1.0
protons	1.1–1.5[a]
C^{6+} ions	1.5–5[a]
fast neutrons	4–5

[a] The higher values occur toward the end of the particle range where LET increases.

be modelled by the *linear-quadratic model*. This model assumes that a cell can either be killed by a single lethal event, or by an accumulation of sublethal events. If these modes of cell death are assumed to be independent, then:

$$S = e^{-(\alpha D+\beta D^2)} , \tag{1.6}$$

where α and β are constants. The resulting curves look like those in figure 1.4, which illustrates the main biological difference between low and high LET radiation. Cells exposed to low LET radiation exhibit a 'shoulder' in their response, whereas for high LET radiation the response is more linear. The graph also illustrates how RBE can be calculated for C^{6+} ions at different survival levels and that it will differ depending on the value of S.

With a higher RBE than protons and a sharper BP (higher peak-to-plateau ratio), some might argue that protons are an intermediate step between photons and carbon ions and perhaps may be made redundant in future. However, in the short term there are many complications with carbon ion treatment planning and dosimetry due mainly to the fragmentation within the patient and the dose tail beyond the BP. The large change in RBE with depth for a C^{6+} beam also means that to produce a biologically flat SOBP at some depth requires very different modulation as less physical dose is required at the distal end of the SOBP than in the proximal. This also requires very accurate modelling

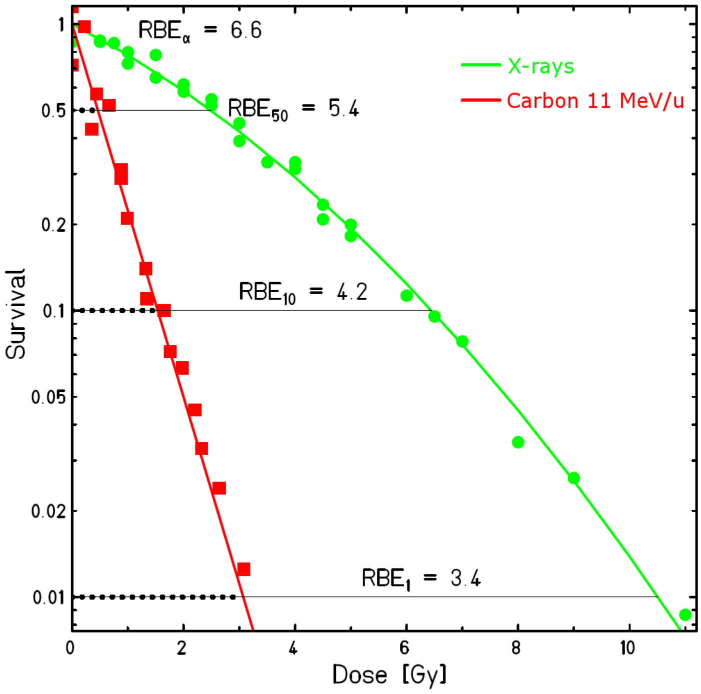

Figure 1.4: Cell survival curves for X-rays and C^{6+} ions. (Reproduced from Weyrather (2005)).

for different tissues in the beam path in order to deliver a biological dose with the same order of certainty as in convetional RT. Potentially however, it can allow for higher doses to be delivered to the target without exceeding normal tissue limits, and permits dose escalation and hypofractionation of treatment to reduce total treatment time and increase patient throughput. But until the biological, dosimetric and economical challenges are overcome, carbon ion therapy is likely to remain the more unfamiliar cousin of proton therapy for the time being.

1.1.4 Treatment delivery techniques

Unlike RT with X-rays and electrons, the accelerators used in IBT are not currently mounted on the same gantry which delivers the beam to the patient. A synchrotron is far too large to be arranged in a gantry, and a cyclotron is generally also too large although recently a concept by Still River Systems (Littleton, MA, USA) incorporating a compact superconducting cyclotron may be the first of its kind to be used clinically. By using a superconducting magnet, chilled to a few degrees Kelvin, more intense magnetic fields can be achieved resulting in a smaller radius of orbit (see equation 1.7 later), hence reducing the size of the device. As of March 2011 it is still awaiting approval by the US Food and Drug Association (Still River Systems, 2011).

In a typical IBT centre, there is just one accelerator which can feed 3–5 treatment rooms and the beam is easily switched between rooms so that patients can be setup while the beam is delievered to another. Once the beam transport systems have delivered the beam to the room, there are two ways of then delivering it to the patient: via a fixed beamline (normally horizontal) or via a rotational gantry for more flexible delivery. The latter option requires a very large mechanical structure and beamline with large magnets in order to take an initially horizontal beam and have it potentially rotate about an isocenter with millimetre precision. A typical gantry can weigh several hundred tons for protons, and even more for heavier ions due to the larger magnets required.

The first IBT treatment systems introduced clinically used passive scattering systems to spread an initially narrow beam into a large uniform field. Often this involves at least two scattering foils with some separation to achieve large fields. An energy modulation device, either a rotating stepped wheel or a ridge filter (Chu et al., 1993) is then required to produce the clinical SOBP in the target volume. Between the nozzle exit and the patient is placed a patient-specific collimator to shape the beam laterally to conform to the tumour, and a range compensator may be used to correct for patient surface irregularities (see figures 1.5 and 1.6).

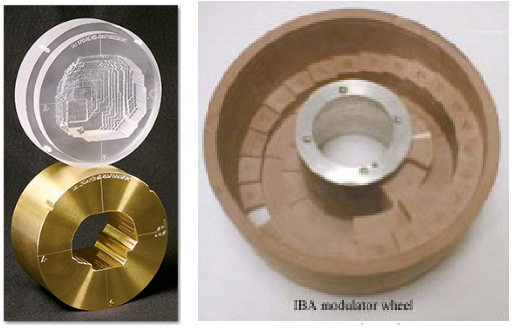

Figure 1.5: Example of a patient-specfic brass collimator and acrylic compensator (left) and an IBA modulation wheel (right). [Images from www.oncolink.org]

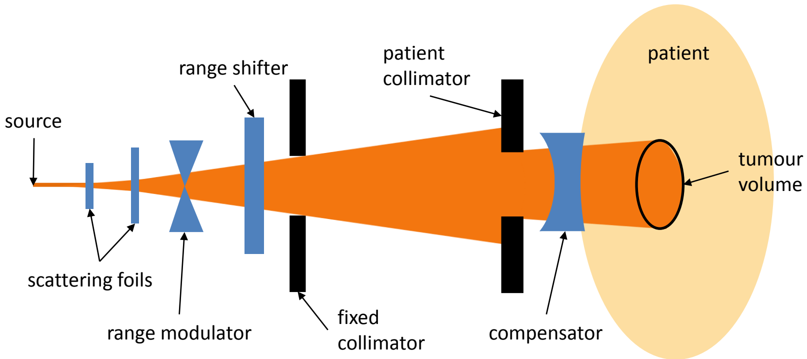

Figure 1.6: Schematic of a passive scattering system. Note the shape of the compensator determines the shape of the distal dose distribution.

More recently, active scanning techniques are being used in place of passive scattering. These involve using sets of magnets to deflect the beam laterally in two dimensions, effectively raster scanning a pencil beam across the target. By using a range shifting wedge (or energy selection from the source) the dose can be ‘painted’ in 3 dimensions by putting a BP in each target voxel (see figure 1.7). This type of treatment is called intensity modulated particle therapy (IMPT) and can deliver a more conformal dose distribution and avoid unwanted secondary neutrons produced in scattering foils and collimators. However, this technique is more sensitive to target movement during treatment and uncertainties in proton ranges in tissue. It is also much more complex to implement, and an intermediary step in delivering this type of treatment is uniform scanning where the scanned beam intensity is uniform over the treatment field, multi-leaf collimators (MLC) define the shape of the field and a compensator is employed as per the passive scattering technique.

1.2 Methods of ion acceleration

1.2.1 Cyclotron

The cyclotron is the best known and most successful device for acceleration of ions to millions of electron volts. It was invented by Ernest Lawrence in 1929, and the first working model produced 80 keV protons in 1930. It uses a large magnet to constrain the

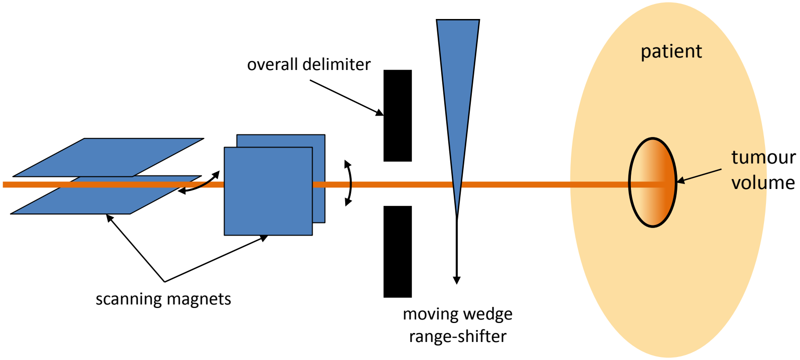

Figure 1.7: Schematic of an active scanning system. Fewer beamline components are necessary, as the beam is raster scanned in all 3 dimensions by use of magnets and an energy shifter or by changing beam energy at the source.

motion of the particles in a spiral path, and they are accelerated by a radio frequency (RF) electric field every time they enter into the opposite semi-circular section (called a “dee”). A large potential difference is applied across the gap between the dees, giving the particles a ‘kick’ on every half-orbit. As they gain energy, the radius of their path increases and so they spiral outward until eventually they are extracted at the maximum radius (and energy) allowed by the cyclotron dimensions. In the non-relativistic case, the centripetal force is constituted of the force due to the transverse magnetic field, B:

$$\frac{mv^2}{r} = Bqv \; , \tag{1.7}$$

where m is the particle mass, v its velocity, r the radius of its orbit and q its charge. Since angular frequency, $\omega = 2\pi f = v/r$, equation 1.7 can be written as

$$f = \frac{Bq}{2\pi m} \; . \tag{1.8}$$

This shows that for a particle with constant mass, f is not dependent on r and so a fixed RF can be used. However, as particles become accelerated to velocities approaching the speed of light this convenience no longer holds. To counter this, there are two possible modifications: operating in pulsed mode with a variable RF (*synchrocyclotron*) or increasing the B field with radius (*isochronous cyclotron*).

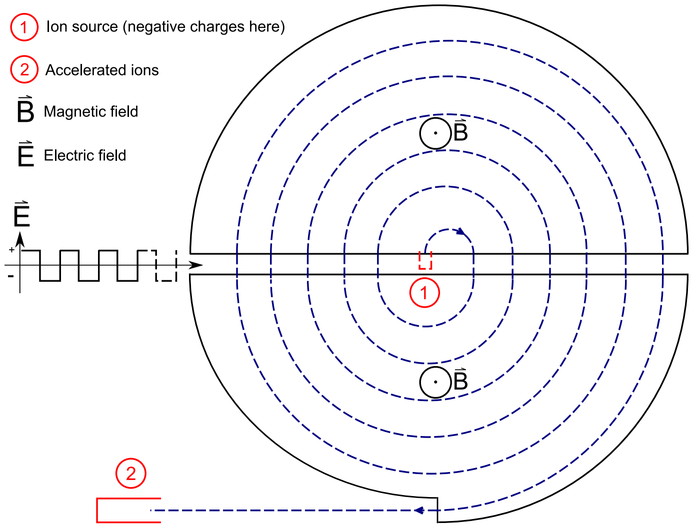

Figure 1.8: Schematic of a cyclotron. The two semicricles are the dees.

The Birmingham cyclotron is a Scanditronix MC40 isochronous cyclotron capable of accelerating protons and light ions to maximum energies of approximately 40 MeV/n and uses a RF of 20 MHz. It is predominantly used to produce protons with a nominal kinetic energy of 29 MeV for the production of ^{81}Rb which is then transported to local hospitals daily for use of its decay product, ^{81m}Kr, in lung ventilation imaging. Protons of this energy and lower are synonymous with therapy protons in the last centimetre of their range, where accurate dosimetry with ion chambers and GafChromic film becomes more difficult due to the non-constant ratio of water to air stopping power ratios with lower proton energies and the steep increase of linear energy transfer (LET). Having easy access to a low-energy beam has allowed for better investigation of these effects, so in this way the Birmingham cyclotron is very well suited for this work.

1.2.2 Synchrotron

The synchrotron was developed to overcome the limitations of the cyclotron imposed by special relativity on the maximum energy attainable. Instead of the orbital radius increasing with energy, it is (more or less) fixed and the particles can therefore be contained within an evacuated beam pipe of customised radius. This can vary from the order of metres (for energies of a few hundred MeV), to kilometres (TeV energies). The particles actually travel in straight segments, with bending magnets in between each segment. The acceleration is provided again by a RF oscillator that supplies an energy boost each time a particle passes through the accelerating cavity. As the particles increase in energy and velocity, the RF must be increased in frequency in order to keep in phase with the angular frequency of the particles and the magnets must be ramped up in synchrony which presents quite a technical challenge. The consequence is that a synchrotron beam is highly pulsed, as bunches of particles must be accelerated one at a time and only when they are at the required energy are they 'spilled' out, and the next bunch can be injected. This has an advantage in that the energy can be changed very rapidly. Conversely, a cyclotron beam is considered virtually continuous but a change in energy requires completely retuning the cyclotron parameters which can take some time.

1.2.3 Promising alternatives

Current developments in designing more compact accelerators, such as the dielectric wall accelerator (DWA) (Mackie et al., 2007; Caporaso et al., 2008), non-scaling fixed field alternating gradient (NS-FFAG) accelerator (Edgecock, 2006) and laser-plasma sources (Bulanov et al., 2004) promise to reduce the footprint and eventually the cost of these systems by simplifying the beam transport systems in different ways.

The DWA being developed at the Lawrence Livermore National Laboratory in partnership with the Compact Particle Accelerator Corporation (CPAC) is a linear accelerator hoped to be capable (when complete) of accelerating protons to around 150 MeV over just a few metres. Such a small accelerator is envisaged to be mounted directly onto a rotating ring style patient gantry, resulting in a single room PT solution that can be installed in most existing linac bunkers. There are three key enabling technologies behind this development: high-gradient insulators which allow for substantial increases in voltage holding capacity, dielectric materials with embedded nano-particles which facilitate the transmission and isolation of extremely high voltages, and optical switches which can control these high power loads compactly and at ultra-high speeds. At the time of writing, CPAC state that the first half of 2013 should see the first clinical shipment of the finished device.

The NS-FFAG accelerator project is being led by the British Accelerator Science and Radiation Onoclogy Consortium (BASROC), and aims to produce a more compact alternative to the conventional cyclotron. Like the cyclotron, it uses fixed magnetic fields but in a more effective way. The three main differences to the cyclotron are more strongly focussing fields, much higher momentum compaction ($\frac{dp/p}{dr/r}$) and non-isochronicity. Essentially it combines the best features of the cyclotron and synchrotron together, providing fast energy selection between pulses but cycling much quicker than a synchrotron. By being smaller and using more compact magnets, this reduces both the size and potentially the cost of the device. At the time of writing, a 10–20 MeV electron proof of principle machine (EMMA) has been successfully built and demonstrated, and work is ongoing with an ion version (PAMELA) which should be capable of delivering 250 MeV protons and 450 MeV/u carbon ions.

Laser-plasma acceleration is a rapidly developing field involving many groups worldwide, and in the UK there is the Laser Induced Beams of Radiation and their Applications (LIBRA) consortium, which this work is part of and is discussed in the next section.

1.3 Laser-plasma acceleration and LIBRA

1.3.1 Introduction and motivation

LIBRA is a consortium funded by Research Councils UK under the Basic Technologies scheme. The principle aims are to produce high quality radiation beams (primarily X-ray, proton, and ion) via ultra high-intensity laser pulses incident on wafer targets, that can be used for a wide range of applications such as RT, semiconductor production and rapid detection of hidden explosives. There are 9 member institutions involved in developing and testing the technology, assigned to the following four categories of investigation: A - targetry, B - interaction environment and detectors, C - source property demonstration and D - application tests. The work of the Birmingham group falls into the latter, specifically focussing on the task of dosimetry during the developmental stages and demonstrating the treatment potential from the final laser-proton/carbon ion source. A list of all the members of LIBRA and their roles is given in table 1.2.

Table 1.2: The identities and roles of the institutions forming the LIBRA consortium.

Institution	Area of investigation
University of Birmingham	D
Imperial College London	A
NPL (contractors)	D
University of Paisley	B, C
Rutherford Appleton Laboratory (RAL)	A, B, C
Queens University Belfast (QUB)	B, C
University of Southampton	A, B
University of Strathclyde	B, C
Surrey Ion Beam Centre	D

In existing proton/carbon ion therapy centres, the gantries which deliver the radiation to the patients are colossal machines weighing approximately 100–600 tons (for protons and carbon ions respectively) that must be rotated about a patient with millimetre accuracy. This part of the treatment delivery system represents a significant portion of the total cost, and if a laser based acceleration system could be used instead, large magnets could be replaced by simple optics and the target could be situated in the gantry a few metres or so from the patient. Laser technology is advancing such that within the projected timescale of such a facility being built, high power lasers will have become more affordable and compact than the cyclotrons/synchrotrons currently required to perform the particle acceleration, or at least comparable in both aspects.

The Birmingham group are also joined in this work by NPL who have been subcontracted to provide dosimetry equipment and act as a consultancy. During the work of

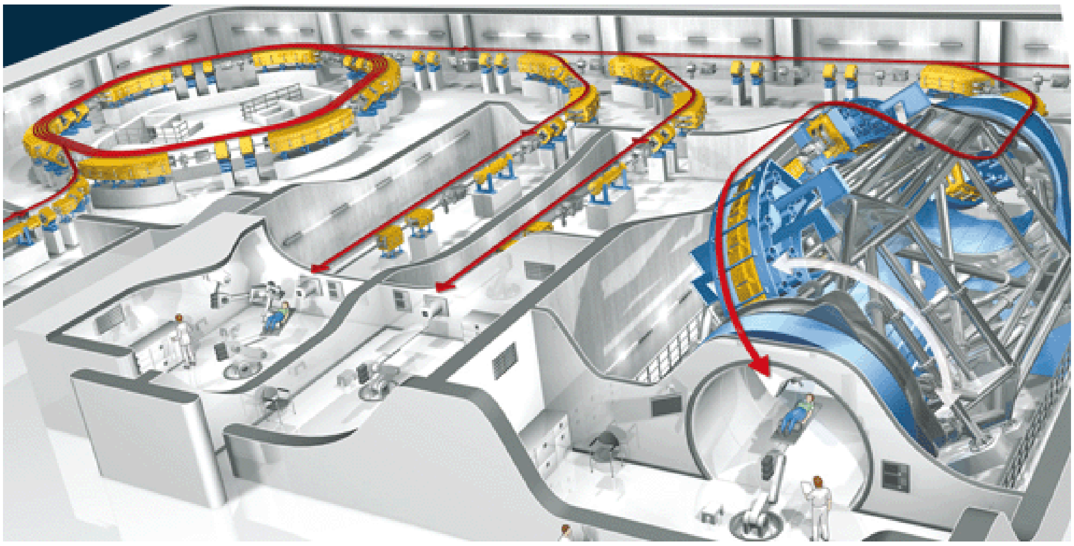

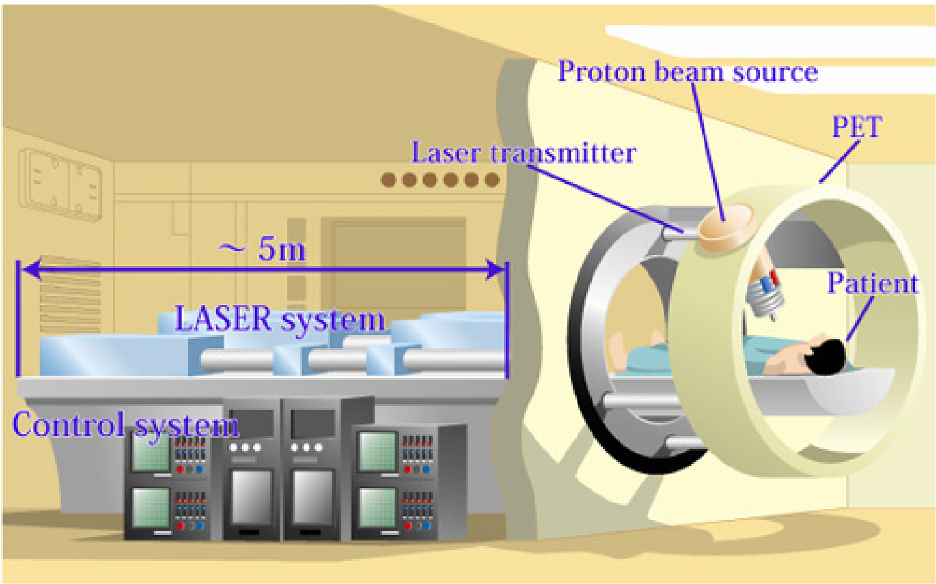

Figure 1.9: Schematic of the beamlines and multiple-ion gantry at the Heidelberg Ion-therapy Centre (top) and illustrative proposal of what a laser-ion treatment facility might look like (bottom; taken from the Photo-Medical Research Centre website (JAEA, 2010)).

this thesis, NPL have loaned the Birmingham group 2 PTW Markus ionisation chambers and passed on much of their knowledge and expertise.

While IBT protocols and techniques are becoming more established, the motivation for further research within the LIBRA project is mainly due to the unique, high intensity pulsed nature of the beam; in contrast, a cyclotron-produced ion beam is regarded as continuous (AAPM, 1986). Currently there is uncertainty as to how conventional dosimeters will respond to the laser-produced pulsed radiation. For air ionisation chambers, a very large ion recombination effect resulting in a severe under-response is expected which limits the use of this type of detector in a laser-ion source. However it is a crucial reference detector for calibrating and quantifying the relative response of passive detectors in a standard particle beam. Passive detectors such as films, gels, calorimeters or thermoluminescent dosimeters (TLDs) are expected to cope better with the short time profile of the radiation pulses, but tend to have a highly energy-dependent response with protons. This tends to happen below energies of around 10 MeV where the higher LET can start to locally saturate sensitive elements of passive detectors. In these early stages of laser-acceleration, the typical proton energies being produced are only up to tens of MeV and so accurate determination of the response to low enegy protons is critical to the use of such a detector in a laser-proton beam. In clinical proton dosimetry, the vast majority of measurements are made in fields of protons with much higher energies and so these effects mainly become significant nearer the end of the proton range.

For laser-accelerated ions heavier than protons, the energies being produced are not sufficient to give them any significant range in a detector compared to the protons and are much fewer in number. They are typically filtered out using a metallic foil unless their acceleration is being specifically investigated, in which case different targets are usually used (such as a diamond-like carbon).

1.3.2 Overview of theory

Charged particles from laser-plasma interactions of energies upto a few MeV have been produced for nearly the past 30 years (Allen et al., 2003). Early experiments at the Helios laboratory at Los Alamos using 'long' nanosecond pulses on foils and wires produced protons and multiple charge states of carbon of energies up to ∼0.5 MeV (Begay and Forslund, 1982). Interestingly, hydrogen and carbon nuclei were accelerated regardless of the composition of the target and the source was attributed to hydrocarbon contaminants within the vacuum system, hence they were accelerated from the surface of the target. The acceleration mechanism was shown to be the result of extremely high (but short-distance) electrostatic fields created by the charge separation in the plasma. The maximum ion acceleration correlated strongly with the temperature of the hot electrons. The laser intensity in this pioneering experiment was around 10^{15} W cm^{-2}, but intensities currently attainable are of the order of 10^{21} W cm^{-2} and this rapid increase owes much to the development of chirped pulse amplification (CPA), as shown in figure 1.10.

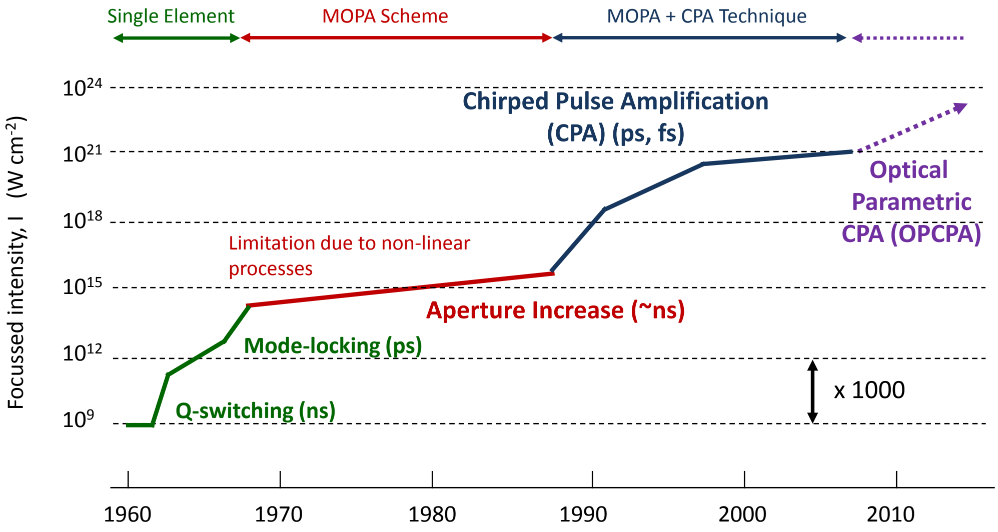

Figure 1.10: The improvement in laser intensity achieved over the last 50 years. Each increment on the vertical axis corresponds to 3 orders of magnitude.

CPA involves 'stretching' the original pulse temporally and spectrally using a pair of dispersive gratings (or prisms), giving a lower intensity wave which is safer to amplify, and then compressing it back to a short pulse using another pair of gratings (or prisms) which reverses the dispersion. It is thought the limit of this technique has been realised, and so to reach higher intensities researchers are looking to combine CPA with optical parametric amplication (OPA) using nonlinear crystals. This technique has the added advantage of providing many decibels of gain without complicated multipass geometries, and so can be simpler and more compact (Paschotta, 2010).

1.3.2.1 Target normal sheath acceleration

Recent experiments with petawatt class lasers and foil targets have achieved proton energies up to a maximum of 58 MeV and heavier ions up to hundreds of MeV (Clark et al., 2000; Hatchett et al., 2000; Allen et al., 2003; Breschi et al., 2004a; Yang et al., 2004; Hegelich et al., 2006). When a laser pulse with intensity around 10^{19} W cm^{-2} impinges on a foil, the laser field interacts with the target electrons and accelerates a large number of them to relativistic velocities. Some of these 'hot' electrons exit the rear surface of the foil as a kind of 'sheath', and in doing so construct an electrostatic field between themselves and their (now stripped) parent nuclei. This field can exceed 1 TV m^{-1} at the rear surface (over a distance of a few μm), which surpasses the typical acceleration field of a conventional accelerator by around 6 orders of magnitude. This potential is then predominantly converted to kinetic energy of the hydrocarbon contaminants that were present on the rear surface. Protons (originating from hydrogen atoms) have the largest charge-to-mass rato by at least an order of 2, and so are the most efficiently accelerated species of ion. This mechanism is referred to as target normal sheath acceleration (TNSA) and is described in more detail by Wilks et al. (2001). The complete picture sees a variety of ion species also with different charge states being accelerated concurrently, as well as escaping hot (multi-MeV) electrons and X-rays (mostly bremsstrahlung). This mix of radiation can be partially tailored by carefully choosing the target composition, geometry and thickness (and even phase), as well as the laser parameters (i.e. energy, pulse duration, polarisation).

Another feature of these interactions is the large peak current of particles generated: a single pulse can generate $\sim$ 1 kA at peak of proton current at 1 mm distance from the target (Yogo et al., 2009). A defining characteristic of a TNSA particle energy spectrum is a Maxwellian distribution, which peaks at low energy and tails off exponentially to higher energies, before reaching the cut-off, or E_{max}. Example spectra are shown in figure 1.11. The relationship between laser intensity, I, and E_{max} for protons has been investigated by Robson et al. (2007) and a simple scaling law of the form $E_{max} = a \cdot I^b$ provides a good fit where $b = 0.5 \pm 0.1$. This indicates that to reach therapeutic energies in excess of 200 MeV with the TNSA regime, laser intensity must increase appproximately 16-fold.

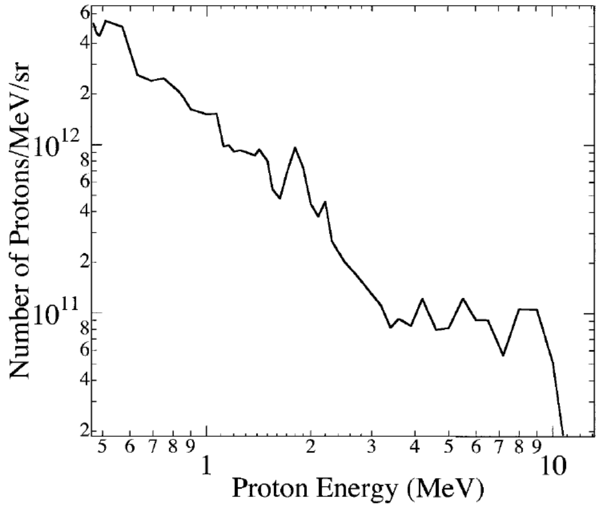

Figure 1.11: An example proton spectrum measured by a Thomson parabola spectrometer. (Reprinted with permission from Clark et al. (2000). Copyright 2001 by the American Physical Society)

A very widely spread energy spectrum is far from ideal in terms of what is required for particle therapy, where often a highly monoenergetic beam is produced to begin with and changed or degraded to the energy profile required to produce the necessary dose distribution in the patient. In this scenario, the only practical solution would be to utilise an energy selection system such as that proposed by Fan et al. (2007) in conjunction with a modulation system such as that proposed by Schell and Wilkens (2009). The disadvantages of this solution is that $\gg 99\%$ of the energy is wasted in unused particles which are dumped, and the corresponding secondary radiation requires significant shielding from the patient and places the target at a further distance than ~ 1 m as ideally proposed.

Double layer targets have been proposed as a means of 'cutting out' the low energy portion of the spectrum to leave a quasi-monoenergetic beam, and work is ongoing (although not within the scope of LIBRA) to realise their potential from particle-in-cell (PIC) simulations in experimental results (Bulanov et al., 2004; Weichsel et al., 2008). Another method of reducing energy spread is described by Ter-Avetisyan et al. (2008), which involves using two quadrupole magnets as a lens to selectively focus and collimate a particular proton energy, which leads to a more monoenergetic beam as protons of other energies will be more divergent. The geometry and field strengths can be tailored in principle to select any energy required.

1.3.2.2 Radiation pressure acceleration

An alternative regime of acceleration was described by Robinson et al. (2008), called radiation pressure acceleration (RPA). In principle this regime is a very efficient means of using lasers to accelerate particles, by imparting momentum directly to the object to be accelerated. Simple analytical models based on momentum conservation imply that $E_{max} \propto (I\tau/\sigma)^{\alpha}$, where τ is the pulse duration and σ is the areal mass of the target foil. When $v_{final}/c \ll 1$ the exponent, $\alpha = 2$ but in the ultrarelativistic limit $\alpha \rightarrow 1/3$ which should provide much more favourable intensity scaling than with TNSA for energies of several hundred MeV (where $v/c \approx 0.5$). The question is whether at any accessible laser parameters, this regime can dominate over TNSA and indeed Robinson et al. (2008) identified a realistic RPA scheme for current laboratory lasers by using circularly polarized light. PIC simulations in one and two dimensions predict a step change in laser-accelerator performance, and narrower energy spreads at higher proton energies. They demonstrate theoretically that a complete switch from TNSA to RPA could be obtained at intensities around 10^{21} W cm^{-2}; within the reach of today's most powerful lasers. However, the simulations used a foil made completely of protons with a corresponding electron density to ensure charge neutrality. In simulations where the target was a mix of protons and

C^{6+} ions, the carbon was accelerated almost as efficiently as if it was a pure carbon foil, whereas the proton energy suffered greatly. This indicates that for the full benefits of RPA for protons to be realised, some technical challenges need to be overcome but it has brighter prospects for heavier elements where pure, solid targets can be constructed more easily. Hydrogen gas jets would appear to be the answer, but it is very difficult to achieve the critical plasma density necessary for RPA (Pogorelsky et al., 2010).

1.4 Scope of work

The work in this thesis is focussed predominantly on the detection and dosimetry of proton and ion beams from a conventional accelerator and a laser-plasma source; namely the Birmingham cyclotron and the TARANIS laser at Queens University Belfast. While there is a great appreciation for how these two types of acceleration work, the work presented in this thesis concerns itself primarily with dosimetry rather than the technology involved in producing these beams.

The early work on the Birmingham cyclotron gave the opportunity to establish a protocol for dosimetry using first an ionisation chamber, and then various models of GafChromic film, a type of radiochromic film. The relatively stable, mono-energetic beam was essential for investigating the dose response of these films versus proton energy so that they could later be used with great accuracy to determine dose as well as spectral information from the much more complex multi-energy, multi-radiation laser-plasma source. By the end of this period of work the films were being successfully applied to radiobiological experiments by measuring dose deposition to cell layers from laser-accelerated protons of different energies. Unfortunately this experiment was still ongoing at the conclusion of this thesis and so only the work done in preparation for this experiment is included here.

Some other, less significant but interesting pieces of work carried out with the Birmingham cyclotron are mentioned in section 7.5.

CHAPTER 2

METHODS OF ION DOSIMETRY

This chapter aims to describe the very well established practice of measuring absorbed dose-to-water using an ionisation chamber (often just referred to as an ion chamber), specifically following the most recent code of practice (CoP) for proton and ion dosimetry in report TRS-398 by the International Atomic Energy Agency (IAEA, 2000). Radiochromic film, in particular the various models of GafChromic film, features heavily in this work and so the necessary considerations in order to perform accurate dosimetry with it are also discussed here.

2.1 Code of practice for proton dosimetry

In all modalities of external beam RT, the air ionisation chamber has become the most important tool in dosimetry. As 3-dimensional conformal RT progresses with ever more complex techniques, so it is necessary for dosimetric technology to develop alongside in order to ensure the safe and accurate delivery of such techniques. Ionisation chambers alone can not always meet this challenge, as they are somewhat less flexible than other passive detectors — however, it is important to stress that they are the gold standard for clinical traceable dosimetry and any other secondary detector should be calibrated by one. Absorbed dose-to-water (D_w) is the main quantity of interest in RT as it is closely related to the biological effects of radiation. There are many advantages of performing calibrations in terms of D_w such as reduced uncertainty, a more robust system of primary standards and use of a simple formalism. More detail of these advantages are given by Rogers (1992). Primary Standard Dosimetry Laboratories (PSDLs) have now generally adopted the use of water or graphite calorimeters (the latter at NPL) to measure absorbed dose, and provide dose-to-water calibration factors, $N_{(D,w)}$ for ^{60}Co. It should be noted that NPL is unique in that it also provides $N_{(D,w)}$ for γ-rays, megavoltage (MV) X-rays and electrons. This switch from air-kerma calibration factors has only happened in the last decade or so, with the intention of reducing uncertainty in the dosimetric chain. PSDLs are now investing in clinical linacs in order to produce sets of calbration factors at different beam qualities, i.e. for electrons and photons at different commonly used energies. The prohibitive cost of a stand-alone proton therapy system means that any primary standard calorimetry work has to be done off-site at a PT centre. NPL are now in the latter stages of developing a portable hadron calorimeter (Palmans et al., 2004), which will aim to bring the standard of proton and heavy ion dosimetry to a similar level as for electrons and photons.

The other challenge in proton dosimetry lies in determining ideal reference dosimeters for characterising depth dose and lateral dose distributions of clinical beams. Generally, an ionisation chamber should be used whenever possible (IAEA, 2000), but for lateral and 2-dimensional dose distributions other dosimetry media are becoming more widely used. Examples of other possible dosimeters are: radiochromic film (RCF), alanine pellets, Fricke or polymer gels, diodes and TLDs.

In choosing a beam quality specifier, past proton dosimetry protocols and recommendations (ICRU, 1999) used an effective energy parameter, which is defined as the energy of a mono-energetic proton beam having the same range as the residual range R_{res} of the clinical beam at a measurement depth z. The definition of R_{res}, in units g cm^{-2} at depth z is

$$R_{res} = R_p - z$$

where z is the depth of measurement and R_p is the practical range of the protons (both expressed in g cm^{-2}). R_p is defined as the depth at which the absorbed dose falls to 10% of the maximum dose on the distal edge of the BP or SOBP. This is illustrated in figure 2.1.

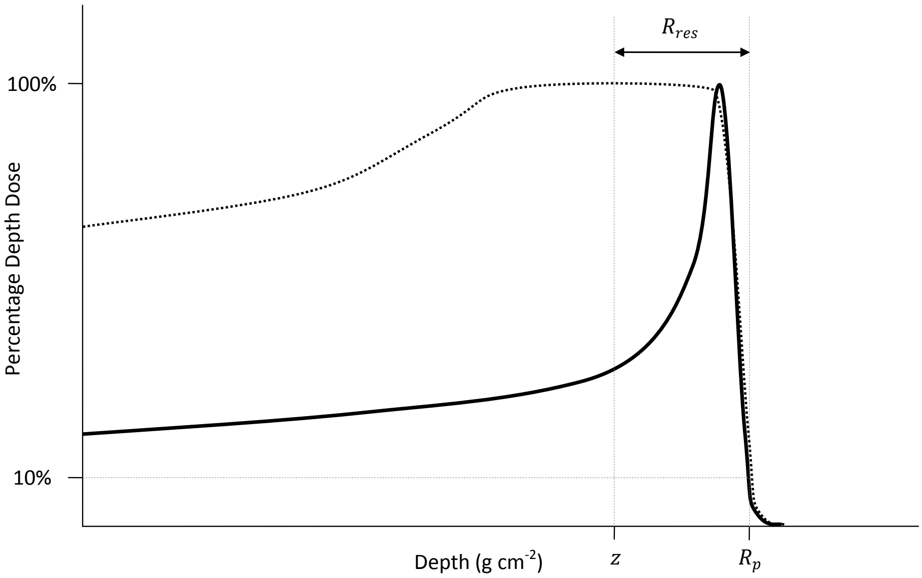

Figure 2.1: Illustration of the definitions of z, R_{res} and R_p on the percentage depth dose (PDD) curves for modulated and un-modulated proton beams of the same maximum energy.

It should be noted that all depths refer to depths in a water phantom, however in the case of low energy protons (< 100 MeV) TRS-398 approves the use of plastic phantoms. In this case, the dosimeter reading should be multiplied by the water-to-plastic fluence scaling factor (which is a function of depth) h_{pl} which is not known. At these lower energies, inelastic scattering or nuclear capture of protons make up less than 1% of the interaction cross-section and so h_{pl} is assumed to be unity; hence only at these lower energies is the use of plastic phantoms approved.

To convert depth in plastic to depth in water, the depth in cm should be multiplied first by the measured density of the plastic, and then by a depth-scaling factor c_{pl} which to a good approximation, can be calculated as the ratio of CSDA ranges in water and plastic. TRS-398 states the value of c_{pl} to be 0.974 for PMMA which is obtained using ICRU recommended stopping powers for protons (ICRU, 1993). These are published in tabulated form, but are available at custom energies from the National Institute of

Standards and Technology online resource called PSTAR (Berger et al., 2005).

Use of a plane-parallel ion chamber is highly recommended for depth-dose measurements, and the effective point of measurement is the inside surface of the entrance window. The window thickness should also be scaled to the water equivalent thickness and be included in the evaluation of measurement depth, z.

2.2 Ionisation chamber dosimetry

Measuring the energy absorbed per unit mass in a medium (i.e. the absorbed dose) which is exposed to ionising radiation requires the insertion of a radiation detector into the medium. Usually this detector will differ in both density and atomic composition to the medium and represents a discontinuity, and is referred to as a *cavity*. In an ion chamber this cavity is usually filled with atmospheric air, partly due to its ready availability but also because radiation exposure (measured in roentgen) is defined in terms of ionisation in air. Consequently, air has been subjected to the highest number of experimental measurements of the mean energy required to create an ion pair, W. This value is always larger than the ionisation potential as some energy is expended in nonionising processes such as excitation.

If an electron liberated by an incident particle has enough energy to excite or ionise another atom, it will eventually lose that energy and become a subexcitation electron. These electrons will then constitute the measured ionisation charge or current measured by the detector. In a gas such as air, they mostly attach to oxygen atoms due to their high affinity for electrons and the polarising voltage applied across the chamber's planar electrodes separates the ion pairs and collects them. Hence the magnitude of collected charge is proportional to the energy deposited in the cavity. The number of ion pairs produced can be calculated by dividing the kinetic energy of the particle absorbed in the air cavity T, by the average energy required to produce an ion pair in air by a particle imparting all its energy to the gas, W_{air}. For protons with more than a few MeV however, the differential value w_{air} is more appropriate as they only deposit a fraction of their kinetic energy, ΔT, while traversing a layer of layer with thickness Δx (Jones, 2006). The relationship between w and W is given by

$$w(E) = \left[\frac{d\left(\frac{E}{W(E)}\right)}{dE} \right]^{-1} \quad ,$$

$$W(E) = \frac{E}{\left[\int_I^E \frac{dE'}{w(E')} \right]} \quad ,$$

where I is the ionization threshold energy of the gas. It can be seen that data on $W(E)$ in the region of E allow derivation of $w(E)$ there, but data on $w(E)$ over the full range from I to E is required to derive $W(E)$.

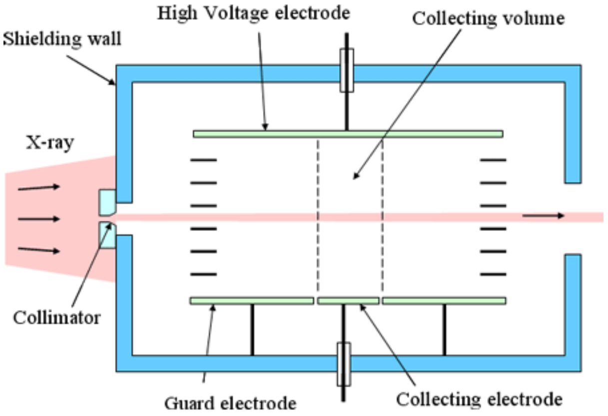

Figure 2.2: Diagram of a simple, parallel plate free-air ionisation chamber. (Image courtesy of www.aist.go.jp)

Figure 2.2 shows the layout of a free-air ion chamber, which although is not of the kind typically used in RT due to its large size, it works via the same principles and they are used at PSDLs. The collecting volume is defined as the column of air equal in cross-sectional area to the collecting electrode area. This relies on the electric field lines being perfectly perpendicular between the high voltage and collecting electrodes, and so guard electrodes are used to surround the collector with the same potential, although they do not contribute to the measured charge. The guard electrodes also serve to prevent leakage current from the high voltage electrode from reaching the collector. The magnitude of the electric field is very important, as it must be sufficiently high for there to be nearly 100% collection efficiency (also referred to as the saturation current) but not so high that charge multiplication effects arise. Figure 2.3 shows the typical behaviour of collected current versus bias voltage for all gas detectors. Ion chambers should function in the plateau region indicated, but too high a field will result in accelerating the secondary electrons to higher energies so they can cause an ‘avalanche’ of ionisation before they are collected. In reality, 100% collection efficiency is impossible as there is always a finite probability of ion pairs recombining resulting in a loss of measured signal. This is discussed further in section 2.2.4.

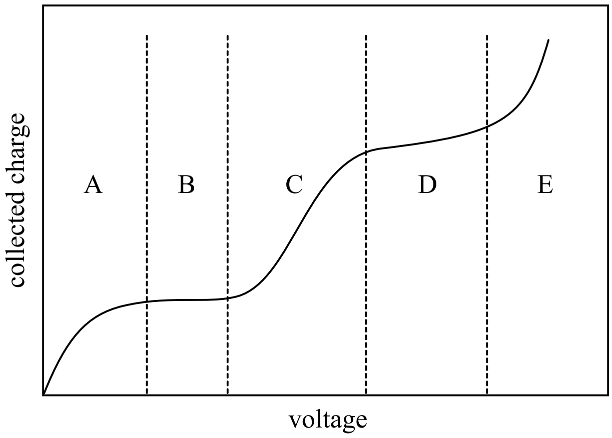

Figure 2.3: The variation in collected ionisation charge as an approximate function of bias voltage (electric field) in a gas detector. The labels represent the regions of A - recombination, B - ion chamber, C - gas multiplication, D - Geiger-Müller, E - continuous discharge.

In order to connect the dose deposited in an air cavity to the dose that would have been deposited in the medium had it not been present, there are some simplifying assumptions which can only hold under certain conditions. These assumptions are the foundations of cavity theory, and are crucial to the validity of using air cavity ionisation chambers as absolute dosimeters.

2.2.1 Cavity theory

In all reference materials, cavity theory is discussed primarily in terms of application to photon and electron dosimetry. In the case of protons and ions, there are some subtle differences but generally the theory can be applied in the same way and this treatment is tailored towards them.

Bragg-Gray (B-G) theory is the foundation of cavity theory. Its basis is contained in the following equation:

$$D_m = \Phi \left(\frac{S_{coll}}{\rho} \right)_m , \tag{2.1}$$

where the dose in a medium D_m due to a fluence Φ of identical particles with energy E can be found by multiplying the fluence by the mass stopping power of particles with that energy. If this fluence crosses an interface between two materials, m and g, then one can write the ratio of the doses either side of the interface as

$$\frac{D_m}{D_g} = \frac{\Phi(S_{col}/\rho)_m}{\Phi(S_{col}/\rho)_g} = \frac{(S_{col}/\rho)_m}{(S_{col}/\rho)_g} \tag{2.2}$$

This assumes that the particle fluence is identical in both materials either side of the boundary. If the material g is considered to be a thin layer sandwiched by m, then this assumption can be expanded to say that the cavity (g) must be so small in comparison to the range of charged particles crossing it that its presence does not perturb the particle fluence. This assumption is often referred to as the B-G condition, and depends on the scattering properties of m and g being sufficiently similar that the mean path length in g cm^{-2} for particles traversing g would be the same if it were replaced by a layer of m with the same mass thickness. It is worth noting that for HCPs, this condition is more easily satisfied than with photon and electrons due to their ballistic properties.

The second B-G condition is that the absorbed dose in the cavity is assumed to be deposited entirely by the charged particles crossing it. This infers that all charged particles in the B-G cavity must originate elsewhere (i.e. outside the cavity) and that charged particles entering the cavity do not stop in it.

For a differential energy distribution,

$$\begin{aligned}\overline{S}_m &= \frac{\displaystyle\int_0^{E_{\max}} \Phi(E)\left(\frac{S_{col}}{\rho}\right)_m \mathrm{d}E}{\displaystyle\int_0^{E_{\max}} \Phi(E)\,\mathrm{d}E} \\ &= \frac{1}{\Phi}\int_0^{E_{\max}} \Phi(E)\left(\frac{S_{col}}{\rho}\right)_m \mathrm{d}E \\ &= \frac{D_m}{\Phi} \qquad (2.3)\end{aligned}$$

By using the same expression for material g, they can be combined to give the ratio of absorbed dose in m to that in g in terms of absorbed dose in the cavity:

$$\frac{D_m}{D_g} = \frac{\overline{S}_m}{\overline{S}_g} \equiv s_{m,g} \qquad (2.4)$$

This defines the average mass stopping power ratio of m to g. Note that a lower-case s is used and the bar to denote average is dropped but still implied by definition.

If the material g in the cavity is a gas in which radiation produces a charge Q, D_g can be expressed (in grays) as

$$D_g = \frac{Q}{m}\left(\frac{W_g}{e}\right) \qquad (2.5)$$

where Q is in coloumbs, m is the mass of g in kg in which Q is produced, and (W_g/e) is the mean energy expended per unit charge produced in J/C. By substitution of equation 2.5 into 2.4, we obtain the B-G relation expressed in terms of cavity ionisation:

$$D_m = \frac{Q}{m}\left(\frac{W_g}{e}\right) s_{m,g} \qquad (2.6)$$

In reality, there are more than two materials of interest as the cavity has a wall of some thickness. So the dose to the wall (D_{wall}) is found by measuring the charge per unit mass in the (air) cavity, and in fact the secondary electrons in the cavity are assumed to have been produced in the wall. However if the wall is sufficiently thin that the fluence of particles is unperturbed, but thick enough such that secondary electrons produced in the medium of interest (water) do not reach the cavity, then the B-G relation is extended so equation 2.4 still holds:

$$\begin{aligned} D_w &= D_{wall}\ s_{w,wall} \\ &= (D_{air}\ s_{wall,air})s_{w,wall} \\ &= D_{air}\ s_{w,air} \end{aligned} \tag{2.7}$$

At higher proton energies, E_{eff} can be found by knowing the R_{res} at the point of measurement, and the stopping power ratio for this energy (as if monoenergetic) can be used as the ratio changes very slowly with energy (Palmans et al., 2006b). This greatly simplifies the calculation. However, at lower energies it is better to integrate the ratio over the energy spectrum as Grosswendt and Baek (1998) have shown that the inaccuracy in doing this goes from ∼0.1% at 200 MeV to ∼0.5% at 25 MeV. To know the detailed spectrum at any depth, verified Monte Carlo simulations of the beam and beam-line component geometry are required which requires much effort.

A refinement to B-G theory was provided by Spencer and Attix (1955) to explain the fact that measurements deviating from B-G theory were found for wall materials of higher atomic number and for differing cavity sizes. It was found that consideration of energetic δ-rays as a subset of the ionising particle fluence had a substantial effect on the integrated stopping power ratio. Spencer and Attix devised a two-group theory for energy losses of secondary electrons, where the energy lost by an electron is considered locally absorbed if the transfer is below a threshold Δ, but greater than Δ the energy loss is carried away as kinetic energy of a δ-particle and no energy is locally absorbed. The δ-particles are then added to the total particle fluence. The choice of Δ which makes sense is the energy required for an electron to have sufficient range to traverse the cavity — a simplistic argument being that electrons receiving less than this energy will deposit all their energy in the cavity otherwise most of it will be deposited in the wall. This gives an idea of what is going on, but in reality many electrons below this threshold will escape and many above will still stop in the cavity, so Δ has little physical meaning. The main consequence of this refinement is the adoption of the restricted mass stopping powers (discussed in section 1.1.1.1) when evaluating $s_{w,air}$.

2.2.2 Absorbed dose-to-water formalism

In routine practice in RT, D_w is not explicitly measured by calculation of all the individual parameters for each radiation type and depth of measurement. PSDLs such as NPL will calibrate field chambers via calorimetry in standard reference conditions for many commonly used radiation qualities in X-ray and electron RT. This simplifies the everyday dose calculation process in RT departments, as the dose-to-water calibration factor, $N_{D,w,Q}$ is known for each radiation quality, Q. This factor has units of dose per unit ionisiation charge (Gy nC^{-1}) in standard reference conditions, and so the full dose calculation then becomes a chain of of factors (each is usually $\approx$1) which correct for deviations of measurement conditions from the reference conditions. These include atmospheric temperature and pressure (also humidity if necessary), bias voltage polarity, recombination effects and chamber-specific perturbation of the radiation field. Discussion of these is included in the following sections.

When a dosimeter is used in a beam quality Q which differs from that used in its calibration, Q_0, the absorbed dose-to-water is given by

$$D_{w,Q} = R_{Q,corr}\, N_{D,w,Q_0}\, k_{Q,Q_0} \tag{2.8}$$

where $R_{Q,corr}$[1] is the dosimeter reading corrected for influence quantities mentioned above, k_{Q,Q_0} corrects for the effects of the difference between beam qualities Q and Q_0. Calibration is currently not available for protons, and so TRS-398 recommends using a calibration

---

[1] In TRS-398, this is referred to as M_Q. The identifier was changed to accommodate use of M later as the monitor chamber reading.

based on ^{60}Co γ-rays and this influences k_{Q,Q_0}.

2.2.3 Beam quality correction

The beam quality correction factor k_{Q,Q_0} is defined as the ratio at the qualities Q and Q_0 of the calibration factors in terms of absorbed dose to water of the ionisation chamber:

$$k_{Q,Q_0} = \frac{N_{D,w,Q}}{N_{D,w,Q_0}} \tag{2.9}$$

The most common reference beam quality Q_0 used for ion chamber calibration is ^{60}Co γ-rays, in which case the notation k_Q can be used.

Ideally, this correction factor should be experimentally determined, for example by calorimetry, in both beam qualities. When this is difficult or not possible, such as currently in the case of protons, then this factor can be determined theoretically. When B-G theory can be applied, equation 2.9 can be combined with the $N_{D,air}$ formalism used in TRS-381 (IAEA, 1997) and other dosimetry protocols. A general expression for k_{Q,Q_0} is given as:

$$k_{Q,Q_0} = \frac{(s_{w,air})_Q}{(s_{w,air})_{Q_0}} \frac{(W_{air}/e)_Q}{(W_{air}/e)_{Q_0}} \frac{p_Q}{p_{Q_0}} \tag{2.10}$$

where $s_{w,air}$ is the mass stopping power ratio for water to air and p is a chamber specific perturbation correction, for both radiation qualities Q and Q_0. Note that all values are considered constant with respect to proton energy except $s_{w,air}$ and theoretically W_{air}/e, however the latter is approximated to be constant and is the subject of much debate; in particular, the method in which all previous experimental values are interpreted and combined to give an average value and associated uncertainty (Jones, 2006). TRS-398 gives recommended values and uncertainties for all the k_{Q,Q_0} terms (show in table 2.1) as well as an analytical fit of $s_{w,air}$ as a function of residual range R_{res} derived from MC calculations by Medin and Andreo (1997). The analytical fit produced is adequate for therapeutic proton energies and ranges, however at the considerably lower energies (at $R_{res} < 0.5$ g cm^{-2}) found in the BP for a nominal 29 MeV beam the values obtained from this fit become increasingly inaccurate. The cause of this is thought to originate from the higher beam energy used in the code that was used to calculate these stopping power ratios in-line during proton transport. For the same value of R_{res} at different initial energies, the proton spectrum can be very different due to the differing amounts of energy straggling in each case. It is for this reason that the FLUKA code is used in this work to determine these stopping power ratios and hence k_{Q,Q_0} for an accurate model of the Birmingham proton beam, and this method is detailed in section 4.2.4.

Table 2.1: Values and uncertainties (1σ) for k_{Q,Q_0} terms given by TRS-398. The p values are specific to the Markus chamber.

k_{Q,Q_0} parameter	value	uncertainty
$(s_{w,air})_{Q_0}$	1.134	0.5%
$(s_{w,air})_Q$	function of E	1.0%
$(W_{air}/e)_{Q_0}$	33.97 eV	0.2%
$(W_{air}/e)_Q$	34.23 eV	0.4%
p_{Q_0}	1.009	1.5%
p_Q	1.0	0.7%

2.2.4 Ion recombination

A further correction to apply to the raw dosimeter reading is that for ion recombination, k_{ion}. Whilst calculating this correction is a well defined practice for high energy photon and electron beams, recommendations in the codes of practice for proton dosimetry are less well defined.

If an ion pair collide in the cavity, it is likely that they will recombine and produce neutral atoms/molecules resulting in a reduction in signal from the chamber. Recombination can be divided into two categories: *initial* and *volume* recombination, both of which contribute to the total effect. *Initial* recombination is that which occurs between ion pairs originating from a single primary particle track, and is therefore highly dependent on the particle LET. Ion pairs that arise from multiple primary particle tracks in the same detector give rise to *volume* recombination and hence this is dependent on the free ion pair density inside the cavity at any given moment. This is dictated by particle flux, but can also be considered proportional to the ionisation current or dose rate (or dose per pulse for a pulsed beam). The dependence of the total recombination on the polarising voltage differs according to the temporal nature of the beam. Boag (1966) shows that the inverse of ionisation current is proportional to the inverse of the polarising voltage for a pulsed beam, and the inverse of the square of the polarising voltage for a continuous beam. For a beam to be classed as pulsed, the pulse duration time must be less than the ion collection time and the time between pulses much longer. Although an isochronous cyclotron beam is pulsed, a typical pulse frequency is about 20 MHz, while the typical ion collection time for a bias of 100 V across a separation of 2 mm is 0.25 ms (Palmans et al., 2006a) and so the second condition is unfulfilled; hence a cyclotron beam can be regarded as continuous.

Unfortunately, TRS-398 only outlines an approach for this correction for pulsed beams (i.e. those from a synchrotron) and so for this work is not good practice to follow. Generally, in experimental literature on ion chamber dosimetry of HCPs if the correction is considered, then the two-voltage technique is adopted which assumes that there are negligible initial recombination effects. For high energy photon and electron dosimetry, this is a reasonable approximation given the low LET of both radiations however for HCPs this approximation is less valid. More accurate guidance on recombination in proton beams is outlined by Palmans et al. (2006a) with a detailed method and experimental results for many common RT ion chambers. This section will briefly summarise this method.

If one considers the saturation current (I_{sat}) to be the ionisation current that would be collected given 100% collection efficiency, then the ratio of I_{sat} to the current at a polarising voltage V for continuous beams can be approximated by:

$$\frac{I_{sat}}{I_V} \approx 1 + \frac{A}{V} + \frac{m^2 g}{V^2} I_{sat} \tag{2.11}$$

where A and g are constants related to the chamber geometry and m^2 is a constant related to the recombination coefficient and the mobility of the ions in air. The $1/V$ and $1/V^2$ dependent terms are the initial recombination and volume recombination components respectively. For a plane-parallel chamber such as the Markus chamber, $g = d^4/6v$, where d is the plate separation and v is the collecting volume of the chamber.

If a $1/n$ fraction of V is used, where $n > 1$ and not necessarily an integer, equation 2.11 becomes:

$$\frac{I_{sat}}{I_{V/n}} = 1 + n\frac{A}{V} + n^2\frac{m^2 g}{V^2} I_{sat} \tag{2.12}$$

By dividing equation 2.12 by 2.11, neglecting higher order terms and approximating I_{sat} with I_V in the last term:

$$\frac{I_V}{I_{V/n}} = 1 + (n-1)\frac{A}{V} + (n^2-1)\frac{m^2 g}{V^2} I_V \tag{2.13}$$

More details on this derivation are given by Boutillon (1998). This equation is therefore only valid if I_V is close to I_{sat}, therefore a value of V close to the upper range of normal operation should be used. However it has been shown by Burns and McEwen (1998) that care must be taken that V is not so high that charge multiplication effects take hold which shift the data away from a linear model of recombination.

Using equation 2.13, an experiment can be devised in order to extract the values of A and $m^2 g$ (and therefore m^2). At a particular depth of interest in a proton beam, repeated measurements can be made using two ion chambers, one as a monitor and the second as the chamber under investigation. The monitor should be set with the same V throughout, but the other chamber should have V varied for several values of n. For each n, multiple measurements should be made with varying beam current, and therefore varying I_V. By plotting $I_V/I_{V/n}$ against $1/I_V$ and extrapolating a linear fit to $I_V = 0$ the coefficients mentioned above can be measured. This allows calculation of the recombination correction factor, k_{ion} for use at that beam quality:

$$k_{ion} \simeq 1 + \frac{A}{V} + \frac{m^2 g}{V^2} I_v \tag{2.14}$$

In reality, it would be impractical to perform this experiment at every measurement depth. Hence some compromise has to be made as to the applicability of A and m^2 to different beam qualities. Palmans et al. (2006a) however found that for measurements in the 60 MeV CCO proton beam (at R_{res} between 0.07–2.69 cm) the experimentally derived correction was always within 0.1% of that using generic values of $A = 0.25$ and $m^2 = 3.97 \cdot 10^3$ s cm^{-1} nC^{-1} V^2.

2.2.5 Temperature and pressure correction

A correction for temperature and pressure is necessary simply because these factors will affect the number of air molecules in the chamber available for ionisation. The Ideal Gas Law states that the number of moles of a gas n is proportional to PV/T, and as the volume V of the chamber is fixed, then n only depends on the ambient air pressure P and temperature T. The standard reference conditions, P_0 and T_0, are 101.3 kPa and 20°C respectively. The correction factor is essentially the ratio of the number of moles of air at reference conditions to measurement conditions, or n_{ref}/n . This yields a correction factor of:

$$k_{TP} = \frac{(273.2 + T)}{(273.2 + T_0)} \frac{P_0}{P} \tag{2.15}$$

2.3 Radiochromic film

Radiochromic film (RCF) is a clear, plastic film with a self-developing active layer which colourises upon exposure to ionising radiation. Unlike photographic films which require chemical processing in order to obtain an image, the active layer of RCF is made of an organic monomer which undergoes polymerisation upon irradiation. The polymer product exhibits significant optical absorption, appearing to darken, and the colour is determined by the absorption spectrum of the polymer molecules. The degree of this colouring is measured by the film's optical density (OD): the reduction in the intensity of light that is transmitted through the film when a light source is shone on it. A crucial requirement of any film used for dosimetry is that the OD is somehow related to the dose absorbed by the film. The relationship between OD and the fraction of light transmitted is:

$$\mathrm{OD} = log_{10}(I_0/I)$$

where I_0 is the light intensity with no film present, and I is the light intensity that passes through the film (Butson et al., 2003). When using a CCD scanner, the pixel value for a particular colour channel (or grayscale) is used as I and the maximum transmission value (in theory 65,535 for a 16-bit channel) is used for I_0. The relationship between OD and dose is usually close to linear in the main range of operation. Recommended practice is to scan the film prior to exposure to obtain the background OD in order to subtract this from the total OD after exposure, which gives the netOD (Paelinck et al., 2007) which will be used later in chapter 5.

RCF can provide an accurate two-dimensional map of absorbed dose, with sub-mm spatial resolution possibly even down to the order of tens of μm depending on the type used. The radiochromic medium, in appropriate quantities and forms, can be used for a wide range of doses from 10^{-3} Gy up to 10^{4} Gy and this makes it attractive to many practical areas of radiation dosimetry. In medical physics, these films can provide important verification of increasingly complex treatment fields such as those used in intensity modulated radiotherapy (IMRT).

For RCF that turns blue upon irradiation, the active layer has an absorption peak in the red part of the visible spectrum. By analysing the film with red light, it is therefore possible to increase the sensitivity of the measurement. The highest OD change per unit dose can be measured by using monochromatic light at the absorption peak wavelength, and it is possible to alter the dynamic range of the film by carefully selecting other visible wavelengths or using the green and blue channels of a white light scanner (Hupe and Brunzendorf, 2006). The former method normally requires use of a scanning densitometer, considered to be a slow and expensive method of digitising the film. However, much cheaper, professional grade charge-couple device (CCD) scanners such as those used by photographic enthusiasts have proved to be very adequate as long as careful considerations are made. Many variables, such as temperature, UV light exposure, non-uniform light fields and polarisation effects can all have serious negative effects on the reproducibility and accuracy of RCF analysis (Niroomand-Rad et al., 1998; Butson et al., 2003). However with careful control and correction protocols, the performance of the most widely used type of RCF, GafChromic film, has been found to be sufficient not just for experimental dosimetry but for clinical verification of radiotherapy treatment. Various models of this brand of RCF form a large focus of this thesis.

2.3.1 Overview of GafChromic film

GafChromic is a brand name for a range of radiochromic films manufactured by International Specialty Products (ISP). They generally consist of clear polyester outer layers with one or two thinner, internal 'active' layers which are sensitive to ionising radiation. They are widely used in all modalities of RT (Butson et al., 2003) as they offer high spatial resolution better than 0.1 mm, have a good tissue/water-equivalence and they require no post-exposure developing. Possibly the first use of these films in proton dosimetry was carried out by (Nichiporov et al., 1995) and since then there have been investigations by Vatnitsky et al. (1997; 1999), Vatnitsky (1997), Daftari et al. (1999), Piermattei et al. (2000), Buenfil et al. (2002) and Kojima et al. (2003) all with MD-55 or HD-810. Since then there has been very little of significance published on proton dosimetry with GafChromic film, although work has started at the new Heidelberg Ion Therapy Center (HIT) where there have been several recent papers on carbon ion and proton dosimetry with EBT by Martišíková and Jäkel (2010a; 2010b; 2010c).

A schematic of the film structures is shown in figure 2.4. The four types of film used in this work are GafChromic EBT, EBT2[1], MD-V2-55 and HD-810, ordered in accordance with their dose range from lowest to highest. For brevity, EBT and EBT2 will be referred together as just EBT unless the distinction is important. Their nominal ranges are 0.001–8 Gy for EBT, 2–100 Gy for MD-V2-55 and 10–400 Gy for HD-810 (ISP, 2007). Most of the literature mentioned previously discusses models of film since discontinued, such as DM-1260, HS, MD-55-1 and MD-55-2 (the last two are often just referred to as MD-55, and denote the 1- and 2-layer models). All of these models had the same active ingredient hence their dosimetric properties remain comparable, while significant improvements have been made to the production process in particular the development of active layer uniformity (ISP, 2007).

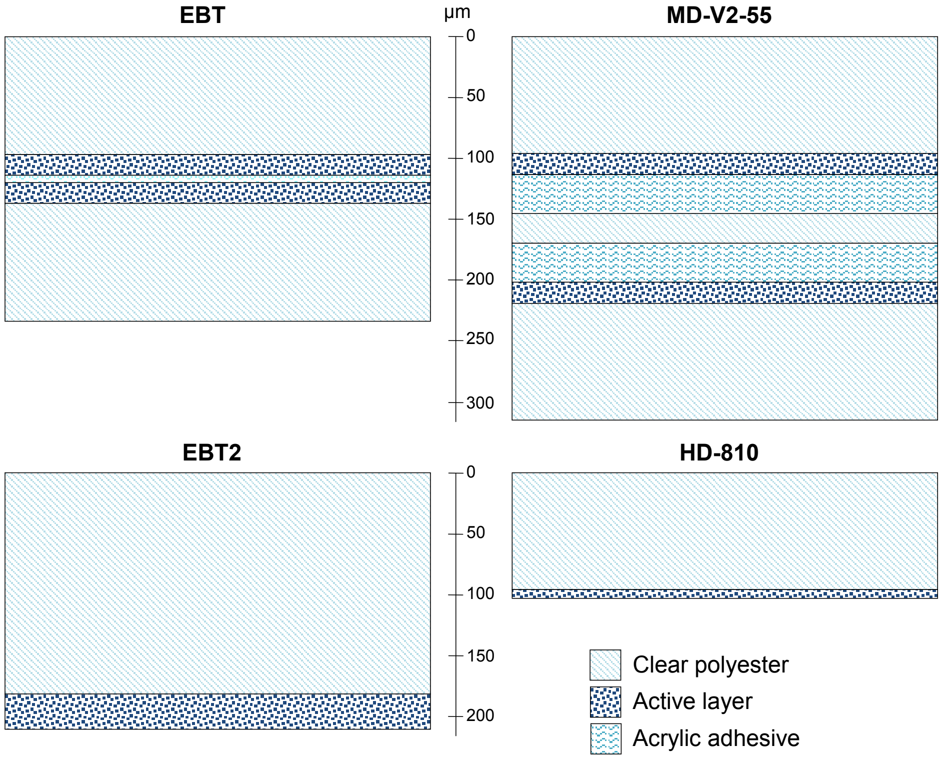

Figure 2.4: Structure of EBT, EBT2, MD-V2-55 and HD-810 films and relative dimensions of layers. Note that EBT2 here shows a special unlaminated version of the film which is commercially unavailable but was kindly provided for research purposes by ISP.

The active ingredient in all of these films is a crystalline diacetylene monomer, sus-

---

[1] This model has now replaced the original EBT.

pended in gelatin. Both the higher range films, MD-V2-55 and HD-810, use a compound called pentacosa-10,12-dyinoic acid (PCDA) whereas EBT contains a modified version, the lithium salt LiPCDA. This stoichiometric change has little effect on the Z_{eff}, the real difference is in the structure and three-dimensional packing of the crystals which largely depends on the type and size of side groups (R_1 and R_2 in figure 2.6) (Rink et al., 2005). As shown in figure 2.5, the monomer crystals are fairly spherical and sand-like for PCDA, but are long and hair-like for LiPCDA. These longer crystal strands overlap with one another and it is likely that this increases the density of possible polymerisation sites (or chromophores) which gives EBT its higher sensitivity compared to MD-V2-55 and HD-810. This feature will be discussed further in section 5.3.3.

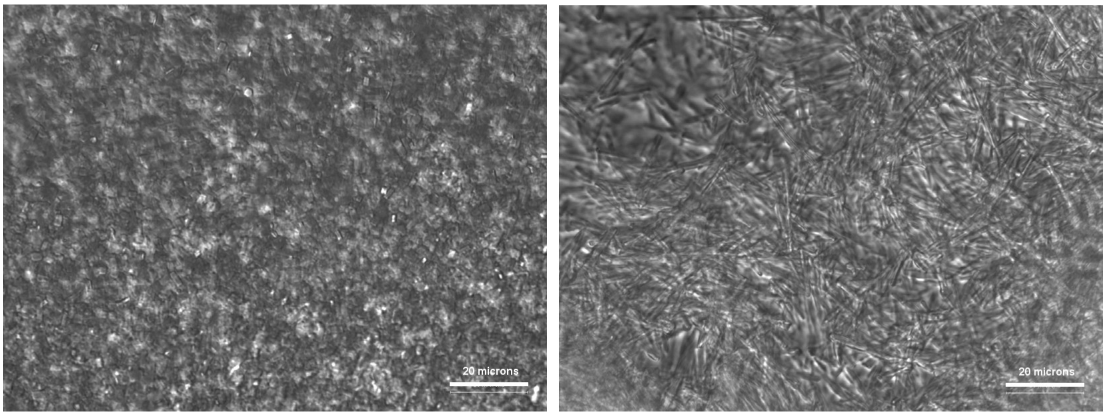

Figure 2.5: Microscope images of the GafChromic film active layers: PCDA in MD-V2-55 and HD-810 on the left; LiPCDA in EBT on the right. Reproduced from Rink et al. (2005) with kind permission from the authors and AAPM.

The conjugated carbon backbone that forms in the acetylene polymer (figure 2.6) is ultimately the feature which is responsible for the characteristic blue colour (Rink et al., 2005). It gives rise to the main optical absorption peaks at 675 nm for PCDA and 635 nm for LiPCDA, and the absorption spectrum of the former (in MD-55) can be seen in figure 2.7. As the abundance of polymer increases with absorbed dose, so does the magnitude of absorption at these wavelengths and hence the film appears a deeper blue. Some investigators use monochromatic light sources to digitise the films which can be tuned to the wavelengths of these peaks to increase sensitivity.

The manufacturer provides composition data for all of their films upon request, based

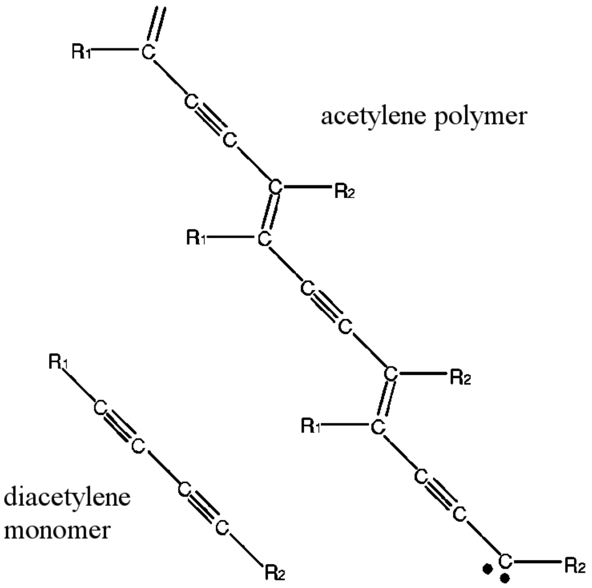

Figure 2.6: Chemical form of a monomer diacetylene and the final polymer acetylene structure. Further monomers join the polymer chain via the carbene end (carbon atom with 2 unpaired electrons).

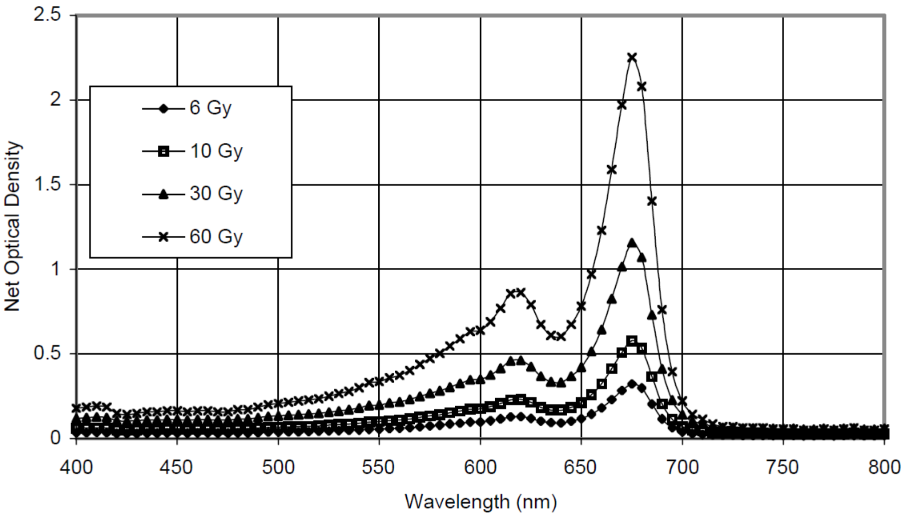

Figure 2.7: The absorption spectrum of MD-55, showing the main peak at 675 nm. (Reproduced from Butson et al. (2003) via Rightslink license 2514211293480).

on the proportion of the chemical ingredients in the formulations. The base layers are made of polyethylene terepthalate, referred to as polyester in figure 2.5 and often known by the trade name Mylar®. The active layer formulations are a mixture of the (Li)PCDA crystals with gelatin and in the case of EBT, doped with trace amounts of higher Z elements (displayed in table 2.2).

Table 2.2: Nominal atomic abundances in the active layers of GafChromic film, based on data received from ISP and not from direct measurement. HD-810 and MD-V2-55 are combined as they have exactly the same composition.

	% atomic abundances								
GafChromic model	C	H	O	N	Li	Cl	Na	S	Br
EBT	28.22	56.89	5.61	5.68	1.66	1.51	–	–	–
EBT2	29.61	58.33	10.79	0.06	0.82	0.19	0.11	0.03	0.06
HD-810/MD-V2-55	29.14	56.80	7.12	6.94	–	–	–	–	–

2.3.2 Energy dependence

No radiation detector's response can ever be completely independent of the energy of the incident particle, except in the case of a water calorimeter where temperature rise is always proportional to the projectile's total energy. Generally speaking though, for almost all low LET radiation GafChromic film has a relatively consistent response compared to other media like radiographic films (Butson et al., 2003). The manufacturer (ISP) claims that the response of the latest version of EBT (and EBT2) is consistent to within 10% for X-rays between 60 kV up to 6 MV energies. This is in contrast to the early EBT models which were quoted as having a 20% reduction in response at 50 kV compared to 6 MV photons (ISP, 2007).

EBT was designed more specifically for X-ray therapy dosimetry, and so there has been an emphasis on introducing small amounts of high Z elements (see table 2.2) the amount of which has been modified over several iterations including the latest version of EBT2 (Lewis, 2010). The purpose of these modifications was to improve the dose response of the film for X-rays below 100 kV where an under-response was found by many authors (Rink et al., 2007b; Richter et al., 2009) to be in the region of 20–30% of the response at MV energies, consistent with the manufacturer's claims. The general accepted explanation for this effect is due to the transition of the dominant interaction process from Compton scattering (CS) to the photoelectric effect (PE) as photon energy drops from the MV to the kV region. The cross-sections for CS and PE are proportional to Z and $Z^{3.5}$ respectively, Hence the Z_{eff} of the film relative to that of water becomes extremely important at these lower energies. It follows that if the Z_{eff} of the film is even slightly less than that of water, then the PE cross-section will be significantly less and the apparent dose response of the film will be reduced. The Z_{eff} values for EBT and EBT2 films (as a whole) are 6.98 and 6.84 respectively[1], compared to water which has Z_{eff} of 7.3 which supports this assertion. There is also the complication of each film layer having a different Z_{eff} and how the kinetic energy released per unit mass (kerma) in the first polyester layer influences the absorbed dose in the active layer.

There is a separate mechanism however for the energy dependence of GafChromic films to heavy charged particles, for which the dominant interaction at almost all relevant energies in IBT is coulombic energy loss with atomic electrons. The higher LET of these particles means that close to a particle track, the microscopic dose exceeds the dose range of the film. In essence, the polymerisation is locally saturated and so a proportion of the energy deposited is not converted to a measurable signal. Relatively little attention has been paid to quantifying the energy dependence of the films to protons or ions until more recently now that hadron therapy is rapidly expanding. The first attempt to measure an explicit dose-correction factor as a function of proton energy in the literature was by Piermattei et al. (2000) using their data and that of Vatnitsky (1997) for MD-55. The measurements by Vatnitsky (1997), Daftari et al. (1999) and Piermattei et al. (2000) show an under-response of PCDA containing films between 5-20% for protons in the BP region, depending on the initial energy of the beam. Kojima et al. (2003) irradiated DM-1260 to

---

[1] This value dropped for EBT2 due to the increase in overall thickness of polyester substrate (Lewis, 2010)

a variety of ion species between 3–45 MeV/n and concluded that the higher the particle LET, the more significant the under-response. Martišíková and Jäkel (2010a) has found for EBT a large under-response of 25–35 % for carbon ions between 100–400 MeV/n and no under-response at all for protons down to 50 MeV.

2.3.3 Dose-rate dependence

The manufacturer claims that there is less than 5% difference in response at dose-rates between 0.034 and 3.4 Gy min^{-1} (radiation type not specified) and this applies to the films containing PCDA as the active component. Considering that they conservatively estimate the dose uncertainty to be ±5% for these films, this infers that no significant dose-rate dependence is observed. The AAPM task group 55 report on radiochromic film dosimetry (Niroomand-Rad et al., 1998) claims this also to be the case for electron beam dose-rates up to 10^6 Gy min^{-1}. For EBT (i.e. LiPCDA), Rink et al. (2007a) finds that only a 1% difference in dose response is observed between dose-rates of 0.016–0.520 Gy min^{-1}, although this concerns real-time dose read-out using a special fibre-optic *in vivo* GafChromic dosimetry system. The author notes that when the polymerisation is allowed to complete ($>$ 2 hours) the effect becomes negligible.

Most of the range of dose-rates in these studies however are typical of radiotherapy or brachytherapy treatments. There has been little investigation into any effects approaching the extreme instantaneous dose-rates in laser-particle beams. The rough order of magnitude dose-rate in a laser source could be as high as $\approx 10^{11}$ Gy s^{-1}, based on a dose of $\approx$ 10 Gy being delivered in a single pulse of protons of $\approx$ 10 ps in length. Li et al. (2000) determined that for pulsed X-rays the film response does not vary significantly up to a dose-rate of 5×10^8 Gy s^{-1}. McLaughlin et al. (1996) delivered a 20 Gy pulse in 50 ns to GafChromic film (a dose-rate of 4×10^8 Gy s^{-1}) and did not report any dose-rate dependence. In addition, McLaughlin claimed that propagation of the polymerization was complete after 2 ms in comparison to a timescale of hours or days for conventional dose-rates from medical accelerators, although it was unclear if this was due to the radiation only or an associated heating effect.

The possibility that GafChromic film does exhibit dose-rate effects in laser-particle beams seems to have either been overlooked or not a concern of many workers, such as Breschi et al. (2004b,a); Cowan et al. (2008); Schollmeier et al. (2008); Nurnberg et al. (2009) and it is likely that if no significant effects are seen over the range of 10^{-3}–10^{8} Gy s^{-1} then without having definitive evidence, it can be presumed with some confidence that this behaviour can be extrapolated to higher dose-rates. Testing this in a laser-driven beam is not trivial as it requires a secondary method of dosimetry which has aboslutely no dose-rate dependence, such as nuclear foil activation.

2.3.4 Temperature effects

Temperature can have an effect on the film's response both during irradiation and scanning. The temperature during irradiation affects the film's dose response permanently, whilst the temperature during scanning has only a temporary and reversible effect on the measured transmission of the light in a given waveband.

During irradiation, a 10% decrease in OD was measured from 22–38°C by Rink et al. (2008) for EBT, but closer to 22°C (i.e. near room temperature) the OD readings appear more stable. The author also reports a shift in the absorption peak to shorter wavelengths at higher temperatures, but the sensitivity to this shift depends on the scanning apparatus. They used a spectrophotometer and averaged the absorption over a narrow waveband of $\approx$ 10 nm, hence were more sensitive to this peak-shift than if they had used a digitiser with a more broadband light-source, such as a commercial flatbed scanner. For a previous model of MD-55, Niroomand-Rad et al. (1998) reported that no significant change in optical absorption occurs at 4 wavelengths between 510–670 nm, for temperatures between 10–30°C during irradiation.

Post-irradiation, a similar absorption peak shift occurs but is reversible with changing temperature (Mack et al., 2003). The magnitude and description of this effect differs between methods from one author to another. For example, for MD-55 Mack et al.

(2003) report a dose-dependent temperature effect of upto -0.3% K^{-1} change in dose for MD-55 between 15–25°C with a polychromatic light source, whereas Klassen et al. (1997) found a change in OD of -0.6% K^{-1} between 0–3 Gy rising to -0.9% K^{-1} at 14 Gy using a photospectrometer of wavelength 676 nm. Note that Mack et al. (2003) investigated doses up to 150 Gy where the maximum effect was seen. The LiPCDA component in EBT suffers from the same peak shifting effect, and the temperature effect was investigated by Rink et al. (2005) with a narrow waveband again and Lynch et al. (2006) using a CCD flatbed scanner. In this case, over the range of 20–30°C, Rink et al. (2005) measured an effect of the order 2% K^{-1} (at an estimated dose of 0.1–0.3 Gy) whereas Lynch et al. (2006) observed a maximum difference of 0.5% K^{-1} for a dose of 0.03 Gy and a minimum of 0.1% K^{-1} at the highest dose used (0.36 Gy).

In conclusion, the magnitude of the temperature effect on dose measurement depends on the type of film, the temperature itself, the dose delivered and the spectral properties of the scanning light source. Although it is difficult to gain a concensus from the literature due to inconsistencies between the above variables, it is clear that by using a light source with a relatively wide waveband this effect can be neglected when the film is used at differing room temperatures between 18–25 °C, as it is considerably less than the overall uncertainty of the dose measurement.

2.3.5 Non-uniformity issues

An ideal 2D dosimeter should exhibit a uniform response across its area when exposed to a uniform field of radiation. GafChromic film uniformity has been a well discussed topic over the last decade or so, with particularly detailed attention paid by Zhu et al. (1997); Klassen et al. (1997); Niroomand-Rad et al. (1998); Butson et al. (2003); Hupe and Brunzendorf (2006) to various versions of MD-55 and by Saur and Frengen (2008); Richley et al. (2010) to EBT. Since the emergence of MD-V2-55 (*circa* 2007) the uniformity of this line of film was supposedly improved (ISP, 2008) but no new investigation has been published by the manufacturer to confirm this. The only reference in the literature was by Massillon-JL and Zúñiga-Meneses (2010) who state that the uncertainty in measurement with MD-V2-55 compared with MD-55 is lower, which they attribute to improved uniformity. Given that the manufacturer quotes the same uniformity specification for both HD-810 and MD-55 (ISP, 2001), it should be assumed that all the data from investigations for MD-55 apply also to HD-810.

The definition of uniformity can be split into local (microscopic) effects and regional (macroscopic) effects. The measured local uniformity can be affected by effective *grain size* of the diacetyline crystals, the spatial resolution of the scanner, electronic noise, pixel size and pixel colour depth. These effects are typically seen as spikes in OD profiles. Regional variations can be introduced by large scanning fields (i.e. A4 flatbed scanners) or be due to uneven distribution of the active layer.

For MD-55, Zhu et al. (1997) found a maximum variation of 15% in one direction and 4% in the perpendicular direction. It became apparent that the uniformity is much better in the direction in which the film is coated during the production process. In reaction to this, the manufacturer started clipping one corner of the film to distinguish the orientation to the customer. To improve measurement accuracy, Zhu et al. (1997) proposed a double irradiation technique which involves first exposing the film to a uniform, low dose. The film is then scanned prior to further radiation, and the pixel OD values are normalised relative to the mean OD for the whole film. This gives an effective sensitivity map, which can be applied to the scan of the film after the secondary exposure (to an unknown dose) in order to correct for the non-uniformity. Applying this correction map however relies on accurate image registration, even more so as the resolution used increases. It also requires the radiation field flatness to be of much smaller uncertainty than the non-uniformity of the film so that it can be neglected. Since this initial investigation, all of the literature listed above report values of non-uniformity for MD-55 which are in agreement. In particular, Hupe and Brunzendorf (2006) found a 15% peak-to-peak variation in dose and an overall uncertainty of $\approx 6\%$ at the 2σ level.

For EBT, measurements of regional non-uniformity have generally only been expressed in the literature in terms of standard deviation (σ) about a mean of multiple regions of interest (ROI) on a sheet of film. Saur and Frengen (2008) reported that above 0.5 Gy, non-uniformity contributes to less than 3% dose uncertainty at a 2σ level. Richley et al. (2010) reported that in terms of raw pixel value, a deviation of 2.4 % at a 2σ level was found for EBT2. This non-uniformity was measured as-is and no use was made of the yellow dye feature of EBT2 and the uniformity correction algorithm. These results indicate that the inherent level of non-uniformity between the two models of EBT are approximately the same, and are significantly better than for the old models of MD-55.

The overall indications are that for accurate measurements with MD-55 (and HD-810), the double exposure method should be investigated whereas for EBT, the uniformity is such that good accuracy is achievable without using this technique. EBT2 allows for an improvement in accuracy by taking advantage of the yellow dye, and this is done simply by extracting both blue and red channel images of the same scan and thus omits the need for a pre-exposure. The manufacturer states that this correction is not obligatory, but should assist in improving accuracy if required.

2.3.6 Light and polarisation effects

Care must be taken when handling GafChromic film to minimise the exposure to UV light (Butson et al., 2003). This includes exposure to sunlight and fluorescent tube indoor lighting, which contains a UV component. Films should be ideally stored in an opaque or light-tight container, and when in use it is preferable to use incandescent lighting if possble. This has the added implication that the light source used for film readout can also have the side-effect of darkening it. Butson et al. (2003) carried out an investigation with three light sources typical of commonly used readout systems: a HeNe laser, an ultra-bright red light emitting diode (LED) and a 40 W fluorescent tube. Each light and film configuration was designed to mimick the standard conditions for dosimetry readout. Figure 2.8 shows that care must be taken when using fluorescent light sources, and that red LEDs are optimal for reducing this effect.

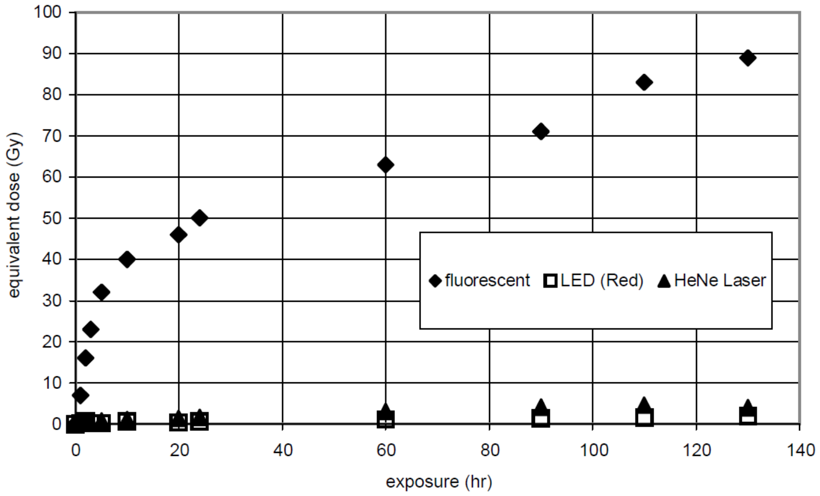

Figure 2.8: The effects of readout light source type on darkening of MD-55. (Reproduced from Butson et al. (2003) via Rightslink license 2514211293480).

Klassen et al. (1997) conducted a thorough investigation into the effect of the orientation of MD-55 on the transmission of polarised light, after finding a 4–10% change in OD using a spectrophotometer when turning the films back-to-front. It was found that the active layers are responsible for a very significant attenuation of polarised light as a function of the rotation angle. It was observed from electron scanning microscopy that the microcrystals of PCDA have a preferred orientation, and so it is possible the monomer and polymer molecules in the crystals have a preferred orientation with respect to the film. This could lead to dichroism, where if light is polarized such that its electric vector interacts most strongly with electrons in the conjugated bonds of the polymer molecules, it is absorbed more strongly. The central Mylar layer also rotated the plane of polarization of the light in the fashion of a 1/2 wave plate. Therefore the measured OD can substantially change when the film is rotated or turned back-to-front in a light source containing polarized light.

For EBT and EBT2, Lynch et al. (2006) found a similar sensitivity to polarized light, with deviations in measured OD of 8–15% for an Epson flatbed scanner and 20–80% for a Microtek flatbed scanner. In both cases, the largest effect was seen with an unirradiated film. All scanning light sources to some degree contain a proportion of polarized light, and so this is an important effect to consider. Consqeuently, a group of calibration and experimental films analysed together must be scanned in precisely the same orientation to reduce uncertainty due to polarization effects. Care must be taken when cutting sheets into small pieces that they are labelled and marked on the sheet *before* cutting so that orientation information is always retained.

CHAPTER 3

MONTE CARLO RADIATION TRANSPORT METHODS

This chapter outlines the principles behind Monte Carlo (MC) particle transport, and compares the features of three codes, SRIM, MCNPX and FLUKA. The former two codes are regarded as class I, while the latter is a class II MC code; the meaning of which is explained later in the chapter. The performance of all three codes is compared for the case of simulating a depth dose curve of a simple monoenergetic 29 MeV pencil proton beam in a PMMA target.

3.1 Monte Carlo charged particle transport

In the context of radiation transport, the MC technique consists of applying probability distributions describing particle behaviour in every relevant aspect and simulating their trajectories, energy transfer events and secondary particles by using random number generators. A source of particles must always be defined, along with explicit description of the spatial, energy and projection information or distributions. By individually simulating a large number of particle histories, an average behaviour is converged upon and can yield detailed information of for example, fluence, energy deposition or angular deflections in a region of interest within complex three-dimensional geometries.

Key to optimising simulations is to investigate which physics processes can be deactivated or simplified without loss of accuracy, but which may result in significant computational savings. Furthermore, biasing techniques which favour specific behaviours of interest improve the compromise between computational time and statistical uncertainty arising from large numbers of histories. Any biasing is accounted for in the final collation of results. A technique commonly used implicitly in these codes is ‘condensed histories’, where for example an electron’s many slowing-down collisions are not simulated individually but in groups (or steps) of multiple collisions. The step size has to be chosen in such a way that the total number of steps is kept as small as possible to save computational time, but large enough that multiple collision models for angular deflections and energy losses are valid (Andreo, 1991). This technique is also referred to as multiple Coulomb scattering.

Berger (1963) classifies the condensed history technique into two procedures:

(1) Class I, which uses a predetermined set of pathlengths and at the end of a step the random sampling of interactions is performed. An appropriate method of determining step size is such that the energy is reduced by a constant fraction of the total particle energy. This results in logarithmic step spacing and satisfies use of multiple scattering theory as angular deflections tend to increase at lower energies.

(2) Class II, which groups together only *minor* collisions below a specified energy loss

threshold where deflections are also small, and considers individually *major* events where a large enery loss or deviation occurs. Continuous energy loss is then determined by using restricted stopping powers while discrete losses are passed on to the secondary particles (usually a δ-ray electron) whose generation is coupled to the primary particle.

In each case, appropriate energy-loss straggling must be used when applying stopping power losses to mimic the random fluctuations in reality from the mean stopping power. This also has the direct consequence of range-straggling, i.e. each particle has a unique final range. However the mean range should be equivalent to the CSDA range multiplied by a *detour* factor (ICRU, 1993) which accounts for angular deflections from a straight path.

3.2 The MCNPX code

The Monte Carlo N-Particle (MCNP) code is a general purpose MC code written in Fortran90 (but compatible with Fortran77) and developed at Los Alamos National Laboratory (LANL). The extended version, MCNPX (MCNP eXtended), combines MCNP4C3, a coupled neutron-photon-electron transport code for energies up to 20 MeV, CEM03, a cascade excitation model for nuclear reactions, and LAHET 2.8, a code for high energy particle transport. Multiple scattering of protons is governed by the Goudsmit-Saunderson theory (Goudsmit and Saunderson, 1940a,b), and energy straggling follows the Vavilov model (Vavilov, 1957). For nuclear interactions it uses the LA150H proton data tables for 41 isotopes, the LA150N neutron data tables for 42 isotopes and the LA150U photonuclear data for 12 isotopes. Nuclear data are tabulated from 1 to 150 MeV, so for higher energies physics models are used. Stopping powers for charged particles follow two separate models for high and low energies which are ‘blended’ together by linear interpolation in the energy range 1.31–5.24 MeV/u.

Throughout this work, MCNPX 2.5.0 (Pelowitz, 2005) has been used although when MCNPX 2.6.0 (Waters et al., 2007) became available some of the simulations were repeated to check there were no significant differences, and the original output data from 2.5.0 were kept in all cases.

One limitation of MCNPX is that being a class I MC code it does not generate any secondary electrons from the electromagnetic interactions with protons, and so all the proton energy loss is considered to be deposited on the spot. In reality, the more energetic electrons (δ-rays) carry this energy a short distance downstream and transfer it to other electrons in successively lower energy collisions. It was shown earlier in equation 1.1 that the maximum electron energy is ≈1/459 of the proton energy, so for a 29 MeV proton this gives a maximum electron energy of ≈ 60 keV. An electron of this energy has a CSDA range of ≈ 60 μm, so this approximation has little effect on the depth-dose curve.

Like all MC codes, a cut-off energy is specified where the particle is no longer transported once its energy reaches this value. The default is 1 MeV for protons, and once a proton reaches this energy the remaining 1 MeV is 'ranged out' and deposited in an approximate fashion based on the remaining range the proton would likely have travelled. For MCNPX version 2.5.0 (and 2.6.0) however, there appears to be a bug[1] which results in this cut-off energy not being deposited or at least not being scored. This has a significant effect on the shape of the BP, shown in figure 3.1. By overriding the default value and setting a 1 keV cut-off (the smallest possible), this problem is effectively eliminated as 1 keV being lost is a negligible portion of the total 29 MeV per proton.

The stepped nature of the plateau in figure 3.1 is due to the discretely binned stopping power values that MCNPX uses. This can be proved by printing the stopping power data in the output, and finding the projected ranges for the first energy (29 MeV) and the second tabulated value. The difference in these two ranges is always the length of the first step. This does not have any effect on energy conservation or the final BP shape or location, it is just an artefact of having an average stopping power applied over a finite energy range. Once energy straggling takes hold at deeper depths and the stopping power bin widths become smaller at lower energies, the stepping artefact disappears.

---

[1] Reported to LANL in April 2008

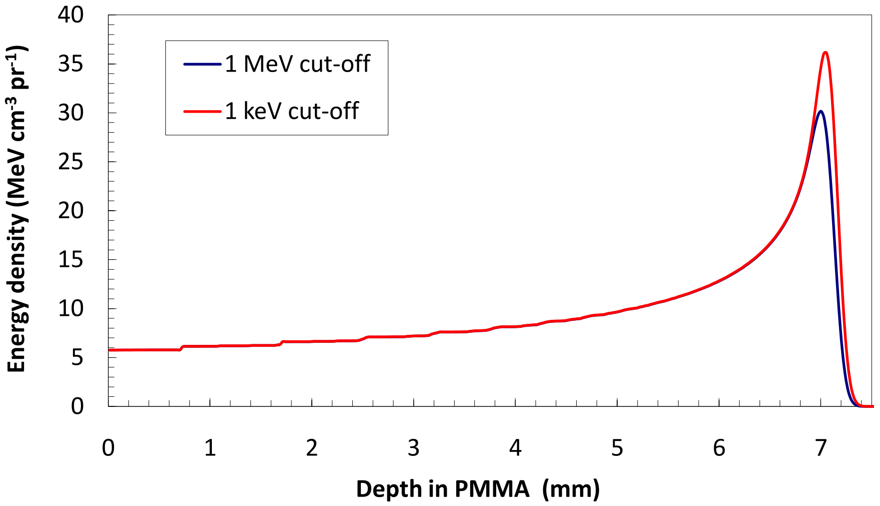

Figure 3.1: The depth-dose curves produced by MCNPX 2.5 for 1 MeV (thick blue line) and 1 keV (thin red line) cut-offs. The energy deposition is scored in 2 μm wide depth bins along the beam axis within a 2.65 mm radius, equivalent to the sensitive area of the Markus chamber.

3.3 The FLUKA code

FLUKA is another Fortran90 based MC code, which has its roots in high energy physics and since 1989 has been developed by collaborators working at CERN, Switzerland and INFN, Italy. It is another general purpose code able to treat hadron-hadron, hadron-nucleus, neutrino, electromagnetic, and μ interactions up to 10,000 TeV. Charged particle transport (including in magnetic fields) includes all relevant processes, desrcibed in much detail by Fassò et al. (1997).

As there is a developing interest in hadron therapy, the code developers have catered for the relatively lower particle energies and preset defaults can be applied specifically for this application. Whilst FLUKA has essentially the same transport capabilities as MCNPX, it is a class II MC code so it has the added ability of producing δ-ray electrons and gives the user more physics options for ion transport than the MCNPX interface. The production of δ-rays has a direct implication for the calculation of tabulated stopping powers. As discussed in section 1.1.1.1, the unrestricted stopping power assumes all energy is deposited on the spot whereas δ-rays carry some of this energy away from the initial interaction site. FLUKA includes a user-defined production threshold energy, above which a δ-ray is created and transported but below which the local deposition approximation is applied. At run-time, FLUKA will calculate and output a table of restricted stopping powers based on the value of this threshold.

In the low-intermediate energy range, the hadron-nucleus interactions are handled by the PreEquilibrium Approach to NUclear Thermalization (PEANUT) model from the transport threshold energy up to as high as 5 GeV. It includes explicit intranuclear cascade smoothly joined to statistical pre-equilibrium emission and followed by evaporation and gamma de-excitation. It is described in more detail by Fassò et al. (1995) and shown to be in excellent agreement with cross-section data.

Where FLUKA has generally lagged behind MCNPX is in its low-energy neutron transport. This is done via energy groups as opposed to MCNPX's point-wise neutron transport. FLUKA 2006 contained cross sections for approximately 30 low-energy groups up to 20 MeV, however the 2008 version can boast a big improvement of 260 neutron groups between 0.01 MeV and 20 MeV (Fassò et al., 2008), so the gap has been closed somewhat on MCNPX in this regard. The specific version used throughout this work is FLUKA 2008.3b (Ferrari et al., 2005; Battistoni et al., 2007) which was the most recent release at the time.

3.4 The SRIM program

SRIM (Ziegler, 2004; Ziegler et al., 2010) is a group of Windows based programs which calculate the stopping and range of ions in matter using a quantum mechanical treatment of ion-atom collisions. It can transport any ion from energies of 10 eV up to 2 GeV. In between these collisions, it uses similar condensed history techniques as other MC codes to average collision results over steps, and determines the amount of energy deposited in terms of that lost to ionisation processes and to target atom recoils. TRIM (the Transport of Ions in Matter) is the core program included, which actually performs the MC calculation and can output in real time various properties of the ion beam. It outputs the three-dimensional distribution of ions in the target and its parameters, such as range, straggling, ionisation, target damage, sputtering, phonon production and produces graphical displays during the run. It accepts simple geometric descriptions of targets as one-dimensional layers, up to a maximum of eight layers. The only possible beam source configuration inherent to the program is a monoenergetic pencil beam. More complicated sources can be described in an auxiliary file which is read in to the program at runtime.

The programs are made so that they can be interrupted at any time, have the input parameters modified, and then resume afterwards. The interface is relatively simple to use in comparison to most MC codes, but then it is not specifically tailored towards flexible and complex simulations in nuclear and particle physics. Its user-base is mostly researchers who are investigating the physical, damaging effects of radiation to semiconductors or other materials and ion beam deposition and lithography in nanoscale physics. As such, TRIM does not accurately model most nuclear processes, neither the production of secondaries nor attenuation of the primary beam. For low ion energies (< 50 MeV), this effect is not so important but for therapeutic energies this deems TRIM inappropriate for simulation of dose deposition.

3.5 Parallel simulations with BlueBEAR

In February 2008, the BlueBEAR high performance computing cluster was brought into operation at the University of Birmingham, with 1536 CPUs across 384 nodes available to registered users in the first phase of operation (soon to be upgraded further). This allows the execution of MC simulations running in parallel on many tens of CPUs, shortening typical simulation times from the order of hours to minutes. The nodes consist of dual-processor dual-core (4 cores/node) 64 bit 2.6 GHz AMD Opteron 2218 worker nodes. Most of these nodes have 8 GB of memory shared between the 4 cores.

Job submission can be automated using BASH scripts, and an example of a script for submitting FLUKA jobs to multiple nodes is in appendix C.1. MCNPX includes a Message Passing Interface (MPI) version for running in parallel, which executes from a single command on up to 64 cores and handles all of the load distribution. FLUKA however does not have a parallel version, but is easy to parallelise by submitting duplicates of the same job to BlueBEAR as long as the random number seed in each input is made unique. FLUKA provides the necessary routine (*usbsuw*) to then combine outputs together, and calculates uncertainties based on the standard deviation between all the statistically independent runs. There are pros and cons of each parallel implementation, however there were some scheduling issues with MCNPX as it would require all cores to be reserved (and kept idle) before the job would run. Often if BlueBEAR was busy, this would take many hours before sufficient cores were all idle simultaneously in which case the time-benefit was virtually lost. The FLUKA implementation meant that individual runs could start even if not enough cores were available initially to run the whole parallel job.

3.6 Code comparison

The most important comparison of these MC codes for proton dosimetry is by looking at their depth-dose curves. The simplest scenario, used here, was to direct a pencil beam of 29 MeV protons perpendicularly into a homogeneous target and score the total energy deposition/ionisation versus depth. The scoring planes were considerably larger than the lateral dimension of the beam. The target material chosen was PMMA rather than water, as this would later be the phantom material used for depth-dose measurements. For the simulation with MCNPX, a proton cut-off of 1 keV was chosen to eliminate the earlier described problem affecting the BP height. For FLUKA it was decided to enable δ-ray production above a threshold of 10 keV and transport cut-off of 5 keV, and a proton cut-off of 100 keV was used to (larger than MCNPX) to reduce computation time. It had earlier been ascertained that using 1 keV or 100 keV made negligible difference to the curve in FLUKA. The depth bin size was 20 μm for both codes. For TRIM there are no transport options available, and there are always 100 bins between the minimum and maximum scoring depths, namely 0 and 7.5 mm giving a bin size of 75 μm. TRIM does not have a variable transport cut-off energy, and appears to transport the protons down to a few eV. This may explain the much longer computational time compared to MCNPX and FLUKA. In all cases, other options not mentioned were left at their default values. The depth-dose data were all scaled to equal one at the entrance due to the slightly different units used by all three codes, and are shown in figure 3.2. The composition of PMMA was identical between the codes, although the density had to be modified in TRIM from 1.20 to 1.19 g cm^{-3} to match the ICRU specified density and that used in the other two codes.

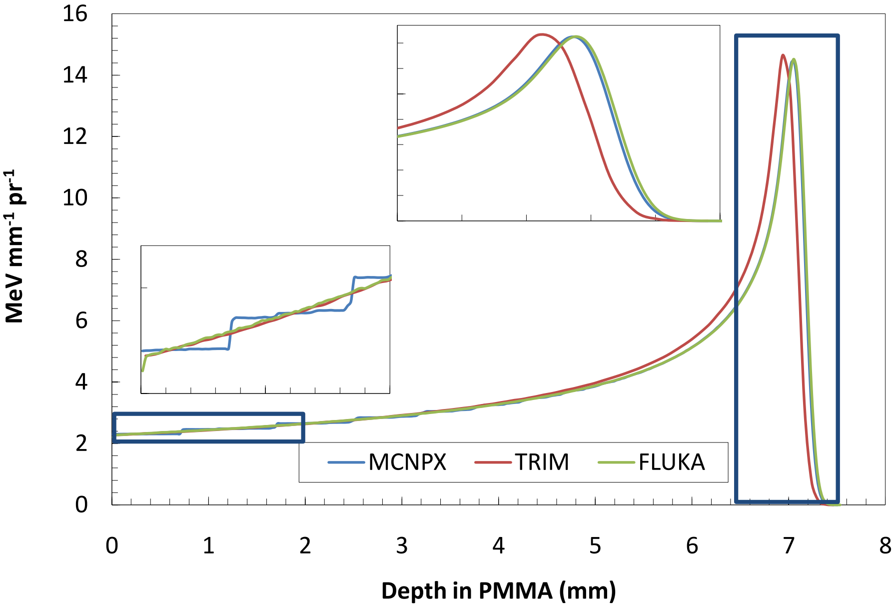

Figure 3.2: Comparison of energy deposited per unit depth per proton in PMMA from MCNPX, TRIM and FLUKA. The plateau and peak regions are magnified for easier comparison.

By comparison of depth-dose curves, MCNPX and FLUKA show very good agreement and FLUKA does not exhibit the stepping artefact due to simulation of the δ-rays which spread the energy loss more ‘smoothly’. Simulation with TRIM gave a similar height peak (slightly taller) but a shorter range than the other two codes. The R_p given by each simulation was 7.205 mm for TRIM, 7.274 mm for MCNPX and 7.287 mm for FLUKA. The large difference for TRIM can be explained by looking at the stopping powers it uses (tabulated in SRIM), and figure 3.3 shows S/ρ for PMMA from all three codes as well as the values given by ICRU49. The most obvious differences lie below around 1 MeV, and this is generally where uncertainties in stopping power become quite significant. Above this, there is generally good agreement although no two curves are the same. However in the energy range from 2–10 MeV, SRIM uses noticeably higher values than the other codes (between 1.6 – 3.8%) and this explains why the proton range is reduced. However SRIM's stopping powers below 1 MeV are lower than the other codes, but this does not result in a lower peak because the mean energy is still 2–3 MeV here and these protons are responsible for most of the dose deposition compared to those in the sub-MeV energy region, who although have a higher stopping power have very little energy left to deposit.

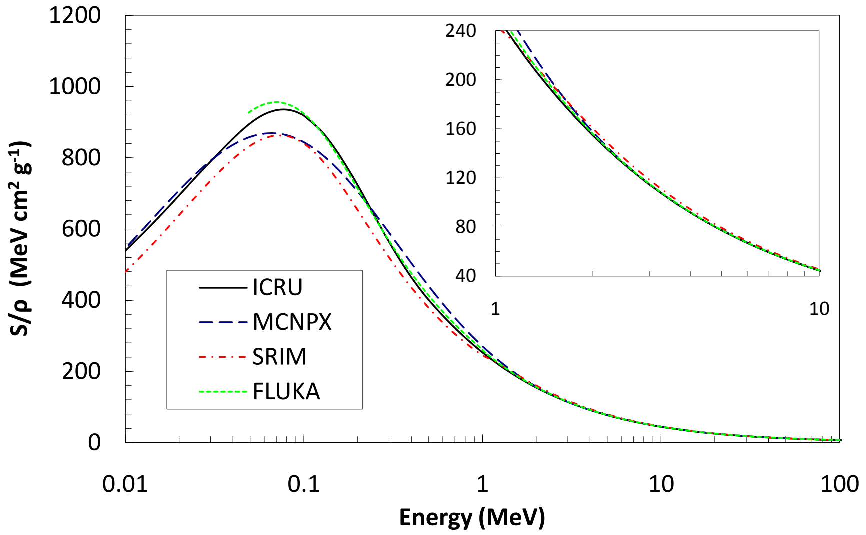

Figure 3.3: Total mass stopping powers in PMMA used and calculated by MCNPX, SRIM and FLUKA. The ICRU49 stopping powers are also shown for comparison.

In a real beam situation, the particle energy is not perfectly mono-energetic. Due to the way particles are accelerated in bunches around an accelerator, those at opposite ends of the bunch experience differing accelerating potentials to those in the middle as they tend to be slightly out of phase with the RF. This and other effects cause there to be a small amount of energy (or momentum) spread that can be represented by a Gaussian distribution about the nominal energy. Including this small amount of momentum spread in the initial beam parameters in FLUKA results in a widened BP which is lower in height, and significant 'sloping' of the distal edge of the BP (see figure 3.4). The R_p increases also as there are a proportion of protons with energy initial higher than the nominal (mean) value. The values of momentum spread are expressed as the σ value of a Gaussian in terms of percentage of the total momentum ($\Delta p/p$). This value must be input into FLUKA as a full width half maximum (FWHM) of a Gaussian, and so the expression FWHM $= 2.355 \cdot \sigma$ is used. MCNPX also allows the user to control this but in terms of spread in energy rather than momentum. TRIM however does not simply allow the user to input any energy/momentum spread which limits the validity of any comparison with measured depth dose data. That in tandem with the inability to simulate non-elastic nuclear collisions renders TRIM to be very much the least preferred choice when compared to FLUKA and MCNPX, and in all of the MC work presented later only simulations from these two preferred codes were considered. TRIM however was useful initially as the barrier to entry was much lower due to the simple Windows interface.

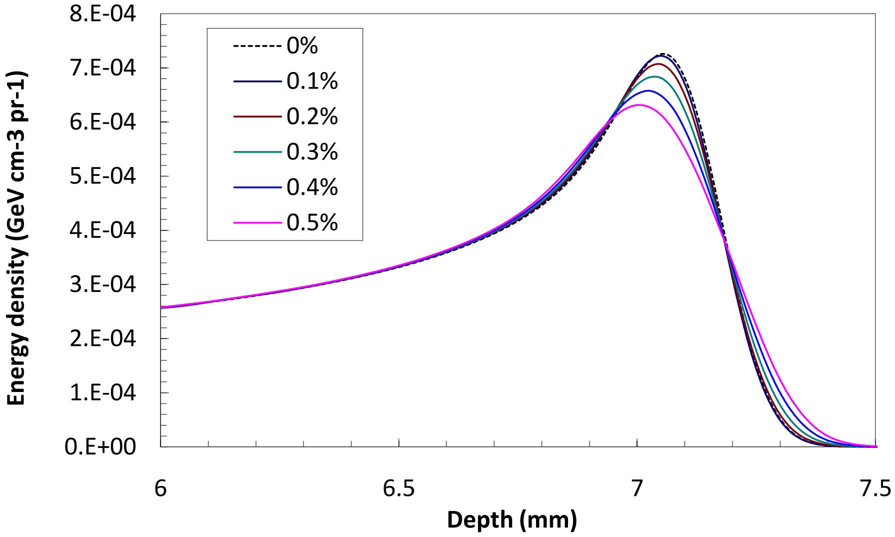

Figure 3.4: The effect of increasing the intital proton momentum spread on the height and shape of the BP. Values denote σ of a Gaussian spread expressed in percentage of the total proton momentum.

CHAPTER 4

IONISATION CHAMBER DOSIMETRY

This chapter covers all of the work using ion chambers to measure depth dose curves for both protons and α-particles using the Birmingham cyclotron. Particular attention is given to how absorbed dose to water is obtained from the measured ionisation charge, and dealing with the short-comings in the IAEA TRS-398 recommendations when dosimetry of low energy beams is considered. In parallel with this, MC simulations are described which facilitated accurate calculation of certain parameters in the dosimetry chain and allowed comparison with the final corrected dose measurements.

Sections of this work were published (Kirby et al., 2010), and the full journal article is available in appendix I.

4.1 Dosimetry equipment and materials

4.1.1 The Perspex dosimetry jig and beam port

In order to perform good, consistent dosimetry using ionisation chambers and any other dosimeters it was necessary to design and construct a jig which was fit for this purpose. The jig had to meet various criteria: be free-standing and portable; be height-adjustable; hold enough plastic to measure depth-doses of protons up to 100 MeV (i.e. in excess of highest energies available in UK or from laser-proton sources); have a spring-loaded device to put pressure on all inserts to reduce any air gaps and hold a monitor ionisation chamber at the front. Photos of the final jig in front of the cyclotron beam exit port can be seen in figure 4.1. Original hand drawings can be found in appendix E.

The cyclotron lacks an accurate system for real-time beam current monitoring, and the only device to intersect the whole beam outside the main vault is a Faraday cup a few metres upstream from the beam exit port which also acts as a beam stop when access to the experimental room is needed. The current measured here did not reflect the current 'on-target' as it was then highly defocussed to provide a field around 40–50 mm in diameter at the beam exit port which was collimated in two stages: firstly by the aluminum surround which supports the window, and secondly by the tantalum collimator deliberately used to reduce the beam spot to 10 mm in diameter (seen later in figure 4.3). The current collected on the collimator could then be used to manually monitor (on an analogue display) the beam during irradiations but not provide any measurable data. This method of monitoring was very coarse, and was only ever used as a guide to the operator in order to keep beam current fluctuations to a minimum. Typically, fluctuations of ±10% over periods of seconds were quite normal and little could be done to improve stability as the cyclotron was being made to operate at the very low end of its current range.

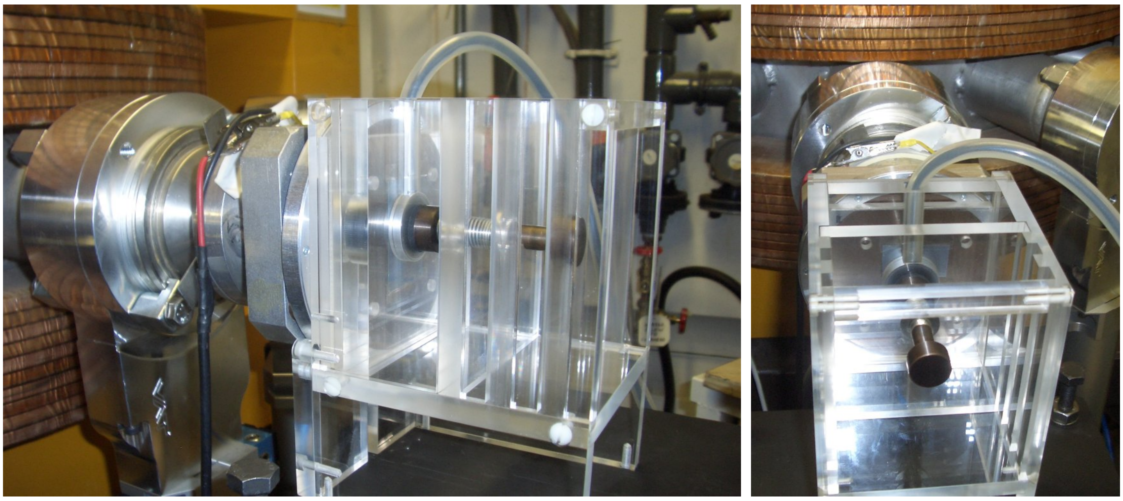

Figure 4.1: Photgraphs of the Perspex jig in use, in front of the cyclotron beam port.

4.1.2 Ionisation chambers

Due to the lack of a beam current regulation system, an ionisation chamber was specially bought and employed as a monitor chamber. Important considerations for such a chamber are relatively thin entrance and exit windows so as to not degrade the beam energy significantly, and be large enough in diameter to completely encompass the field of the beam. A PTW X-ray monitor model 7862 was bought for this purpose and a photo of it is shown in figure 4.2, and a technical drawing is in appendix 4.2. The monitor chamber was not calibrated to give a direct measurement of dose, but used to provide a reference measurement of ionisation (and hence fluence) by which all dose measurements at some depth could be divided by in order to construct a depth-dose curve.

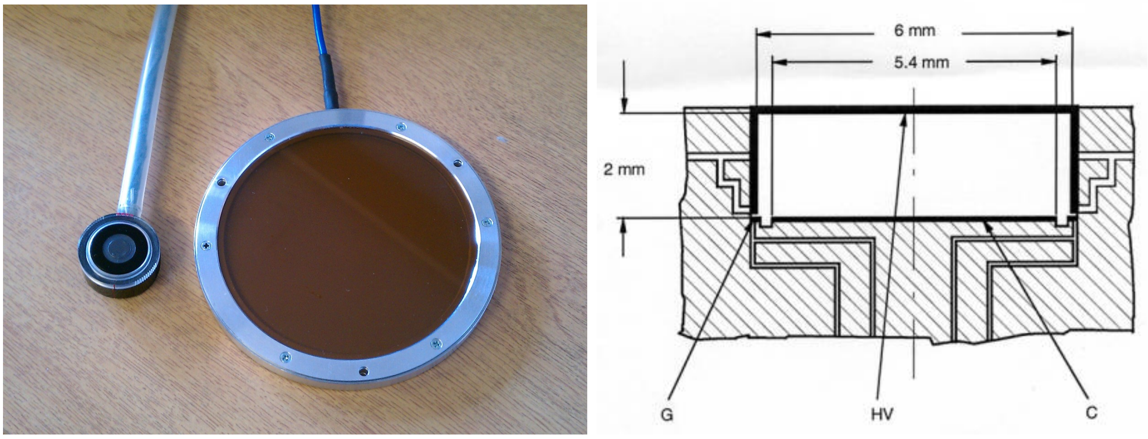

Figure 4.2: Photo (left) of the PTW monitor chamber 7862 and Markus chamber. A technical drawing (right) of the Markus chamber is also shown, where G is the guard ring and C is the collecting electrode.

The ionisation chamber used for all absolute dosimetry was either one of two PTW Markus chambers on loan from NPL (shown in figure 4.2), with serial numbers 2225 and 478. These chambers have plane-parallel electrodes one of which is thinly coated graphite on the inside of a polyethylene window. The main specifications are given in table 4.1 along with those for the monitor chamber. The smaller sensitive region meant that the fluence in both chambers was not identical; while the monitor chamber encompassed the whole beam diameter the Markus chamber measured only a central portion of the beam and hence accurate alignment before each experimental session was crucial. This was routinely done by taping a spare piece of GafChromic film over the front of the chamber so that the beam's position on the chamber window could be seen by eye. The jig was moved sideways by hand and raised or lowered using the adjusting screws until the chamber window was centred on the beam as best as could be judged by eye.

Table 4.1: Specifcations of the monitor chamber and two Markus chambers.

	Monitor 7862	Markus 2225/478
Sensitive region diameter	96.5 mm	5.3 mm
Max measuring volumes	17.6 cm^3	0.055 cm^3
Window thickness	2 x 0.1 mm[a]	0.03 mm
Window material	Polyimide	Polyethylene
Plate separation	2 mm	2 mm
Polarising voltage	-400 V	+100–400 V

[a] In fact four layers of 0.05 mm polyimide, two act as electrodes, each with another layer for structural support.

4.2 Dosimetry of 15 and 29 MeV protons

Throughout this work, the beam was highly defocussed and passed through a 10 mm diameter tantalum collimator. The resulting beam was uniform typically to around 4% or less (1σ) in the central circular region defined by a radius of 4 mm, measured using EBT after subtraction of average film background noise. The beam was unmodulated at all times, and exited the evacuated beam pipe through a 30 μm Havar window. For 29 MeV, the current on-target was measured to be approximately 15 pA with a Faraday cup, and gave a typical surface dose rate of about 1 Gy s^{-1}, corresponding to about 5 Gy s^{-1} at the BP. At the lower energy of 15 MeV, the beam current was reduced in order for the surface dose rate to be maintained. The reference monitor chamber current is both cases was 6 nA, and for convenience a monitor unit (MU) was defined as 6 nC of collected ionisation charge[1]. The dose rates here are higher than those used clinically

---

[1] This differs from the approach in clinical RT, where linacs are calibrated so that 1 MU is equivalent to for example, 1 cGy at a reference depth under certain measurement conditions.

which incorporate passive scattering devices; for comparison, the typical therapeutic dose rate in the CCO beam is around 0.5 Gy s^{-1} (Palmans et al., 2006a). This is despite using what are actually very low beam currents, however using scattering foils greatly diffuses the proton field and accounts for a significant removal of protons from the final field. Due to these higher dose rates, ion recombination in the Markus chamber was therefore an important effect to consider, and work on this is described in section 4.2.3.

The bias voltage applied to the Markus chamber was ±100 V. The polarity was not always kept the same, as the polarity of the leakage current measured by the connecting NE 2670 Farmer electrometer was not consistent and it was not capable of displaying negative current. In order for leakage to be subtracted using the auto-zero function, it had to be positive. Normally a correction for polarity would be applied in the dose calculation but due to these circumstances this could not be determined with this combination of electrometer and chamber, as the auto-zero function would not work for both polarities in the same session to make the measurements required. In practice, this correction is (and should be) negligible and so it was assumed to equal unity. The leakage current was a minor but noteworthy issue with this electrometer as it was found that after switching on, the leakage would increase over many hours although it peaked at about 3 pA. The electrometer was normally switched on the evening before measurements in order for this to stabilise before an auto-zero was performed. Unfortunately there was not an alternative electrometer available. The monitor chamber was connected to a PTW UNIDOS E electrometer with a bias of -400 V and typically exhibited a leakage of less than 0.1 pA after 5–10 minutes of being switched on.

4.2.1 Experimental method

The dose formalism from report TRS-398 (ICRU, 1999) was adopted throughout wherever possible for measuring absorbed dose to water. The recommended unit of depth is g cm^{-2} rather than mm or cm, as it represents a depth which is independent of density and is more comparable between different materials. The recommended method of converting a thickness of one material to another is by taking the ratio of CSDA ranges in both materials at the energy of interest. For instance, the depth-scaling factor to convert depth in PMMA to water, c_{pl}, is defined as:

$$c_{pl} = \frac{\text{CSDA}_{water}}{\text{CSDA}_{PMMA}} \quad . \tag{4.1}$$

The ranges of 29 and 15 MeV protons in water are approximately 0.8 and 0.25 g cm^{-2} respectively so the majority of measurements were made at values < 0.5 g cm^{-2}, in which case TRS-398 states that PMMA is a suitable replacement for water as a phantom material at these energies. For the proton energy of 29 MeV, the phantom consisted of various sheets of PMMA ranging from 1–5 mm thick, and all were measured using a micrometer. The measurements indicated that the centers of the sheets (where the proton beam was directed) were in some cases several tens of microns thinner than the outer regions. This invalidated the use of weighing the sheets to find the mass thicknesses as this technique assumes uniform thickness. Instead, the central thicknesses were used and multiplied by the average measured density from all the PMMA sheets which was 1.192 $\pm$ 0.005 g cm^{-2}. A value for c_{pl} of 0.974 was used as advised by TRS-398.

At the energy of 15 MeV, it was impossible to solely use PMMA as it is not available in sheets that are thin enough. Instead, a range of polyethylene terephthalate (PET) shims with mass thicknesses between 7.3 and 44 mg cm^{-2} were used in addition with the thinnest sheet of PMMA. The PET shims were converted to water equivalent thickness with a scaling factor c_{pet} of 0.929 derived from the ratio of ICRU CSDA ranges of water to PET for 15 MeV protons in accordance with equation 4.1.

Due to the use of very thin phantom materials, the uncertainty in their mass thickness was such that an additonal uncertainty in D_w at a given depth was attributed to the uncertainty in depth multiplied by the local dose gradient. This additional uncertainty varied from 0.02–2.0% depending on the depth of measurement, and was combined in quadrature to the dosimetric uncertainties in D_w outlined in table G.1.

Referring to the $D_{w,Q}$ formalism in equation 2.8, the ion chamber reading $R_{Q,corr}$ is found by multiplying the raw reading R by the corrections for influence quantities other than beam quality:

$$R_{Q,corr} = R \cdot k_{TP} \cdot k_{ion} \tag{4.2}$$

where k_{TP} and k_{ion} have the same meanings as in chapter 2. When performing a series of measurements in a beam with current fluctuations, use of a monitor chamber is crucial to provide accurate relative measurements such as depth dose curves. In radiotherapy, dose output is usually defined in terms of Gy per MU and so this convention is used here; equation 4.2 is modified by including the monitor reading divided by 6, where R and M are in units of nC:

$$\frac{R_{Q,corr}}{\mathrm{MU}} = \frac{R}{M/6} \cdot k_{TP} \cdot k_{ion} \cdot k_{pol} \tag{4.3}$$

Measurements with other dosimeters such as GafChromic film can then be plotted alongside ion chamber measurements. This retains absolute dose differences between dosimeters without rescaling (or 'normalising') datasets to be equal at some arbitrary depth, as has been the case in other work involving proton dosimetry with ion chambers and GafChromic film (Vatnitsky, 1997; Daftari et al., 1999; Piermattei et al., 2000).

Three sets of depth dose measurements are presented, one for 15 MeV and two for 29 MeV. The ion chamber and GafChromic film measurements were performed together and the first 29 MeV exposures (with MD-V2-55) were carried out 6 months before the 15 MeV (EBT and MD-V2-55) and other 29 MeV (EBT) exposures. Initially the corrections to find $R_{Q,corr}$ were applied and the values plotted against depth-dose curves from MC simulations. The kinetic energy and momentum spread values in the codes were varied until best agreement with the range and slope of the BP distal edge. To ultimately find $D_{w,Q}$ the beam quality correction factor k_Q must be calculated at each depth of measurement and this in turn depends on knowing the energy spectrum from MC simulation output (as previously discussed in section 2.2.3). The final depth-dose data are shown later in section 4.2.5.

4.2.2 MCNPX and FLUKA simulations

Two Monte Carlo codes, MCNPX 2.5.0 (Pelowitz, 2005) and FLUKA 2008.3b (Ferrari et al., 2005; Battistoni et al., 2007) were used to provide cross-comparison with each other and with experimental measurements. A slightly simplified beamline geometry to that visible in figure 4.1 was described in the input cards, details not included were outside an appreciable radius of the beam axis and so would have negligible influence on the beam characteristics. The modelled geometry is shown in figure 4.3 along with a schematic of the beamport and Perspex jig to illustrate the components.

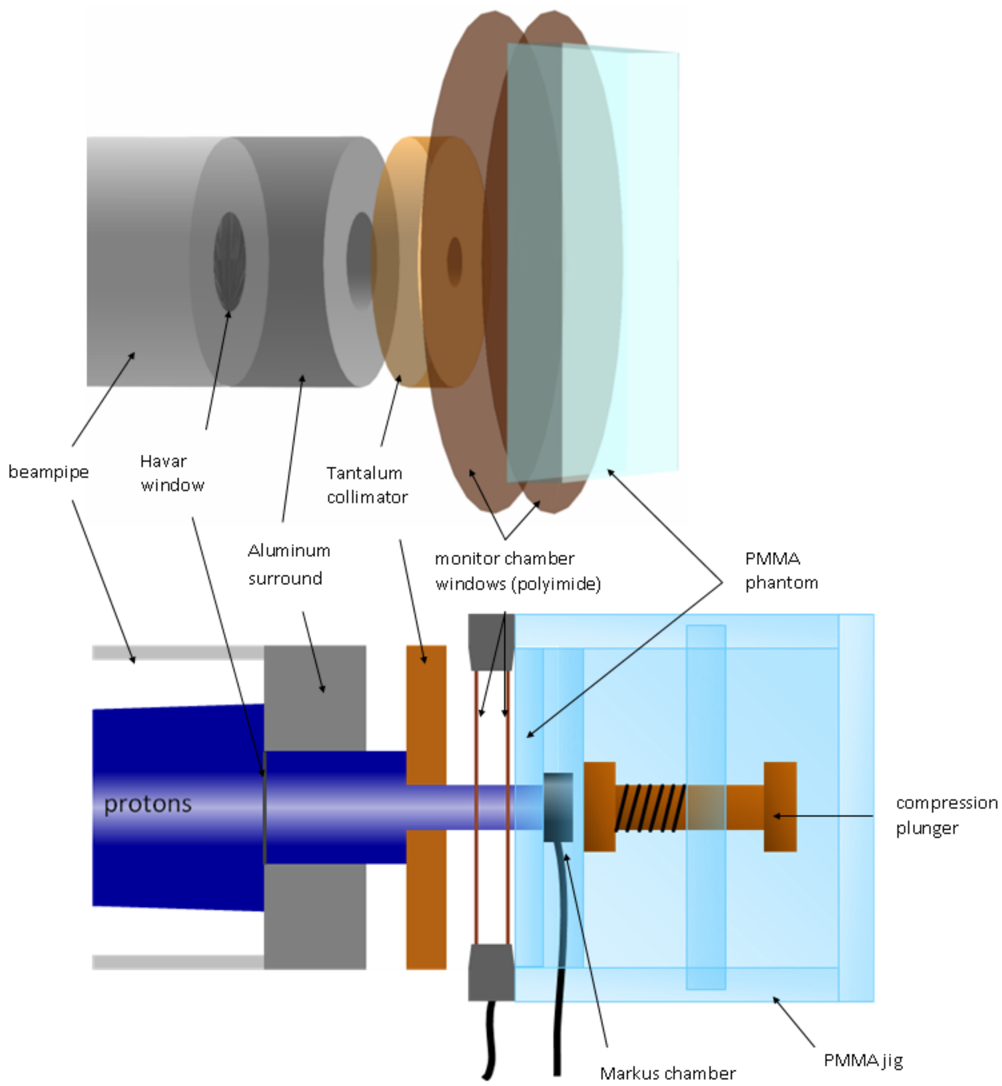

Figure 4.3: Schematic of the beamline and jig arrangment along with visualised geometry used for Monte Carlo simulations.

Divergence and collimation of the beam were accurately modeled, as was the thickness and composition of the beam exit port window and monitor chamber windows. The nominal energies of 15 and 29 MeV were refined iteratively to match the range of the BP measured with the Markus chamber, and in the same manner a Gaussian momentum spread, ($\Delta p/p$) specified in terms of σ, was applied and adjusted so that the slope of the BP distal edge was in close agreement. The same beam parameters and geometry were used in the simulations with both codes to provide a direct comparison.

With regards to physics models, in FLUKA the PEANUT model was used for hadron-nucleus interactions and the HADROTHErapy[1] defaults for transport but with reduced energy cut-off values for δ-rays (10 keV). In MCNPX, no delta-rays are transported so the default Vavilov model for energy straggling was used along with the LA150H proton nuclear cross-section library. A proton energy cut-off of 1 keV was used to override the 1 MeV default. Such a low value was needed as there appeared to be no deposition of the remaining cut-off energy, meaning the BP height was underestimated by approximately 20% (for 29 MeV protons) with a 1 MeV cut-off. This behavior was still apparent in the later version 2.6.0 of MCNPX and was reported as a bug.

A 1-dimensional cylindrical voxel mesh was used for energy deposition scoring in both codes, with a 2.65 mm radius consistent with Markus chamber cavity dimensions and a voxel thickness of either 10 or 20 μm for the 15 and 29 MeV cases respectively. Sufficient numbers of particles were run to keep statistical uncertainties significantly to around or below 0.2% until the distal edge of the BP where the proton fluence began to reduce. For 29 MeV simulations, the CPU time per particle was 17 ms with FLUKA versus 4.5 ms with MCNPX, and typically 8 million histories were run with FLUKA and 18 million with MCNPX to obtain similar statistical uncertainties. In total CPU time, this resulted in 37.8 hours per FLUKA run and 22.5 hours per MCNPX run. Clearly, MCNPX will simulate a history in significantly less time due to lack of δ-ray transport while FLUKA achieves a similar uncertainty with fewer histories for the same reason as more particles

---

[1] The odd capitalisation is how the Fluka manual refers to it, as only the first 8 characters are used in the input

per history are depositing energy. Jobs were always sent to multiple cores, generally more than 4 and less than 40. The number of cores requested of BlueBEAR was often tailored depending on the time of day and job load on the cluster. For example, sending a job to run at the end of the day did not require a fast turn-around and at times when BlueBEAR was overloaded with jobs there was no net time benefit in requesting more than 4–8 cores.

4.2.3 Recombination (k_{ion}) correction

This correction is described in section 2.2.4 along with the theoretical basis for determining k_{ion}. This depends on the two unknown parameters A and m^2 which relate to the initial and volume recombination effects respectively. These parameters were previously measured for the actual Markus chamber (serial no. 478) used in this work by Palmans et al. (2006a) at various depths in the CCO modulated and unmodulated proton beam. It was attempted here to try and measure them in the Birmingham cyclotron 29 MeV beam at two depths: 2.0 mm (in the plateau region) and at 6.7 mm (in the BP). The value of A should in theory be larger in the BP due to the higher LET of the protons there, and the total k_{ion} should also be larger for the same measured ionisation current.

The same setup was employed as for earlier dosimetry measurements: the beam was collimated by the 10 mm diameter Ta collimator and the monitor chamber, PMMA sheets and Markus chamber were supported by the dosimetry jig, with the monitor chamber window situated no more than 10 mm away from the collimator. Ideally, these measurements require a stable beam current which can be precisely controlled so that measurements can be made for different ionisation currents by varying the beam current. Due to the cyclotron current's significant variability, total charge measurements were made over 10 s to obtain an average ionisation current, and then repeated twice further. Repeated measurements were disregarded if the average current was different by more than several percent. The electrometer was switched on for many hours before the first measurement to warm up and for the leakage current to stabilise, so that the autozero function could be used appropriately.

Measurements were made for six different voltages (n = 1.00,1.75, 2.33, 3.50, 5.30, 7.00) from 175 V downwards. The upper limit was enforced by a reluctance of the electrometer to apply any voltage higher than this to the Markus chamber (#478), the reason for which was never determined but perhaps to do with the chamber insulators or the cable. The Markus is desrcibed as having an operating voltage between 100–400 V and so the upper end of this range was out of reach. At each voltage, measurements were taken for four different beam currents which nominally were between 15–45 pA for measurements in the plateau and 15–40 pA in the BP. These corresponded roughly to dose rates of 1–3 Gy s^{-1} and 5–12 Gy s^{-1} with the lowest values being representative of the usual beam current/dose rate used for depth-dose measurements.

Figure 4.4 shows plots of $I_V/I_{V/n}$ versus I_V at both depths, and from the linear fits values A and m^2 were determined for each value of n. The nominal chamber volume was used to find g, rather than by deriving it from the calibration factor. The values of A and m^2 are shown in table 4.2 and are compared with values found by Palmans et al. (2006a) for similar proton beam qualities in the CCO beam. There are inevitably some differences in beam quality between the two sets of data. However, the change in quality from R_{res} of 1.28 to 0.58 g cm^{-2} would result in a relatively modest increase in LET of 42% (based on S/ρ values) compared to 303% from 0.58 g cm^{-2} to 0.05 g cm^{-2}. Therefore it is most important to find a k_{ion} which is most accurate in the BP, where recombination is greater both due to initial effects and due to higher ionisation current. It is also not practical to use different recombination parameters at different depths, and so a value of A and m^2 must be chosen that best represents recombination for the whole proton range.

The data from Palmans et al. (2006a) yields lower values of k_{ion} and with much lower uncertainties than the work undertaken here. One likely reason for the reduced uncertainty is that the method adopted by Palmans used two Markus chambers placed together with their windows face-to-face in a water phantom, with the beam passing through the rear of the first chamber. This ensured that the fluence in both the first (the monitor) and the second chamber were extremely well correlated. Secondly, the CCO

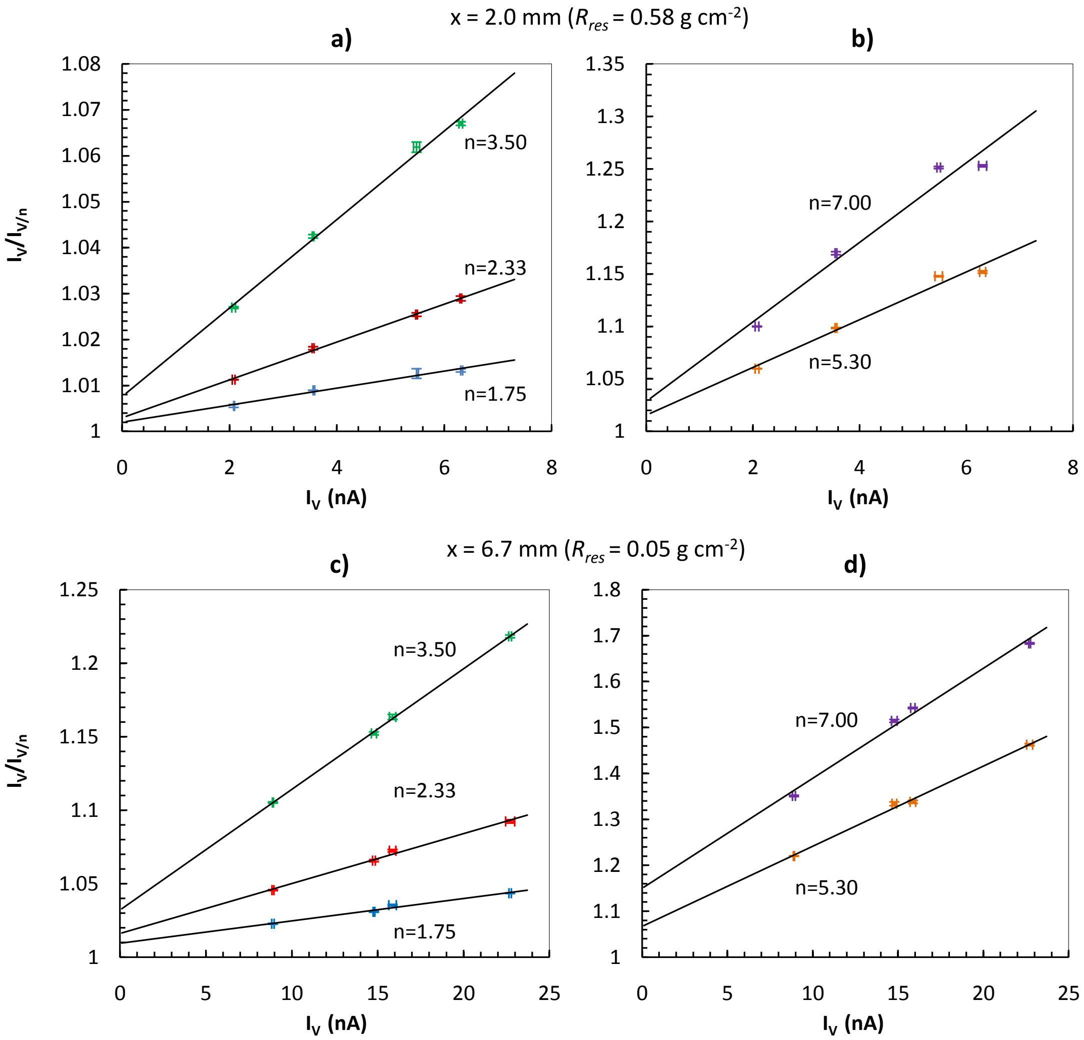

Figure 4.4: Plots of $I_V/I_{V/n}$ versus I_V for protons with the Markus (#478) chamber at various values of n, at a depth in PMMA (and effective R_{res} in water) of 2.0 mm (0.58 g cm^{-2}) and 6.7 mm (0.05 g cm^{-2}). These depths correspond to the plateau and BP regions respectively.

Table 4.2: Mean values of A and m^2 for the Markus (#478) ion chamber derived from linear fits to $I_V/I_{V/n}$ versus I_V. Values found in this work are shown alongside values from Palmans et al. (2006a) at the nearest comparable beam qualities. Also, k_{ion} is calculated from all of these values at the typical I_V measured with a proton beam current of 15 pA. Percentage uncertainties are shown in brackets.

	This work		Palmans et al.	
R_{res} (g cm^{-2})	0.58	0.05	1.28[a]	0.07[b]
A (V)	0.57 (30)	2.74 (35)	0.28 (3.0)	0.51 (5.0)
m^2 (cm^{-1} nA^{-1} V^2)	$4.37 \cdot 10^3$(6.3)	$3.42 \cdot 10^3$(16)	$3.73 \cdot 10^3$(4.0)	$2.07 \cdot 10^3$(7.0)
k_{ion} (15 pA)	1.011[c](0.2)	1.045[d](1.0)	1.008[c](0.02)	1.016[d](0.08)

[a] Measured in an unmodulated beam

[b] Measured in a modulated beam

[c] when applied to I_V measured in plateau

[d] when applied to I_V measured in BP

beamline has a highly regulated beam current, necessary for RT, and so fluctuations were much lower than with the Birmingham cyclotron. Taking this into account, it was decided that the Palmans parameters would be used and figure 4.5 shows k_{ion} versus I_V over the range of interest. At 15 pA of beam current, I_V was approximately 1.7 nA at the entrance depth (i.e. no PMMA) increasing to 8.4 nA at the BP.

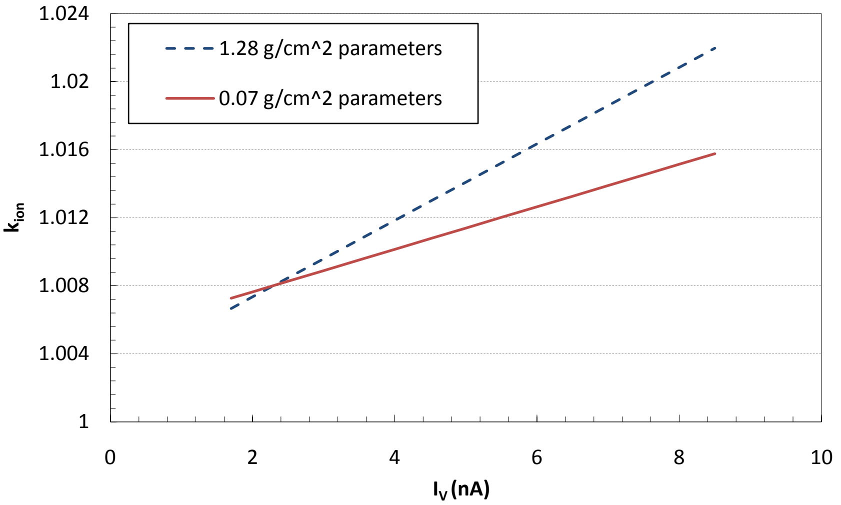

Figure 4.5: How k_{ion} varies with measured ionisation current I_V where $V = 100$ V, for the parameters obtained at R_{res}= 1.28 and 0.07 g cm^{-2}.

At the lower end of the range of I_V, both sets of recombination parameters give very similar values of k_{ion}. Therefore it was decided most appropriate to use the parameters at $R_{res} = 0.07$ g cm^{-2} to cover the whole range of measurements.

4.2.4 Beam quality (k_Q) correction

As described in section 2.2.3, the purpose of this factor is to correct for the dose to water calibration factor being valid for ^{60}Co radiation and not for protons, and the quantities involved in deriving it are shown in equation 2.10. Prime amongst them is $s_{w,air}$ for protons which varies with proton energy and hence depth of measurement. To calculate this value, knowledge of the proton spectrum is required but this can only be estimated through MC simulations. FLUKA has a boundary crossing fluence scoring card called USRBDX as well as a track-length estimator USRTRACK that does a similar job but works over a volume rather than across a plane. One limitation of using these cards is that whenever future measurements need to be made, full simulations will need to be repeated with these scoring cards at the necessary depths which would be an inefficient use of CPU time. To avoid this, an in-house routine was written to score a spectrum at any requested depth much more quickly from a dump file containing track vertex coordinates and proton energy for every history during a single MC run. This method assumes that setup geometry and cyclotron energy are reproducable between measurement sessions.

The FLUKA routine *mgdraw* was modified and called from within the input file with the USERDUMP card so that the x, y, z and E values were dumped to a file for all tracks with at least one vertex inside a radius of 2.65 mm of the beam axis; equivalent to the radius of the Markus chamber sensitive volume. While secondary electron production was turned on, only proton tracks were evaluated along with their unrestricted stopping powers, and secondary protons from non-elastic interactions were included. To perform this calculation more accurately with electron contributions the restricted proton stopping powers calculated internally by FLUKA are needed, but as they are not wholly consistent with ICRU49 stopping powers (Parodi and Squarcia, 2001) this method was not used. According to calculations by Medin and Andreo (1997) this can lead to differences of up to 0.5%. The dump file was then processed by a specially written Fortran program called FLUBOUND (available in appendix B.1), which for a given depth would score the proton fluence passing an imaginary boundary at this depth in a similar way to a USRBDX scoring card in FLUKA. A problem occurs when deciding what energy value to score, as a track crossing a boundary has two energy values, one either side. To reduce any step-length artifacts resulting from selecting a halfway or single random value, 1000 random values between the two energies were scored, which resulted in a smooth distribution without obvious artifacts. This method relies upon relatively short track-lengths to work, and typically the tracks were between 10 and 40 μm long at all sampled depths. These track lengths corresponded to the distance between secondary electron generation events. To check that FLUBOUND was producing appropriate spectra it was compared to the FLUKA track-length estimator USRTRACK in a Markus cavity equivalent volume (2 mm of air $\approx$ 2 μm of PMMA) at four depths in a simulated beam with proton energy of 29.15 MeV. The spectra are shown in 4.6, and are in excellent agreement.

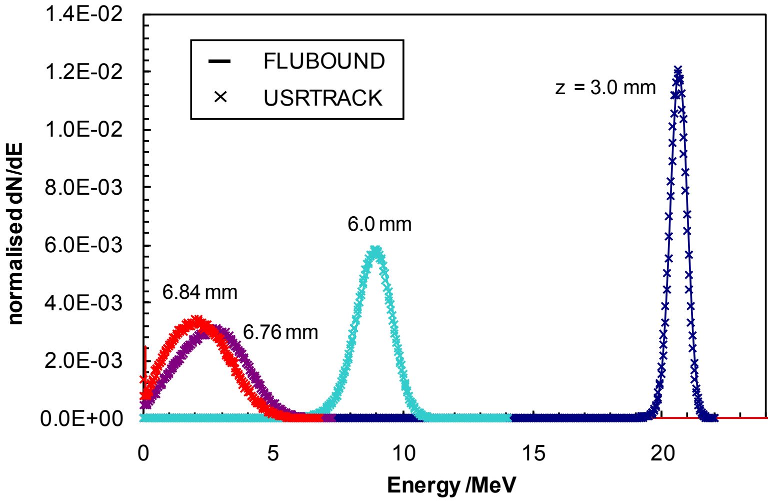

Figure 4.6: Plot of normalized proton spectra produced by the FLUKA track-length estimator USRTRACK (crosses) and user written FLUBOUND program (solid lines) at four depths in a PMMA phantom. Two spectra are from different depths in the plateau region of the depth-dose curve, and two are at points in the BP.

The final Markus depth-dose measurements include the FLUBOUND generated k_Q factors, which were individually calculated for each depth of measurement using the relevant simulation for all three datasets. In figure 4.7 they are plotted as a function of R_{res} in water using the scaling factor c_{pl} of 0.974, and compared with TRS-398 values which were provided by Medin and Andreo (1997), which were a compromise of the different values calculated for proton energies between 50–250 MeV. The report only gives tabulated values down to R_{res} = 0.5 g cm^{-2}, but using the analytical fit for $s_{w,air}$ in the appendix it is possible to plot a continuous function of k_Q down to R_{res} = 0 g cm^{-2}. By looking directly at the article by Medin and Andreo (1997), $k_Q$values for the 50 MeV case are fully tabulated down to R_{res}= 0 g cm^{-2}, which is also shown for comparison and agrees more closely with those calculated here than for the TRS-398 fit, which appears to be greatly influenced the values for higher energies. A difference of up to 0.5% is evident at larger R_{res}, which is explained by the use of unrestricted stopping powers in this work, whereas Spencer-Attix cavity theory was applied by Medin and Andreo using restricted stopping powers.

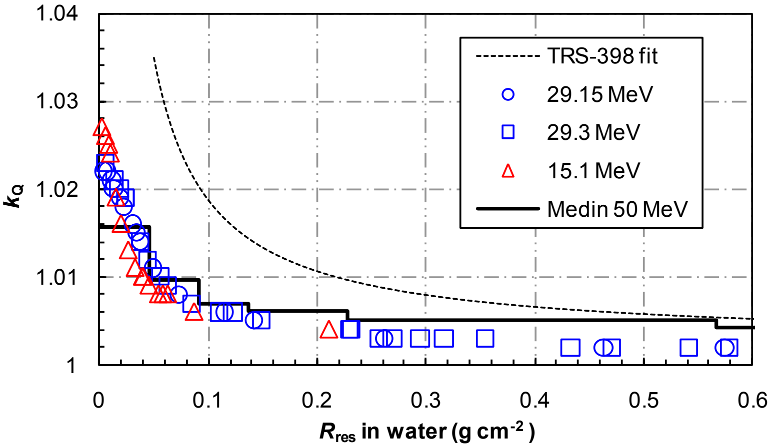

Figure 4.7: Plot of FLUBOUND calculated $k_Q$values versus R_{res} in water (symbols) for protons compared with TRS-398 values valid for all energies between 50 and 250 MeV (dashed line) and Medin and Andreo's values specifically for 50 MeV.

TRS-398 gives an uncertainty budget for the various factors in k_Q, which totals 2.1% for a plane-parallel chamber. The uncertainty for $s_{w,air}$ is the largest component at 1.0%, and there is 0.3% attributed to the assigment of $s_{w,air}$ to the beam quality which is due to the spectrum at any R_{res} differing slightly depending on initial beam energy. The latter contribution should be considered eliminated here as the assignment has been made directly to the spectrum at every depth of measurement, and so there is no amibiguity. However, the statistical uncertainty in each energy bin of the spectrum calculated by FLUKA should be accounted for. It was found that propagating this uncertainty in the $s_{w,air}$ calculation in FLUBOUND usually resulted in an uncertainty of 0.3% and so by happy coincidence the total uncertainty can be considered unchanged from the TRS-398 estimate.

4.2.5 Fully corrected depth-dose measurements

After finalising all the dose corrections, the depth dose curves were compared to the FLUKA simulations with energy parameters that best matched the data to the nearest 50 keV and 0.05% $\Delta p/p$. The beam energies used were 15.05, 29.15 and 29.30 MeV with momentum spreads in terms of σ of 0.4, 0.3 and 0.25% respectively; these values are quite reasonable for this type of cyclotron. The depth dose data and simulations are shown in figure 4.8 although for the two 29 MeV data sets, only one is shown in full accompanied by simulation (29.15 MeV) while just the cubic spline fit to Markus data is shown for 29.3 MeV (shown later in more detail in figure 5.12). The agreement in energy with the nominal cyclotron values is quite good, to within 1%. Between the two 29 MeV runs (which were six months apart), some parts of the cyclotron were replaced and maintenance performed which may be the main cause for this difference. Successive measurements since the second run (data not shown here) over many months have been in excellent agreement which suggests that normally the cyclotron energy is very reproducable. These measurements should not be considered direct measurements of energy as the depth dose curves are quite sensitive to any difference in the actual densities of PMMA and PET versus the simulated densities, and also the I-value used in the stopping power formula. FLUKA calculates and uses its own I-value which has some uncertainty and is considered another ‘tunable’ parameter in order to achieve a fit to data. Unfortunately there has been no direct measurement of proton energy performed on the cyclotron to allow any kind of comparison.

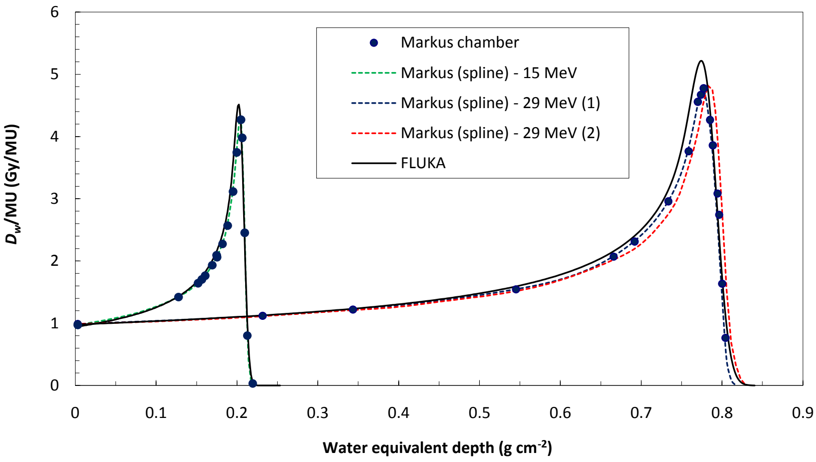

Figure 4.8: Depth dose curves for 15 and 29 MeV protons measured with a Markus chamber, with an interpolated fit by cubic spline. A second 29 MeV measurement is shown only by spline fit, to show the small difference that occurred between measurements six months apart. Simulations with FLUKA are shown with energies and momentum spreads (in terms of σ) of 15.05 MeV, 0.4% and 29.15 MeV, 0.3%. Markus error bars are omitted as they are smaller than the size of the symbol.

The data in figure 4.8 are scaled to the shallowest (open) Markus measurement depth, equivalent to that of the chamber window water equivalent thickness. This is mainly because scaling to the peak may not be reliable due to the rapidly changing dose gradient and uncertainty as to whether the absolute peak value has been measured. Also, for an unmodulated beam, TRS-398 recommends selecting a reference depth in the plateau. This depth is considered beyond the influence of any MC artefacts at the air-PMMA inerface. One common observation for each energy is that the peak-to-plateau ratio is around 5–10% larger in the FLUKA simulations. There could be many reasons for this: inaccuracy of FLUKA stopping powers at lower energies in the BP, underestimated nuclear attenuation of protons with depth, larger collimator scatter in the measurements producing low energy contamination boosting dose in the plateau and underestimated dose correction factors (i.e. k_Q, k_{ion}). A known inaccuracy of the W_{air}/e term in k_Q occurs at energies below 1 MeV, where W_{air}/e starts to increase but from the data and theory available, summarised by Grosswendt and Baek (1998) and Jones (2006), the possible increase at the typical energies in the BP would be insufficient to explain the discrepancy.

4.3 Dosimetry of 38 MeV α-particles

4.3.1 Experimental method

The same procedures and protocols were followed as for dosimetry with protons. The only differences in TRS-398 arising for 'heavy ions' (i.e. heavier than protons) are a larger W_{air}/e value (34.5 J C^{-1}), larger uncertainty in k_Q of 3.2% for a plane-parallel ion chamber and use of α-particle stopping powers. A practical difference was that all the PMMA sheets were too thick to use at this α-particle energy, and so the PET shims were used as the phantom material in addition to some thinner Melinex® films of the same material with thicknesses in the range 1–7 mg cm^{-2}. The water equivalent thickness correction, c_{pet}, was found to be 0.929; the same value as for protons.

The beam current was adjusted so that 6 nA of ionisation current was observed from the monitor chamber, to be consistent with the surface dose rate of 1 Gy s^{-1} used for protons and previous definition of a MU. The significant increase in LET of α-particles compared to protons suggested that ion recombination could be a more significant effect, and with no available data for the Markus chamber the appropriate parameters had to be determined separately. This is discussed in section 4.3.4.

Due to the use of very thin phantom materials, the uncertainty in their mass thickness was such that an additonal uncertainty in D_w at a given depth was attributed to the uncertainty in depth multiplied by the local dose gradient. This additional uncertainty varied from 0.3–6.0% depending on the depth of measurement, and was combined in quadrature with the dosimetric uncertainties in D_w outlined in table G.1. The reason for doing this was to allow consideration of this uncertainty in the total uncertainty in the relative effectiveness (RE) of the film.

4.3.2 FLUKA simulations

The publicly available version of FLUKA does not include full physics treatment of nucleus-nucleus interactions for heavy ions below 100 MeV/n, so no secondaries other than δ-ray electrons are generated. However, a developmental version which includes a so-called Boltzmann Master Equation theory (BME) event generator (Cavinato et al., 2001), is available from the code authors but is still in beta release. This allows nuclear interactions to be modelled and hadronic secondaries/recoils to be produced and transported by invoking the EVENTYPE card with SDUM=DPMJET for ions with energy below 100 MeV/n. This version was used here.

Using the same geometry as for protons, simulations with α-particles at energies around 38 MeV in PET with several momentum spreads of 0.2–0.3% were carried out until the best agreement to the experimental depth dose data was found, again focussing on matching the range and distal slope of the BP. Once the best-fit parameters were found, the simulation was repeated invoking the USERDUMP card and the modified *mgdraw* routine to dump to file the α-particle energy and track vertex coordinates that were within a column of equal diameter to the Markus sensitive volume.

4.3.3 Beam quality (k_Q) correction

TRS-398 again gives guidance on calculating k_Q for heavy ions, and shows a plot of $s_{w,air}$ versus energy per nucleon for a range of ions from He to Ne. Above 1 MeV/n, the values are fairly similar and change only slightly with increasing energy. For simplifcation and due to a lack of experimental data, a constant value of 1.13 is recommended regardless of ion type or energy with a larger uncertainty, relative to protons, of 2% to account for this simplifcation. This value and uncertainty is quoted from Hartmann et al. (1999), who originally proposed they be used for carbon ions but not in the BP when a monoenergetic beam is used. In that paper it was shown that $s_{w,air}$ increases by up to $\approx 4\%$ in the BP. In light of this, it was decided that as previously done for protons the value of $s_{w,air}$ should be calculated by simulation of α-partcle spectra at each depth of measurement, leading to more accurate determination of k_Q.

The FLUBOUND program was used again, but naturally using water and air stopping powers for α-particles. Compared to protons, α-particles with the same energy per nucelon have a higher propensity for creating charged secondaries through non-elastic reactions. However, at 38 MeV (9.5 MeV/n) any influence of non-elastic secondaries on the measurement of dose should be very small. In fact, simulations with FLUKA indicated that less than 0.3% of all particles transported were charged (hadronic) secondaries, so their contribution to the total $s_{w,air}$ was considered to be negligible. The other terms in k_Q were taken from TRS-398; most notably, a different W_{air}/e to protons is recommended (34.5 eV ± 1.5%). The terms relating to the ^{60}Co beam quality remain the same.

The values of k_Q are shown in figure 4.9 compared with the constant k_Q obtained using the ICRU assumption of a constant $s_{w,air}$ of 1.13. It is clear that this assumption is not valid at the lower energies used here compared to therapeutic energies, and so a substantial improvement in accuracy is obtained by using this method. It also results in a reduction in the quoted uncertainty of 2%; the estimated contribution due to variation by particle type and energy was subtracted in quadrature leaving a new uncertainty of 1.5%.

4.3.4 Recombination (k_{ion}) correction

The correction for recombination could be more significant for α-particles than for protons due to the increase in LET and thus initial recombination in particular. There were no previous measurements of A and m^2 for the Markus chamber with α-particles available, and so they had to be carried out using the cyclotron once again using the same method as attempted previously for protons. Further consideration was given as to how to reduce experimental uncertainties, as it appeared during several repeated exerimental sessions that there was a slow drift exhibited by the detectors in measuring R/M of the order of a few tenths of a percent, which is significant for these very sensitive measurements. It was

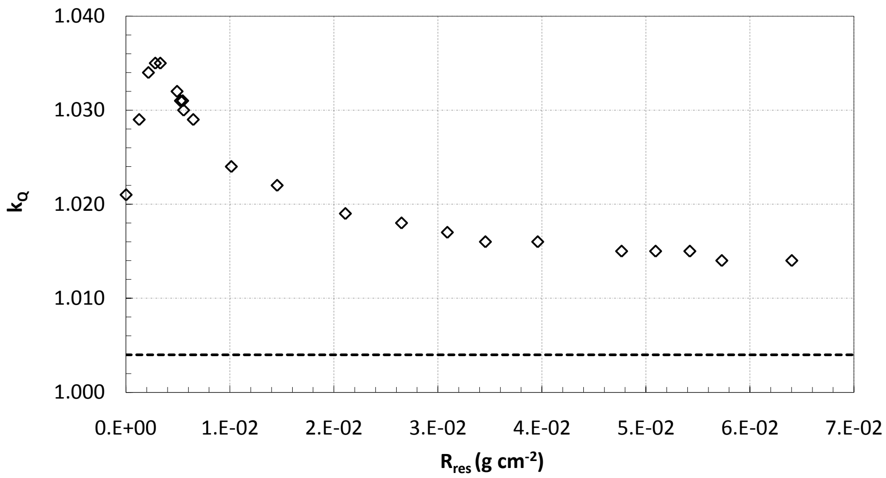

Figure 4.9: Calculated values of k_Q for 38 MeV α-particles as a function of R_{res} (diamonds) compared to the constant value obtained by using the TRS-398 recommended value of $s_{w,air}$ (dashed line).

hypothesised that over time and when using high currents there could be enough particle energy dumped in the Ta collimator to give a temperature rise of a few degrees Kelvin. As the monitor chamber was vented to air very close to the collimator, it was plausible that perhaps the cavity air temperature was not consistent between the monitor and Markus chambers. A digital temperature probe (thermocouple) was placed on the collimator and the monitor chamber window soon after a high current irradiation, and they were found to be 1.0–1.5 K above the ambient temperature and slowly cooling while the beam was off. A temperature difference of 1 K between the two detector cavities would account for $\approx 0.3\%$ difference in R/M and a similar change in $I_V/I_{V/n}$.

To reduce the heating effect, the air gap between the collimator and jig was increased to 40 mm and a desktop fan was used to circulate air between them. Additionally, to improve the correlation of fluence between the two detectors a smaller aperture was chosen of 3 mm diameter, i.e. within the Markus active region diameter. This was so that the same fluence (as much as possible) was measured by both detectors. Measurements were then made in a similar fashion as for protons for four different voltages (V/n, where n=1.0, 2.0, 3.0 and 4.0) with the Markus #2225 chamber this time which would permit a V of 400 V downwards. Six different beam currents were used, resulting in dose rates between 30–

250 Gy min^1 and the measurement times varied between 35–100 s as necessary to optimise the uncertainty due to the resolution of the electrometers (e.g. to obtain readings near the upper limit of a decade). The number of repeated measurements per current were also increased to as many as thirteen in one case to ascertain that the chamber response had settled after changing the voltage. Only the last few measurements were used to obtain an average, however.

To obtain a single set of recombination parameters that best represented the correction to be applied over the whole range, the measurements were performed at a depth of 0.036 g cm^{-2} of PET; approximately half of the α-particle range in PET after passing through the various beamline components. A plot of $I_V/I_{V/n}$ against I_V is shown in figure 4.10, where error bars indicate the s.d. of repeated measurements which were dominated by the effect of beam current fluctuations.

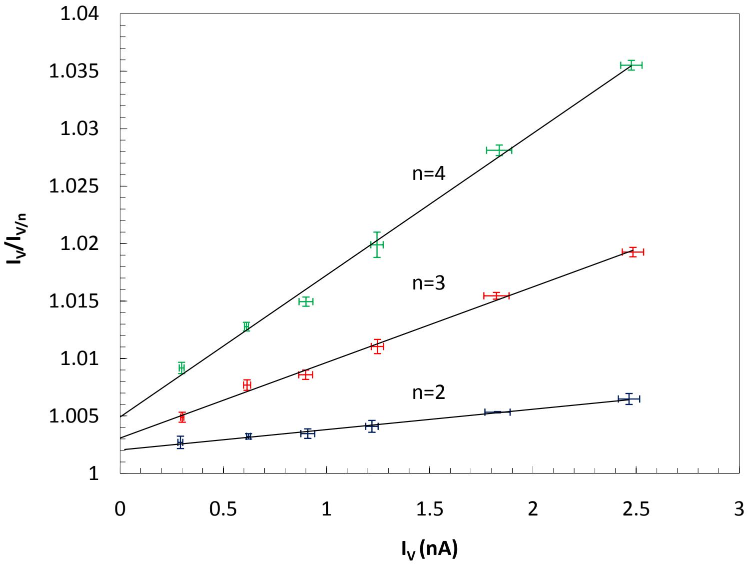

Figure 4.10: Plots of $I_V/I_{V/n}$ versus I_V for α-particles at various values of n, at a depth of 0.036 g cm^{-2} in PET with linear fits applied.

The recombination parameters obtained from each linear fit are shown in table 4.3 along with the weighted mean values and standard uncertainties. Surprisingly, compared to protons in the plateau region the initial recombination parameter A is only slightly higher, but is significantly less than for protons measured at the BP. It is slightly higher for both depths than the values from Palmans et al. (2006a) shown in table 4.2, however. The most significant difference is the increase in the volume recombination term m^2g, which is almost an order of magnitude greater. This gives rise to significantly higher values of k_{ion} than for protons for the same ionisation current, I_V; an expected result. Although a voltage of 400 V was used to determine these data, for the depth dose measurements it was set to 100 V as previously used for protons. There is also an assumption that ion recombination in the #2225 chamber is equal to that for the #478 chamber which was used to perform the depth dose measurements, which appears to be valid given the data for protons for both detectors in Palmans et al. (2006a).

Table 4.3: Values of A and m^2 for α-particles with the Markus (#2225) chamber derived from linear fits to $I_V/I_{V/n}$ versus I_V for $n = 2$, 3 and 4. Values of k_{ion} at the surface and BP for an ionisation current equivalent to an entrance dose rate of 1 Gy s^{-1} are given, for an operating voltage of 100 V. Standard percentage uncertainties are shown in brackets.

	m^2 (cm^{-1} nA^{-1} V^2)	A (V)	$k_{ion}\|^{z=0}$	$k_{ion}\|^{z=BP}$
$n = 2$	$1.56 \cdot 10^4$ (4.5)	0.819 (5.5)	1.026 (0.1)	1.089 (0.3)
$n = 3$	$2.17 \cdot 10^4$ (3.6)	0.611 (11)	1.031 (0.1)	1.118 (0.4)
$n = 4$	$2.18 \cdot 10^4$ (3.2)	0.656 (11)	1.032 (0.1)	1.119 (0.3)
$\bar{x}_w$	**$1.96 \cdot 10^4$(11)**	**0.736 (9.8)**	**1.030 (0.3)**	**1.108 (1.0)**

4.3.5 Fully corrected depth-dose measurements

After finalising all the dose corrections, the depth dose curve was compared to the FLUKA simulation (with BME event generator) using a beam energy of 38.0 MeV and a $\Delta p/p$ of 0.25%. The Markus depth dose data and FLUKA simulation is shown in figure 4.11 along with a cubic spline fit to the Markus data.

The agreement in energy with the nominal cyclotron value is excellent, although again it appears the peak-to-plateau ratio is 7% larger with FLUKA compared with measurement. This suggests that perhaps there is some physical effect due to the beamline which is not being correctly modelled. It was later found that before the vacuum window, about 25 cm upstream there was a graphite aperture 35 x 25 mm in size which was approxi-

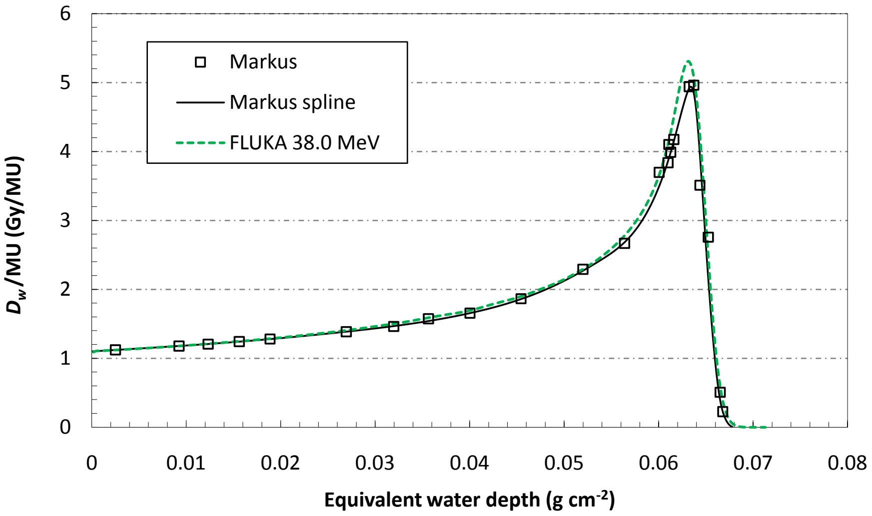

Figure 4.11: Depth dose (per MU) in PET converted to water equivalent thickness. Markus measurements are shown along with a cubic spline fit, and the best matched simulation with FLUKA (38.0 MeV, 0.25% $\Delta p/p$).

mately 15 mm thick. This could act as an extra source of low energy scatter in addition to the main collimator, but subsequent incorporation of this aperture into the simulations had negligible effect. The source origin was modelled as a point source 4 m upstream of the vacuum window at the approximate location of the (de)focussing quadrupoles with divergence large enough to just cover the largest dimension of the graphite aperture. In reality there is some perturbation due to a port switching magnet just before the graphite aperture which may result in a different beam path to that which is simulated which could affect scattering processes, but further detailed simulations were not attempted due to a lack of detailed information regarding the precise geometry which was fairly closed off and difficult to access in order to make measurements.

CHAPTER 5

GAFCHROMIC FILM DOSIMETRY

This chapter describes much of the work done with GafChromic EBT, MD-V2-55 and HD-810 films with mono-energetic proton and α-particle beams produced by the Birmingham cyclotron. The main challenge was to perform accurate, absolute dosimetry with these films and in the process a beam quality correction was proposed using a similar approach as for ion chambers. Such an approach has not been considered before for RCF in any known literature. The most significant component of this correction factor was to compensate for the reduced relative effectiveness (RE) of the film when measuring dose from particles of lower energy or with LET significantly higher than the beam quality at which the films were calibrated. A simple model to describe the dose response of these films versus energy was calculated for protons. This response function could then be incorporated into MC dose calculations with FLUKA to enable simulation of the film's dose response to poly-energetic proton beams, such as those from a laser-plasma source

Sections of this work were published (Kirby et al., 2010), and the full journal article is available in appendix I..

5.1 Nikon Super Coolscan 35mm film scanner

Prior to the work described here, the only scanner available to hand was a Microtek (Hsinchu, Taiwan) Scanmaker 35t+ 35mm slide scanner, with a bit depth of 8 bits per colour channel. A masters degree project preceded this PhD work (Kirby, 2007), in which the performance of this scanner was evaluated in terms of scanning GafChromic film for proton dosimetry. It was apparent that this slightly dated model was not ideal for many reasons: its bit-depth per colour channel was only 8-bit, the light source was a fluorescent tube containing a UV component and the images it provided exhibited a severe banding effect possibly indicating that the charge coupled device (CCD) array contained some elements that were faulty. Hence some research was undertaken to find an ideal replacement, bearing in mind all the technicalities of accurately and reproducibly digitising RCF previously discussed in section 2.3.

In summary, an ideal RCF scanner would have:

- a highly uniform light field,
- no UV component in the light source,
- minimal heating of the film by the light source,
- minimal polarisation of the light source,
- capacity to scan large numbers of films quickly, and
- highly reproducable scanning.

5.1.1 Specifications

In RT quality assurance, often the radiation fields requiring analysis are large such that they require scanners with large scanning fields ($\gtrsim 20$ cm), hence A3 or A4 sized flatbed scanners are often the best option. It was anticipated that much smaller fields would be of interest in this work, which opened up a wider range of possible scanners. One type which stood out was the Nikon (Tokyo, Japan) Super Coolscan (NSC) range, apparently the first to use red (R), green (G) and blue (B) LEDs as the light source in place of a fluorescent tube. They are designed to scan various smaller formats of photographic and medical film. The two higher specification models (the NSC 5000 ED and 9000 ED[1]) were excellent candidates, with the main technical differences between them only being the scanning field size, CCD array size and method of multi-film scanning. The specifications of both are compared below in table 5.1.

Table 5.1: Main specifications of the Nikon Super Coolscan 5000 ED and 9000 ED models.

	NSC 5000	NSC 9000
Scanning system	Fixed media, movable plane single-pass scanning	Fixed optical, movable media, single-pass scanning
Image sensor	2-line linear CCD	3-line linear CCD
Optical resolution	4000 px/inch	
Bit depth	16-bit per colour	
Light source	R, G, B and IR LEDs	
Colour separation	Performed by RGB LEDs	
Scan time (4000 px/inch)	20 s	40 s
Batch scan mode (qty)	SF-210 slide feeder (50)	FH-835M slide holder (5)
Weight	3 kg	9 kg
Dimensions	25 x 50 x 20 cm	10 x 17 x 31 cm
Approximate cost (2008)	£1200 (inc. SF-210)	£2000

From the specifications, some of the conditions listed are fulfilled whereas some of them could only be tested once the scanner was available for use. For instance, the RGB LED light source greatly reduces both the heating and UV effects compared to a fluorescent tube, and special accessories for these scanners permit batch scanning. An additional requirement was that the scanner was very portable in order to take it to off-site experiments. This, and the enhanced batch-scanning capability, meant that the NSC 5000 was more attractive than the NSC 9000 overall. However, the NSC 9000 was (by chance) already owned by the laser group at RAL and so they permitted loaning it to Birmingham for approximately a year. After this period, the NSC 5000 was purchased by the Birmingham group for further measurements. Most of the operational tests in the next section were carried out on the NSC 5000, but are thought to represent the

---

[1] The 'ED' part of the name is dropped from here onwards.

performance of the NSC 9000 to a good approximation due to large degree of similarity between them.

5.1.2 Operational tests

A selection of operational tests were performed with the NSC 5000, using different exposed GafChromic films where appropriate, depending on the test. The scan parameters used here are shown in table 5.2 will be referred to as the *default* parameters and are used throughout this work unless otherwise specified.

Table 5.2: Usual (or *default*) scanning options and parameters selected in the supplied Nikon Scan 4 software, used throughout this work.

Option/parameter	Value
Gamma	2.2
Resolution	150 px/inch
Auto-focus	on
Digitcal ICE4 Advanced™	off
Auto-exposure	off
Bit-depth	16-bit
Multi-sample scanning	1x
Analogue gain	R, G, B all 0

5.1.2.1 Reproducibility

The effect of repeated scans on EBT and HD-810 films was investigated in 3 slightly different ways. Firstly, the NSC 5000 was turned on and left for half an hour for the electronics to warm-up before the first scan. Then using the slide feeder (SF-210), the two films were scanned in batch mode every five minutes, nine times in succession. In between repeated scans, the films were situated in the slide feeder and so were outside of the scanner so that any heat effects on them from being inside were avoided. This also reflected the usual scanning conditions. A shorter repeat of this test was performed only with HD-810 for five scans, where the scanner was switched off for three minutes in between scans. The scanner was switched on one minute before a scan to enable recalibration and general start-up procedure, and again turned off one minute after the scan commenced. The time taken per scan was around 10 s. For the third test the slide feeder was removed and the film left inserted throughout 11 repeated scans, this time scanned every 60 s. The purpose of this was to determine if any heating effects were observed when the film is left in the scanner throughout, with less potential cooling time in between scans. The data are presented in terms of relative change in OD (ΔOD) of the red channel in figure 5.1 a) for the two 5-minute tests and b) for the 1-minute test. The films were exposed to a 10 mm diameter proton beam from the Birmingham cyclotron approximately 1 year previously, and so any prolonged chemical reaction in the active layer would have completely ceased and not contribute to ΔOD in these tests. The initial OD of the beam spot in each film was ≈ 0.66 for EBT and ≈ 0.47 for HD-810 and a unique film was used for each test. No error bars are present because the only source of variability would come from within the measured ROI, and the standard deviation would typically be much larger than the changes in OD displayed and so not very useful. The ROI used for analysis was the size of the Markus chamber sensitive diameter (5.3 mm) centred on the proton beam spot on the films, leading to an area covering 804 pixels.

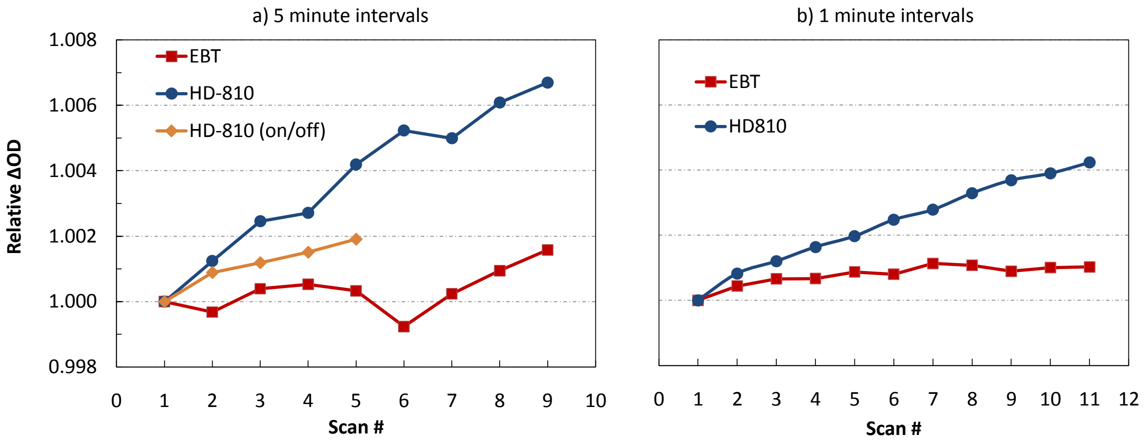

Figure 5.1: Relative change in OD (ΔOD) for repeated scans made at a) 5-minute intervals and b) 1-minute intervals for EBT (red squares) and HD-810 (blue circles). The second set of HD-810 data (orange diamonds) in a) was taken with switching the scanner on and off in between scans.

The results of the tests show that there is a very small darkening of the films with successive scanning, which is more significant for HD-810 than for EBT, where a trend is only just discernible. A maximum ΔOD of 0.7% was found after the 9th scan in the 5-minute regimen for HD-810. Slightly unexpected is that the darkening appears reduced when the film is left inside the scanner, and it is not clear why this should be the case. Analysis of the green channel images (not shown) is highly correlated with that of the red channel, which is indicative of a permanent darkening rather than a shift in absorption wavelength due to increased film temperature. Whereas with some fluorescent tube CCD scanners a few successive scans are required to warm-up the lamp before the measured OD becomes consistent (Paelinck et al., 2007), the LED light source in the NSC 5000 does not require this. To put this into context, Paelinck et al. (2007) found successive changes in OD of $\approx 1\%$ for the first two scans of EBT. After that, a similar minor amount of darkening as found here was observed. The darkening does not appear to be due to a "drifting" effect of the scanner, as otherwise the on/off test would exhibit no trend. It is presumed there must still be a small amount of UV light from the blue LED which is causing this effect. Based on these measurements, it would appear that taking the first scan is sufficient and preferable to repeated scanning and then averaging the measured OD as this appears to affect the film slightly.

5.1.2.2 Multi-pass noise reduction

The NSC scanners are advertised with a multi-sampling (up to 16x) capability built into the software, with the promise of noise reduction by internally averaging pixel values over successive scans. It is performed as if a single scan is taking place, but of course the total time taken to scan increases. A simple test of this was performed on an unirradiated EBT film, keeping the film *in situ* inside the scanner throughout. Successive scans were carried out at 150 px/inch for all of the different multi-pass values: 1x, 2x, 4x, 8x and 16x, in that order with 1 minute between scans. Two measurements on the resulting images were made: a horizontal OD profile was measured across a central 0.5 inch line (75 px), and a central ROI 0.5 x 0.5 inch^2 (5625 px^2) was analysed and the mean OD and s.d. were found. The results are shown in figure 5.2.

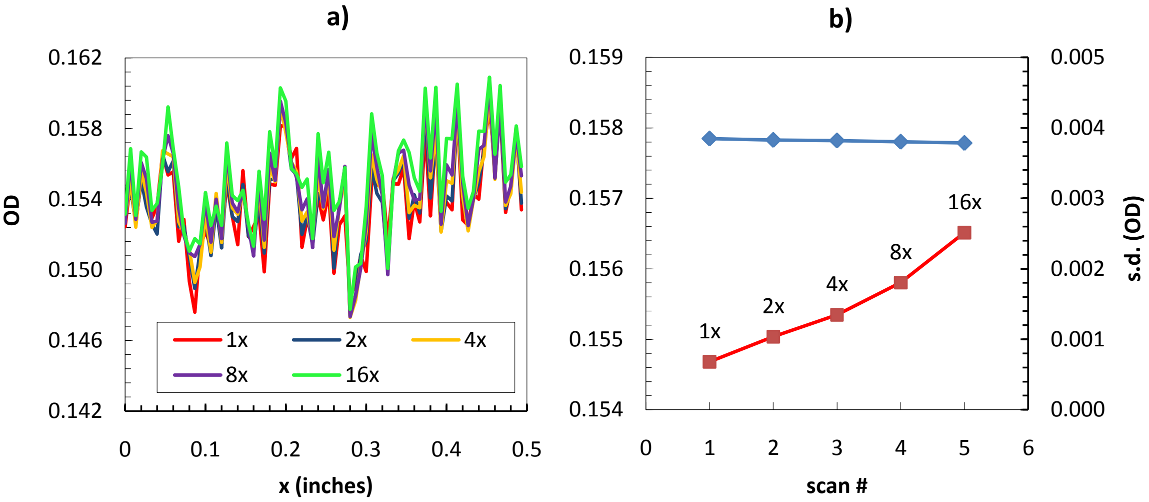

Figure 5.2: a) shows an OD profile in the horizontal (x) dimension across the centre of an unirradiated EBT film for different multi-pass values, while b) shows the mean OD in a square ROI of the same film (red squares), along with the s.d. of OD for each multi-pass value (blue diamonds).

Both plots show that little reduction in (what appears to be) noise is achieved by multi-pass scanning, and an apparent darkening occurs with successive scanning akin to what was shown previously in 5.1. This demonstrates that virtually all of the fluctuations of pixel values seen are due to real structure in the film layers, and are very reproducible scan after scan. It is more likely that when scans are performed at resolutions close to the maximum performance of the scanner (4000 px/inch) that noise reduction becomes more relevant as the number of photons per pixel reduces greatly. The conclusion from this test is that multi-pass scanning is a redundant feature for GafChromic film dosimetry at the resolution used.

5.1.2.3 Light polarisation effects

Again a film each of HD-810 and EBT exposed to protons from the Birmingham cyclotron were scanned with the same 5-minute, scanner always on regimen from the reproducibility test but the films were rotated manually inside the mount between scans. The ΔOD values are shown in figure 5.3, ranging from the original orientation rotated through 360° in 45° steps. Error bars are not shown for the angle, but are estimated to be ± 5°. The initial OD of each film was ≈ 0.66 for EBT and ≈ 0.47 for HD-810.

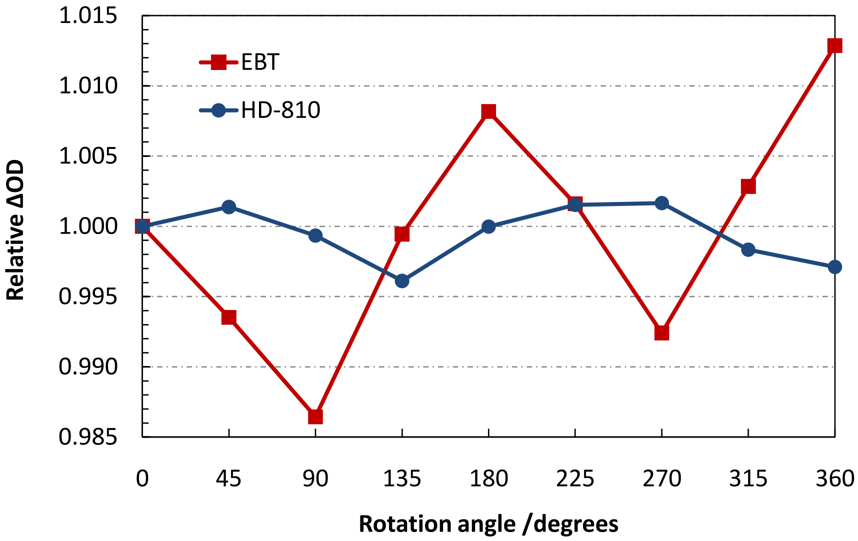

Figure 5.3: Relative change in OD for EBT (red squares) and HD-810 (blue circles) versus film rotation angle.

It is clear that there is some proportion of polarised light from the RGB LED source, however the largest peak-to-peak variation is for EBT and is approximately 2%, significantly lower than reported by Lynch et al. (2006) for a fluorescent tube scanner. There is an overall linear increase in ΔOD combined with the sinusoidal variation, consistent with the increase shown in figure 5.1 for EBT but HD-810 does not exhibit an overall increase in this case. The hair-like particles of LiPCDA in the EBT active layer may be a factor leading to increased dichroism, explaining the larger effect with respect to HD-810, or it may be due to the greater overall thickness. Overall, these data show that the light polarisation effect when scanning GafChromic film is very small from the NSC 5000, although if a consistent orientation is maintained throughout then this effect will be made redundant altogether.

5.1.2.4 LED analogue gain linearity

One of the software options is to modify the intensity of the RGB LEDs individually (or together by the *master* gain), by altering the analogue gain of each LED. The range of values is slightly arbitrary, from -2 to +2, where 0 is the default. This feature could offer increased flexibility when analysing very under- or over-exposed films by shifting the dynamic range higher or lower as required. Of course if a gain value is modified for experimental measurement of dose, then the corresponding calibration films must be scanned with the same gain settings. For interest, this function was tested for linearity by scanning an entire set of EBT X-ray calibration films (described later in section 5.3.1) at master gain values of 0, 1.0, 1.25, 1.5, 1.75 and 2.0 and comparing the calibration curves of OD versus dose. The resulting curves are shown in figure 5.4, along with a calibration curve produced by the NSC 9000 for comparison. It is noteworthy that the two scanners visibly appeared to produce different quality images for EBT films, examples of which are included in appendix F. There appeared to be an additional grey component to the NSC 5000 scans, resulting in a darker OD in each colour channel and a different shape to the calibration curve. Whilst the source of this difference was investigated (and discussed with Nikon technical support) it was never resolved, but it did not appear to affect the reliability or dose uncertainty. Changing the gain was also attempted in trying to resolve this, but as the data show, the calibration curve with the NSC 9000 could never be reproduced by doing this.

To quantify the relative difference in OD between gain values, the difference between OD with gains of 0 and 1.0 was found for each dose value and then the rest of the OD data was expressed in multiples of this difference. As shown in figure 5.5, the linearity of the effect on OD of changing the gain is very good for the large proportion of the dynamic range and behaves as would be expected.

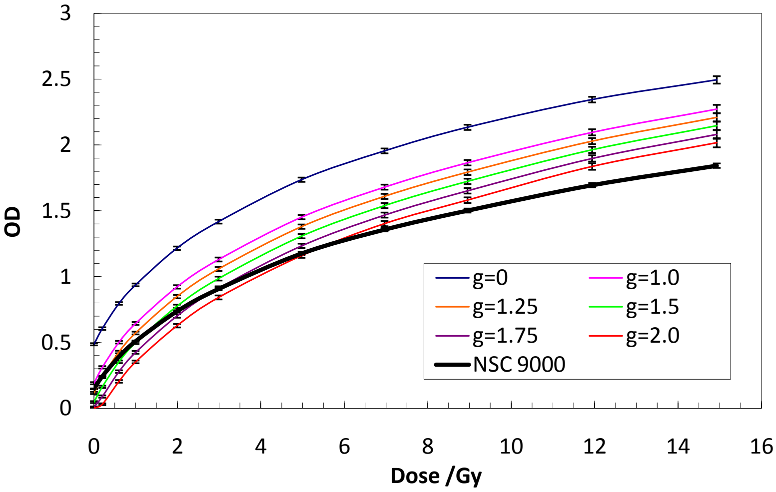

Figure 5.4: Comparison of an EBT calibration curve scanned originally by the NSC 9000, and then by the NSC 5000 at different analogue gain levels (maximum gain = 2.0).

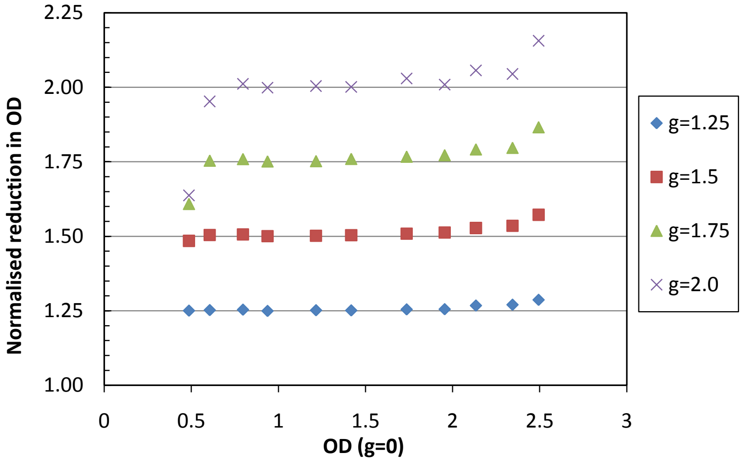

Figure 5.5: The reduction in OD in terms of multiples of the difference between OD measured with a gain of 0 and 1.0, for gain values of 1.25, 1.5, 1.75 and 2.0 plotted as a function of the OD measured with gain of 0.

5.2 Concept of g_{Q,Q_0} beam quality correction factor

5.2.1 Definition of g_{Q,Q_0}

In the same vein that a beam quality correction is needed for ion chambers that are calibrated for D_w in a ^{60}Co field, a similar correction should apply to GafChromic films calibrated in a different beam quality to the one which they are used for dosimetry. In the case of protons, the beam quality is continuously changing with depth and so this should apply even for films calibrated in protons, both for relative and absolute dosimetry. Analogous to the k_{Q,Q_0} definition as in equation 2.10, a proposed definition of a beam quality correction factor for GafChromic film, g_{Q,Q_0}, is given below:

$$g_{Q,Q_0} = \frac{(s_{w,film})_Q}{(s_{w,film})_{Q_0}} \frac{G_{Q_0}}{G_Q} \tag{5.1}$$

where $s_{w,film}$ is the ratio of mass stopping powers for water and film active layer, and G is the yield of polymerized (Li)PCDA in mol J^{-1}. Note that $1/G$ is the chemical analogy to W_{air}/e for ion chambers, representing the average energy required per unit of signal in each case. At lower proton energies, as the response of GafChromic film begins to quench it can be expressed as a reduction in G_Q and hence g_{Q,Q_0} will increase in order to correct for this effect. The value of $s_{w,film}$ can be calculated using particle spectra obtained with Monte Carlo simulation and theoretical stopping powers for the active layer.

The intended usage of g_{Q,Q_0} is such that if adequately calculated or measured for any beam quality Q, multiplication by the film dose-to-water calibration function, $d_{w,Q_0}(net\text{OD})$, obtained using beam quality Q_0, will yield an accurate value of dose-to-water for the given beam quality. As such, this dose quantity should also be equivalent to the fully corrected dose-to-water measured by an ion chamber, $(D_{w,Q})_{\text{ic}}$, as shown here:

$$(D_{w,Q})_{ic} = (D_{w,Q})_{film} = d_{w,Q_0}(net\text{OD})\ g_{Q,Q_0} \tag{5.2}$$

5.2.2 Film stopping powers

For many materials, stopping powers can be obtained from NIST online database called PSTAR (Berger et al., 2005) which are compliant with the recommended stopping powers in ICRU49 (ICRU, 1993). However the database of materials is limited and does not contain the GafChromic active layer materials PCDA or LiPCDA so they had to be calculated manually. Other programs, like SRIM or FLUKA can calculate these stopping powers but as shown in section 3.6 they will not be consistent with the ICRU49 method of calculating stopping powers.

In order to calculate the mass collision stopping power for a compound or mixture, the Bragg additivity rule shown below can be used to combine the elemental stopping powers, as a first approximation:

$$\left(\frac{S_{col}}{\rho}\right) = \sum_j w_j \left(\frac{S_{col}}{\rho}\right)_j \tag{5.3}$$

where w_j is the atomic fraction by weight and (S_{col}/ρ) is the mass collision stopping power of j^{th} constituent (ICRU, 1993). The mean excitation energy for a compound using the Bragg's rule I is given by:

$$\ln I = \frac{\sum_j w_j \left(\frac{Z_j}{A_j}\right) \ln I_j}{\left\langle \frac{Z}{A} \right\rangle} \tag{5.4}$$

where

$$\left\langle \frac{Z}{A} \right\rangle = \sum_j w_j \left(\frac{Z_j}{A_j}\right) \tag{5.5}$$

However this rule fails to account for the influence of chemical binding effects. ICRU49 guidance follows that for stopping powers of electrons and positrons in ICRU report 37 (ICRU, 1984), which recommends that if experimental measurements of I are not available then Thompson's rule should be used which accounts for the type of chemical bond each element exhibits in organic compounds. Palmans et al. (2006b) mentions another option of using an adapted Bragg rule calculation where different I-values are assigned to the constituent elements depending on the physical phase of the compound. Palmans et al. also notes that calibrations of ion chambers performed in ^{60}Co beams involve electron stopping powers, and so for consistency the same I-values used for electrons should be used for protons (Medin and Andreo, 1992). ESTAR, the NIST online database for electron stopping powers (Berger et al., 2005) can calculate this I-value given the atomic composition of the compound. They are listed in table 5.3 for both PCDA and LiPCDA, using the compositions previously shown in table 2.2 where LiPCDA refers to the formulation used in EBT rather than EBT2. It should be noted that stopping powers for the formulation in EBT2 were not calculated at this point.

Table 5.3: Calculated I-values for both active layer compounds used in GafChromic films (not including EBT2): the Bragg rule and ICRU/Thompson rule values

Active layer compound	I_{Bragg}	I_{ICRU}
PCDA	67.3 eV	66.6 eV
LiPCDA	68.3 eV	69.6 eV

The correction term to be added to the raw (S_{col}/ρ) obtained via the Bragg rule can be expressed as follows (taken from Palmans et al. (2006b)):

$$\Delta_I = 0.307075 \left\langle \frac{Z}{A} \right\rangle \frac{1}{\beta^2} \ln \left(\frac{I_{Bragg}}{I_{ICRU}} \right) \tag{5.6}$$

This expression effectively subtracts the I_{Bragg} term and replaces it with I_{ICRU} in the Bethe formula from equations 1.2 and 1.4. There is another ammendment to be made to the Bragg rule regarding the Barkas correction, which is due to different values for the scaled minimum-impact parameter b that is used for molecular hydrogen and hydrogen in compounds (Palmans et al., 2006b). Therefore an additional correction term is defined:

$$\Delta_{Barkas} = 0.307075 \left\langle \frac{Z}{A} \right\rangle \frac{1}{\beta^2} w_H \left[\frac{\gamma Z \alpha^3}{\beta^2} \left\{ F\left(\frac{b_{comp} Z^{1/2} \alpha}{\beta} \right) - F\left(\frac{b_{mol} Z^{1/2} \alpha}{\beta} \right) \right\} \right] \tag{5.7}$$

where w_H is the fraction by weight of hydrogen in the compound, γ is a constant ($=$ 1.29), α is the fine structure constant ($= 1/137.036$), b_{comp} ($= 1.8$) and b_{mol} ($= 0.6$) are the scaled minimum-impact parameters for hydrogen in compounds and molecular hydrogen respectively. The function F is obtained from Ashley et al. (1972), and includes a complex integral which was solved numerically in the paper to provide a plot of F. Tabulated values used to be available from the *National Auxiliary Publication Service* in the United States, but this service dissolved many years ago. Instead, the printed plot was manually extracted at several points along the minor gridlines and recreated using a cubic spline function in Excel, so there will be some error in its evaluation. However, its effect on the stopping power is relatively small and so this error can be considered negligible. The density effect ($\delta/2$) correction was neglected, as it only reaches the 1% level for stopping powers above proton energies of 500 MeV (ICRU, 1993) which greatly exceeds the energy range of interest in this work.

These corrections were applied above an energy threshold of 500 keV, and for 200 keV and below just the bare Bragg rule was used. In between 200–500 keV a cubic spline fit to the data on a Fano plot (i.e. $\beta^2(S_{col}/\rho)$ versus log E) was used to interpolate between these two energy regions. This method is consistent with that used in ICRU49 for most compounds.

To determine the total mass stopping power, the nuclear stopping power (S_{nuc}/ρ) was also required. In keeping with ICRU49, a screened Coulomb potential based on the Thomas-Fermi model was used (Molière, 1947). Classical mechanics is used when the de Broglie wavelength of the projectile is smaller than the collision diameter, otherwise the quantum mechanical elastic-scattering cross section of Molière (1947) is used above an energy of $Z/10$ in MeV. For protons, S_{nuc}/ρ is then found via use of a dimensionless, scaled nuclear stopping power $\hat{S}_{nuc}(\hat{T})$:

$$\frac{S_{nuc}}{\rho} = \frac{5105.3 \cdot Z^{2/3}}{A(1 + A/m_p)} \cdot \hat{S}_{nuc}(\hat{T}) \tag{5.8}$$

where m_p is the projectile mass in atomic mass units, and $\hat{T}$ is a scaled kinetic energy parameter given as:

$$\hat{T} = \frac{32536 \cdot E}{Z^{4/3}(1 + m_p/A)} \tag{5.9}$$

where E is the proton kinetic energy in MeV. The values of $\hat{S}_{nuc}(\hat{T})$ are tabulated in ICRU49, and so these were extracted and interpolated by a cubic spline function. While ICRU49 did not stipulate the method of finding Z and A for a compound, Z_{eff} was used (as per the Spiers method of raising to the power of 2.94) along with an average $\langle A \rangle$ found by summing the product of A_j with the fraction by weight w_j of each element j. For the two film active materials, the ratio of S_{nuc}/S_{col} is at most 0.17–0.23 at 1 keV and decreases to ≤ 0.01 around 18–22 keV and so the contribution of S_{nuc} is fairly insignificant at the energies relevant to this work, but it is included nonetheless.

For comparison, the MC codes FLUKA, MCNPX and SRIM were used to generate film stopping powers (as tabulated output) and the ratio of ICRU compliant stopping powers to these is shown in figure 5.6. As the stopping powers between codes varied significantly, their average was found and included in this comparison.

It appears that the ICRU compliant stopping powers are to a good approximation a compromise between all three of the MC codes, as above 500 keV the average of the MC stopping power data differs by no more than ± 2% to the ICRU compliant values. Considered individually however there is quite a significant distribution which is surprising given that the corrections to the Bethe formula are normally around a few percent in magnitude between 1–100 MeV. Below energies of 1 MeV, stopping powers are considered to be much less accurately known and so larger differences here are expected. It is perhaps no surprise that the best overall agreement is found with SRIM, as it tries to

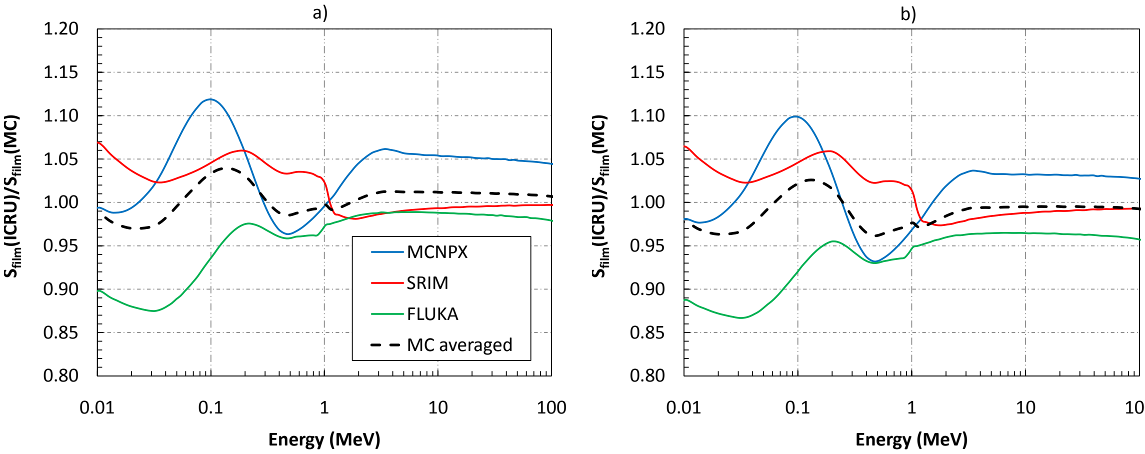

Figure 5.6: Ratio of ICRU compliant stopping powers and those calculated by MC codes FLUKA, SRIM and MCNPX and their average for a) PCDA and b) LiPCDA.

account for chemical bonds in the molecular formula so should be in good agreement with Thomson's rule. However none of these sets of stopping powers can really be considered more "correct" than another, as the uncertainties for materials which have no experimental data are not trivially small. However using the ICRU method leads to improved internal consistency when ICRU49 stopping powers have been used throughout.

The treatment here has assumed that the compound is a homogeneous mixture, and does not account for types of chemical bonds and the fact that in reality the monomer crystals are dispersed within a gelatin matrix and additionally that this structure evolves during irradiation. However in the interest of macroscopic dosimetry, the dose in the active layer will depend on secondary electrons produced within both the gelatin and monomer crystals so it is reasonable to treat the two separate components together.

The calculation of the film stopping powers allows for one of the terms in the g_{Q,Q_0} expression to be determined, namely the ratio of water to film stopping powers, $(s_{w,film})_Q$ where Q refers to the particle spectrum at the depth of measurement. This ratio as a function of proton energy is shown in figure 5.7.

In addition to proton stopping powers, α-particle stopping powers were calculated via the same method. The only difference in approach was in calculating S_{nuc}; ICRU49 states that for α-particles, $\hat{S}_{nuc}(\hat{T})$ is found via Ziegler-Biersack-Littmark universal potential

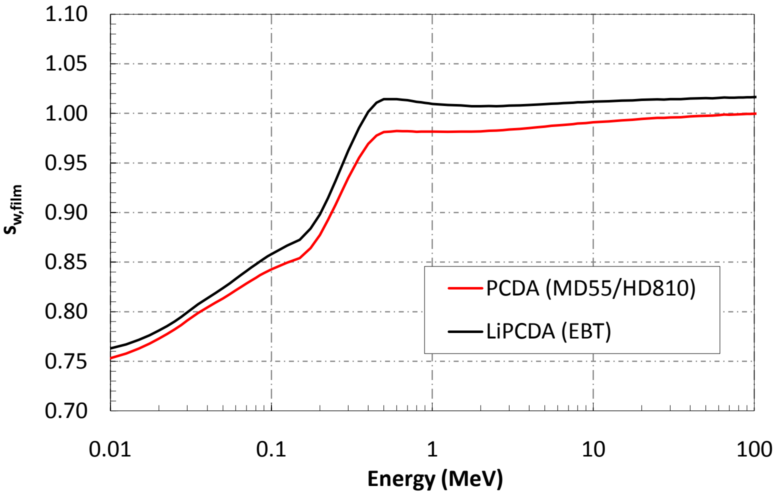

Figure 5.7: Water to film stopping power ratios, $s_{w,film}$, versus proton energy. The GafChromic film stopping powers were calculated following the method used by ICRU49 for compounds.

which is approximated by two formulae depending on the value of $\hat{T}$, and the $Z^{2/3}$ term in equation 5.8 is replaced with $(z^{0.23} + Z^{0.23})$ where z is 2 for an α-particle. Total mass stopping powers for (Li)PCDA and $s_{w,film}$ for α-particles are shown in figure 5.8.

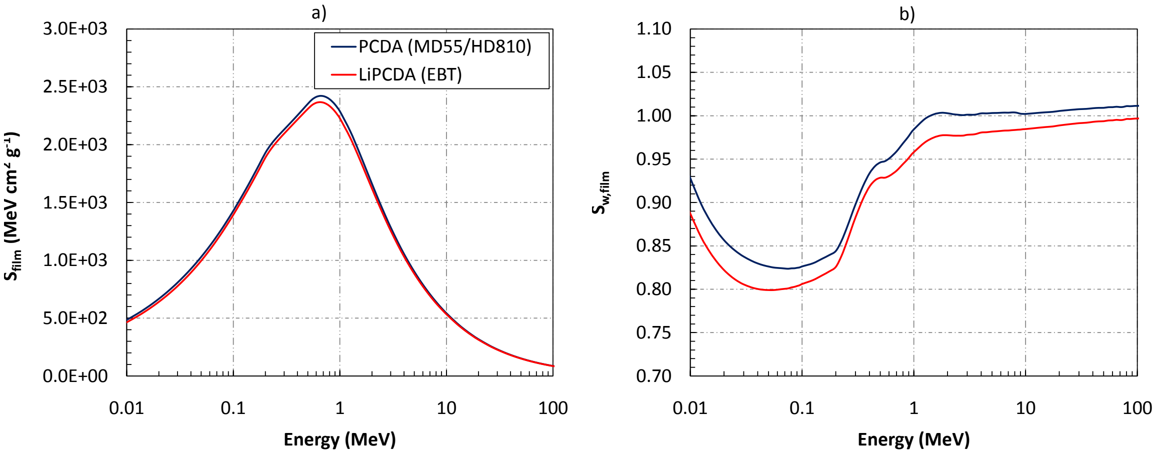

Figure 5.8: Part a) shows film stopping powers for α-particles and b) shows the water-to-film stopping power ratio, $s_{w,film}$.

5.3 Dosimetry of 15 and 29 MeV protons

5.3.1 Calibration with 6 MV X-rays

In total, films from two sheets of 12.5 x 12.5 cm^2 format MD-V2-55 (lot #P0127MDV2) and one of 20 x 25 cm^2 format EBT (lot #47207-031) were irradiated across three separate sessions of work spread over a period of several months; two using 29 MeV protons and the other using 15 MeV protons. A calibration was necessary for each sheet, and two were performed for the single EBT sheet as films from it were irradiated in two sessions separated by about 5 months. The films were cut into 2.5 x 2.5 cm^2 squares, and irradiated with 6 MV X-rays from a Varian (Palo Alto, CA, US) Clinac 600C at the University Hospital Birmingham, at a depth of 10 cm in Solid Water (RMI 457 model, Gammex, Middleton, WI) in a 10 x 10 cm^2 field at 90 SSD.

The OD measurements were obtained using the free image analysis program ImageJ (National Institute of Health, Bethesda, MD, US) which extracted 16-bit red channel data from images produced by the NSC 9000, scanned with a resolution of 150 px/inch. A central region of 2 x 2 cm^2 was analysed for each film, and a median filter applied to reduce the effect of scratches and small debris on the film.

Figure 5.9 shows examples of calibration curves obtained, using ordinary least squares (OLS) third order polynomial fits. Crop et al. (2008) discuss the possible bias introduced by employing OLS inverse regression rather than a weighted least squares (WLS) inverse prediction method. The latter requires polynomial inversion, and assumes the variances of OD values are heteroscedastic, i.e. not equal for each value measured. In this work, the uncertainties of the OD measurements were based on scanner related uncertainties and not the variance due to multiple calibrations as used by Crop et al.. Therefore it was unclear whether WLS inverse prediction would have any kind of statistical benefit.

In all cases, the scans were performed at least 48 hours after irradiation to allow post-exposure OD growth to stabilize (Butson et al., 2003). The calibration films were always scanned together with the experimental films, so that the ambient temperature was the same for both sets. Consistent with the analysis procedure outlined by Devic et al. (2005), OD measured before irradiation was subtracted from the OD measured after irradiation, to give the net optical density, *net*OD.

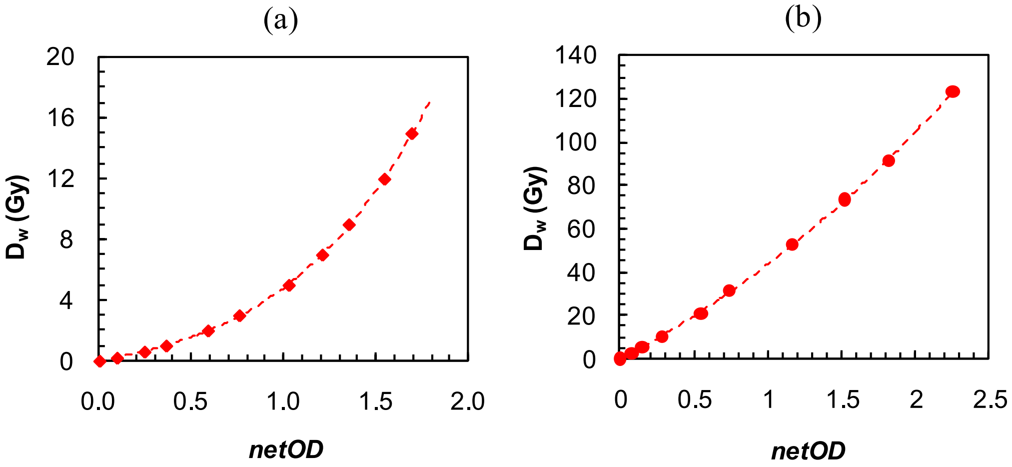

Figure 5.9: Calibration curves obtained for a) EBT and b) MD-V2-55 using 6 MV X-rays.

The uniformity of the active layer in these films is claimed by the manufacturer to be much better than previous models. To provide confirmation of this, at the same time as calibration was performed (usually a few days before proton irradiations) all EBT and MD-V2-55 films to be used for measurements were initially given absorbed doses of 1.0 Gy and 10.5 Gy respectively with the same beam conditions as for calibration. They were later cut into 2.5 x 2.5 cm^2 square pieces, placed inside protective sleeves and stored in a dark cupboard along with calibration film in the same room as the scanner to negate any temperature change from storage to scanning. These *pre-irradiated* films were scanned as late as possible before proton irradiations, and at least 48 hours after X-ray irradiation so that any OD growth post-scanning and pre-proton irradiation would be minimized.

The normalized dose response from a sample of EBT and MD-V2-55 films is shown in figure 5.10. As EBT exhibits absorption peaks at slightly shorter wavelengths than MD-V2-55, analysis of the green channel also yields a response that is quite significant at low doses. Hence for EBT the green channel was also calibrated in the same way as described previously. The lack of a strong correlation between deviations from the mean in the red and green channel dose values suggests that the main cause for the film-to-film fluctuations for EBT is related to the imperfect flatness of the X-ray field and not due to dose variations from the calibration process or the non-uniformity of the film. MD-V2-55 however showed a definite pattern of non-uniform dose response, which can be traced back to how the uniformity varies across a sheet. Films cut from the same side of the MD-V2-55 sheet (#1, 6, 11, 16) had a similar response to each other, but gave doses on average 5% lower than the rest of the sheet. The X-ray dose profile is expected to be only flat (uniform) to within around ±2% so only for these films was a non-uniformity correction applied.

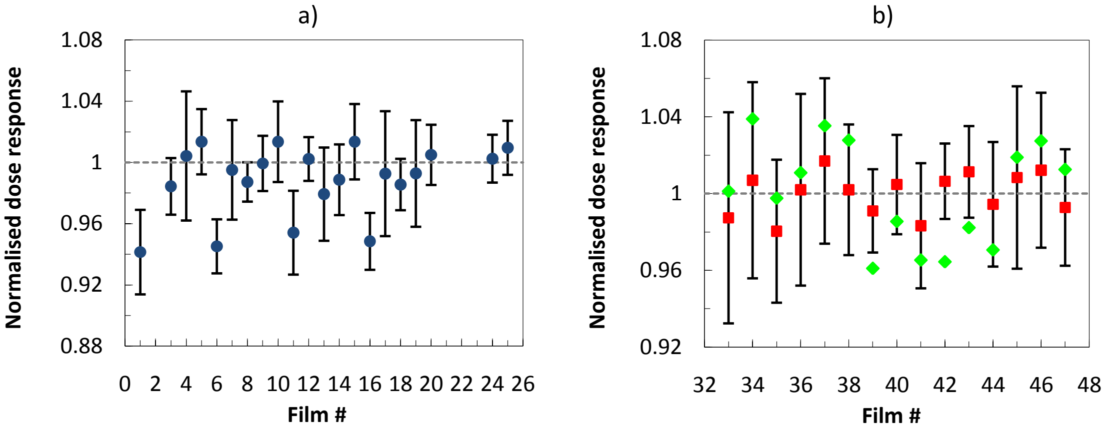

Figure 5.10: Normalised dose response for a sample of pre-irradiated films. Plot a) shows MD-V2-55 red channel data and plot b) shows EBT red and green channel data. Error bars indicate 2 s.d. of pixel dose values within a 1 x1 cm^2 ROI.

5.3.2 Depth-dose measurements

While the films are considered quasi-water-equivalent, higher accuracy was required in this work as the film thickness was comparable to the full-width-half-maximum (FWHM) of the BP. Using the composition data for all layers of MD-V2-55 and EBT (included in appendix A), Monte Carlo simulations with MCNPX were used to determine their water equivalent thickness for incident proton energies of 6, 9, 12, 18, 24 and 30 MeV. This was done by running two simulations for each energy: a pencil beam into a cuboid target of water, and a pencil beam into a full representation of the film and its layers followed again by water. The fluence versus depth was scored, and the depths where fluence dropped to 50% of that at the surface were compared for both simulations. This allowed for the water-equivalent thicknesses of the films to be determined, and the ratio of water-equivalent to nominal thickness (in g cm^{-2}) gave the effective depth-scaling factors, c_{md55} (= 0.943) and c_{ebt} (= 0.930). These are average values across these energies, and the s.d. gave uncertainties of 0.3% and 0.4% respectively.

The thickness of each film was measured by weighing them individually with a precise, calibrated analogue balance and dividing by their area, to obtain the mass thickness in g cm^{-2}. Their areas were found by scanning them on an A4 flatbed scanner at 1200 px/inch and using ImageJ to manually outline each film and use the area measurement function. The measurements were all repeated three times and the average value taken, and the uncertainty accounted for the s.d. of measurements and the resolution of both methods. Typically the uncertainty in mass thickness was between 0.40–0.63%, although this did not take into account any deviation of the scales from their last calibration.

For Markus chamber measurements the point of measurement was taken to be the inside surface of the entrance window, and for GafChromic films the central point between the two active layers was used, i.e. exactly half the full thickness of the films. The same PMMA sheets were used as before to vary the depth of measurement, and Markus chamber readings were additionally taken behind the films to test the accuracy of c_{md55} and c_{ebt}. The raw Markus ionisation reading divided by monitor ionisation (R/M) is shown versus water equivalent depth for PMMA only (as obtained in chapter 4), behind EBT and behind MD-V2-55 in figure 5.11 at 29 MeV. The good agreement of all the data indicates that the depth-scaling factors are quite accurate, especially as some points were taken behind a stack of up to three films and so sensitivity to errors was larger. For irradiations at 15 MeV, films were arranged either individually or in small stacks behind different thicknesses of PET.

The film irradiations were performed in the same respective sessions as for the Markus chamber depth-dose measurements presented in section 4.2.5 for nominal 15 and 29 MeV

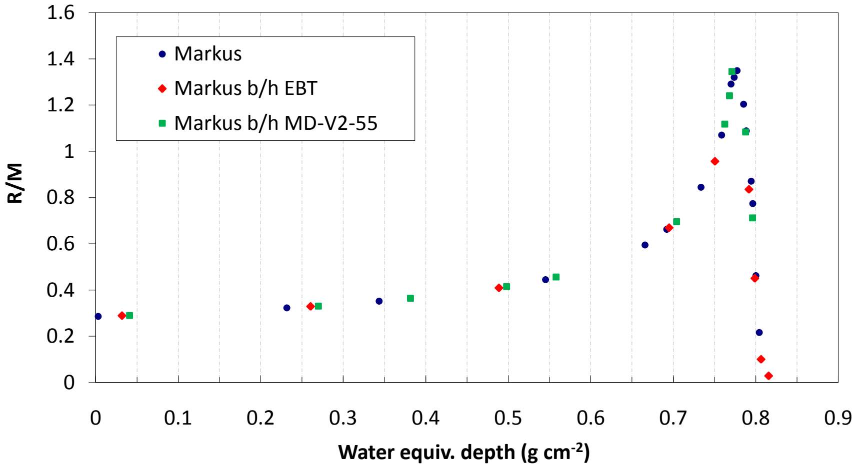

Figure 5.11: Relative depth-ionisation curves measured in PMMA with a Markus chamber and additional data measured behind irradiated EBT and MD-V2-55. All depths are converted to water equivalent, and this demonstrates the accuracy of the depth-scaling factors c_{ebt} and c_{md55}.

proton beams. The two sets of 29 MeV depth-dose data — one for MD-V2-55 and one for EBT — exhibited a slightly different range and BP height between the two sessions, and so the data is presented separately in parts b) and c) in figure 5.12.

It can be seen from the data that both types of film give measured doses which agree very well with the Markus chamber in the plateau regions. However at deeper depths, the difference in dose becomes greater and the most significant under-response is seen around the BP region. This behaviour is in agreement with previous measurements by Vatnitsky (1997), Daftari et al. (1999) and Piermattei et al. (2000) with earlier versions of MD55. It is believed that the data presented here were the first published depth dose measurements in a proton beam with EBT and the under-response in the BP is noticeably less pronounced than for MD-V2-55.

5.3.3 Relative effectiveness

On the topic of relative effectiveness, there are subtle differences as to how this can be defined. Briefly, in the more established literature on the RE of alanine, they fall into two categories: RE defined as an isoresponse dose ratio, or as an isodose response ratio. The

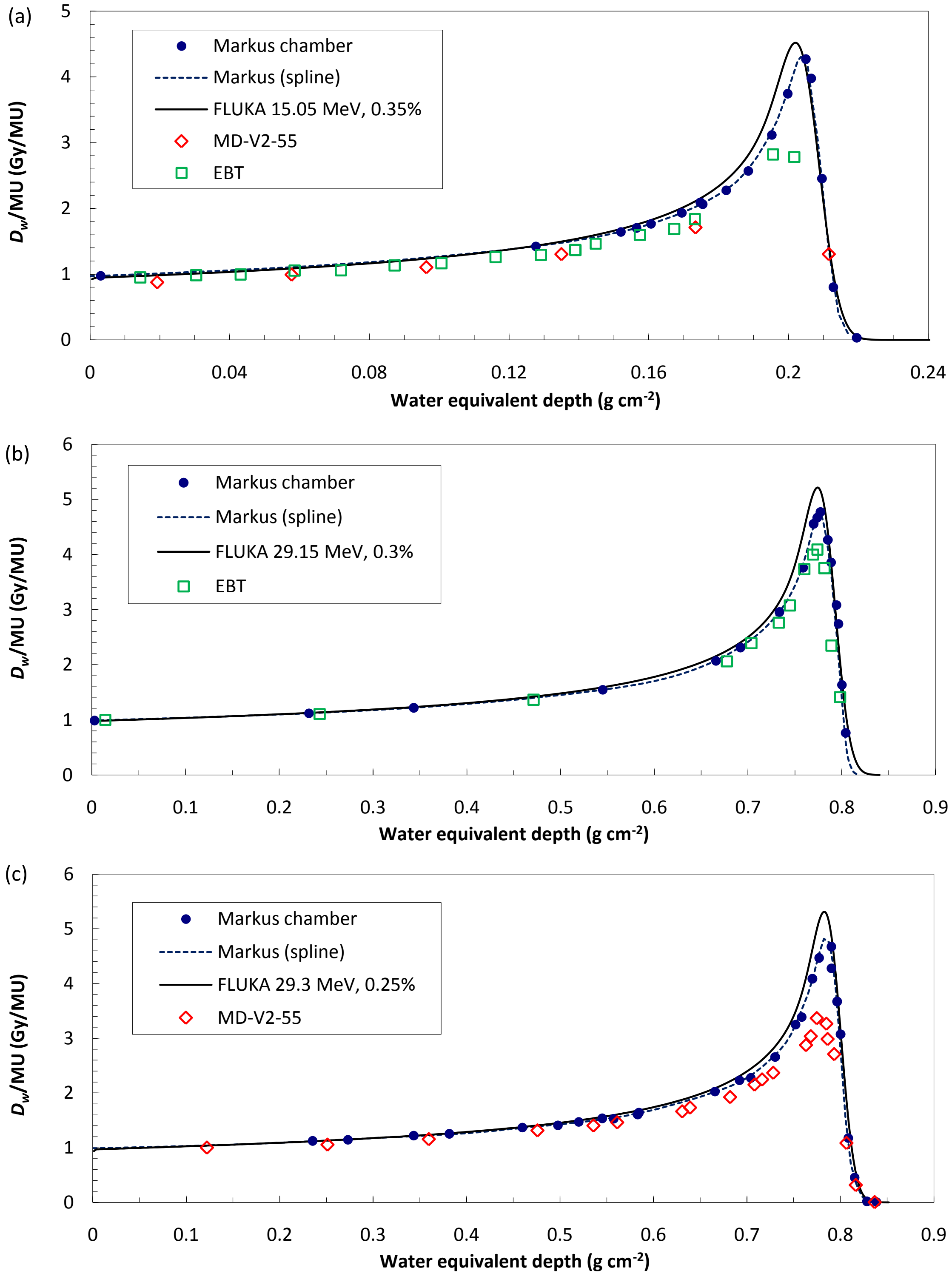

Figure 5.12: Depth-doses of MD-V2-55 and EBT for nominally a) 15 MeV protons and b,c) 29 MeV protons. Fully corrected Markus chamber doses are included along with best-matched FLUKA simulations showing energy and momentum spread in terms of σ.

former is the ratio of doses measured for two different radiation qualities which result in the same response or signal, and the latter is the ratio of response/signal for the same dose administered by two different radiation qualities. The isoresponse dose ratio definition is the one which applies in this work, although more generally it is calculated as the absolute dose-to-water response of GafChromic film (based on 6MV X-ray calibration) relative to the absolute dose-to-water measured by Markus chamber for the same effective depth of measurement.

To provide a Markus dose value at every film depth, a cubic spline was applied but only through a reduced sample of data points to preserve smoothness, and the average residual value taken as an estimate of uncertainty for any point on the spline. The double active layer structure of both GafChromic films required attention with regard to how a single dose value is obtained at any effective point of measurement. If each layer is regarded as a separate dosimeter responsible for half of the total dose signal, then it follows that when their signals are combined during readout, the measured dose is an average of the two layers and the two individual signals are lost. At depths where the second derivative of the depth-dose curve is highly negative or positive (high curvature), the Markus measured dose, $(D_w)_{ic}(z)$, at depth z, the effective point of measurement in the film, may be larger or smaller than the double layer average dose $[(D_w)_{ic}(z)]$; defined as the average of the Markus doses at depths z'_a and z'_b (the depths of the centers of the two active layers). This is illustrated by figure 5.13. In this notation, specifying z has replaced the need for Q.

The active layer thickness, separation and total thickness of EBT and MD-V2-55 stated by ISP are shown in table 5.4. It is clear that the closer the active layers are, the smaller the difference becomes between $(D_w)_{ic}$ and $[(D_w)_{ic}]$; hence for EBT this difference is much smaller than for MD-V2-55. This issue could have been avoided completely for PCDA by using HD-810 instead of MD-V2-55, however calibrating HD-810 using an RT linac would not have been feasible due to the high doses required, relatively low dose-rate and the time constraints of using it 'out of hours' whilst supervised by a RT physicist employed by the hospital.

If, for sake of brevity, a modified dose calibration function partly corrected for beam quality is defined, but in terms of depth z in a proton beam instead of Q,

$$d_w(net\text{OD}, z) = d_{w,Q_0}(net\text{OD}) \cdot \frac{(s_{w,film})_Q}{(s_{w,film})_{Q_0}} \tag{5.10}$$

then the mathematical definition of RE at z can be expressed as:

$$RE(z) = \frac{d_w(net\text{OD}, z)}{[(D_w)_{ic}(z)]} \ . \tag{5.11}$$

This establishes a relationship between the yield factor and RE (specific to this work):

$$RE = \frac{G_Q}{G_{Q_0}} \ . \tag{5.12}$$

The numerator in eq. 5.11, defined in eq. 5.10, is the measured film dose, with part of the g_{Q,Q_0}correction applied. This is equivalent to $(D_{w,Q})_{film} \cdot RE$, and is the quantity displayed in all figures where film depth-dose measurements are shown.

Table 5.4: Active layer thickness, separation (to centers) and total thickness of EBT and MD-V2-55.

	EBT	MD-V2-55
Active layer thickness	2 x 17 μm	2 x 17.5 μm
Separation $(z'_b - z'_a)$	23 μm	108 μm
Total thickness	234 μm	317.5 μm

Analysis of the full depth-dose curve allowed conversion of depth z in PMMA to the residual range in water, R_{res}, and use again of the FLUBOUND routine and previous FLUKA simulations described in section 4.2.2 yielded the peak proton energy at this depth.

The RE data are presented for MD-V2-55 and EBT in figure 5.14 both as functions of R_{res} and FLUKA determined peak proton energy. Uncertainties which are estimated for each data point individually, include the subtraction of initial X-ray dose, non-uniformity

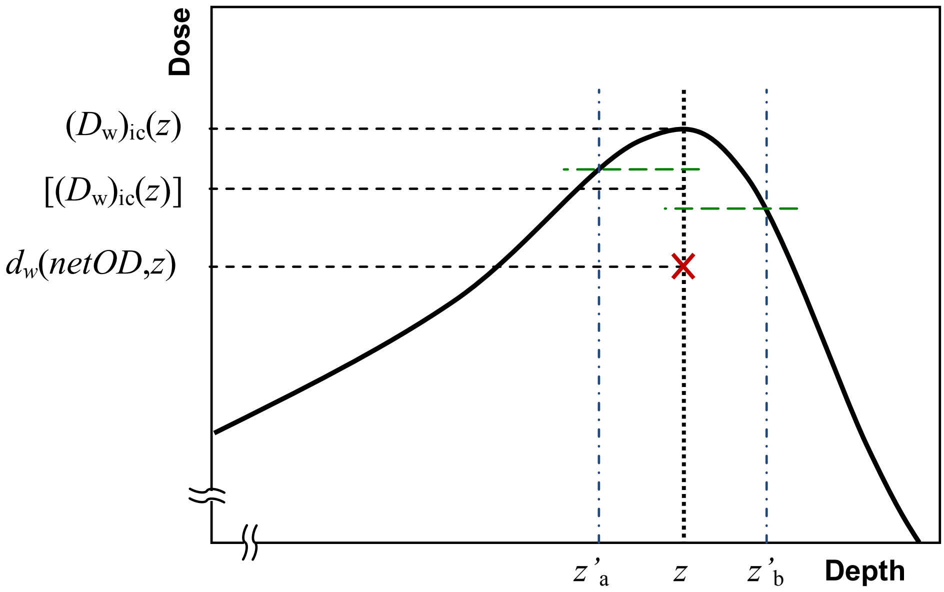

Figure 5.13: Illustration of how the double layer average dose at depth z, $[(D_w)_{ic}(z)]$, derived from the Markus dose (thick solid line) at active layer depths z'_a and z'_b, can differ from the dose at the centre of the film, $(D_w)_{ic}$, in a region such as the BP. The red cross represents a typical under-responding film dose value, $(D_w)_{film}(z)$. The active layer separation relative to the width of the BP is exaggerated for illustration purposes.

correction (where applied), and all dosimetric uncertainties listed in appendix G. The uncertainty in R_{res} was a sum in quadrature of the uncertainties in D_{10} and z. For peak proton energies at each depth obtained using FLUKA and FLUBOUND, the spectrum was approximated as Gaussian and the s.d. was derived from the measured FWHM and used as the uncertainty. Comparative data from Piermattei et al. (2000) from measurements made in a 21.5 MeV proton beam with GafChromic MD-55-2 film are included in figure 5.14(a). They used an ionisation chamber to measure a depth-dose curve, and determined an energy correction factor, P_{en}, at each depth of measurement and hence effective proton energies. They have been equated to RE by taking $1/P_{en}$, and converted to a function of R_{res} (which effective energy is derived from). There is good agreement with the values calculated here for MD-V2-55, which has the same active layer as its predecessor MD-55-2. It must be noted however that relative dosimetry was performed, and so the data was scaled to RE = 1.0 at $R_{res} = 0.314$ g cm^{-2}. No correction was made for the dual layer separation, notable by the higher value at $R_{res} = 0.014$ g cm^{-2}, distal to the BP where this correction becomes significant, and no uncertainties were provided.

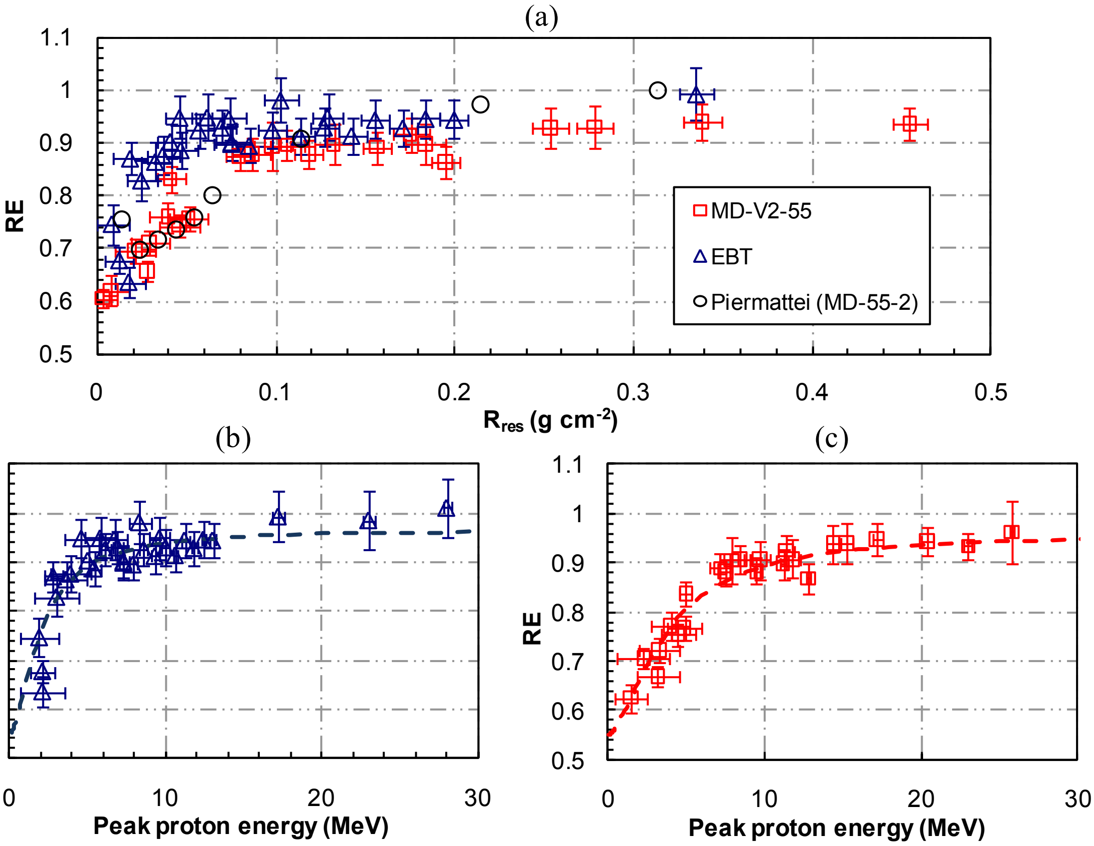

Figure 5.14: Plots of RE for MD-V2-55 (red squares) and EBT (blue triangles) in (a) against R_{res} in water, and in (b, c) against peak proton energy derived from FLUKA, with weighted sigmoidal fits. Note that data for $R_{res} > 0.5$ g cm^{-2} are omitted from (a).

The weighted sigmoidal curves are of the form:

$$RE = RE_0 + \frac{\Delta RE}{1 + exp[-C \cdot (\log E - \log E_m)]} \tag{5.13}$$

where E is the proton energy, and all other parameters are adjusted in order to produce a best weighted sigmoidal fit to the RE data. This type of function was chosen as it was also used by Palmans et al. (2006b) to describe the RE of alanine pellets in protons. The parameter values for EBT and MD-V2-55 are shown in table 5.5.

The proton energies at which RE becomes 90% of the maximum film response are 6.7 and 3.2 MeV for MD-V2-55 and EBT respectively, based on the weighted sigmoidal curves. Hence claims that EBT shows less of an under-response than MD-V2-55 are in

Table 5.5: Sigmoidal fit parameters for RE of MD-V2-55 and EBT.

	RE_0	ΔRE	C	$\log E_m$
MD-V2-55	0.55	0.41	3.79	0.57
EBT	0.55	0.42	3.88	0.31

agreement here to a certain extent, but more accurately, the LET quenching occurs at lower proton energies and hence higher LET for EBT than MD-V2-55.

It is concluded that the increased microscopic dose deposition close to proton tracks with higher LET locally saturate the RCF polymerisation capacity to a degree that a significant proportion of the total macroscopic dose does not yield further polymerisation. Investigations by Rink (2008) into the chemical structure of both films could help to explain why the films might differ in their response to high LET particles. As mentioned in section 2.3.1, LiPCDA in EBT film is made up of hair-like monomer particles much longer than the more spherical PCDA particles in MD-V2-55. This may give ionizing radiation more opportunity to initiate polymerization within a single chain, and/or increase the proximity of the monomers to each other. Either can be thought of as effectively increasing the density of potential polymerization sites, offering a higher reaction cross-section. Hence the same volume of LiPCDA will result in more polymerization events for the same absorbed dose than PCDA. This is likely to be responsible for the increased general dose sensitivity of EBT, but it should also follow that a higher density of ionization is necessary for LiPCDA polymerization sites to become locally saturated.

There have been some investigations into alanine response incorporating track structure theory (Bassler et al., 2008) which have suggested that the response upturns at very low energies. To test this would require very low energy proton beams, which in turn make absolute dosimetry with ion chambers more difficult and would lead to larger uncertainties. For the therapeutic applications of protons, the behavior of RE at these very low energies is not significant and so whether the sigmoidal approximation is appropriate in this region is perhaps not important.

5.4 FLUKA simulation of GafChromic film proton response

The characterisation of RE as a function of energy allowed implementation of this as a dose response function in FLUKA. The *comscw* routine was modified so that the energy deposited at each step in the simulation was multiplied by an evaluation of the sigmoidal RE function at the proton energy in that step. To account for the differences between FLUKA and Markus data, the RE values were re-evaluated with the FLUKA simulated depth dose curve replacing the Markus chamber spline fit. This resulted in quantifying the film dose response relative to FLUKA, and weighted sigmoidal fits were applied again in the same way and these functions incorporated into *comscw* (see appendix D.1.3) with the parameters shown in table 5.6.

Table 5.6: Sigmoidal fit parameters for a FLUKA dose response function of MD-V2-55 and EBT.

	RE_0	ΔRE	C	$\log E_m$
MD-V2-55	0.505	0.45	4.3	0.56
EBT	0.490	0.51	3.3	0.23

The resultant film response depth dose curves are shown in figure 5.15, along with film data to verify the accuracy of the response functions. The successful implementation and verification opened up the possibility of simulating GafChromic film response to protons in very different scenarios to the simple mono-energetic beams extracted from the cyclotron, for instance in a modulated beam or from a laser-proton source.

5.5 Dosimetry of 38 MeV α-particles

Due to the shorter range and steeper dose gradient with depth for α-particles, MD-V2-55 film was deemed unsuitable for use due to the relatively large separation distance between the two active layers, the correction for which would contain larger uncertainties

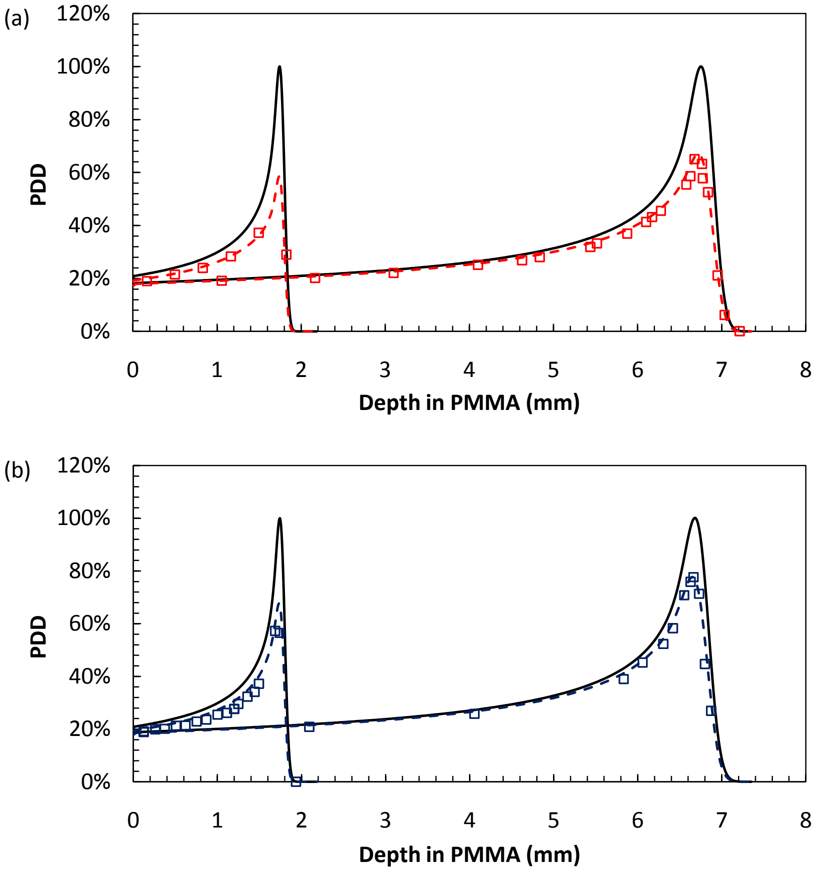

Figure 5.15: Full energy deposition simulations with FLUKA (black line) and film dose response simulations (dashed lines) along with dose measurements (squares), for a) MD-V2-55 and b) EBT.

than for protons especially near or in the BP. Instead, HD-810 film with its thinner, single active layer was irradiated along with EBT to provide comparison of dose response to α-particles between the two active components, PCDA and LiPCDA.

5.5.1 Calibration

Due to the decision to use HD-810, a 6 MV X-ray calibration using a hospital linac was not feasible as previously mentioned due to the high doses required to cover the full dose range of the film. Instead, it was decided calibration in the cyclotron proton beam would be the next best solution, at an energy where the dose response is close to that of X-rays. Calculation of absolute D_w in the proton beam was by this point a simpler task given the previous work to define k_Q and k_{ion}.

The same experimental setup was used as previously described, with the same 10 mm Ta collimator and distances between detectors and beamline components, as best as possible. An alignment check was initially performed with some spare RCF attached in front of the Markus chamber to visually verify that the beam spot was centred on the Markus window. A single sheet of EBT and HD-810 film were used for both the calibration and experimental exposures, with lot numbers 47207-03I and Q2435H810 respectively, and the films were again cut into 2.5 x 2.5 cm^2 squares and the usual handling procedures were followed.

Each film was irradiated individually and placed behind a PMMA sheet of 1.97 mm thickness with the Markus chamber directly behind the film. For HD-810, the active layer was closest to the Markus whereas for EBT the active layers are central in the film. To determine the D_w in the film active layers, first three repeated measurements of R/M were made without any film to determine the reference output in Gy/MU. The same measurement was made behind every film, and then by linear interpolation the Gy/MU was determined at the active layer depth and multiplied by the number of MU for that irradiation. A linear interpolation between points on the plateau region of a proton depth dose curve is a valid method only when the difference in depth is very small compared to the proton range. In this case, the difference in depth was at most the thickness of an EBT film which is about 1/30 of the total range of 29 MeV protons.

The films were scanned with the NSC 5000 using the slide feeder and settings as previously described in table 5.2, and their *net*OD measured using ImageJ. An alternative method of finding *net*OD was used here; rather than scanning the films twice (pre- and post-irradiation), the films were only scanned once and because the calibration films were not fully covered with dose as previously for proton measurements, the unexposed area around the beamspot could be measured and the average OD taken to be a proxy for the background OD in the exposed area. This method was also preferred because it was consistent with the approach of all measurements being taken in the same scanning session to reduce scan-to-scan differences between sessions. Figure 5.16 shows the calibration plots for both film types, although the uncertainties are not shown as they would be indiscernible on this scale.

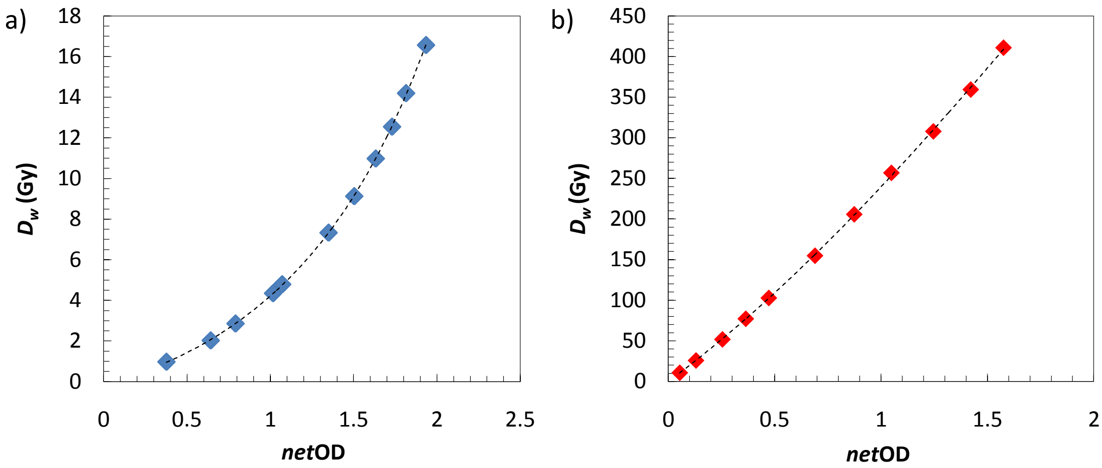

Figure 5.16: Calibration curves obtained for a) EBT and b) HD-810.

An ImageJ macro was written at this point to help automate the analysis of both the calibration and experimental films. This macro (slightly modified) is used again later in chapter 6. After scanning all of the films, they were imported as a stack in ImageJ. This allows operations to be performed on a number of images together (e.g. registration, alignment, measurement) so is extremely useful for batch processing. The stack was then cropped in size to include only the film area and be as large as possible without including the hand-written labels or the film edges. The macro was then run which performed the following operations, in order:

- duplicate initial image stack,
- convert duplicate stack to binary images, producing a black circular region for the beamspot and turning the rest white,
- for each image, find the centre of mass (COM) and store as (XM,YM) in an array,
- close duplicate stack,
- for each image in initial stack:
- create circular selection centred on (XM,YM) for that image with diameter equal to Markus active region (5.3 mm),
- measure s.d. for ROI and apply median filter (”Remove outliers” to filter out darker pixels outside 2σ),
- measure mean pixel value and convert to OD,
- create circular selection slightly larger than beam spot (12 mm) and invert so as to select everything else,
- measure mean pixel value for film background and convert to OD,
- calculate and output netOD.

5.5.2 Depth-dose measurements

A total of 22 EBT and 27 HD-810 films were irradiated at different depths in PET. Each film was weighed to find their mass thickness, and was multiplied by c_{ebt} or c_{hd} to obtain water equivalent thicknesses. These water-equivalent scaling factors had to be calculated independently for α-particles from protons. They were determined by combining c_{pet} for the PET substrate with the CSDA ratio of water-to-active layer, weighted by the relative thickness of each layer. The CSDA ranges for the two active layers for 38 MeV α-particles were found by using the reciprocal of the stopping powers calculated in section 5.2.2, as per equation 1.5. The 6 μm of adhesive/surface layers in EBT (and 0.75 μm in HD-810) were omitted from the calculation by virtue of their negligible thickness. The values calculated were $c_{hd} = 0.934$ and $c_{ebt} = 0.939$, the latter being almost 1% larger than the equivalent value for protons.

The irradiations were performed the day after proton calibration, and the films were left for a week before scanning to enable the OD darkening to substantially stabilise so that all the films could be scanned together. In accordance with the recommendations for MD-V2-55 of performing a uniformity check/correction, all of the HD-810 films were later irradiated again using the same uniform 6 MV X-ray field with the same conditions as for the calibration performed in section 5.3.1. They were each given 20 Gy, and left for 5 days before rescanning. By using the ImageJ macro described earlier, the film areas outside of the α-particle beam spot were analysed giving the OD due to X-rays for each film, and the normalised OD values for all the films are shown in figure 5.17. It can be seen that the range of OD values is just within ± 2%, which is significantly better uniformity than seen previously for MD-V2-55. By virtue of the X-ray field being regarded as ‘flat’ to within the same tolerance (of dose), it seemed unwise to perform any corrections when there is no certainty that any apparent uniformity is due to the film rather than the X-ray field. The final depth dose data are shown in figure 5.18 alongside Markus chamber measurements and the FLUKA simulation.

5.5.3 Relative effectiveness

The RE for each film was calculated via equations 5.10 and 5.11, which required the ratio $(s_{w,film})_Q/(s_{w,film})_{Q_0}$ to be calculated for each film where Q_0 in this case is the proton beam quality at the calibration depth. Using the FLUBOUND program, the energy

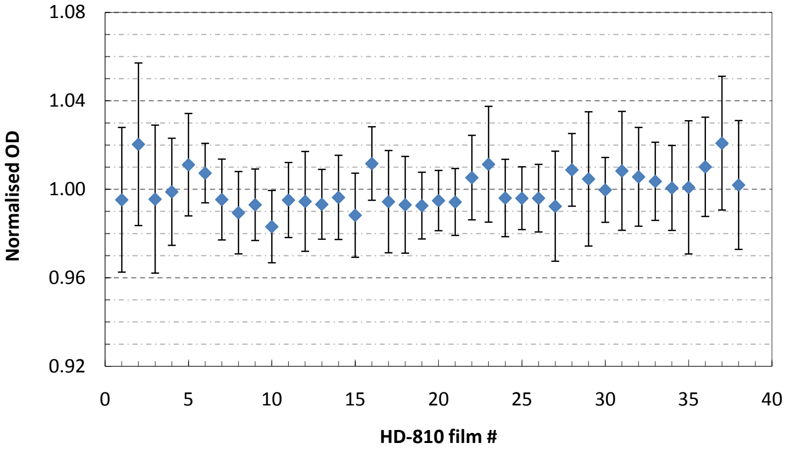

Figure 5.17: Normalised OD values for HD-810 films exposed to a flat 6 MV X-ray field from a hospital linac. Error bars indicate the s.d. measured within the ROI.

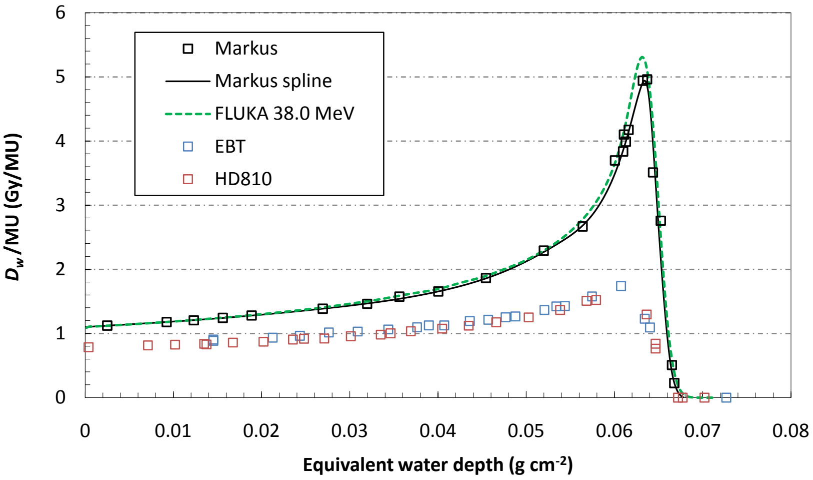

Figure 5.18: Depth dose curves for 38 MeV α-particles, measured with a Markus chamber (cubic spline fit included), EBT and HD-810 films and simulated with FLUKA.

at each film active layer was found following the same process as for proton FLUKA simulations with α-particles.

At depths in or around the BP, the beam spot on the films exhibited an unusual speckled dose pattern which was isolated to being caused by a non-uniform vacuum window, perhaps due to some contaminant deposition on the inside surface. This resulted in a spatially dependent variation in α-particle range but essentially could be thought of as an extra contributor to the effective momentum spread of the beam as measurements were integrated over the Markus chamber area. However, due to this effect and also the sharply changing dose gradient near the BP, films close to the BP were not included in the RE analysis as they would have very large associated uncertainties. Figure 5.19 shows the final RE data for α-particles, which can also be considered the ratio of polymer yields (as in equation 5.12) for α-particles (Q) and 23.0 MeV protons (Q_0).

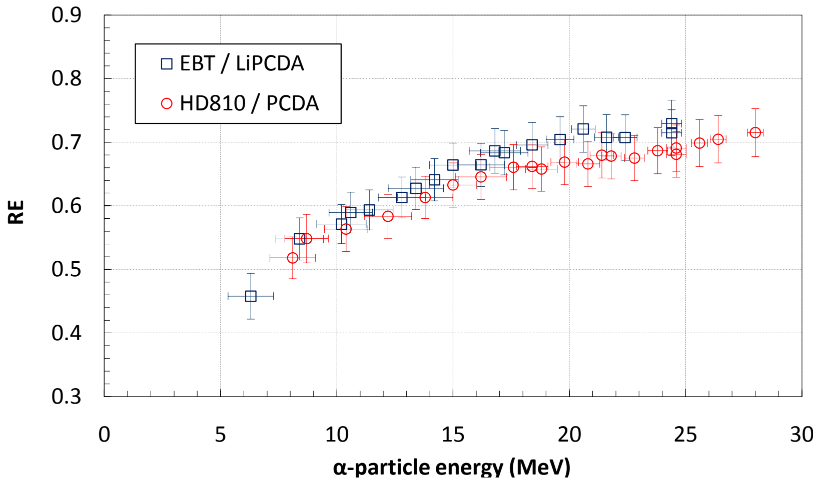

Figure 5.19: Relative effectiveness of EBT and HD-810 film versus α-particle energy.

The RE of α-particles is slightly lower than for protons with the same total energy, owing to their much greater LET. A direct comparison of the proton and α-particle data as a function of stopping power (as a proxy for LET) is shown in figure 5.20, without uncertainties. The stopping power values are those corresponding to the peak energy in the film active layer, and it can be seen that there is not a clear continuity between the proton and α-particle datasets. The reduction in G_Q is dependent on the microscopic

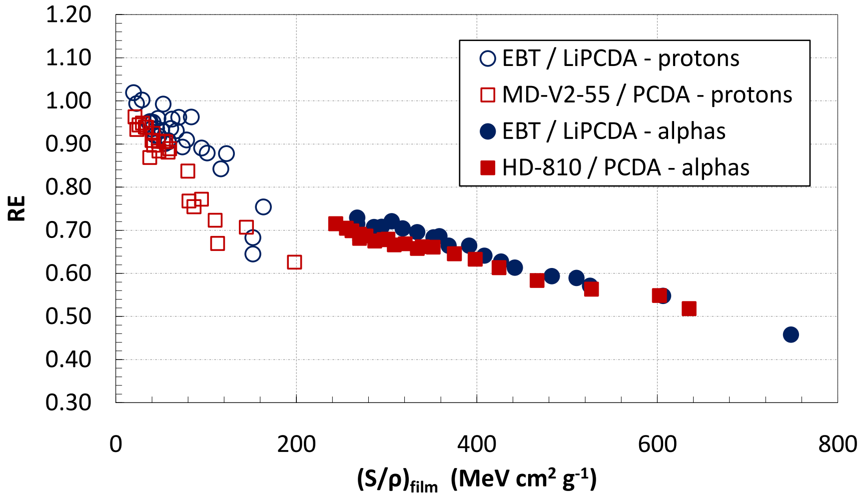

Figure 5.20: Combined plot of RE for protons and α-particles, as a function of mass stopping power for their respective film active materials

radial dose distribution about the primary particle track which is dictated by the range and direction of secondary particles. For example, a 3 MeV proton in water has a LET of $\approx$ 4.5 keV μm^{-1}; an α-particle with the same LET has a total energy of $\approx$ 69 MeV. Referring back to equation 1.1, the maximum energy of a δ-ray electron is nearly six times greater when generated by an α-particle than by a proton of the same nominal LET. This illustrates that the two different species will undoubtedly distribute dose microscopically in a different manner, and so RE for the same stopping power/LET value for different ion species should not be expected to be the same.

Whilst α-particles are not currently in clinical use in external beam RT, over 2000 patients were treated at Berkeley with α-particles up until 1992 (PTCOG, 2010) and there is renewed interest in investigating their potential for treatment. This work may also be useful to the field of ‘hot particle’ dosimetry, where some investigators (Darley et al., 2000) use RCF to measure radial dose distributions due to radionuclides contained in small particles found in the environment. It could also be useful for any future work that attempts to find a track structure model which can describe GafChromic film response to different particle species and energies akin to the work done by Hansen and Olsen (1985). This would be of particular interest in carbon ion RT where fragmentation causes a significant number of α-particles (among other particles) to be produced within the primary field and the ability to accurately model the Gafchromic film response to all fragmentation products could be extremely valuable.

CHAPTER 6

LASER-ACCELERATED PROTON DOSIMETRY AND SPECTROSCOPY

This chapter describes experimental work carried out in the Centre of Plasma Physics at QUB. The first experiment concerned irradiations of GafChromic film stacks with (primarily) protons generated by the Terawatt Apparatus for Relativistic Applied Non-linear Interdisciplinary Science (TARANIS) laser, in order to measure depth dose profiles and from that data infer some information regarding the energy spectrum of the laser-induced protons.

The aim of the second experiment was to perform laser-proton irradiations of V79 chinese hamster cells using a similar setup to the first experiment, but with some means of controlling the proton energy impinging on the cells using magnetic separation. It was a collaboration under LIBRA of QUB, Surrey University and Birmingham. Ultimately it was hoped to obtain the cell survival fraction as a function of dose from laser-induced protons and then repeat the experiment using the same cell techniques and similar proton energies on the Birmingham cyclotron, to investigate the radiobiological effect of ultra-short irradiations. At the time of writing, this experiment was still ongoing. Another student will continue to see this work through to its conclusion and the method may evolve as the experiment progresses.

The work in section 6.1 has been published (Kirby et al., 2011), and the full journal article is available in appendix I.

6.1 Dosimetry and RCF stack spectroscopy of a laser-proton source

6.1.1 Introduction

In many laser-plasma experiments (Breschi et al., 2004b; Clarke et al., 2008; Schollmeier et al., 2008) stacks of RCF have been used as a method of proton detection with high spatial resolution and no need for processing. In particular, GafChromic film models HD-810 and MD-55 tend to be used in tandem to cater for the high doses observed. Close to these sources, surface doses up to 1 kGy can be deposited. From a stack of RCF alone it is possible to deconvolve the initial proton spectrum from the dose profile, if the dose due to extraneous radiation (i.e. X-rays and electrons) can be sufficiently excluded. Notable methods of RCF spectroscopy are described by Breschi et al. (2004b), Hey et al. (2008) and Nurnberg et al. (2009) and often rely on stopping powers for the RCF active layers calculated by SRIM for calibration dose calculations and to determine the relative sensitivity of each film to protons of different energies based on their depth on the stack.

To date, some published RCF spectroscopy methods are limited in their dosimetric accuracy due to two factors: the lack of an accurate dose calibration of RCF in a proton beam using a PSDL-calibrated ion chamber, and the assumption that RCF dose response is independent of proton energy. It has been shown that there is a quenching of the film's response in the BP which is attributed to the significant increase in LET (Vatnitsky, 1997; Daftari et al., 1999; Piermattei et al., 2000; Kojima et al., 2003). The work in section 5.3.3 quantifies the RE of GafChromic film by comparing measured absolute doses to an ion chamber at different depths in 29 and 15 MeV proton beams. At energies below 3 MeV the response can be at least 25% less than for 20 MeV protons and failing to account for this will lead to a significant underestimation of proton fluence at low energies in RCF spectroscopy. Considering that the vast majority of protons produced in TNSA thus far have energies of only several MeV or less, this effect is expected to be significant when integrated over the whole spectrum and so its magnitude is investigated in this work.

This work has three main objectives: to bring D_w radiotherapy standards into the field of laser-proton dosimetry/spectroscopy; to use Monte Carlo simulations of RCF dose response in order to extract proton spectra from RCF depth-dose measurements; and to correct this spectrum for energy losses in the filter placed in front of the RCF stack. The filter is usually an Al foil in order to protect the stack from laser light, target debris, soft X-rays and heavy ions. A correction to the spectrum was devised using FLUKA and a matrix inversion technique. A relatively simple Fortran routine combined all steps of the spectroscopic analysis.

6.1.2 GafChromic film calibration

In order to obtain accurate dose information from RCF, a calibration of film optical density (OD) versus absorbed dose must be carried out ideally using the same radiation quality as for experimental exposures. For spectra which vary from shot to shot and with typical energy spreads of ∼100% from laser-plasma interactions, a calibration in a controlled but representative radiation field is virtually impossible. It was decided that the RCF should be calibrated with a reliable and reproducible setup in a nominal 29 MeV proton beam from the Birmingham cyclotron.

The basic methodology follows that described previously in section 5.5.1. The monitor and Markus chambers, PMMA and jig were arranged in the usual configuration (see figure 4.1). The dose output in Gy/MU at 1.97 mm depth (referred to as depth A) was measured with a statistical accuracy of $< 0.1\%$, allowing this depth-dose to be accurately known for any irradiation without the Markus chamber present. At this depth were positioned the RCF pieces for calibration with the Markus chamber directly behind. The proton energy in the film active layers is calculated to be 23.0 ± 1.0 MeV. The uncertainty accounts for beam energy spread as well the small difference at each film depth. The HD-810 films were positioned with the active layer closest to the Markus chamber, while for EBT the active layers are central in the film. In total, three sheets of HD-810 and two of EBT were calibrated (lot numbers Q2435H810 and 47207-03I) and eleven pieces of size 2.5 x

2.5 cm^2 were taken from each sheet of HD-810 and twelve from each sheet of EBT. A film from each sheet (of the same type) was placed in a stack at depth A. The dose output was measured behind the films for each irradiation (depth B), and a linear interpolation between depths A and B was used to determine the D_w/MU value at the centre of the active layer(s) in each film (see figure 6.1). This was then multiplied by the number of MU measured by the monitor chamber for each irradiation to give D_w at the relevant depth.

The dose rate used was approximately 1.2 Gy s^{-1} which yields a value of k_{ion} of 1.008 based on recombination parameters used previously in section 4.2.3. The beam quality correction k_Q was calculated using the same method described in section 4.2.4. The total uncertainty at the 68% confidence level in the determined dose in the RCF layers was estimated to be 3.5%. The calibration curves are shown in figure 6.2.

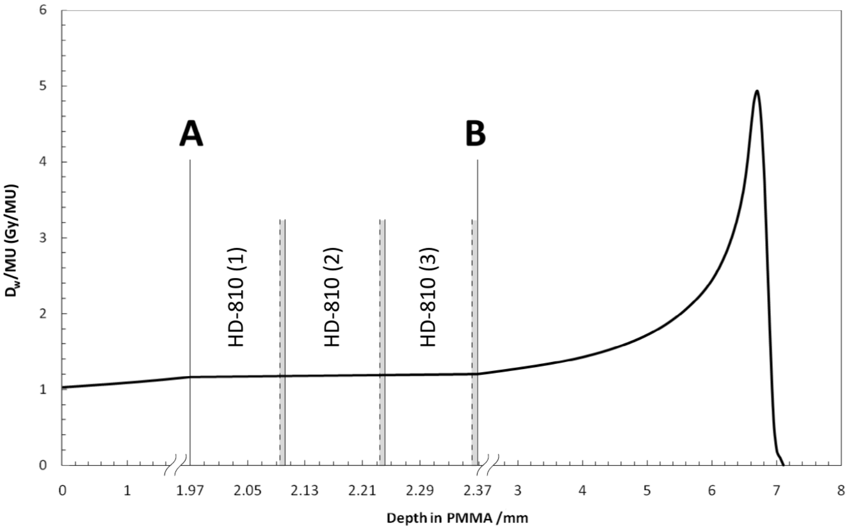

Figure 6.1: The 29 MeV depth-dose curve in terms of dose output, indicating the position of HD-810 films for calibration.

Whereas in chapter 5 the *net*OD is found for each film, in this work the background OD was assumed to be constant from film to film and was not subtracted. This was mainly due to reasons of practical convenience, as a large number of films were later irradiated with the laser and so scanning each one prior to irradiation was considered too time consuming. Measuring a representative background OD from the same post-irradiation

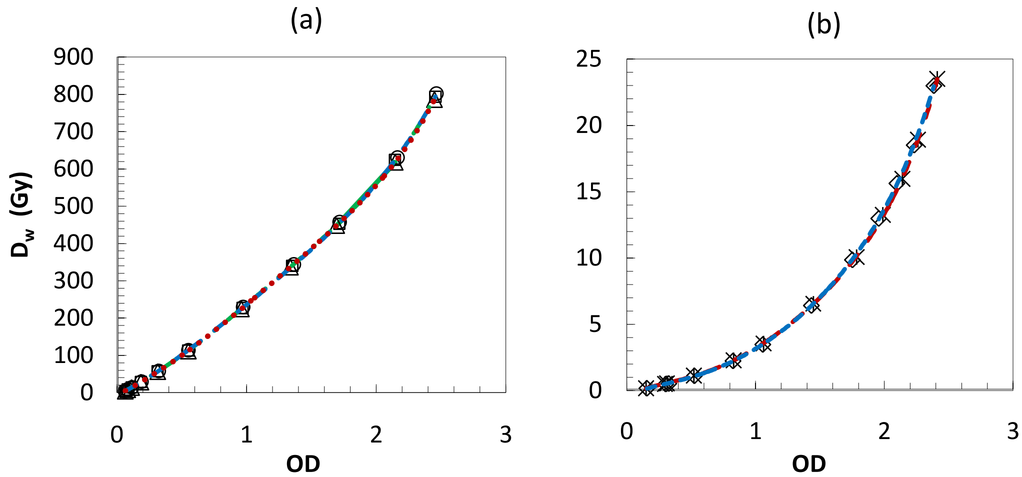

Figure 6.2: Calibration plots of D_w versus OD for a) HD-810, sheets 1-3 (circles, squares and triangles respectively) and b) EBT, sheets 1 and 2 (asterisks and diamonds). Each set of points has a fitted 5th order polynomial, although due to excellent consistency between sheets these fits are virtually indistinguishable.

scan was not possible with the laser-irradiated films as they were completely exposed, unlike the calibration films which contained a significant unexposed area. This meant that a calibration in terms of gross OD had to be used, however this was not seen to be a problem as HD-810 films are much thinner and so absolute differences in background OD are negligible. An alternative approach would have been to subtract a representative background from an unexposed film, but doing this would have added additional uncertainty to the overall measurement without gaining a significant improvement in accuracy, in the author's opinion.

6.1.3 Post-exposure OD growth

To investigate the claims by McLaughlin et al. (1996) that an ultra-short pulsed exposure may complete the OD darkening almost instantly rather than continuing for hours or days, irradiated pieces of EBT and HD-810 were scanned repeatedly after irradiation in a stack configuration typical of that described later. Only a single film of each type was analysed, but with multiple ROIs to obtain data for different OD values. The ROIs were chosen so that the OD was fairly uniform within them. Figure 6.3 shows the data measured from 0.5 to 24 hours after irradiation.

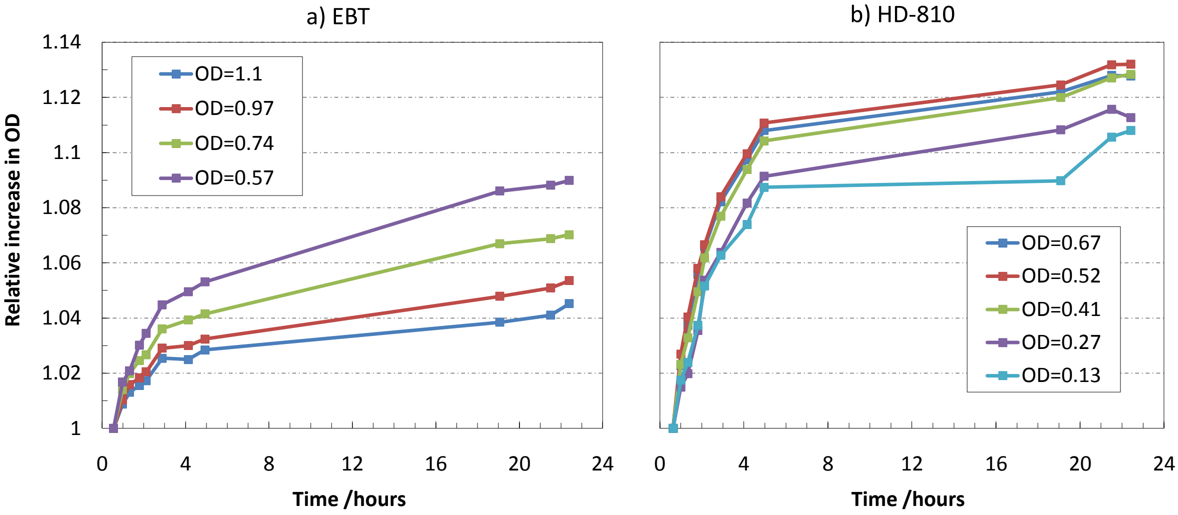

Figure 6.3: Relative change in OD versus time since irradiation for a) EBT and b) HD-810. The OD values in the legend are those measured from the earliest scan.

It is clear from the data that significant OD darkening continues after laser-particle irradiation, in contradiction to the observations by McLaughlin et al. (1996). The field was an uncollimated mix of protons, electrons and X-rays whereas McLaughlin et al. (1996) used a pulsed X-ray source. It is indicated from Martišíková and Jäkel (2010a) that the kinetics of the reaction differ depending on the LET of the radiation, as for carbon ions the darkening proceeds more slowly than for ^{60}Co X-rays and can continue for weeks at a significant level (i.e. several percent). This may possibly explain the contradiction, however McLaughlin et al. (1996) did not rule out a significant heating effect which may have fixed the OD of the film. In any case, the usual protocol of allowing several days (if possible) to elapse post-irradiation before scanning should still be exercised for laser-particle RCF analysis.

6.1.4 Main experimental method

The irradiations were performed with the TARANIS Nd:Glass multi-terawatt laser using CPA at QUB. The laser is described in more detail by Dzelzainis et al. (2010).

The laser was focussed by a $f/3$ parabolic mirror onto a 10 μm Au foil, and an RCF stack was placed 2.5 cm away along the axis of the target normal. A 20 μm Al foil was used as a filter for soft X-rays, heavy ions, debris and laser light. A Cu collimator of 1 cm diameter was placed in front of the stack in order for the spectrum deconvolution method to be valid, as follows. FLUKA calculations simulated a parallel beam with a scoring plane much larger than the source diameter. It was important therefore to collimate the laser-proton source so that the plane integrated depth-dose measured was not affected by divergence causing protons to miss RCF layers toward the rear of the stack. As a consequence, some of the wider angle emitted protons would not be detected or accounted for in the spectroscopic analysis. The experimental setup is shown in figure 6.4.

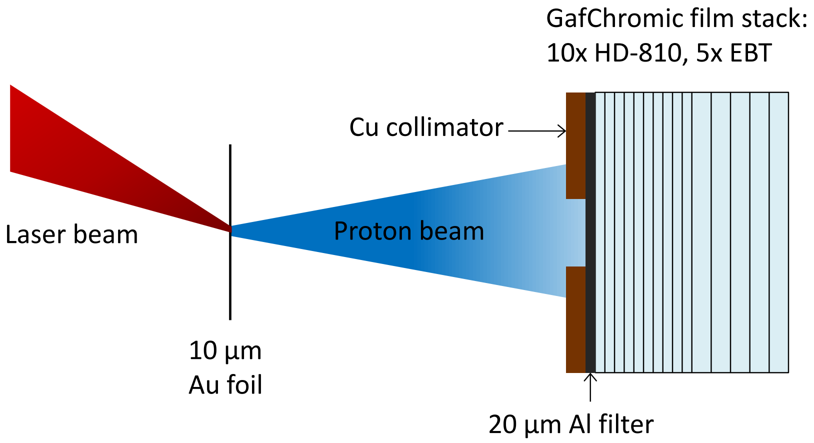

Figure 6.4: Simple schematic of the experimental setup at QUB. The proton beam ‘cone’ also contains electrons and X-rays.

The RCF stack was arranged so that HD-810 was present until the expected range of the highest energy protons, and then layers of the more sensitive EBT followed which would be able to measure the comparably small electron/X-ray background more accurately. The configuration consisted of ten HD-810 films followed by five EBT films. Use of MD-V2-55 was avoided because it has double the thickness of HD-810 which would result in fewer depth-dose measurements. This resulted in lower signal-to-noise near the back of the stack where proton dose was much lower, but still within the dynamic range of the film.

Various slightly different configurations were tried, i.e different numbers of films, without a collimator and with a multi-hole collimator mask. However only the data from two laser shots using the configuration described above were fully analysed and are presented here.

6.1.5 Monte Carlo method

Using FLUKA, the *comscw* subroutine can be customised in order to modify the amount of energy deposition scored by a specific USRBIN tally which means that energy dependent response functions can be incorporated into dose scoring. Hence (as already described in section 5.4), the RE of MD-V2-55 film as a function of energy can be incorporated, therefore simulating the depth-dose curves that would be measured using this type of RCF. There are structural differences between MD-V2-55 and HD-810 however the composition of the active layer is identical, so the RE for protons of both models can be safely assumed to be the same.

The response function used was of the same form as the sigmoidal fit curve (equation 5.13). The fit parameters used were the same as those given in table 5.6 except RE_0 and ΔRE were changed to 0.536 and 0.478 respectively in order to scale the function so that RE = 1 for the calibration energy of 23.0 MeV.

FLUKA was then used to generate a library of proton depth-response curves in water for energies from 0–15 MeV, in 0.5 MeV steps using the RE function (figure 6.5). The proton source was defined as a pencil beam with a uniform energy distribution from 0–15 MeV, and the deposited energy density was scored in a thin cylindrical mesh of thickness 5 μm and radius of 5 cm. Rather than produce 30 separate simulations for each energy bin, a more elegant method was found by modifying the *comscw* routine yet again and specifying 30 unique USRBIN cards each with same mesh geometry. For this single simulation, the average CPU time per history was 15 ms and 20 million were required to obtain statistical uncertainties to around 0.1–0.2%. It was sent to 16 cores on BlueBEAR and completed after 5.2 hours. For every energy deposition event during run-time, the *comscw* routine would determine the starting energy of the tracked proton and assign the energy deposition scored to the USRBIN dedicated to the relevant energy bin. Note that in FLUKA, the units of deposited energy density are in GeV cm^{-3} per primary proton (pr^{-1}). For later comparison, a library of full response curves were also produced to investigate the effect of simulating the RE of HD-810.

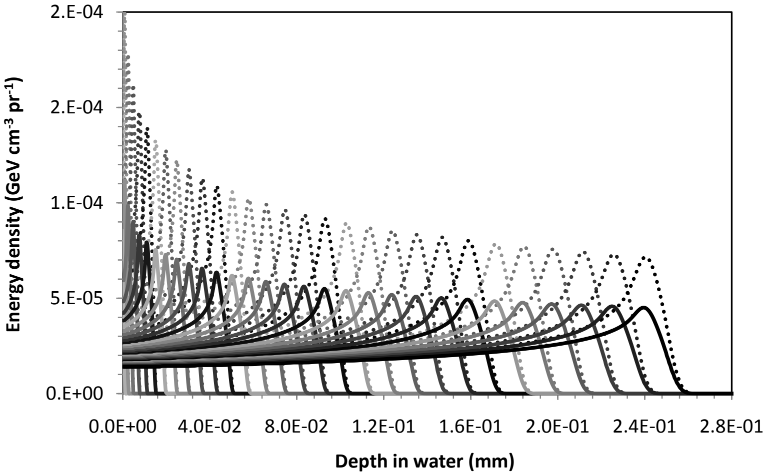

Figure 6.5: FLUKA library of RE simulated depth-response curves (solid lines) and unmodified depth-dose curves (dashed lines) in water for 0–15 MeV protons, in 0.5 MeV steps.

As the last part of the spectrum deconvolution process, FLUKA was also used to generate a matrix, $\mathbf{M}_{\mathrm{i,j}}$, to represent the degradation of the proton energy spectrum after passing through a 20 μm Al foil. Each value in the matrix represented a normalised bin height after the energy loss in the foil. The i variable represented a transmitted energy bin and j the initial energy bin. If the initial and final energy spectra are represented by 1-dimensional arrays $\mathbf{E}_{\mathrm{j}}$ and $\mathbf{E}'_{\mathrm{i}}$, it follows that:

$$\mathbf{M_{i,j}} \times \mathbf{E_j} = \mathbf{E_i}'$$

which in full matrix form looks like

$$\begin{bmatrix} M_{1,1} & 0 & 0 & \cdots & 0 \\ M_{2,1} & M_{2,2} & 0 & \cdots & 0 \\ \vdots & \vdots & \vdots & & \vdots \\ M_{30,1} & M_{30,2} & M_{30,3} & \cdots & M_{30,30} \end{bmatrix} \begin{bmatrix} E_1 & E_2 & \cdots & E_{30} \end{bmatrix} = \begin{bmatrix} E'_1 \\ E'_2 \\ \vdots \\ E'_{30} \end{bmatrix}$$

To populate the matrix, a series of 30 virtual beams were set up with a top-hat distribution ranging from 0–15 MeV in 0.5 MeV steps. For each beam, the transmitted spectrum was scored on the rear surface of the Al foil. Any values with an uncertainty greater than a few percent were omitted and the remaining bins renormalised as including them could lead to large oscillations after matrix inversion. This only occurred in bins with a relatively negligible number of protons.

By finding the inverse of **M**, this could then be multiplied by the measured spectrum derived from RCF to find the initial energy spectrum before the Al foil. The (generalized) pseudo-inverse matrix was obtained by using the *geninv()* function in MathCAD® 14, because the true inverse could not be found as **M** had a determinant of zero. Both **M** and $\mathbf{M}^{-1}$ are available in appendix H.

To verify this inverted matrix, a simulation was performed with a completely uniform spectrum from 0–15 MeV through a 20 μm Al foil and the transmitted spectrum was matrix multiplied by $\mathbf{M}^{-1}$ as a test to reproduce the initially flat spectrum. For energy bins above 1 MeV, the mean deviation from the initial spectrum was 0.15% and the maximum was 0.58%. In the two energy bins below 1 MeV, the data is lost as all the protons stop in the foil. This is represented in **M** as the first two rows consisting of only zeros (see appendix H).

6.1.6 Spectrum search algorithm

Firstly the RCF depth doses were integrated over beam area in order for the FLUKA pencil beam simulations to be applicable. As the real situation was a diverging beam, the region of interest (ROI) used for analysis was carefully increased for each successive film so that a constant proton fluence was theoretically maintained in the ROI. The front film's ROI was determined by using the threshold tool in ImageJ to include pixels above a darkness threshold resulting in the maximum integrated dose to neglect influence from the scattered low dose 'halo'. The sensitivity of decreasing the ROI threshold from 75% to 25% of the mean ROI dose was at worst a 1.5% reduction in integrated dose, and so any potential bias from poorly selecting subsequent film ROI was very small. The mean EBT area-integrated dose was subtracted as electron/X-ray background from the HD-810 film doses.

Multiplying the mean doses by the measurement area and by the RCF active layer density yielded units of J cm^{-1}, i.e. total energy absorbed per unit depth in the RCF stack, denoted by $\mathrm{d}E/\mathrm{d}x|_{\mathrm{RCF}}(x)$. The FLUKA depth-doses (in GeV cm^{-3} pr^{-1}) were then converted to J cm^{-1} pr^{-1} by multiplying by scoring area and the conversion factor $1.6022 \cdot 10^{-10}$ J GeV^{-1} and are denoted by a 2-dimensional array of $\mathrm{d}E/[\mathrm{d}x{\cdot}\mathrm{pr}]|_{\mathrm{MC}}(E,x)$. In terms of units, it is clear that division of the former by the latter in the correct way will yield the number of protons.

The Fortran routine written to solve for the spectra would first read in the RCF depths and doses along with the FLUKA BP library. It ascertains the depth of each BP, and also the range of each energy by finding the depth at which the dose falls to 10% of the BP value (which is equivalent to R_p, defined by TRS-398). It calculates interpolated doses at the depth of each BP in the library using a cubic spline routine, so that each energy bin has a similar importance in the search algorithm. These interpolated doses (along with original RCF doses) form the new set of "measured" depth doses.

The routine then searches for the lowest energy with a range exceeding the last RCF depth, and divides $\mathrm{d}E/\mathrm{d}x|_{\mathrm{RCF}}$ by $\mathrm{d}E/[\mathrm{d}x{\cdot}\mathrm{pr}]|_{\mathrm{MC}}$ for this energy at this depth, giving the number of protons for the highest energy bin. The rest of the spectrum is initialised at this value, and a direct search takes place by modifying each energy bin in turn in order from high to low in order to find a least squares solution. The resulting depth-dose curve associated with the spectrum is evaluated at each iteration and compared to the measured values. The routine then proceeds for as many passes as required before a stable solution is found, with the step size reducing on each pass. The spectrum is then matrix multiplied by $\mathbf{M}^{-1}$ to reverse the effect of energy losses in the Al foil. Uncertainty propagation was performed by repeating the calculation for 1000 randomly modified RCF dose sets (within uncertainties) to obtain a mean spectrum and uncertainty for each energy bin.

6.1.7 Results

The data from two laser shots were used for analysis. Shot 1 recorded an estimated laser energy on target of 7.1 J and shot 2 recorded 7.8 J, with pulse lengths of about 550 and 600 fs respectively. The estimated intensity was around $1.6 \cdot 10^{19}$ W cm^{-2} in each shot and hence the maximum proton energy in each shot should be similar. Figure 6.6 shows the scanned films from the RCF stack for shot 2. The RCF depth doses are shown in figure 6.7 along with the solved depth-dose curves produced by the Fortran routine. Note that the last point for shot 1 is from the first EBT film in the stack, which showed significant dose above the background. All other EBT films after average background subtraction gave doses close enough to zero (i.e. so that zero was within their uncertainties) to be deemed beyond the range of the highest energy protons.

RCF data for both shots were processed by the Fortran routine using both the RE-simulated and full energy deposition BP libraries for comparison, and the spectra were matrix multiplied (as 1-dimensional matrices in i) by $\mathbf{M}^{-1}$ to obtain the final corrected spectra. Figure 6.8 part (a) compares the effect of including the RE function, and part (b) the effect of correcting for energy losses in the Al foil. It was assumed that the proton spectrum followed a 1-dimensional Maxwellian distribution and N and kT were varied to give a weighted fit. The parameter N is representative of the total number of protons,

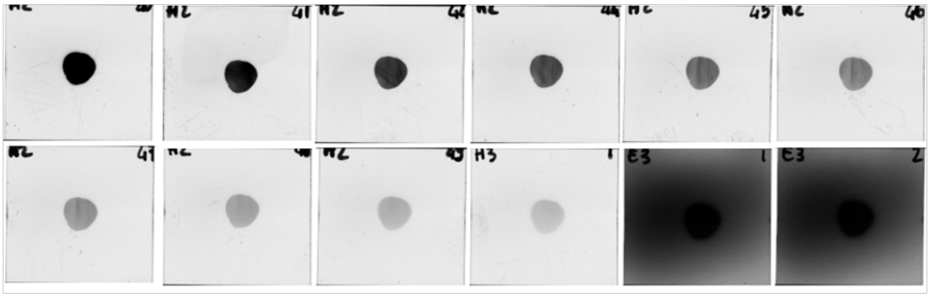

Figure 6.6: From left-to-right, top-to-bottom are the HD-810 films from shot 2 in order followed by the first two subsequent EBT films in the stack. Images are the extracted red channel presented in greyscale.

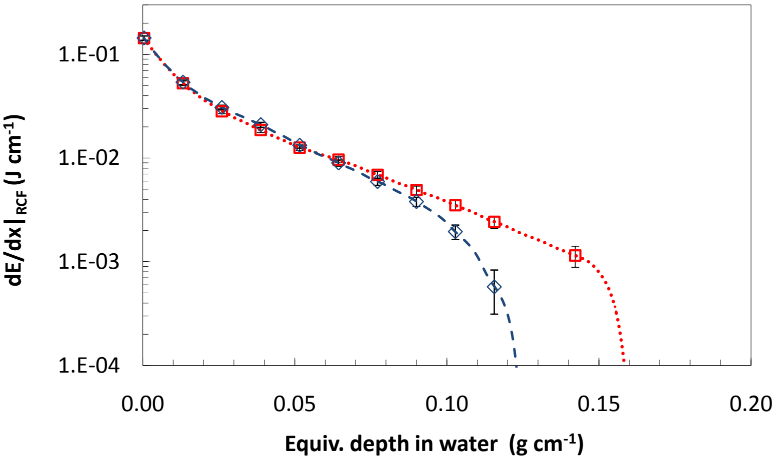

Figure 6.7: The measured values of $\mathrm{d}E/\mathrm{d}x|_{\mathrm{RCF}}$ from HD-810 films after subtraction of electron and X-ray background measured by EBT films for shot 1 (red squares) and shot 2 (blue diamonds). Solved depth-dose curves produced by the spectroscopic algorithm are also shown for shot 1 (red dotted line) and shot 2 (blue dashed line). RCF thicknesses have been converted to equivalent depth in water.

and so the effect on N of these improvements as well as on the total spectrum integrated over energy is shown in table 6.1.

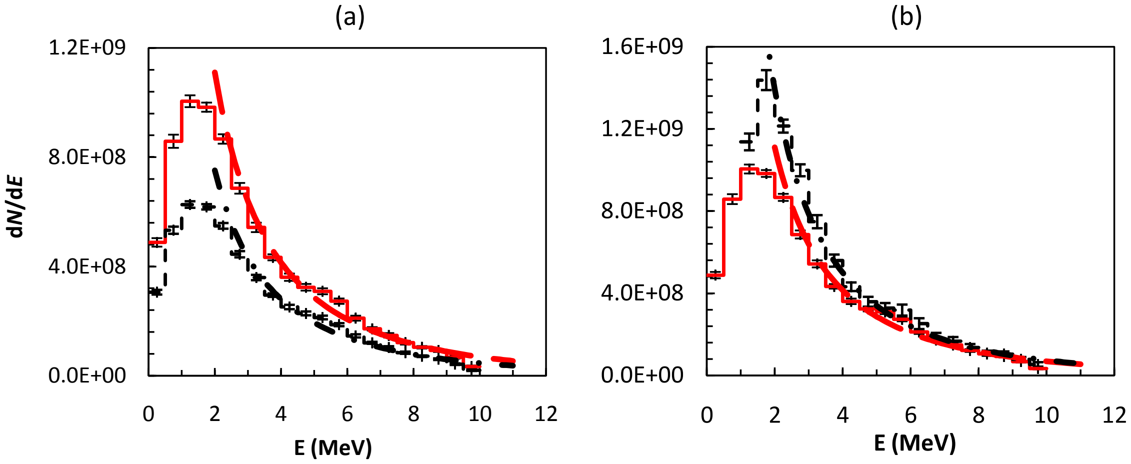

Figure 6.8: Plot (a) shows a comparison of proton spectra for shot 2 calculated using the RE response of HD-810 (solid red line) and without, i.e. full energy deposition (dashed black line). Plot (b) then compares the former spectrum (again, solid red line) before and after (dashed black line) multiplication by $\mathbf{M}^{-1}$ to correct for energy losses in the Al foil. All data were weight-fitted to a Maxwellian distribution (thicker dashed and dot-dashed lines).

Table 6.1: Percentage increases in total integrated dN/dE, as well as N derived from the fitted Maxwellian distribution for both shots, occurring as a result of including the RE function of HD-810 and correcting for energy losses in the Al foil.

	RE function		Energy loss in foil	
Increase in:	Shot 1	Shot 2	Shot 1	Shot 2
integrated dN/dE	53.4%	53.6%	6.6%	6.6%
fitted N	47.0%	47.7%	56.0%	30.7%

It is clear from both shots that by including the RE function of HD-810 that around 50% more protons are estimated in total. The matrix multiplication should leave the total integrated number unchanged, as it can not possibly give any information regarding protons which stopped in the foil. Its purpose is to calculate the up-shift of protons to higher energies, and the energy bins 0–1 MeV are empty in figure 6.8 part (b) because all of these protons are stopped by the foil. However it appears that 6.6% extra protons appear, which will be an artifact arising from uncertainties in **M** combined with uncertainties in the inversion process. This level of uncertainty is acceptable given that the resultant changes to the spectra correspond to large increases in N of 56% and 31% respectively. The difference between these values is likely due to the sensitivity of N to small differences at low proton energies.

The final corrected spectra for shots 1 and 2 are shown in figure 6.9. They show maximum proton energies of 11.5 MeV and 10 MeV respectively, which concurs with the difference in range of the RCF depth-doses shown in figure 6.7. Values of N and kT for weighted Maxwellian fits are given but these only represent the central portion of the beam which was transmitted through the collimator, i.e. inside a divergence half-angle of $\approx 11°$.

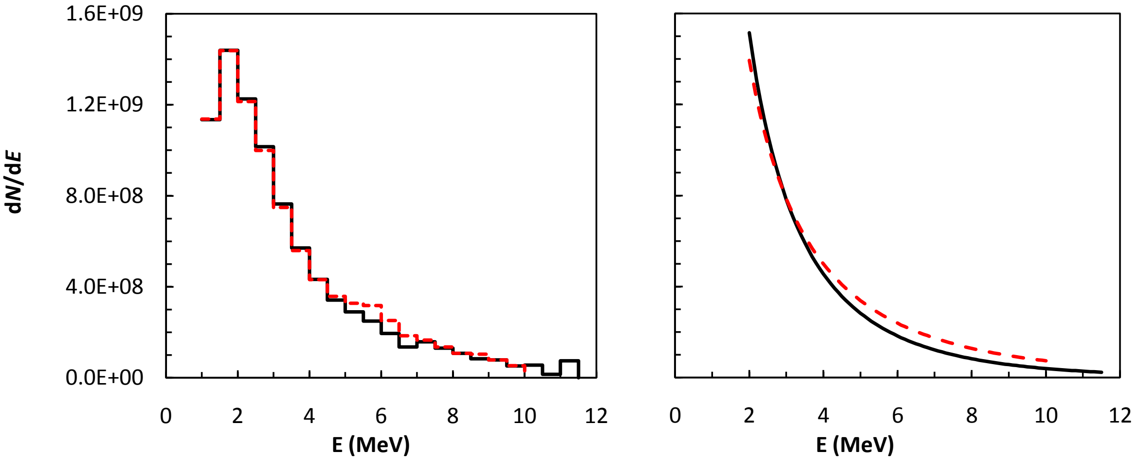

Figure 6.9: Final corrected spectra for shot 1 (solid line) and shot 2 (dashed line). Due to similarity of spectra, for clarity the Maxwellian fits are presented separately.

In conclusion, failure to consider the relative response of RCF to lower proton energies and neglecting energy losses in a RCF stack filter foil can potentially lead to significant underestimates of the total number of protons in RCF spectroscopy. It is expected however that these effects will be reduced for higher energy spectra.

6.2 Towards cell survival measurements in a laser-proton source

6.2.1 Introduction

The extremely short pulsed nature of the incident laser light dictates that all the following acceleration processes also happen on a similarly short time scale, resulting in a burst of particles that from a biological target's point of view, arrive instantaneously. The exact length of the ion pulse can be from a few tens of picoseconds to nanoseconds and largely depends on the distance of the target from the source and also the breadth of the energy (velocity) spectrum as multi-MeV energies are not relativistic. This feature of laser-plasma acceleration is what makes it most different from conventional particle acceleration, and until now there have been no experiments conducted to examine the reaction of living cells to this extremely high instantaneous dose rate. Hence there is large interest and motivation to irradiate cell samples with a laser-ion pulse and determine the characteristics of their response.

The simplest experiment with which to benchmark laser-induced radiobiology is to irradiate a mammalian cell line with different doses and construct a cell survival curve of the type discussed in section 1.1.3. This should be accompanied by a parallel experiment with the same cell line and (if possible) beam quality from a conventional accelerator. It is fairly well known from the literature (Hall, 1972; Chadwick and Leenhouts, 1973; Steel et al., 1986) that differences in survival can occur for dose rates ranging from a few Gy hr^{-1} and a few Gy min^{-1} as the irradiation time is of a similar order to the cell repair time and so lower dose rates generally result in increased survival for the same total dose delivered. However when the irradiation time becomes appreciably shorter, the cell has negligible ability to repair during irradiation and so it is hypothesised that extrapolating to dose rates of $\approx 10^9$ Gy s^{-1} should not exhibit any difference. Another argument is that such a short pulse may cause a momentary spike in temperature and could be a viable mechanism for cell death in addition to that of DNA damage by ionisation.

At the time this thesis was written, work was still ongoing to develop a reliable and optimal method for cell irradiation capable of delivering doses ranging from 1–10 Gy with a single laser shot, with cell handling techniques and proton delivery (energy and intensity) being the factors requiring most improvement. Described in this section is the preparative work performed with FLUKA to simulate the beam delivery onto cell targets in particular to investigate proton spectra and dose distributions. The purpose of these simulations was to guide the initial experimental geometry towards reducing proton energy spread across an area of cells whilst delivering sufficient dose.

It was proposed that GafChromic film be used to measure dose directly behind the cell monolayer. The only model of film with the active layer at the surface is HD-810, which is not useful for measuring doses of only a few Gy. Fortunately, ISP could offer us a limited amount of an unlaminated version of EBT2 which was made during some pre-production runs and was not available commercially. This film was ideal as it was very sensitive in the desired dose range and the active layer was very near the surface below a 5 μm protective layer. In order to measure dose accurately from low energy protons, the correction factor g_{Q,Q_0} had to be calculated which would require knowledge from experiment and simulation of the proton energy in the film active layer. This pointed towards using a film stack as before, although as these films were 210 μm thick it meant that no more than five films in a stack would be irradiated. This would not be sufficient to perform a spectroscopic calculation, and so a different method of energy measurement was devised.

6.2.2 Overview of setup

In order to irradiate the cells solely with protons from a laser-plasma source, a magnetic field was required to separate the protons from electrons and X-rays. This field would result in a band of protons exiting the magnet at different points corresponding to different energies, as their radius of curvature in a magnetic field is proportional to velocity (see equation 1.7). As the source is a cone with appreciable divergence, by allowing all the protons to enter the magnet there will still be a large spread of protons at any point at the rear of the magnet. To reduce the spread, a collimating slit was proposed to go between the source and the magnet. A sketch of the proposed setup and particle trajectories is shown in figure 6.10 and the plane on the right hand side represents the target plane.

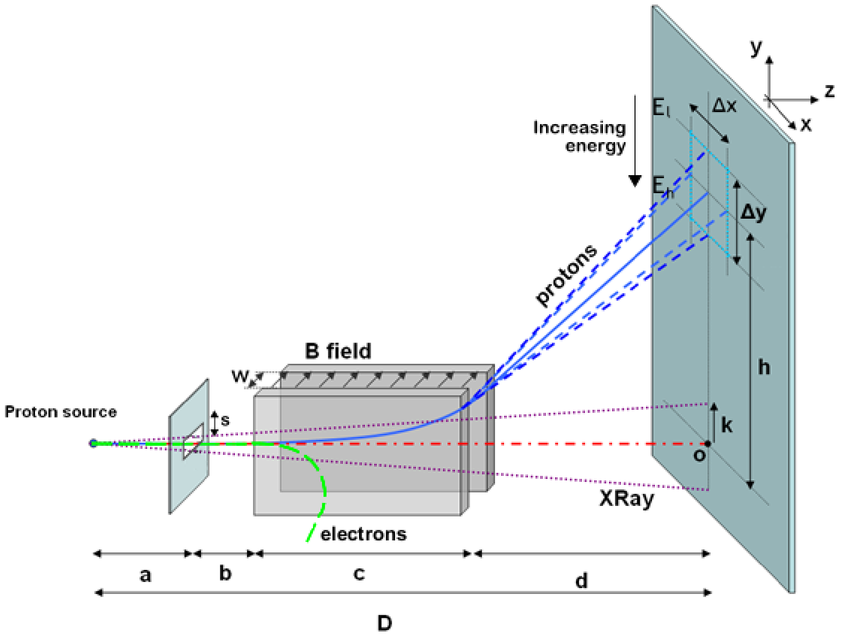

Figure 6.10: Sketch of proposed setup, including source, slit aperture, magnet and target plane. Important distances and parameters are labelled, which are subject to optimisation. (Figure contains elements of an original diagram by D. Doria, QUB)

The main parameters of significance in figure 6.10 are either fixed or variable:

- $a = 10$ mm and the size of the aperture slit in the range of 100 μm$< s <$ 300 μm;
- $b = 0$ mm;
- c, the length of the magnet is between 25–150 mm;
- B, the magnetic field is assumed to be uniform at 0.7 T across w of 5 mm;
- D is the source-to-cells distance along the y-axis, depends on other variables;
- h is the projected distance along the z-axis of the deflected protons;

- assuming a cell target area of size $A = \delta x \cdot \delta y$, E_l and E_h are the lowest and highest energies of the protons incident at the extreme edges of this area;
- k is the maximum projection of the X-ray field emitted through the aperture.

The cell dish would be placed vertically for the duration of the irradiation, which is not considered to be a problem for a cell monolayer as long as it returns to being horizontal within 5–10 minutes otherwise the cells tend to slide under gravity, according to colleagues from Surrey who were mainly responsible for the handling, preparation and analysis of the cells. The team as a whole (QUB, Surrey, Birmingham) decided that ideally proton energies between 5–7 MeV should be targeted at the cells, for several reasons: firstly, that above 3 MeV, the LET is low enough that the cells respond in a similar way as they would to X-rays which makes initial comparison of results easier; secondly, as protons travel through the cell layer they will easily pass through without stopping in the cells and so the dose gradient is minimised; and thirdly, the correction for GafChromic film under-response to protons will be less significant and better defined than at lower energies. Consequently, E_h and E_l were set to 7 and 5 MeV respectively. Based on these energies, and a fixed separation (δy) of 10 mm, D. Doria from QUB calculated possible source-to-cells distance (D) values as a function of magnet length, c. From this function, two scenarios were chosen with the parameters shown in figure 6.2.

Table 6.2: Key setup parameters that were investigated for two different irradiation scenarios.

	Scenario 1	Scenario 2
c	25 mm	100 mm
D	1200 mm	335 mm
h	∼60 mm	∼60 mm
s	100/200/300 μm	100/200/300 μm

6.2.3 FLUKA simulations

For both scenarios in table 6.2, simulations were run with FLUKA using three aperture sizes of 100, 200 and 300 μm. The source was represented as a point source with a divergence less than that in reality chosen so the field was only slightly larger than the aperture size. Increasing the divergence any further would result in wasted source particles being dumped in the collimator. A point source was a valid approximation as the real source exhibits high laminarity and so is effectively a virtual point source at a small distance behind the real source. The source energy spectrum was modelled by a simple exponential fit to the earlier solved spectrum measured by an RCF stack in section 6.1, shown in figure 6.11 (note units of fluence are per steradian here). FLUKA does not have a built in exponential source, so the *source* routine was modified to calculate the probability density function (pdf) between a user selected minimum and maximum energy cut-off in the SOURCE card. The benefit of using an exponential function was that integration was much simpler to calculate analytically for the pdf than the full Maxwellian model of the source which could only be integrated numerically, using for example, Simpson's method. The latter was initially attempted, but resulted in significantly increased computational time per particle.

The material for the collimator/aperture was initially chosen to be Cu and defined to be thicker than the range of 15 MeV protons (3 mm). To examine the effect of scatter from the aperture the simulations were also carried out with the material set to 'blackhole', which in FLUKA is defined as a material where any particle entering it is killed immediately. This allowed comparison of a real collimator with a virtual 'perfect' collimator, and isolation of the low and high energy tails resulting from inelastic scatter and in general any increased spread in energy at the target plane. Similarly, while the presence of the magnetic field was always maintained, the magnet itself (approximated as two cuboid blocks separated by 5 mm) was simulated as both made of Fe and 'blackhole' material to check for any significant scatter. At the target plane, a layer of Mylar representing the vacuum window of the laser target chamber and covering layer on top of the cells was specified to

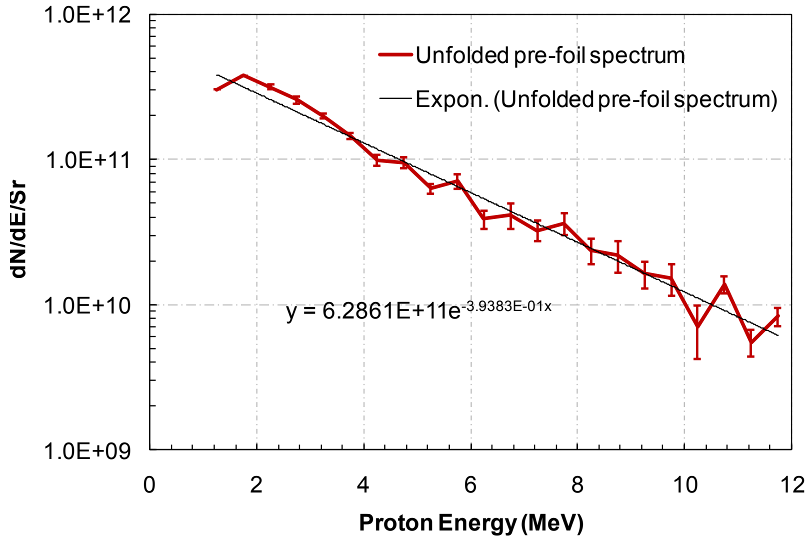

Figure 6.11: Fully corrected laser-proton spectrum calculated from shot 1 from section 6.1.7 per unit solid angle, with simple exponential fit function used to model the source in FLUKA.

be initially 75 μm thick. Immediately behind was a water layer 60 μm thick to represent 50 μm of cell medium which would cover a 10 μm thick cell monolayer. All thicknesses for these design simulations were approximate best guesses. In the FLUKA input, δ-rays were turned off and the proton step size was set to 5% energy loss in FLUKAFIX. The proton transport cut-off was 10 keV, and the source energy limits were set to 3 and 12 MeV. The lower energy limit was determined to be the energy required to penetrate the Mylar. In terms of defining cell areas, the layer was approximated as water and within it there were six rectangular regions 8 x 2 mm, spaced 5 mm apart defined purely for fluence and dose scoring. It had been previously discussed by the team that having several cell regions would be beneficial as then parallel sets of data could be obtained for different proton energies, and Surrey confirmed that this region would fit sufficient cells ($\gtrsim 10^4$) to obtain a reasonable statistical accuracy when cell survival fractions are less than 1%. The average CPU time per history in FLUKA was 1.4 ms and 1.7 ms for the 'blackhole' and Cu collimator simulations respectively. In both cases, 80 million particles were run which while quite large, still resulted in slightly noisy tails to the spectra but this level of uncertainty was acceptable as the overall magnitude of the tails was quite evident from the simulations.

From figure 6.12 it can be seen that increasing the aperture size significantly broadens the proton energy 'peak' at each cell area, and the scattering from the inside of the aperture creates both high and low energy tails but they contribute no more than about 1% of the total fluence. Including the physical magnet in the simulation indicated no significant additional scatter from the inside of the magnet walls. This simulation was performed with a larger number of particles (1.2 billion) which is why there are fewer statistical fluctuations of the high and low energy tails. It is also evident that scenario 2 results in a narrower peak and reduced scattering at the target plane due to the stronger energy separation of the larger magnet. Figure 6.13 shows more clearly the difference between the two scenarios.

The obvious conclusion is that scenario 2 is preferable for several physical reasons, but it also makes the setup more practical as D becomes much shorter and easier to fit inside a target chamber. Smaller aperture sizes are also preferable, however the negative side is that fewer protons reach the cells, reducing the dose they will receive. So reaching the necessary 1–10 Gy may be more difficult.

As part of the same simulations, dose was also scored across the target plane in the y-axis at the cell depth. FLUKA outputs energy deposition in terms of GeV cm^{-3} pr^{-1}, so this was converted to Gy Sr pr^{-1} so that an approximate dose could be calculated by multiplying these values by the integrated number of protons per steradian from the spectrum in figure 6.11. The dose profile is shown in figure 6.14, and indicates the positions of the cell areas.

The integrated number of protons per steradian between the energy limits (3–12 MeV) for this representative spectrum was $9.3 \cdot 10^{11}$ Sr^{-1}, and so multiplying by the values in figure 6.14 indicates that the required range of doses should in theory be achievable within the bounds of the suggested experimental parameters.

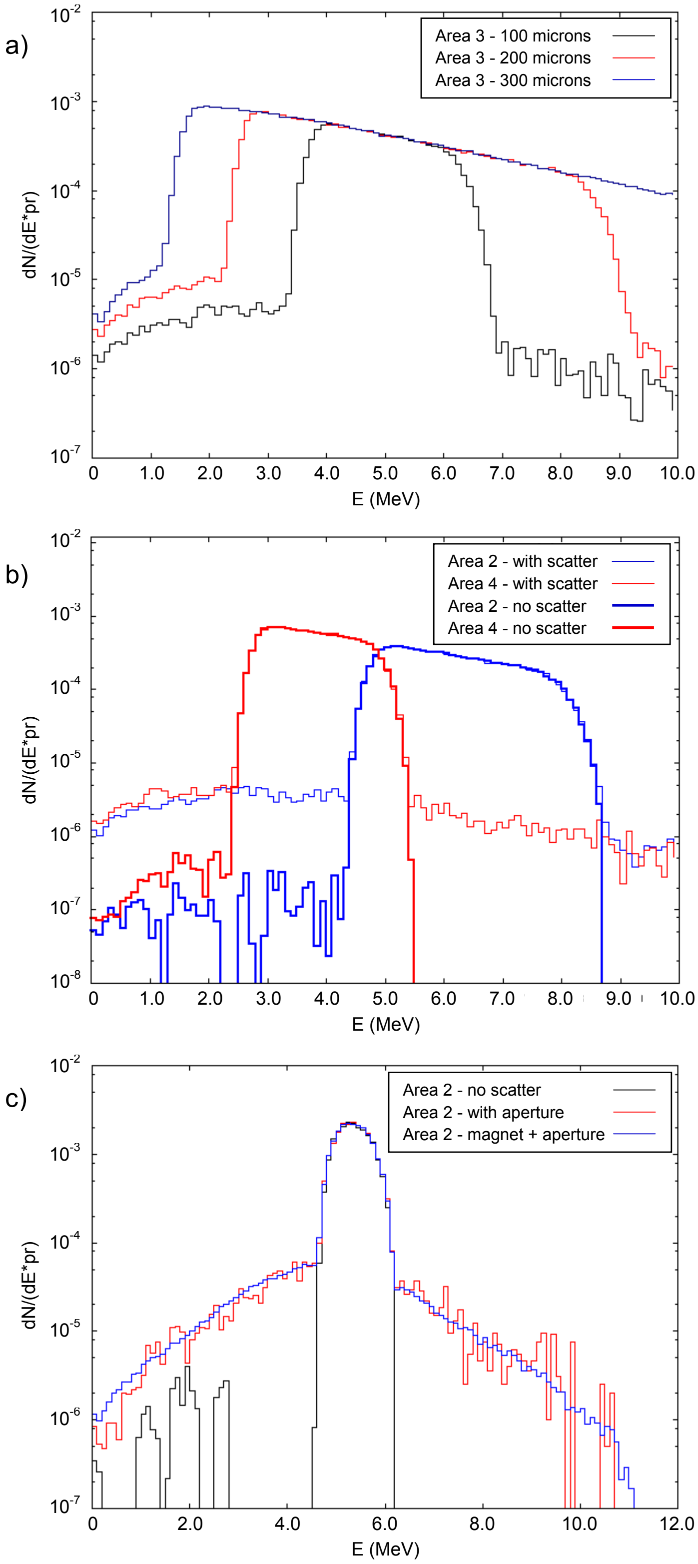

Figure 6.12: Log scale plot of energy fluence for a) scenario 1, cell area 3, for $s = 100$, 200 and 300 μm; b) scenario 1, cell areas 2 and 4, $s = 100$ μm and with and without collimator scatter (no magnet scatter); c) scenario 2, cell area 2, $s = 100$ μm with no scatter, collimator scatter, and magnet plus collimator scatter.

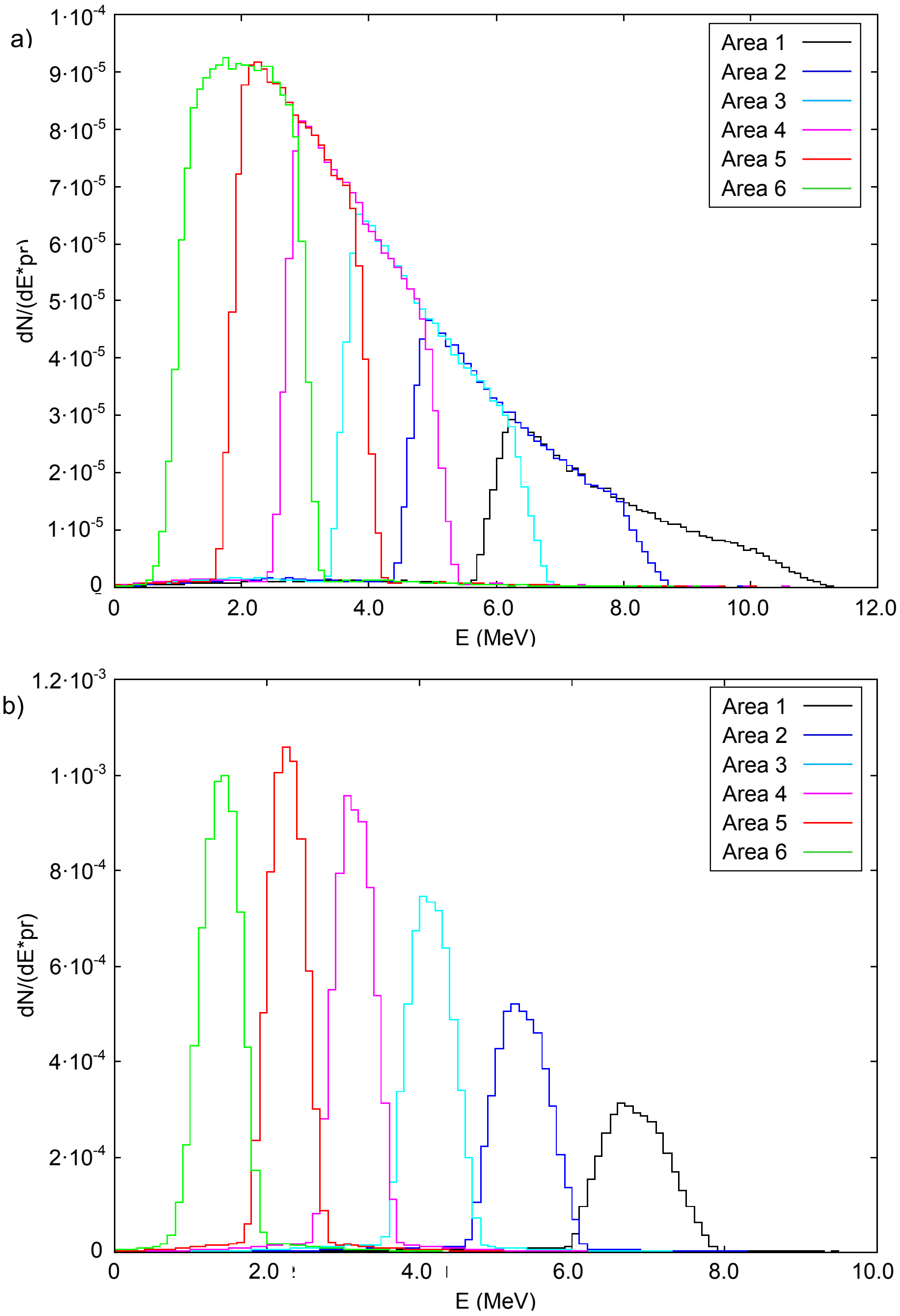

Figure 6.13: Log scale plot of energy fluence in all six cell areas with $s = 100\ \mu$m for a) scenario 1, and b) scenario 2.

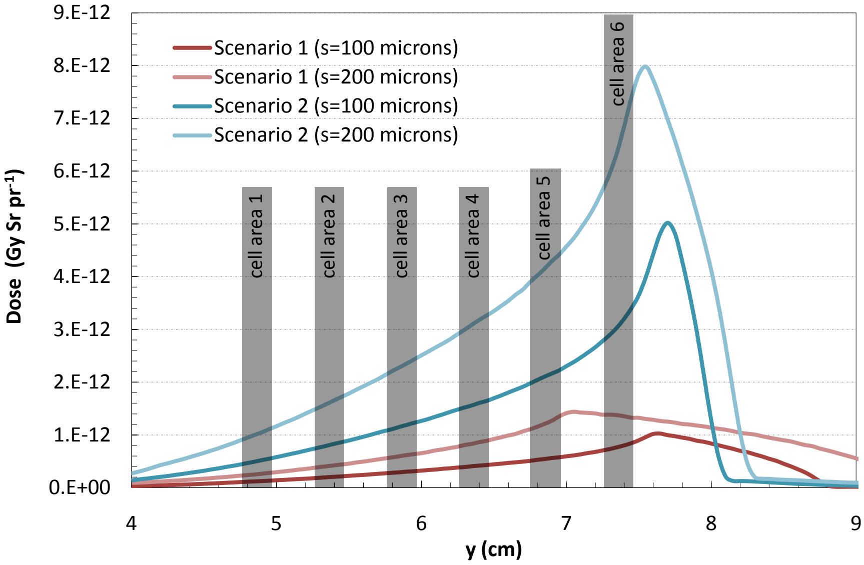

Figure 6.14: Estimated dose (per source proton per steradian) versus y in the simulated geometry, for both scenarios each with $s = 100$ and 200 μm.

6.2.4 Proposed dosimetry method

As alluded to earlier, the proposed method of dosimetry was to deploy a stack of five EBT2 films directly behind the cell layer as close as possible. In theory, there would only be a layer of 3 μm Mylar between the cells and the first film which the cells are grown on and attached to. The proximity of the first active layer to the cell layer means that D_w obtained from the film would be a very good approximation to the dose in the cells, although FLUKA could be used to perform a correction once initial dosimetry tests had verified that the simulations were accurately predicting the proton energy along the y-axis. A method of verification proposed was to analyse each film in the stack and obtain the 'dose edge', i.e. the position (in y) where the dose falls off to zero. Finding the dose edges for each film would effectively give a rough estimate of the maximum proton energy in the y-direction, knowing the energy required to penetrate successive films in the stack. This could then be compared to the locations of these dose edges predicted by FLUKA to compare the spacing between them and also as a means of cross-referencing the geometrical alignment from one shot to the next.

In theory, while the proton source spectrum can vary from shot to shot, the projections of the protons should remain fixed through the magnet and on the target plane. However, each individual laser target may not be oriented perfectly with its normal perpendicular to the magnetic field. Any small changes in the laser target normal will affect the direction of proton entry into the magnet and affect the spectra incident on the cell areas. Hence an EBT2 stack had to be deployed for every shot to determine these spectra based on FLUKA simulation, and also to determine the spectra in the areas of first film active layer which corresponded to the projection of protons through the cells. The g_{Q,Q_0} beam quality correction factor then had to be applied to obtain a value of D_w that was independent of proton energy and the LET quenching effect, as discussed in section 5.2.

6.2.5 EBT2 response verification

As can be seen in table 2.2, the active layer of EBT2 does not have the same composition as in EBT. Whilst the active component is still LiPCDA, the gelatin within which the LiPCDA is suspended has been deliberately modified. EBT2 includes the addition of a yellow dye and is also doped with other higher Z elements in order to reduce the under-response seen with low energy X-rays by increasing the photoelectric cross-section. In order to use the g_{Q,Q_0} correction proposed in section 5.2 for radiobiological dose measurements, the RE of EBT2 must first either be calculated independently or verified to be no different to the RE of EBT. In theory, they should exhibit the same RE by virtue of containing the same diacetylene monomer, and so irradiations were performed in the 29 MeV proton beam in the same way as has been described previously.

Twelve 2.5 x 2.5 cm^2 films were used for dose calibration, and individually exposed at a depth of 1.97 mm in PMMA with the active layer facing the Markus chamber. The Markus chamber #2225 was used with a voltage of 100 V, and the final $D_{w,Q}$ value was corrected by -0.25% due to being effectively measured $\approx 44\ \mu$m of PMMA downstream of the centre of the active layer. This small correction was found via interpolation with a cubic spline to previous 29 MeV depth-dose data. A 5$^{\text{th}}$ order polynomial was fitted to the calibration data, and an uncertainty due to this fit of 0.8% was estimated from the mean residual dose.

Seven EBT2 films were irradiated to approximately 6 Gy at different depths in PMMA, arranged again with the active layer side closest to the Markus chamber window. The entrance dose rate used was $\approx$ 1 Gy s^{-1} consistent with previous measurements, and films placed nearer the BP required shorter exposures due to increased dose rate at depth. The calibration and experimental exposures were carried out in the same session and left for seven days before scanning with the NSC 5000 using the default settings in table 5.2. As this film had not previously been scanned with this scanner, a consistency check was performed by scanning the calibration films three times in succession, turning the scanner off and on in between. Standard deviations of OD in both the beam spot and the surrounding background were calculated for each film, and the mean s.d. was 0.07% with the largest value being 0.12%. After finding the netOD for each repeated scan, the mean s.d. rose to 0.14% with the maximum being 0.67%. This reproducibility was considered to be excellent, given that not only was the reproducibility of the scanner being tested, but also the analysis macro which automatically locates the centre of the beam spot. Unlike previous tests where the film remains inside the scanner between scans and the ROI is static, there is random variation due to the slide feeder and so the ROI was often not precisely the same for all three scans of any film.

The only depth dose measurements with the Markus chamber performed here were behind each film during their irradiation, and were used to verify that the previous data were still valid. This was shown to be the case in figure 6.15

Referring to equations 5.1 and 5.12, RE is defined so that it excludes the effect of $s_{w,film}$ which had to be calculated separately for EBT2 due to its different composition to EBT. The method of calculating stopping powers was consistent with ICRU49, and followed the method previously described in section 5.2.2. Due to the addition of Na, Br and S, none of which have stopping powers available from ICRU, their stopping powers were found from SRIM and used in the modified Bragg rule as before. The ESTAR program from NIST (Berger et al., 2005) was used to find I_{ICRU} (= 68.7 eV) and I_{Bragg}

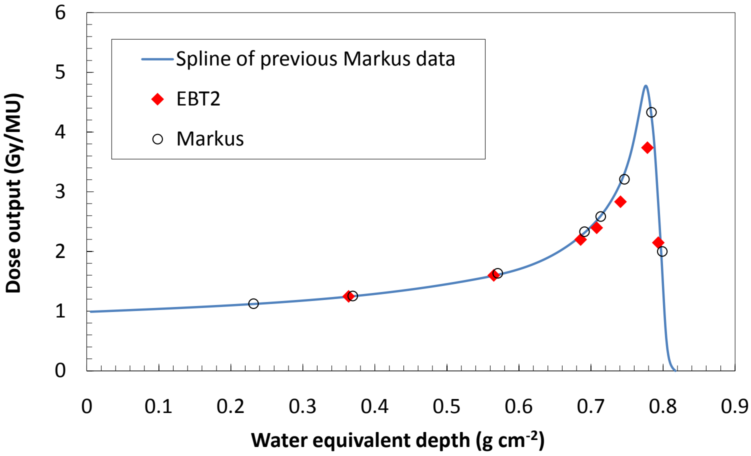

Figure 6.15: Depth dose data for EBT2 in terms of dose output compared with the Markus spline fit from the 29.15 MeV data in section 4.2.5.

was calculated to be 66.6 eV in order to apply the Δ_I correction (equation 5.6). Figure 6.16 shows $s_{w,film}$ versus proton energy for EBT2 compared with EBT and HD-810/MD-V2-55 (PCDA).

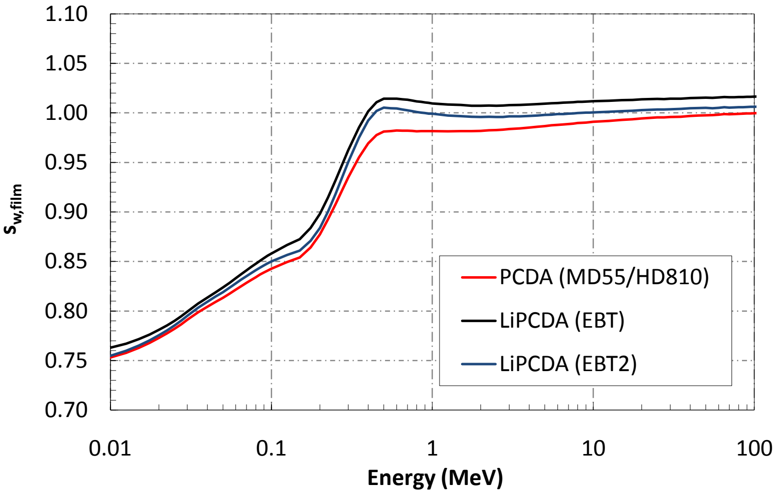

Figure 6.16: Water-to-film mass stopping power ratios for PCDA and both versions of LiPCDA calculated by following the ICRU modified Bragg rule for compounds.

The RE values for EBT2 were calculated via equations 5.10 and 5.11, where $s_{w,film}$ for calibration beam quality Q_0 was calculated at the active layer depth using the same method to find k_Q in section 4.2.4 but with some minor alterations to the Fortran routine.

Fair comparison with the RE for EBT required some attention as the calibration beam quality used then was 6 MV X-rays. If we refer to beam qualities by the indices p for any energy protons, and p' and X for the proton and 6 MV X-ray spectra at respective calibration depths, then in terms of the polymer yield G a relationship can be established as follows:

$$RE_{p,p'} = \frac{RE_{p,X}}{RE_{p',X}} = \frac{G_X}{G_p} \cdot \frac{G_{p'}}{G_X} = \frac{G_{p'}}{G_p} \tag{6.1}$$

where $RE_{p,X}$ is the quantity measured for EBT and $RE_{p,p'}$ is that measured for EBT2. Hence in order to compare the two films, each RE data point for EBT was divided by the RE value at 23 MeV ($RE_{p',X}$). Only the 29 MeV data for EBT was used for comparison as it was the most appropriate, and the comparison is shown in figure 6.17.

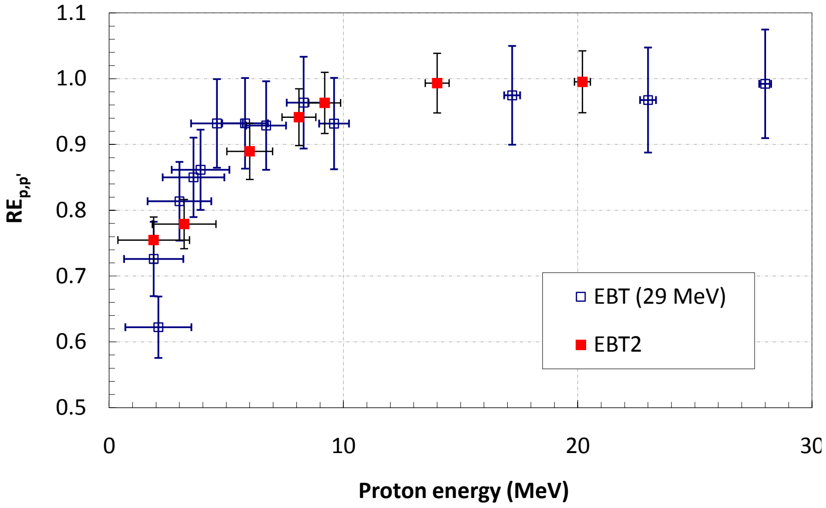

Figure 6.17: Comparison of $RE_{p,p'}$ versus proton energy for EBT and EBT2.

As expected, there is no significant difference between the RE of the two films. Consequently, the same sigmoidal fit function as used previously (table 5.5) can be used to give RE as a continous function of energy, and combined with $s_{w,film}$ for EBT2 gives the g_{Q,Q_0} correction to be applied to the films to calculate the beam quality independent D_w. The correction factor is shown in figure 6.18, and the low energy region is deliberately cropped as it should not be considered accurate there due to lack of data below 2 MeV.

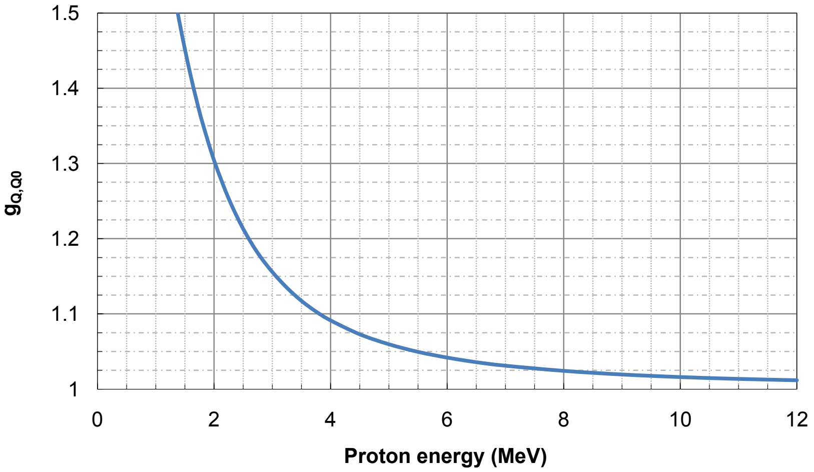

Figure 6.18: Beam quality correction factor for EBT2 as a function of proton energy, where Q and Q_0 are p and p' respectively.

In conclusion, this preparatory work has set in place all the tools required to perform accurate RCF dosimetry of a cell sample, given reliable knowledge of the separated proton spectra from FLUKA. The 'dose edge' test should help to tie together the geometries in the target space of the simulation and the experiment, as well as verify the simulation of proton trajectories through the beam separation device.

CHAPTER 7

SUMMARY

This final chapter summarises the main results and outcomes of the work described in this thesis. It also describes some miscellaneous work that did not warrant a full description but may be of interest to the reader, and discusses some possible future work to continue what has been achieved so far.

7.1 Ionisation chamber dosimetry

Dosimetry using a PMMA phantom was performed in 15 and 29 MeV proton and 38 MeV α-particle beams from the Birmingham cyclotron, with a PTW Markus parallel-plate ionization chamber. A PMMA jig was designed and built for this purpose. The dose-to-water formalism was adopted from the IAEA TRS-398 CoP (IAEA, 2000) and particular attention was paid to calculation of the beam quality correction factor (k_Q) with depth as these energies were outside of the range of validity for the given values in the CoP. Ion recombination was more significant for α-particles than for protons and the parameters for the correction factor were determined, accounting for both initial and volume recombination.

Simulations of the depth-dose curves were performed with FLUKA 2008.3d and MCNPX 2.5.0, which agreed almost perfectly with each other in range and only differed by 2% in the Bragg peak (BP) region. FLUKA was also used to find the peak energy at each depth of measurement in order to determine k_Q. FLUKA depth-dose simulations overestimated the BP height measured by ion chamber by 5–10%, where the initial proton momentum spread was estimated by fitting to the slope of the measured BP distal edge. Agreement between FLUKA and measurement for BP height was better for α-particles.

7.2 Relative effectiveness of GafChromic film

Depth dose measurements in proton and α-particle beams were performed using GafChromic EBT and MD-V2-55 film in parallel with the Markus chamber measurements. The proton films were calibrated using 6 MV X-rays from a Varian Clinac 600C whereas the α-particle films were calibrated with 23 MeV protons. Both GafChromic films showed an under-response in the BP compared to ion chamber, as expected due to local saturation of the film in the microscopic high dose regions very close to the primary particle tracks. However, EBT begins to suffer from this effect at lower energies than MD-V2-55. A possible reason for this was attributed to the shape and arrangement of the monomer particles being different in the active components of EBT and MD-V2-55.

The RE of both films for protons was calculated both as functions of residual range R_{res} in water and peak proton energy determined by FLUKA, with considerations for the spatial separation of the two active layers in each film. The proton energies at which RE reduces to 90% of maximum film response are 6.7 and 3.2 MeV for MD-V2-55 and EBT respectively. A beam quality correction factor (g_{Q,Q_0}) is proposed for both GafChromic films akin to k_Q for ion chambers, factoring water-to-film stopping power ratios evaluated using ICRU recommendations and a polymer yield factor. This required calculation of proton stopping power ratios of both the EBT and MD-V2-55 active compounds, PCDA and LiPCDA, to water, which have been tabulated for energies ranging between 1 and 300 MeV. RE in this work is equated to the reciprocal of the polymer yield factor. The calculated values of $s_{w,film\mathrm{Q}}/s_{w,filmQ_0}$ are constant within 2.1% and 1.2% across the proton energy range of 1–300 MeV for EBT and MD-V2-55 respectively. As expected, the polymer yield factor predominantly accounts for the LET quenching effect.

The RE of both HD-810 and EBT for α-particles decreased quite similarly from 0.73 to 0.46 between total α-particle energies of 28.2 to 6.2 MeV. For these much higher LET fields (compared to protons) there was only a very small distinction between the RE of EBT versus HD-810 noticeable around 30 MeV, where again EBT responded slightly better.

7.3 GafChromic film spectroscopy of a laser-proton source

A unique approach to spectroscopy of laser induced proton beams using RCF was developed, bringing dosimetry traceable to primary standards into the field of laser-induced radiation beams for the first time. The films were irradiated in a stack configuration using the TARANIS Nd:Glass multi-terawatt laser at Queens University Belfast which can accelerate protons to 10-12 MeV, and a depth-dose curve was measured from a collimated beam.

The RE of GafChromic film as a function of energy was implemented into the energy deposition routine in FLUKA. A Bragg peak (BP) 'library' for proton energies 0–15 MeV was generated, both with and without the RE function. These depth-response curves were iteratively summed in a Fortran routine to solve for the measured RCF depth-dose using a simple direct search algorithm. By comparing resultant spectra with both BP libraries, it was found that the effect of including the RE function accounted for an increase in the total number of protons by about 50%.

To account for the energy loss due to a 20 μm aluminium filter in front of the film stack, FLUKA was used to create a matrix containing the energy loss transformations for each individual energy bin. Multiplication by the pseudo-inverse of this matrix resulted in 'up-shifting' protons to higher energies. Applying this correction to two laser shots gave further increases in the total number of protons of 31% and 56%.

Failure to consider the relative response of RCF to lower proton energies and neglecting energy losses in a stack filter foil can potentially lead to significant underestimates of the total number of protons in RCF spectroscopy of the low energy protons produced by laser ablation of thin targets.

7.4 Laser-proton radiobiology experiment

Simulations with FLUKA determined a preferred experimental setup in the TARANIS target chamber to result in beams with narrow proton energy spread impinging on cell monolayer targets, whilst maintaining sufficient proton flux to deliver a relatively uniform dose of few Gy of dose in a single laser pulse. A RCF dosimetry technique was envisaged to provide dose measurement and energy verification using a special unlaminated version of GafChromic EBT2 film. The g_{Q,Q_0} correction factor for EBT2 was calculated as a function of proton energy, once the RE had been determined to be no different to that for EBT. This correction function could then be convolved with spectra calculated by FLUKA to be present in each cell area to derive final dose corrections for proton energy. This experiment was still ongoing at the time of writing.

7.5 Miscellaneous work

This section briefly summarises a few pieces of work which are not part of the main thesis but may be of interest to the reader.

7.5.1 Other LIBRA collaborative work

As part of LIBRA, the remit of the Birmingham group was to provide dosimetry expertise and support to the other groups. GafChromic film was already regularly used by LIBRA collaborators in laser-plasma experiments although previously the calculation of energy deposition was crude and a calibration curve published by ISP was the best information they had in determining dose. This calibration was not specific to the readout method and scanner being used by the laser groups, and was not specific to protons. Once a protocol to accurately measure D_w in the Birmingham proton beam was established, accurate calibration of GafChromic film with protons was possible. Other collaborating groups were then very keen for us to calibrate remnant pieces of film they had used in earlier experiments to improve upon their data analysis. The calibration method used followed that described in section 5.5.1 and this service was performed on three separate occasions with extremely positive feedback from the heads of the relevant groups with regards to the improvement this new calibration had once applied to their existing data.

The suitability of the Birmingham cyclotron as a calibration facility was further utilised by the group from RAL. They had designed and built a scintillator detector which used three different scintillators in a stack configuration. Each scintillator was different, and emitted a different wavelength of light so that their signals could be separately measured. As protons reached different depths and hence different scintillators, real time spatial energy information could be extracted for every laser shot. This technique was envisaged to replace the need for RCF stacks which would become cumbersome to replace for each shot and analyse later, especially when laser repetition rates would begin to reach the order of Hz. For the detector to produce a meaningful measurement however, calibration of light output versus proton energy was necessary and so the detector was brought to the Birmingham cyclotron for this purpose. Beams of 29, 15, 12 and 8.5 MeV were used to cover a wide energy range by using PMMA and PET shims to degrade the nominal energy to values in between. Calibration was required to energies of around 3 MeV with relatively narrow energy spreads, hence the use of lower energy beams than previously used in this work. The original FLUKA model and FLUBOUND was used to estimate the mean energy and spread at different depths for each nominal energy beam, which helped justify using FLUBOUND instead of the USRBDX card in FLUKA as in instances such as this it could provide spectral information at any depth required post-simulation without requiring a rerun, and was quicker to implement than writing many cards in the input file.

In addition to the cell irradiation experiment carried out using the TARANIS laser at QUB, a parallel cell experiment was conducted at Birmingham using the 29 MeV proton beam with a view to having comparative cell survival data with a lower dose rate source. FLUKA was used to determine the thickness of PMMA phantom required to obtain a similar mean energy and spread that was incident on one of the cell areas in the laser setup. Cell dishes were prepared by students from QUB and a piece of EBT2 was placed behind each dish to ascertain any relative dose differences between cell areas due to non-uniformity of the beam. The absolute doses were calculated by knowing the dose output per MU at the effective depth of the cell layer along the central beam axis using a Markus chamber. Unfortunately, after the incubation period following irradiation it appeared that the vast majority of the cultivated cells were contaminated and so no useful data was obtained from this particular experiment. The QUB team went away to review their cell handling technique and it was hoped this experiment would be successfully repeated at a later date.

7.5.2 FLUKA and CT data import

With the ever increasing affordability and capability of CPUs, the use of MC techniques in RT treatment planning systems (TPS) is finally becoming a reality (Spezi and Lewis, 2008). Medium sized computing clusters or grids can perform the more computationally intensive calculations associated with MC in reasonable timeframes and offer more detailed and accurate predictions of dose distributions. Faster MC algorithms even allow acceptable computational times on individual multi-core machines. FLUKA was briefly investigated for its potential to predict dose distributions in real patient geometry obtained from a computed tomography (CT) scan, which was more readily enabled due to FLUKA's voxel geometry input format and a prototype routine *writect.f*. This routine would read in a file consisting of a string of Hounsfield units (HU) and define a series of HU ranges so that each HU group would correspond to a unique tissue or organ and be associated with its own MATERIAL definition card in the FLUKA input file. Much work has been done by Schneider et al. (2000) to characterise many tissue types, compositions, mass densities and their typical HU so that this conversion from HU to material type and density is possible, to a certain degree of approximation.

A comparison of FLUKA-predicted patient dose distributions with a typical commercial TPS for proton therapy was performed by (Parodi et al., 2007a), and the ability of FLUKA to also predict the distribution of positron emitting isotopes in the patient was investigated. Positron emitters can be used as a means of dose validation by comparing the predicted distribution from FLUKA with patient PET scans immediately after a PT treatment Parodi et al. (2007b). It was envisaged that by recreating a similar CT geometry interface for FLUKA that further studies could be conducted to compare proton TPS performance in the presence of metallic implants versus FLUKA, and also the possible clinical impact of a new type of spinal implant made of polyether ether ketone (PEEK) which should exhibit better water equivalence. Unfortunately, due to time constraints only the CT interface was developed but this built the base on which further investigations could be made in the future. Figure 7.1 shows a sample of what was achieved: an anonymous dental CT set was obtained and a monoenergetic beam of 90 MeV was set up to enter the head at an arbitrary angle and location. This was only to test the function of the whole process, rather than to mimic an actual (or even sensible) plan.

7.5.3 Half-range modulator wheel for 29 MeV protons

An MSc project was proposed to design a half-range modulator wheel to produce a SOBP between depths of approximately 3.4 and 6.8 mm. A previously measured depth dose curve was used as the basis to determine the relative angular sizes of 0.2 mm stepped thickness sectors of a wheel made of PMMA. While the MSc student was repsonsible for determining the design, the calculations were independently carried out to verify the design before construction of the wheel (shown in figure 7.2) was commissioned. The student was also greatly assisted in carrying out depth ionisation measurements to test

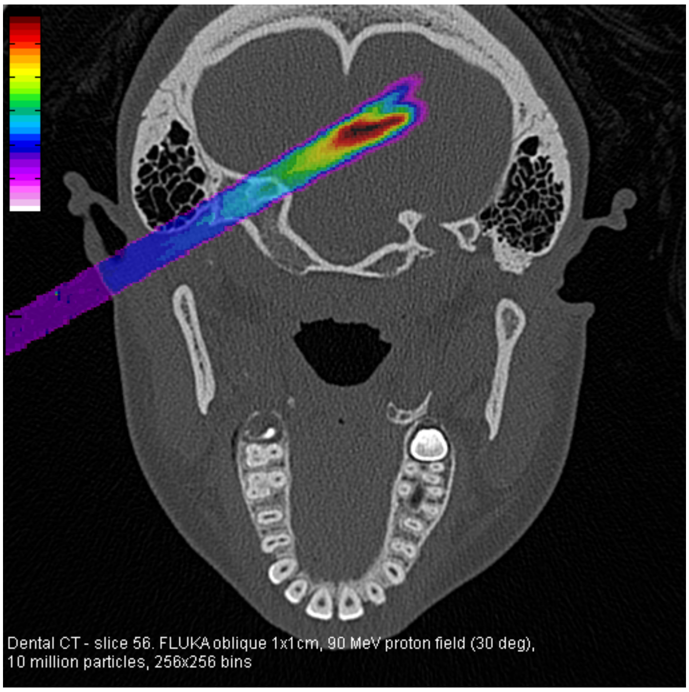

Figure 7.1: Dose distribution calculated by FLUKA in a dental CT voxel geometry, with a 1x1 cm field of 90 MeV protons entering obliquely into the brain.

the wheel's performance, and the data are shown in figure 7.3. The measurements were not converted to D_w as k_Q would be more difficult to determine due to the non-trivial spectrum at any depth, but in terms of ionisiation it can be seen that the SOBP was flat to within ±2% of the mean value which was the desired level of performance, and a very successful outcome.

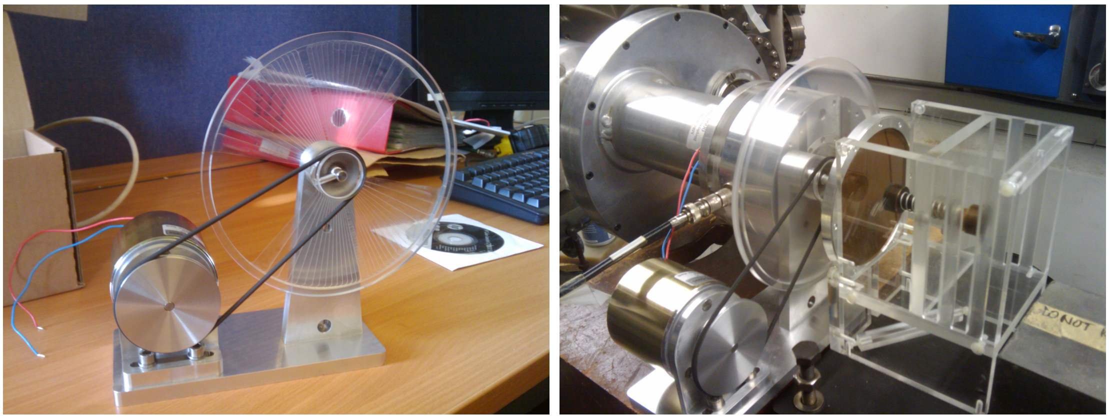

Figure 7.2: A half-range modulator wheel designed for the 29 MeV proton beam from the Birmingham cyclotron.

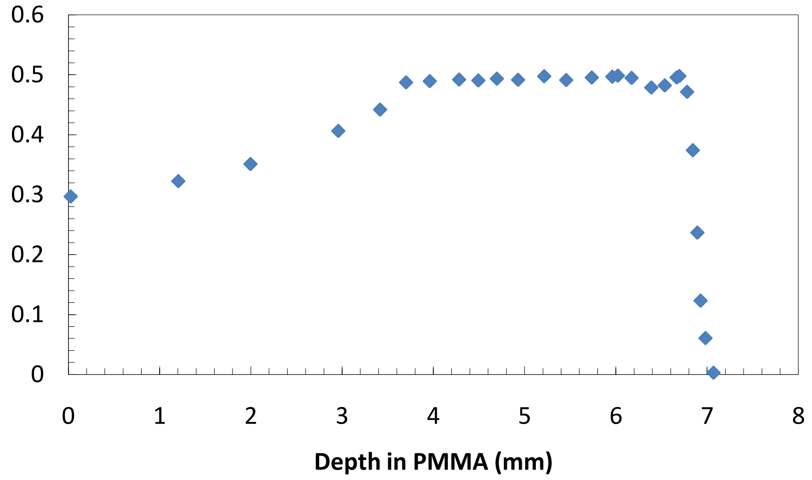

Figure 7.3: The depth ionisation curve measured with a Markus chamber in PMMA using a custom designed half-range modulator wheel.

7.6 Future work

There is a large amount of scope for work which could continue and build upon that undertaken in this thesis. Regarding the RE of GafChromic film, a theoretical model based on track theory to explain the observed response versus proton and α-particle energy and predict its response for other high LET particles has yet to be developed, to the author's best knowledge. With the increasing popularity of GafChromic film in RT dosimetry and the increasing number of IBT centres, this would be a natural and useful progression from the experimental work already undertaken.

The Birmingham cyclotron is enhancing its reputation in the UK as being a unique and highly accessible beamline for various ions of multi-MeV energy, and has recently been engaged in cell irradiation studies with collaborating institutions. Some further developments of the beamline could include: design of a scattering foil system to produce a more diffuse, lower dose rate beam more useful for radiobiology experiments; removal of a graphite aperture upstream of the exit port which limits the extent to which the beam could be scanned by the quadrupole magents across larger targets for instance in semiconductor radiation hardness experiments; and further dosimetry of different ion species which can in theory be accelerated given the right ion source and power supplies –

to date, N^{5+} can be accelerated to about 62 MeV but the range of these ions is insufficient and more highly charged ions could be produced in the near future to higher energies.

Under the LIBRA project, aside from the technological challenges there is some work to be done on how to translate this novel method of particle acceleration to commercial IBT systems. Work has already begun to examine the biological effect of highly pulsed laser-induced proton beams, and this must be continued with controlled cell irradiations from conventional sources with very similar energy profiles to ensure a like-with-like comparison. In addition, there remains the question of how a future laser-based ion gantry could be designed to incorporate shielding, energy selection and beam scanning components. The solutions will also depend on the physical accelerating regimes at higher laser intensities (such as RPA) required to achieve the necessary high energies for therapy, and how highly peaked these future energy spectra are.

The work done with FLUKA to import CT voxel structures for possible MC comparison of TPS plans and/or investigations concerning the performance of metal versus PEEK spinal implants is considered a project that has been started and requires the time and dedication of another student to take to a successful conclusion. It is unfortunate that time constraints and other work prevented this project from progressing any further, but the foundations are in place for this work to be continued.

LIST OF REFERENCES

AAPM. Protocol for Heavy Charged-Particle Therapy Beam Dosimetry. Technical report, New York, 1986.

M. Allen, Y. Sentoku, P. Audebert, A. Blazevic, T. Cowan, J. Fuchs, J. C. Gauthier, M. Geissel, M. Hegelich, S. Karsch, E. Morse, P. K. Patel, and M. Roth. Proton spectra from ultraintense laser–plasma interaction with thin foils: Experiments, theory, and simulation. *Physics of Plasmas*, 10(8):3283–3289, 2003.

P Andreo. Monte Carlo techniques in medical radiation physics. *Physics in Medicine and Biology*, 36(7):861, 1991.

J. C. Ashley, R. H. Ritchie, and Werner Brandt. Z_1^3 Effect in the Stopping Power of Matter for Charged Particles. *Phys. Rev. B*, 5(7):2393–2397, Apr 1972.

N. Bassler, J. W. Hansen, H. Palmans, M. H. Holzscheiter, S. Kovacevic, and A. A. Collaboration. The antiproton depth-dose curve measured with alanine detectors. *Nuclear Instruments & Methods in Physics Research Section B-Beam Interactions with Materials and Atoms*, 266(6):929–936, Mar 2008.

G. Battistoni, S. Muraro, P. R. Sala, F. Cerutti, A. Ferrari, S. Roesler, A. Fasso, and J. Ranft. The FLUKA code: Description and benchmarking. AIP Conference Proceeding 896.

F. Begay and D. W. Forslund. Acceleration of multi-species ions in CO_2 laser-produced plasmas: Experiments and theory. *Physics of Fluids*, 25(9):1675–1685, 1982.

M. J. Berger. *Monte Carlo calculation of the penetration and diffusion of fast charged particles*, volume 1 of *Methods in Computational Physics*. Academic Press, New York and London, 1963.

M. J. Berger, J. S. Coursey, M. A. Zucker, and J. Chang. ESTAR, PSTAR, and ASTAR: Computer Programs for Calculating Stopping-Power and Range Tables for Electrons, Protons, and Helium Ions (version 1.2.3). [Online] Available: http://physics.nist.gov/Star. (National Institute of Standards and Technology, Gaithersburg, MD.

H. A. Bethe. Molière's Theory of Multiple Scattering. *Phys. Rev.*, 89(6):1256–1266, Mar 1953.

H. Bischel and T. Hiraoka. Energy loss of 70 MeV protons in elements. *Nuclear Instruments and Methods in Physics Research Section B: Beam Interactions with Materials and Atoms*, 66(3):345 – 351, 1992.

J. W. Boag. Ionization chambers. *Radiation Dosimetry*, page vol 2 ed F H attix and W C Roesch (New York: Academic), 1966.

M. Boutillon. Volume recombination parameter in ionization chambers. *Phys Med Biol*, 43(8):2061–72, Aug 1998.

E. Breschi, M. Borghesi, D. H. Campbell, M. Galimberti, D. Giulietti, L. A. Gizzi, L. Romagnani, A. Schiavi, and O. Willi. Spectral and angular characterization of laser-produced proton beams from dosimetric measurements. *Laser and Particle Beams*, 22 (04):393–397, 2004a.

E. Breschi, M. Borghesi, M. Galimberti, D. Giulietti, L. A. Gizzi, and L. Romagnani. A new algorithm for spectral and spatial reconstruction of proton beams from dosimetric measurements. *Nuclear Instruments and Methods in Physics Research Section A: Accelerators, Spectrometers, Detectors and Associated Equipment*, 522(3):190–195, 2004b.

A. E. Buenfil, C. Ruiz-Trejo, I. Gamboa-deBuen, P. Avilés, O. Avila, C. Olvera, R. Robledo, M. Rodríguez-Ponce, H. Mercado-Uribe, M. Rodríguez-Villafuerte, and M. E. Brandan. Response of radiochromic dye films to low energy heavy charged particles. *Nuclear Instruments and Methods in Physics Research Section B: Beam Interactions with Materials and Atoms*, 197(3-4):317–322, 2002.

S. V. Bulanov, H. Daido, T. Z. Esirkepov, V. S. Khoroshkov, J. Koga, K. Nishihara, F. Pegoraro, T. Tajima, and M. Yamagiwa. Feasibility of Using Laser Ion Accelerators in Proton Therapy. In *THE PHYSICS OF IONIZED GASES: 22nd Summer School and International Symposium on the Physics of Ionized Gases; Invited Lectures, Topical Invited Lectures and Progress Reports*, volume 740, pages 414–429, Bajina Basta (Serbia and Montenegro), 2004. AIP.

D T Burns and M R McEwen. Ion recombination corrections for the NACP parallel-plate chamber in a pulsed electron beam. *Physics in Medicine and Biology*, 43(8):2033, 1998.

M. J. Butson, P. K. N. Yu, T. Cheung, and P. Metcalfe. Radiochromic film for medical radiation dosimetry. *Materials Science and Engineering: R: Reports*, 41(3-5):61–120, 2003.

G.J. Caporaso, T.R. Mackie, S. Sampayan, Y.-J. Chen, D. Blackfield, J. Harris, S. Hawkins, C. Holmes, S. Nelson, A. Paul, B. Poole, M. Rhodes, D. Sanders, J. Sullivan, L. Wang, J. Watson, P.J. Reckwerdt, R. Schmidt, D. Pearson, R.W. Flynn, D. Matthews, and J. Purdy. A compact linac for intensity modulated proton therapy based on a dielectric wall accelerator. *Physica Medica*, 24(2):98 – 101, 2008.

M. Cavinato, E. Fabrici, E. Gadioli, E. Gadioli Erba, and G. Riva. Monte Carlo calculations of heavy ion cross-sections based on the Boltzmann Master equation theory. *Nuclear Physics A*, 679(3-4):753 – 764, 2001.

K H Chadwick and H P Leenhouts. A molecular theory of cell survival. *Physics in Medicine and Biology*, 18(1):78, 1973.

W. T. Chu, B. A. Ludewigt, and T. R. Renner. Instrumentation for treatment of cancer using proton and light-ion beams. *Review of Scientific Instruments*, 64(8):2055–2122, 1993.

E. L. Clark, K. Krushelnick, M. Zepf, F. N. Beg, M. Tatarakis, A. Machacek, M. I. K. Santala, I. Watts, P. A. Norreys, and A. E. Dangor. Energetic Heavy-Ion and Proton Generation from Ultraintense Laser-Plasma Interactions with Solids. *Physical Review Letters*, 85(8):1654, 2000.

R. J. Clarke, P. T. Simpson, S. Kar, J. S. Green, C. Bellei, D. C. Carroll, B. Dromey, S. Kneip, K. Markey, P. McKenna, W. Murphy, S. Nagel, L. Willingale, and M. Zepf. Nuclear activation as a high dynamic range diagnostic of laser-plasma interactions. *Nuclear Instruments & Methods in Physics Research Section a-Accelerators Spectrometers Detectors and Associated Equipment*, 585(3):117–120, Feb 2008.

J. S. Cowan, K. A. Flippo, and S. A. Gaillard. Characterization of radiochromic film scanning techniques used in short-pulse-laser ion acceleration. 2008.

F. Crop, B. V. Rompaye, L. Paelinck, L. Vakaet, H. Thierens, and C. D. Wagter. On the calibration process of film dosimetry: OLS inverse regression versus WLS inverse prediction. *Phys Med Biol*, 53(14):3971–84, 2008.

I. Daftari, C. Castenadas, P. L. Petti, R. P. Singh, and L. J. Verhey. An application of GafChromic MD-55 film for 67.5 MeV clinical proton beam dosimetry. *Phys Med Biol*, 44(11):2735, 1999.

P.J. Darley, Charles M. W., Othman I. E., A. Sh. Al-Aydarous, and Mill A. J. Origins and dosimetry of 'hot particles' from nuclear plant operation. *Radiat Prot Dosimetry*, 92:131–37, 2000.

S. Devic, J. Seuntjens, E. Sham, E. B. Podgorsak, C. R. Schmidtlein, A. S. Kirov, and C. G. Soares. Precise radiochromic film dosimetry using a flat-bed document scanner. *Med Phys*, 32(7):2245–2253, 2005.

M. Dingfelder, D. Hantke, M. Inokuti, and H. G. Paretzke. Electron inelastic-scattering cross sections in liquid water. *Radiation Physics and Chemistry*, 53(1):1 – 18, 1999.

T. Dzelzainis, G. Nersisyan, D. Riley, L. Romagnani, H. Ahmed, A. Bigongiari, M. Borghesi, D. Doria, B. Dromey, M. Makita, S. White, S. Kar, D. Marlow, B. Ramakrishna, G. Sarri, M. Zaka-Ul-Islam, M. Zepf, and C.L.S. Lewis. The TARANIS laser: A multi-Terawatt system for laser-plasma investigations. *Laser and Particle Beams*, 28:451–461, 2010.

Rob Edgecock. Introduction to the Non-scaling Electron Model FFAG EMMA. *Nuclear Physics B - Proceedings Supplements*, 155(1):321 – 322, 2006. Proceedings to the 7th International Workshop on Neutrino Factories and Superbeams.

J. Fan, W. Luo, E. Fourkal, T. Lin, J. Li, I. Veltchev, and C.-M. Ma. Shielding design for a laser-accelerated proton therapy system. *Phys Med Biol*, (13):3913, 2007.

A. Fassò, J. Ferrari, A.and Ranft, and P.R.s Sala. FLUKA: Performances and applications in the intermediate energy range. In *Proc. 1st AEN/NEA Specialists' Meeting on Shielding Aspects of Accelerators, Targets and Irradiation Facilities (SATIF 1)*, pages 287–304, Arlington, Texas, 1995. OECD Documents.

A. Fassò, A. Ferrari, J. Ranft, and P.R. Sala. New developments in FLUKA modelling of hadronic and EM interactions. In H. Hiravama, editor, *Proc. 3rd Workshop on Simulatin Acceleration Radiation Environments (SARE 3)*, KEK Proceedings 97-5, page 32, KEK, Tsukuba, Japan, 1997.

A. Fassò, A. Ferrari, J. Ranft, P. R. Sala, G. Battistoni, F. Cerutti, T. Empl, M. V. Garzelli, M. Lantz, A. Mairani, V. Patera, S. Roesler, G. Smirnov, and V. Vlachoudis. 6th FLUKA Course, 2008.

A. Ferrari, P. R. Sala, A. Fasso, and J. Ranft. FLUKA: a multi-particle transport code. *CERN 2005-10, INFN/TC_05/11, SLAC-R-773*, 2005.

Emmanouil Fokas, Gerhard Kraft, Hanxiang An, and Rita Engenhart-Cabillic. Ion beam radiobiology and cancer: Time to update ourselves. *Biochimica et Biophysica Acta (BBA) - Reviews on Cancer*, 1796(2):216 – 229, 2009.

B. Gottschalk. Comments on 'Calculation of water equivalent thickness of materials of arbitrary density, elemental composition and thickness in proton beam irradiation'. *Phys Med Biol*, 55(9):L29, 2010.

S.A. Goudsmit and J.L. Saunderson. Multiple Scattering of Electrons. *Phys Rev*, 57: 24–29, 1940a.

S.A. Goudsmit and J.L. Saunderson. Multiple Scattering of Electrons. II. *Phys Rev*, 58: 36–42, 1940b.

B. Grosswendt and W. Y. Baek. W values and radial dose distributions for protons in TE-gas and air at energies up to 500 MeV. *Phys Med Biol*, (2):325, 1998.

Eric J. Hall. Radiation Dose-Rate: A Factor of Importance in Radiobiology and Radiotherapy. *Br J Radiol*, 45(530):81–97, 1972.

J. W. Hansen and K. J. Olsen. Theoretical and Experimental Radiation Effectiveness of the Free Radical Dosimeter Alanine to Irradiation with Heavy Charged Particles. *Radiation Research*, 104(1):15–27, 1985.

G. H. Hartmann, O. Jäkel, P. Heeg, C. P. Karger, and A. Krießbach. Determination of water absorbed dose in a carbon ion beam using thimble ionization chambers. *Physics in Medicine and Biology*, 44:1193–1206, May 1999.

S. P. Hatchett, C. G. Brown, T. E. Cowan, E. A. Henry, J. S. Johnson, M. H. Key, J. A. Koch, A. B. Langdon, B. F. Lasinski, R. W. Lee, A. J. Mackinnon, D. M. Pennington, M. D. Perry, T. W. Phillips, M. Roth, T. C. Sangster, M. S. Singh, R. A. Snavely,

M. A. Stoyer, S. C. Wilks, and K. Yasuike. Electron, photon, and ion beams from the relativistic interaction of Petawatt laser pulses with solid targets. In *The 41st annual meeting of the division of plasma physics of the american physical society*, volume 7, pages 2076–2082, Seattle, Washington (USA), 2000. AIP.

B. M. Hegelich, B. J. Albright, J. Cobble, K. Flippo, S. Letzring, M. Paffett, H. Ruhl, J. Schreiber, R. K. Schulze, and J. C. Fernández. Laser acceleration of quasi-monoenergetic MeV ion beams. *Nature*, 439(7075):441–444, 2006.

D. S. Hey, M. H. Key, A. J. Mackinnon, A. G. MacPhee, P. K. Patel, R. R. Freeman, L. D. Van Woerkom, and C. M. Castaneda. Use of GafChromic film to diagnose laser generated proton beams. *Review of Scientific Instruments*, 79(5):4, May 2008.

O. Hupe and J. Brunzendorf. A novel method of radiochromic film dosimetry using a color scanner. *Med Phys*, 33(11):4085–4094, 2006.

IAEA. The use of plane-parallel ionization chambers in high-energy electron and photon beams. An International Code of Practice for Dosimetry. Technical report, International Atomic Energy Agency, Vienna, 1997.

IAEA. Absorbed dose determination in external beam radiotherapy: an international code of practice for dosimetry based on standards of absorbed dose to water. Technical report, International Atomic Energy Agency, Vienna, 2000.

ICRU. Stopping powers and ranges for electrons and positrons. Technical Report 37, International Commission on Radiation Units and Measurements, Bethesda, MD, 1984.

ICRU. Stopping powers and ranges for protons and alpha particles. Technical Report 49, International Commission on Radiation Units and Measurements, Bethesda, MD, 1993.

ICRU. Clinical proton dosimetry, Part I: beam production, beam delivery and measurement of absorbed dose. Technical Report 60, International Commission on Radiation Units and Measurements, Bethesda, MD, 1999.

ISP. GafChromic® HD-810 radiochromic dosimetry film and D-200 pre-formatted dosimeters for high-energy photons: configuration, specifications and performance data, http://gafchromic.com, updated Sept 2001.

ISP. GafChromic® EBT self-developing film for radiotherapy dosimetry, http://www.gafchromic.com, updated Aug 2007.

ISP. http://gafchromic.com, accessed August 2008.

JAEA. http://wwwapr.kansai.jaea.go.jp/pmrc_en/org, accessed July 2010.

D. T. L. Jones. The w-value in air for proton therapy beams. *Radiation Physics and Chemistry*, 75(5):541–550, 2006.

D. Kirby, S. Green, H. Palmans, R. Hugtenburg, C. Wojnecki, and D. Parker. LET dependence of GafChromic films and an ion chamber in low-energy proton dosimetry. *Phys Med Biol*, 55(2):417–433, 2010.

D. Kirby, S. Green, F. Fiorini, D. Parker, L. Romagnani, D. Doria, S. Kar, C. Lewis, M. Borghesi, and H. Palmans. Radiochromic film spectroscopy of laser-accelerated proton beams using the FLUKA code and dosimetry traceable to primary standards. *Laser and Particle Beams*, 29(02):231–239, 2011.

Daniel Kirby. Dosimetry of 29 MeV protons using GafChromic film. Master's thesis, University of Birmingham, UK, 2007.

N. V. Klassen, L. van der Zwan, and J. Cygler. GafChromic MD-55: Investigated as a precision dosimeter. *Med Phys*, 24(12):1924–1934, 1997.

T. Kojima, H. Sunaga, H. Takizawa, H. Hanaya, and H. Tachibana. 3-45MeV/u ion beam dosimetry using thin film dosimeters. *Radiation Physics and Chemistry*, 68(6):975–980, 2003.

M Krämer, O Jäkel, T Haberer, G Kraft, D Schardt, and U Weber. Treatment planning for heavy-ion radiotherapy: physical beam model and dose optimization. *Phys Med Biol*, 45(11):3299, 2000.

Y. Kumazaki, T. Akagi, T. Yanou, D. Suga, Y. Hishikawa, and T. Teshima. Determination of the mean excitation energy of water from proton beam ranges. *Radiation Measurements*, 42(10):1683 – 1691, 2007.

David Lewis. Private communication, May 2010.

Z. Li, D. Wen, D. Chen, S. Peng, L. Zhang, and K. Shi. A study of dosimetry characteristics of GAF DM-1260 radiochromic films. *Rad. Phys. Chem.*, 57(2):103–113, 2000.

B. D. Lynch, J. Kozelka, M. K. Ranade, J. G. Li, W. E. Simon, and J. F. Dempsey. Important considerations for radiochromic film dosimetry with flatbed CCD scanners and EBT GAFCHROMIC film. *Med Phys*, 33(12):4551–6, Dec 2006.

Andreas Mack, Gunther Mack, Dirk Weltz, Stefan G. Scheib, Heinz D. Bottcher, and Volker Seifert. High precision film dosimetry with GAFCHROMIC® films for quality assurance especially when using small fields. *Medical Physics*, 30(9):2399–2409, 2003.

T Mackie, G Caporaso, S Sampayan, Y Chen, D Blackfield, J Harris, S Hawkins, C Holmes, S Nelson, A Paul, B Poole, M Rhodes, D Sanders, J Sullivan, L Wang, J Watson, P Reckwerdt, R Schmidt, D Pearson, R Flynn, D Matthews, and J Purdy. TH-C-AUD-09: A Proposal for a Novel Compact Intensity Modulated Proton Therapy System Using a Dielectric Wall Accelerator. *Medical Physics*, 34(6):2628, 2007.

M. Martišíková and O. Jäkel. Dosimetric properties of Gafchromic® EBT films in monoenergetic medical ion beams. *Phys Med Biol*, 55(13):3741, 2010a.

M. Martišíková and O. Jäkel. Study of Gafchromic® EBT film response over a large dose range. *Phys Med Biol*, 55(10):N281, 2010b.

M. Martišíková and O. Jäkel. Gafchromic® EBT films for ion dosimetry. *Radiation Measurements*, In Press, Corrected Proof:–, 2010c.

G Massillon-JL and L Zúñiga-Meneses. The response of the new MD-V2-55 radiochromic film exposed to ^{60}Co gamma rays. *Physics in Medicine and Biology*, 55(18):5437, 2010.

W. L. McLaughlin, M. Al-Sheikhly, D. F. Lewis, A. Kovács, and L. Wojnárovits. *Radiochromic Solid-State Polymerization Reaction*, chapter 12, pages 152–166. 1996.

J. Medin and P. Andreo. Monte Carlo calculated stopping-power ratios, water/air, for clinical proton dosimetry (50 - 250 MeV). *Phys Med Biol*, 42(1):89–105, 1997.

Joakim Medin and Pedro Andreo. Stopping powers for the ion-chamber dosimetry of radiotherapeutic heavy-particle beams. *Nuclear Instruments and Methods in Physics Research Section B: Beam Interactions with Materials and Atoms*, 69(1):64 – 75, 1992.

V. G. Molière. Theorie der Streuung schneller geladener Teilchen, I. Einzelstreuung am abgeshirmten Coulomb-Field. *Z. Naturforschg.*, 2a:133–145, 1947.

D. Nichiporov, V. Kostjuchenko, J. M. Puhl, D. L. Bensen, M. F. Desrosiers, C. E. Dick, W. L. Mclaughlin, T. Kojima, B. M. Coursey, and S. Zink. Investigation of applicability of alanine and radiochromic detectors to dosimetry of proton clinical beams. *Applied Radiation and Isotopes*, 46(12):1355 – 1362, 1995.

A. Niroomand-Rad, C. R. Blackwell, B. M. Coursey, K. P. Gall, J. M. Galvin, W. L. McLaughlin, A. S. Meigooni, R. Nath, J. E. Rodgers, and C. G. Soares. Radiochromic film dosimetry: Recommendations of AAPM Radiation Therapy Committee Task Group 55. *Med Phys*, 25(11):2093–2115, 1998.

F. Nurnberg, M. Schollmeier, E. Brambrink, A. Blazevic, D. C. Carroll, K. Flippo, D. C. Gautier, M. Geissel, K. Harres, B. M. Hegelich, O. Lundh, K. Markey, P. McKenna, D. Neely, J. Schreiber, and M. Roth. Radiochromic film imaging spectroscopy of laser-accelerated proton beams. *Review of Scientific Instruments*, 80(3):033301–13, 2009.

L. Paelinck, W. D. Neve, and C. D. Wagter. Precautions and strategies in using a commercial flatbed scanner for radiochromic film dosimetry. *Phys Med Biol*, 52(1):231–42, 2007.

H. Paganetti. Nuclear interactions in proton therapy: dose and relative biological effect distributions originating from primary and secondary particles. *Phys Med Biol*, 47(5): 747, 2002.

H. Palmans, R. Thomas, and A. Kacperek. Ion recombination correction in the Clatterbridge Centre of Oncology clinical proton beam. *Phys Med Biol*, 51(4):903–17, Feb 21 2006a.

H. Palmans, R. Thomas, D. Shipley, and A. Kacperek. Light-ion beam dosimetry. Technical report, (National Physical Laboratory report DQL-RD 003), 2006b.

Hugo Palmans, Russell Thomas, Mary Simon, Simon Duane, Andrzej Kacperek, Alan DuSautoy, and Frank Verhaegen. A small-body portable graphite calorimeter for dosimetry in low-energy clinical proton beams. *Physics in Medicine and Biology*, 49 (16):3737, 2004.

K. Parodi and S. Squarcia. Improvement of low-energy stopping power algorithms in the FLUKA simulation program. *Nuclear Instruments and Methods in Physics Research Section A: Accelerators, Spectrometers, Detectors and Associated Equipment*, 456(3): 352–368, 2001.

K. Parodi, A. Ferrari, F. Sommerer, and H. Paganetti. Clinical CT-based calculations of dose and positron emitter distributions in proton therapy using the FLUKA Monte Carlo code. *Phys Med Biol*, 52(12):3369–3387, 2007a.

K. Parodi, H. Paganetti, E. Cascio, J. B. Flanz, A. A. Bonab, N. M. Alpert, K. Lohmann, and T. Bortfeld. PET/CT imaging for treatment verification after proton therapy: A study with plastic phantoms and metallic implants. *Med Phys*, 34(2):419–435, 2007b.

R. Paschotta. Encyclopedia of Laser Physics and Technology. accessed July 2010.

D. Pelowitz. MCNPX User's Manual. *LANL Report*, pages LA–CP–05–369 (Los Alamos, NM: Los Alamos National Laboratory), 2005.

A. Piermattei, R. Miceli, L. Azario, A. Fidanzio, S. d. Canne, C. De Angelis, S. Onori, M. Pacilio, E. Petetti, L. Raffaele, and M. G. Sabini. Radiochromic film dosimetry of a low energy proton beam. *Med Phys*, 27(7):1655–1660, 2000.

I.V. Pogorelsky, M. Babzien, M. N. Polyanskiy, V. Yakimenko, N. P. Dover, C. A. J. Palmer, Z. Najmudin, J. Schreiber, M. Ispiryan, P. Shkolnikov, and G. Dudnikova. Laser energy conversion to solitons and monoenergetic protons in near-critical hydrogen plasma. Proceedings of IPAC'10, Kyoto, Japan, 2010.

PTCOG. Patient statistics, http://ptcog.web.psi.ch, accessed March 2010.

L Richley, A C John, H Coomber, and S Fletcher. Evaluation and optimization of the new EBT2 radiochromic film dosimetry system for patient dose verification in radiotherapy. *Phys Med Biol*, 55(9):2601, 2010.

C. Richter, J. Pawelke, L. Karsch, and J. Woithe. Energy dependence of EBT-1 radiochromic film response for photon (10 kVp–15 MVp) and electron beams (6–18 MeV) readout by a flatbed scanner. *Med Phys*, 36(12):5506–5514, 2009.

A. Rink. *PhD thesis: Point-based ionizing radiation dosimetry using radichromic materials and a fibreoptic readout system.* PhD thesis, University of Toronto, Canada, 2008.

A. Rink, I. A. Vitkin, and D. A. Jaffray. Characterization and real-time optical measurements of the ionizing radiation dose response for a new radiochromic medium. *Med Phys*, 32(8):2510–2516, 2005.

A. Rink, I. A. Vitkin, and D. A. Jaffray. Intra-irradiation changes in the signal of polymer-based dosimeter (GAFCHROMIC EBT) due to dose rate variations. *Phys. Med. Biol*, (22):N523, 2007a.

A. Rink, I. A. Vitkin, and D. A. Jaffray. Energy dependence (75 kVp to 18 MV) of radiochromic films assessed using a real-time optical dosimeter. *Med Phys*, 34(2):458–463, 2007b.

A. Rink, D. F. Lewis, S. Varma, I. A. Vitkin, and D. A. Jaffray. Temperature and hydration effects on absorbance spectra and radiation sensitivity of a radiochromic medium. *Med Phys*, 35(10):4545–4555, Oct 2008. ISI Document Delivery No.: 353TT Times Cited: 0 Cited Reference Count: 32 Rink, Alexandra Lewis, David F. Varma, Sangya Vitkin, I. Alex Jaffray, David A. AMER ASSOC PHYSICISTS MEDICINE AMER INST PHYSICS.

A. P. L. Robinson, M. Zepf, S. Kar, R. G. Evans, and C. Bellei. Radiation pressure acceleration of thin foils with circularly polarized laser pulses. *New Journal of Physics*, (1):013021, 2008.

L. Robson, P. T. Simpson, R. J. Clarke, K. W. D. Ledingham, F. Lindau, O. Lundh, T. McCanny, P. Mora, D. Neely, C. G. Wahlstrom, M. Zepf, and P. McKenna. Scaling of proton acceleration driven by petawatt-laser-plasma interactions. *Nat Phys*, 3(1): 58–62, 2007.

D. W. Rogers. The advantages of absorbed-dose calibration factors. *Med Phys*, 19(5): 1227–39, Sep-Oct 1992.

S. Saur and J. Frengen. GafChromic EBT film dosimetry with flatbed CCD scanner: A novel background correction method and full dose uncertainty analysis. *Med Phys*, 35 (7):3094–3101, 2008.

S. Schell and J. J. Wilkens. Modifying proton fluence spectra to generate spread-out Bragg peaks with laser accelerated proton beams. *Phys Med Biol*, 54(19):N459–N466, 2009.

W. Schneider, T. Bortfeld, and W. Schlegel. Correlation between CT numbers and tissue parameters needed for Monte Carlo simulations of clinical dose distributions. *Phys Med Biol*, 45(2):459–478, 2000.

M. Schollmeier, K. Harres, F. Nurnberg, A. Blazevic, P. Audebert, E. Brambrink, J. C. Fernandez, K. A. Flippo, D. C. Gautier, M. Geissel, B. M. Hegelich, J. Schreiber, and M. Roth. Laser beam-profile impression and target thickness impact on laser-accelerated protons. *Physics of Plasmas*, 15(5):12, May 2008.

M. Soukup, M. Fippel, and F. Nuesslin. 133 The importance of nuclear interactions for dose calculations in proton therapy. *Radiotherapy and Oncology*, 68(Supplement 1): S52 – S52, 2003. 7th Biennial Estro Meeting on Physics and Radiation Technology for Clinical Radiotherapy.

L. V. Spencer and F. H. Attix. A theory of cavity ionization. *Radiation Research*, 3: 239–254, 1955.

Emiliano Spezi and Geraint Lewis. An overview of Monte Carlo treatment planning for radiotherapy. *Radiation Protection Dosimetry*, 131(1):123–129, 2008.

G. Gordon Steel, Julian D. Down, John H. Peacock, and Trevor C. Stephens. Dose-rate effects and the repair of radiation damage. *Radiotherapy and Oncology*, 5(4):321 – 331, 1986.

R. M. Sternheimer. The Density Effect for the Ionization Loss in Various Materials. *Phys. Rev.*, 88(4):851–859, Nov 1952.

Still River Systems. The Monarch250$^{\text{TM}}$ PBRT System, http://www.stillriversystems.com, accessed March 2011.

S. Ter-Avetisyan, M. Schnrer, R. Polster, P.V. Nickles, and W. Sandner. First demonstration of collimation and monochromatisation of a laser accelerated proton burst. *Laser and Particle Beams*, 26(04):637–642, 2008.

S. M. Vatnitsky. Radiochromic film dosimetry for clinical proton beams. *Appl. Radiat. Isot.*, 48(5):643–51, 1997.

S. M. Vatnitsky, R. W. Schulte, R. Galindo, H. J. Meinass, and D. W. Miller. Radiochromic film dosimetry for verification of dose distributions delivered with proton-beam radiosurgery. *Phys Med Biol*, 42(10):1887–98, 1997.

S. M. Vatnitsky, D. W. Miller, M. F. Moyers, R. P. Levy, R. W. Schulte, J. D. Slater, and J. M. Slater. Dosimetry techniques for narrow proton beam radiosurgery. *Phys Med Biol*, 44(11):2789–801, 1999.

P. V. Vavilov. Ionization losses of high-energy heavy particles. *Soviet Physics Jetp-Ussr*, 5(4):749–751, 1957.

L. S. Waters, G. W. McKinney, J. W. Durkee, M. L. Fensin, J. S. Hendricks, M. R. James, R. C. Johns, and D. B. Pelowitz. The MCNPX Monte Carlo radiation transport code. In *Hadronic Shower Simulation Workshop, Batavia, IL, SEP 06-08, 2006*, volume 896 of *AIP Conference Proceedings*, pages 81–90, 2007.

J Weichsel, T Fuchs, E Lefebvre, E d'Humières, and U Oelfke. Spectral features of laser-accelerated protons for radiotherapy applications. *Phys. Med. Biol.*, 53(16):4383, 2008.

W. K. Weyrather. Carbon ion radiobiology, http://www.gsi.de/forschung/bio/KWeyrather_PTCoGSat.pdf (accessed 30/8/10).

S. C. Wilks, A. B. Langdon, T. E. Cowan, M. Roth, M. Singh, S. Hatchett, M. H. Key, D. Pennington, A. MacKinnon, and R. A. Snavely. Energetic proton generation in ultra-intense laser–solid interactions. *Physics of Plasmas*, 8(2):542–549, 2001.

J. M. Yang, P. McKenna, K. W. D. Ledingham, T. McCanny, S. Shimizu, L. Robson, R. J. Clarke, D. Neely, P. A. Norreys, M. S. Wei, K. Krushelnick, P. Nilson, S. P. D. Mangles, and R. P. Singhal. Nuclear reactions in copper induced by protons from a petawatt laser-foil interaction. *Applied Physics Letters*, 84(5):675–677, 2004.

A. Yogo, K. Sato, M. Nishikino, M. Mori, T. Teshima, H. Numasaki, M. Murakami, Y. Demizu, S. Akagi, S. Nagayama, K. Ogura, A. Sagisaka, S. Orimo, M. Nishiuchi, A. S. Pirozhkov, M. Ikegami, M. Tampo, H. Sakaki, M. Suzuki, I. Daito, Y. Oishi,

H. Sugiyama, H. Kiriyama, H. Okada, S. Kanazawa, S. Kondo, T. Shimomura, Y. Nakai, M. Tanoue, H. Sasao, D. Wakai, T. Kawachi, H. Nishimura, P. R. Bolton, and H. Daido. Radiobiological study by using laser-driven proton beams. In *LASER-DRIVEN RELATIVISTIC PLASMAS APPLIED TO SCIENCE, INDUSTRY AND MEDICINE: 2nd International Symposium*, volume 1153, pages 438–447, Kyoto (Japan), 2009. AIP.

Y. Zhu, A. S. Kirov, V. Mishra, A. S. Meigooni, and J. F. Williamson. Quantitative evaluation of radiochromic film response for two-dimensional dosimetry. *Med Phys*, 24 (2):223–231, 1997.

J. F. Ziegler. SRIM-2003. *Nuclear Instruments and Methods in Physics Research Section B: Beam Interactions with Materials and Atoms*, 219-220:1027–1036, 2004. doi: DOI: 10.1016/j.nimb.2004.01.208.

James F. Ziegler, M. D. Ziegler, and J. P. Biersack. SRIM - The stopping and range of ions in matter (2010). *Nuc. Inst. Methods. Phys. Res. B.*, 268(11-12):1818–1823, JUN 2010. 19th International Conference on Ion Beam Analysis, Cambridge, ENGLAND, SEP 07-11, 2009.

APPENDIX A

FULL GAFCHROMIC FILM COMPOSITION DATA

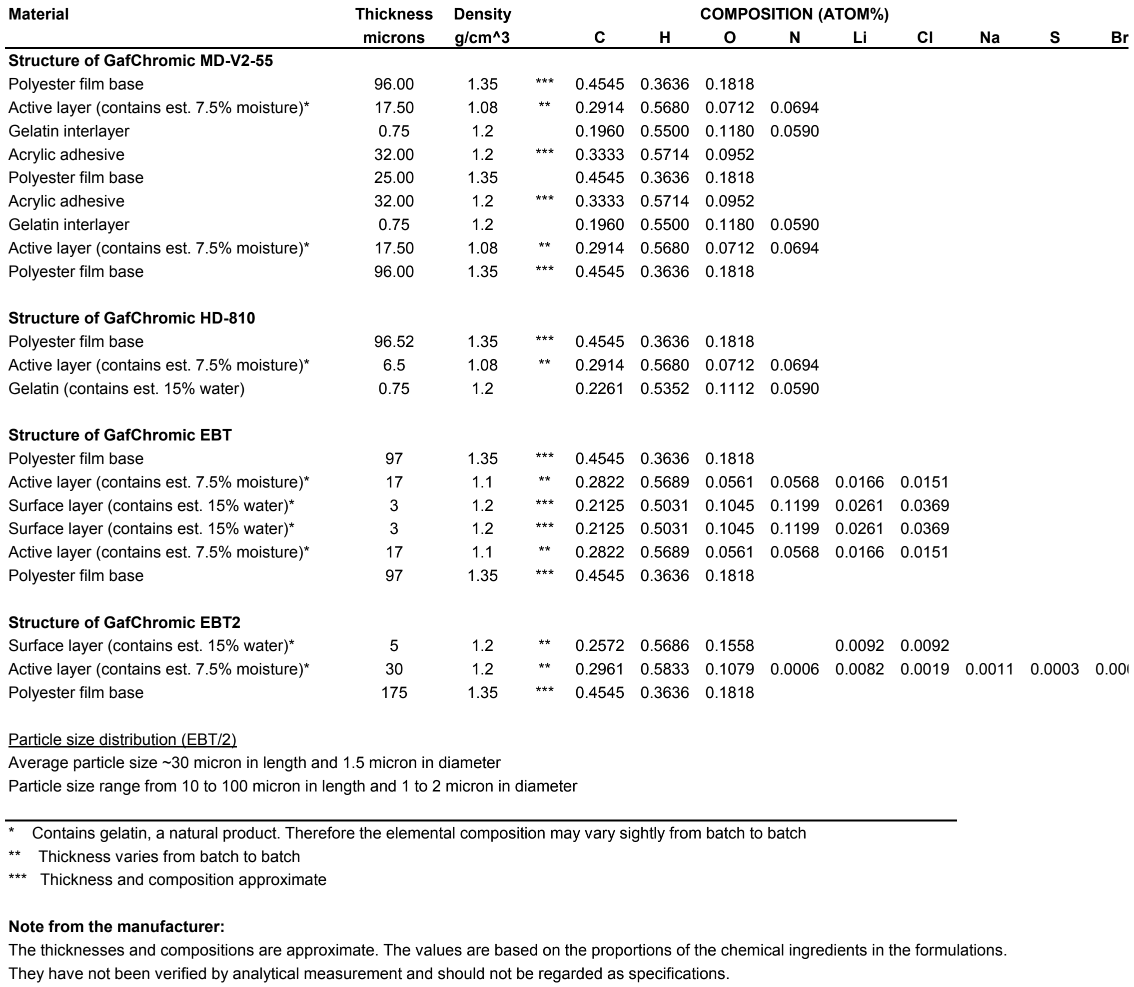

Material	Thickness	Density		COMPOSITION (ATOM%)								
	microns	g/cm^3		C	H	O	N	Li	Cl	Na	S	Br
Structure of GafChromic MD-V2-55												
Polyester film base	96.00	1.35	***	0.4545	0.3636	0.1818						
Active layer (contains est. 7.5% moisture)*	17.50	1.08	**	0.2914	0.5680	0.0712	0.0694					
Gelatin interlayer	0.75	1.2		0.1960	0.5500	0.1180	0.0590					
Acrylic adhesive	32.00	1.2	***	0.3333	0.5714	0.0952						
Polyester film base	25.00	1.35		0.4545	0.3636	0.1818						
Acrylic adhesive	32.00	1.2	***	0.3333	0.5714	0.0952						
Gelatin interlayer	0.75	1.2		0.1960	0.5500	0.1180	0.0590					
Active layer (contains est. 7.5% moisture)*	17.50	1.08	**	0.2914	0.5680	0.0712	0.0694					
Polyester film base	96.00	1.35	***	0.4545	0.3636	0.1818						
Structure of GafChromic HD-810												
Polyester film base	96.52	1.35	***	0.4545	0.3636	0.1818						
Active layer (contains est. 7.5% moisture)*	6.5	1.08	**	0.2914	0.5680	0.0712	0.0694					
Gelatin (contains est. 15% water)	0.75	1.2		0.2261	0.5352	0.1112	0.0590					
Structure of GafChromic EBT												
Polyester film base	97	1.35	***	0.4545	0.3636	0.1818						
Active layer (contains est. 7.5% moisture)*	17	1.1	**	0.2822	0.5689	0.0561	0.0568	0.0166	0.0151			
Surface layer (contains est. 15% water)*	3	1.2	***	0.2125	0.5031	0.1045	0.1199	0.0261	0.0369			
Surface layer (contains est. 15% water)*	3	1.2	***	0.2125	0.5031	0.1045	0.1199	0.0261	0.0369			
Active layer (contains est. 7.5% moisture)*	17	1.1	**	0.2822	0.5689	0.0561	0.0568	0.0166	0.0151			
Polyester film base	97	1.35	***	0.4545	0.3636	0.1818						
Structure of GafChromic EBT2												
Surface layer (contains est. 15% water)*	5	1.2	**	0.2572	0.5686	0.1558		0.0092	0.0092			
Active layer (contains est. 7.5% moisture)*	30	1.2	**	0.2961	0.5833	0.1079	0.0006	0.0082	0.0019	0.0011	0.0003	0.00
Polyester film base	175	1.35	***	0.4545	0.3636	0.1818						

Particle size distribution (EBT/2)
Average particle size ~30 micron in length and 1.5 micron in diameter
Particle size range from 10 to 100 micron in length and 1 to 2 micron in diameter

* Contains gelatin, a natural product. Therefore the elemental composition may vary sightly from batch to batch
** Thickness varies from batch to batch
*** Thickness and composition approximate

Note from the manufacturer:
The thicknesses and compositions are approximate. The values are based on the proportions of the chemical ingredients in the formulations.
They have not been verified by analytical measurement and should not be regarded as specifications.

Figure A.1: Composition data for all GafChromic films used in this thesis. This table was compiled from separate spreadsheets supplied by ISP, who insist they are accurate only for the most recently available version at the time of issue.

APPENDIX B

FORTRAN CODE

B.1 FLUBOUND program

```
C     KQDBL (batch) Version 2.32 (Finds Emax and sigma E)

      PROGRAM FLUBOUND

***** VARIABLES

      IMPLICIT DOUBLE PRECISION (A-H,O-Z)

      INTEGER i,k,n,m,ierg,iocatch,iprotons,zinp,itrax
      INTEGER ichar,inodes,icycles,inps,ksamples,noflag,Eflag
      CHARACTER*1 node1,cyc
      CHARACTER*2 node2
      CHARACTER*15 fluinp
      CHARACTER*4 zid
      CHARACTER*9 suffix
      CHARACTER*70 dummy
      DOUBLE PRECISION Eper(263),Sper(263),Eair(263),Sair(263)
      DOUBLE PRECISION FLUSPEC(263,100),KQ(263),FLUERR(263),FLUAVE(263)
      DOUBLE PRECISION KQERR,KQAVE,Kconst,TOTKQ(100)
      DOUBLE PRECISION FLUMAX,FHWM1,FWHM2,FLUSIG,EMAX

      PARAMETER ( ZERZER = 0.D+00 )
      PARAMETER ( ONEONE = 1.D+00 )
      PARAMETER ( TWOTWO = 2.D+00 )
      PARAMETER ( pi = 3.14159265D+0 )

      iprotons=0
      itrax=0
      suffix='_TRCKDUMP'
      erg0=ZERZER
      FLUMAX=ZERZER


C     NEED TO READ IN REQUIRED DEPTH HERE
C     ***********************************

      print *,'Cavity depth in microns:'
      read *,zinp
      write(zid,'(I4)') zinp

      zcav0=DBLE(zinp)/1.D+4

C     NUMBER OF RANDOM ENERGY VALUES CREATED
C     **************************************
      ksamples=1000

      rcav=0.265D+0

      DATA FLUSPEC/26300*0.D+0/,KQ/263*0.D+0/,FLUAVE/263*0.D+0/
      DATA FLUERR/263*0.D+0/TOTKQ/100*0.D+0/
      TOTFLU=ZERZER
      KQAVE=ZERZER
      KQERR=ZERZER


      Kconst=0.8817D+0

***** MAIN PROGRAM

C     OPENS AND READS STOPPING POWER FILES
C     ***********************************

      open(10, file='/bb/phy/djk191/jobs2008/water.msp', status='old',
     &         form='formatted')
      open(11, file='/bb/phy/djk191/jobs2008/air.msp', status='old',
     &         form='formatted')
      open(12, file='flu'//zid//'.out', status='new', form='formatted')
      open(13, file='kqdbl.csv', status='old', form='formatted')
      do i=1,2
         read(10,*) dummy
         read(11,*) dummy
      enddo

      do i=1,263
         read(10,50) Eper(i),Sper(i)
         read(11,50) Eair(i),Sair(i)
         KQ(i)=Kconst*Sper(i)/Sair(i)
      enddo



C     PROCESSES _TRCKDUMP FILE AND CALCULATES KQ VALUES
C     ***********************************************

      open(9, file='.fluka', status='old', form='formatted')
      read(9,*) fluinp,inodes,icycles,inps
      close(9)
      print *,inodes,icycles


      DO 100 m=1,icycles

      write(cyc,'(I1)') m

      DO 200 n=1,inodes

      IF (n .GE. 10) THEN
          write(node2,'(I2)') n
          open(20, file='run'//node2//'00'//cyc//suffix,
     & status='old', form='formatted')
```

```
      print *,'Processing run',node2,'00',cyc

      ELSE
           write(node1,'(I1)') n
           open(20, file='run'//node1//'00'//cyc//suffix,
     & status='old', form='formatted')
      print *,'Processing run',node1,'00',cyc
      ENDIF

      iocatch=0

C     READS IN _TRCKDUMP FILE
C     ***********************

      DO WHILE (iocatch .EQ. 0)
       read(20,51,IOSTAT=iocatch) x1,y1,z1,erg1

      erg1=erg1*1.D+3

      IF (erg1 .GT. erg0) THEN

           iprotons=iprotons+1
           GOTO 999
      ENDIF

      ztrack=z1-z0
      xtrack=x1-x0
      ytrack=y1-y0

C     *****************************************************
C     CHECKS IF TRACK CROSSES CAVITY FACE & CREATES SPECTRUM
C     *****************************************************


      IF (z1 .GT. zcav0 .AND. z0 .LT. zcav0) THEN

           delz=(zcav0-z0)/ztrack
           delx=xtrack*delz
           dely=ytrack*delz

           IF ((x0+delx)**2.+(y0+dely)**2. .LE. rcav**2.) THEN
              itrax=itrax+1
             DO k=1,ksamples
                rnderg=erg0+(erg1-erg0)*rand()
                i=ierg(rnderg,Eper)
                FLUSPEC(i,n)=FLUSPEC(i,n)+ONEONE
             ENDDO
           ENDIF
      ENDIF


 999  CONTINUE
           erg0=erg1
           x0=x1
           y0=y1
           z0=z1


      ENDDO
      close(20)

 200  CONTINUE

 100  CONTINUE
      print *,'Number of tracks entering cavity ', itrax
      print *,'Number of histories in file ', iprotons

      DO i=1,263
        DO n=1,inodes
          FLUAVE(i)=FLUAVE(i)+FLUSPEC(i,n)
          TOTKQ(n)=TOTKQ(n)+FLUSPEC(i,n)*KQ(i)
        ENDDO

        FLUAVE(i)=FLUAVE(i)/DBLE(inodes)

        TOTFLU=TOTFLU+FLUAVE(i)

        DO n=1,inodes
          FLUERR(i)=FLUERR(i)+(FLUSPEC(i,n)-FLUAVE(i))**2.0
        ENDDO

        FLUERR(i)=SQRT(FLUERR(i))/DBLE(inodes-1)
        TOTERR=TOTERR+FLUERR(i)
      ENDDO


      TOTERR=TOTERR/TOTFLU

      DO n=1,inodes
         TOTKQ(n)=TOTKQ(n)/TOTFLU
          print *,n,TOTKQ(n)
         KQAVE=KQAVE+TOTKQ(n)
      ENDDO

      KQAVE=KQAVE/DBLE(inodes)
          print *,'Average kQ: ',KQAVE

      DO n=1,inodes
         KQERR=KQERR+(TOTKQ(n)-KQAVE)**2.0
      ENDDO

      KQERR=SQRT(KQERR)/DBLE(inodes-1)
      print *,'St. Dev: ',KQERR
```

```
         write(12,53) 'kQ: ',KQAVE,' err: ',KQERR/KQAVE*1.D+2,'%'
         write(12,*) 'E /MeV      dN/dE       Error       kQ(E)'
      DO i=2,262
         FLUAVE(i)=FLUAVE(i)/(DBLE(ksamples)*itrax)
         write(12,52) Eper(i),2.D+0*FLUAVE(i)/(Eper(i+1)-Eper(i-1)),
     &                    FLUERR(i)/(DBLE(ksamples)*itrax),KQ(i)

         IF (2.D+0*FLUAVE(i)/(Eper(i+1)-Eper(i-1)) .GT. FLUMAX) THEN
            FLUMAX= 2.D+0*FLUAVE(i)/(Eper(i+1)-Eper(i-1))
            EMAX=Eper(i)
         ENDIF

      ENDDO

      print *,'Emax = ',EMAX
      Eflag=0


C     ********************************************
C     CALCULATES SIGMA ENERGY SPREAD BASED ON FWHM
C     ********************************************

      DO i=2,262
        IF (2.D+0*FLUAVE(i)/(Eper(i+1)-Eper(i-1)) .GE. FLUMAX/TWOTWO
     &       .AND. Eflag .LT. 1) THEN
             FWHM1=Eper(i)
             print *,'FWHM1 = ',FWHM1
             Eflag=1
        ENDIF
        IF (2.D+0*FLUAVE(i)/(Eper(i+1)-Eper(i-1)) .LE. FLUMAX/TWOTWO
     &       .AND. 2.D+0*FLUAVE(i)/(Eper(i+1)-Eper(i-1)) .GT. ZERZER
     &       .AND. i .GT. ierg(EMAX,Eper)
     &       .AND. Eflag .GT. 0) THEN
             FWHM2=Eper(i)
             print *,'FWHM2 = ',FWHM2
             Eflag=0
        ENDIF
      ENDDO

      FLUSIG=(FWHM2-FWHM1)/2.355D+0

      print *,'flu.out created'
      close(12)

      iocatch=0
      DO WHILE (iocatch .EQ. 0)
       read(13,*,IOSTAT=iocatch) dummy
      ENDDO

      write(13,54) zcav0,KQAVE,KQERR,EMAX,FLUSIG
      close(13)

 50   format(2(d9.4,1x))   ! Read stopping powers
 51   format(2(1x,d11.5),1x,d13.7,1x,d9.4)   ! Read TRCKDUMP
 52   format(4(1x,d10.5))   ! Write flu output
 53   format(a4,1x,d10.5,a6,d9.4,a1)    ! Write kq
 54   format(5(1x,d9.4))   ! Write to kqdbl.csv

      END



      FUNCTION ierg(erg,Elist)

C ***** Finds energy bin closest to proton energy

      DOUBLE PRECISION Ediff,erg,Elist(263)
      INTEGER ierg

          ierg=0
          Ediff=1.D+2
          DO WHILE (ABS(erg-Elist(ierg+1)) .LT. Ediff)
            Ediff=erg-Elist(ierg+1)
            ierg=ierg+1
          ENDDO
      RETURN
      END
```

B.2 RCF spectrum solver

```
      PROGRAM SHOTSOLVER
      implicit none

C *** DECLARE ARRAYS
      double precision fluX(535)
      double precision fluD(30,535)
      double precision fluDerr(30,535)
      double precision fluDtot(535)
      double precision fluDtot1(535)
      double precision fluDtot2(535)
      double precision initfilmX(12)
      double precision initfilmD(12)
      double precision filmDerr(12)
      double precision filmX(50)
      double precision filmD(50)
      double precision residual(50)
      double precision residual1(50)
      double precision residual2(50)
      double precision range(30)
      double precision bpmax(30)
      double precision spec(1000,30)
      double precision meanspec(30)
      double precision transpec(30)
      double precision sdspec(30)
      double precision sdtranspec(30)
      double precision splout(12)
      double precision M(30,30)

      double precision meanfilmD(12)

C *** DECLARE VARIABLES
      double precision temp,dmax,xBP,f,sumres,fluDtotd,lastsumres
      double precision tolerance,Eplus,Eminus,specstep,fluDtotd1,fluDtotd2
      double precision sumres1,sumres2,stconst,Dp,Dpp,null,rnd,dummy
      double precision sumspec,sumsqspec,ijprod,sumerr
      integer E,x,i,j,d,n,s,shotnum,Emax,Nfilms,Ndoses,Nsets,istep,flag
      character*1 dummychar
      character*1 shotchar
      character*1 cycle

C *** DECLARE FUNCTIONS
      integer findenergy,nearestx
      double precision interp
      double precision ZBQLU01


C *** NUMBER OF MEASURED AND INTERPOLATED DOSE POINTS
      Nfilms=12
      Nsets=1000

C *** TITLE

      print *,'*** Laser-shot depth-dose to spectrum routine ***'
      print *,'*** Written by Dan Kirby, Uni. of Birmingham  ***'
      print *,''
      print *,'Please enter (1-digit) shot number: '
      read *,shotnum
      print *,'No of iterations: '
      read *,istep
      print *,'Cycle number: '
      read *,cycle
C     print *,'Enter tolerance as average fractional residual: '
C     read *,tolerance
C     print *,'Enter stconst (bin step scaling parameter less than 1): '
C     read *,stconst
      stconst=0.95
      print *,'Processing shot',shotnum,'.csv ...'

      write (shotchar,100) shotnum

      open(10,file='bp15pnalledep.csv',status='old',form='formatted')
      open(11,file='bp15pnallerr.csv',status='old',form='formatted')
      open(15,file='shot'//shotchar//'films.csv',status='old',
     &  form='formatted')

C *** Skip first two lines of text in files

      read(10,*) dummychar
      read(11,*) dummychar

      do x=1,535
        read(10,101) fluX(x),(fluD(E,x),E=1,30)
        read(11,101) temp,(fluDerr(E,x),E=1,30)
      enddo


C     CONVERTS FLUKA EDEP TO J/cm/proton
C     ************************************

      do E=1,30
        do x=1,535
          fluD(E,x)=fluD(E,x)*3.141592654*2.5D+0*3.0D+1*1.6022E-10
        enddo
      enddo


C    FIND DEPTH OF BP AND 5% RANGE FOR EACH ENERGY
C    **********************************************
```

```
      do E=1,30

        do x=2,535
           if(fluD(E,x).LT.(.99*fluD(E,x-1))) then
              dmax=fluD(E,x-1)
             xBP=x-1
             GOTO 50
           endif
        enddo

 50     bpmax(E)=fluX(x-1)


        x=xBP
 51     if(fluD(E,x).GT.(dmax/20.0)) then
          x=x+1
          GOTO 51
        endif

        range(E)=fluX(x-1)

C       print *,E,' ',bpmax(E),' ',range(E)

      enddo


      do x=1,Nfilms
         read(15,102) initfilmX(x),meanfilmD(x),filmDerr(x)
      enddo


C     START OF LOOP FOR MANY RANDOM SETS
C     *********************************

      s=1

C *** Initialise externally written random number generator

      call ZBQLINI(0)


 52   CONTINUE

      print *,'Processing set ',s

      do x=1,Nfilms
         rnd=ZBQLU01(DBLE(s*x))-0.5
C        print *,'Random no. ',rnd
         initfilmD(x)=meanfilmD(x)+rnd*filmDerr(x)
         flag=0
         if(initfilmD(x).LT.1.0D-6) then
           initfilmD(x)=1.0D-6
             print *,'Negative dose made 1E-6 at x:',x,' set:',s
           endif
           initfilmD(x)=DLOG10(initfilmD(x))

      enddo

      do x=1,535
         fluDtot(x)=0.D+0
      enddo

      call spline_cubic_set(Nfilms,initfilmX,initfilmD,0,0,0,0,splout)

      x=1
      E=1
      i=1

C     POPULATE DOSE DATA POINTS WITH CUBIC SPLINE INTERPOLATIONS
C     AT THE DEPTH OF EVERY BRAGG PEAK IN THE ENERGY LIBRARY
C     **********************************************************

 53   CONTINUE

      if(bpmax(E).LT.initfilmX(x)) then
         filmX(i)=bpmax(E)
         E=E+1
      else
         filmX(i)=initfilmX(x)
         x=x+1
      endif

      call spline_cubic_val(Nfilms,initfilmX,initfilmD,splout,filmX(i),
     &                           filmD(i),Dp,Dpp)

      filmD(i)=(1.D+1)**filmD(i)
C     write(6,102) filmX(i),filmD(i),filmDerr(i)

      i=i+1

      if(x.LE.Nfilms) GOTO 53

      Ndoses=i-1

C     FIND LOWEST E WITH RANGE LARGER THAN DEEPEST DOSE POINT
C     *******************************************************

      Emax=findenergy(range,filmX,Ndoses)

C     FIRST PASS TO INITIALISE SPECTRUM
C     *********************************

         do x=1,535
            fluDtot(x)=fluDtot(x)+0.D+0
```

```
         enddo

      spec(s,Emax)=filmD(Ndoses-1)/fluD(Emax,nearestx(fluX,filmX(Ndoses-1)))

      do E=1,Emax-1
        spec(s,E)=spec(s,Emax)
      enddo
      do E=Emax+1,30
        spec(s,E)=0.D+0
      enddo

      do E=1,30
         do x=1,535
            fluDtot(x)=fluDtot(x)+spec(s,E)*fluD(E,x)
         enddo
      enddo

      do d=1,Ndoses
         fluDtotd=fluDtot(nearestx(fluX,filmX(d)))
         residual(d)=((fluDtotd-filmD(d))/filmD(d))**2
         sumres=sumres+residual(d)
      enddo

C     print *,'All residuals: '
C     print *,(residual(d),d=1,Ndoses)

C     print *,'Initial Mean Residual: ',SQRT(sumres)/DBLE(Ndoses)
C     print *,'Print initial data and exit? (Y or N)'
C     read *,dummychar
C     if (dummychar.EQ.'Y') GOTO 70

C     MAIN ITERATION LOOP
C     ********************

      i=1
      n=0
      specstep=5.D-2

 60   CONTINUE

      n=n+1

      if(specstep.GT.(0.001)) then
         specstep=specstep*stconst
      else
         specstep=5.D-2
         print *,'*** Specstep reset'
      endif

      do E=Emax,1,-1

 61   CONTINUE

         sumres=0
         sumres1=0
         sumres2=0

C     CALCULATE CURRENT RESIDUALS
C     ***************************

         do d=1,Ndoses
            fluDtotd=fluDtot(nearestx(fluX,filmX(d)))
            residual(d)=((fluDtotd-filmD(d))/filmD(d))**2
            sumres=sumres+residual(d)
         enddo

      if(flag.GT.0) print *,'flag 3',E

CCC   DO INCREMENT/DECREMENT SEARCH TO IMPROVE SUM OF RESIDUALS
C     ****************************************************************

         do x=1,535
            fluDtot1(x)=fluDtot(x)+specstep*spec(s,E)*fluD(E,x)
            fluDtot2(x)=fluDtot(x)-specstep*spec(s,E)*fluD(E,x)
         enddo

         do d=1,Ndoses
            fluDtotd1=fluDtot1(nearestx(fluX,filmX(d)))
            residual1(d)=((fluDtotd1-filmD(d))/filmD(d))**2
            sumres1=sumres1+residual1(d)
         enddo

         do d=1,Ndoses
            fluDtotd2=fluDtot2(nearestx(fluX,filmX(d)))
            residual2(d)=((fluDtotd2-filmD(d))/filmD(d))**2
            sumres2=sumres2+residual2(d)
         enddo

         if (MIN(sumres1,sumres2).LT.sumres) then
C           print *,'sumres1+2: ',sumres1,sumres2,sumres
            if (sumres1.LE.sumres2) then
               spec(s,E)=spec(s,E)+specstep*spec(s,E)

               do x=1,535
                  fluDtot(x)=fluDtot(x)+specstep*spec(s,E)*fluD(E,x)
               enddo

            endif

            if (sumres2.LE.sumres1) then
               spec(s,E)=spec(s,E)-specstep*spec(s,E)

               do x=1,535
                  fluDtot(x)=fluDtot(x)-specstep*spec(s,E)*fluD(E,x)
```

```
                  enddo

                endif

                GOTO 61

              endif

C       print *,E
        enddo

        i=i+1

        if (i.LE.istep) GOTO 60

        s=s+1

        print *,'Chi-sq: ',SQRT(sumres)/DBLE(Ndoses)

        if (s.LT.(Nsets+1)) GOTO 52

 70     print *,'Iterations stopped by user'


C       FIND MEAN ENERGY SPECTRUM
C       *************************

        do E=1,Emax
          sumspec=0.0D+0
          do s=1,Nsets
             sumspec=sumspec+spec(s,E)
          enddo
          meanspec(E)=sumspec/DBLE(Nsets)
        enddo


C       FIND ST.DEV. FOR EACH ENERGY BIN
C       ********************************

        do E=1,Emax
          sumsqspec=0.0D+0
          do s=1,Nsets
             sumsqspec=sumsqspec+(spec(s,E)-meanspec(E))**2
          enddo
          sdspec(E)=SQRT(sumsqspec/DBLE(Nsets-1))
        enddo

C       MATRIX MULTIPLICATION
C       *********************

        open(16,file='matrix30.csv',status='old',form='formatted')

C *** READ MATRIX FILE

        do i=1,30
          read (16,105) (M(i,j),j=1,30)
          do j=1,30
             if (DABS(M(i,j)).LT.1.D-10) M(i,j)=0.D+0
          enddo
        enddo

        do j=1,30
          sumerr=0.D+0
          ijprod=0.D+0
          do i=1,30
            ijprod=ijprod+meanspec(i)*M(i,j)
            sumerr=sumerr+(M(i,j)*sdspec(i)/meanspec(j))**2
          enddo
          transpec(j)=ijprod
          sdtranspec(j)=SQRT(sumerr)*transpec(j)
        enddo


C       WRITING TO FILE
C       ***************

        open(14,file='shot'//shotchar//'spec'//cycle//'.csv',status='new',
     &       form='formatted')

        do E=1,Emax
           write(14,103) E,meanspec(E),sdspec(E),transpec(E),sdtranspec(E)
        enddo


        close(10)
        close(11)
        close(14)
        close(15)
        close(16)

        print *,'Files written ok'

 100    format(i1)
 101    format(E11.4,30(1p,E11.4))
 102    format(E10.4,2(E11.4))
 103    format(i3,4(E11.4))
 104    format(E10.4,E11.4)
 105    format(E11.4,29(E12.4))

        END

CCC     ----------------------------------------------------------
```

```
      INTEGER FUNCTION nearestx(array1,depth)

C *** Finds nearest Fluka depth bin to given film depth

      double precision array1(535),depth
      integer xpoint

      xpoint=535

 201  if (depth.LT.array1(xpoint)) then
        xpoint=xpoint-1
        GOTO 201
      endif

      if (DABS(array1(xpoint+1)-depth).LE.DABS(array1(xpoint)-depth))
     &      xpoint=xpoint+1

      nearestx=xpoint

      END

CCC   ------------------------------------

      INTEGER FUNCTION findenergy(array1,array2,xpoint)

C *** Finds lowest energy that has range greater than
C *** depth of measurement point

      double precision array1(50),array2(50)
      integer xpoint,E

      E=30

 200  if (E.GT.0) then
        if (array1(E).GT.array2(xpoint)) then
          E=E-1
          GOTO 200
        endif
      endif

      findenergy=E+1

      END
CCC   ------------------------------------

      DOUBLE PRECISION FUNCTION interp(x1,x2,d1,d2,xi)

C *** Linear interpolation between two Fluka dose points

      double precision x1,x2,d1,d2,xi
      interp=(xi-x1)/(x2-x1)*(d2-d1)+d1

      END
CCC   ------------------------------------
```

APPENDIX C

BASH SCRIPTS

C.1 BlueBEAR submission example (FLUKA)

```
#!/bin/sh

ROOTDIR=‘pwd‘
echo ’Specify Fluka input:’
read FLUKAINP

### USER INPUTS
until [ -z $FLUKAINP ]; do

  echo ’How many nodes? (default 1)’
  read NODES
  if [ -z $NODES ]; then
      NODES=’1’
  fi
  echo ’Cycles per node? (default 1)’
  read CYCLES
  if [ -z $CYCLES ]; then
      CYCLES=’1’
  fi
  echo ’Total number of particles? (default 1000)’
  read TOTNPS
  if [ -z $TOTNPS ]; then
      TOTNPS=’1000’
  fi
  echo ’Select walltime:’
  echo ’1 - 00:30:00 <default>’
  echo ’2 - 02:00:00’
  echo ’3 - 08:00:00’
  echo ’4 - 24:00:00’
  echo ’5 - 240:00:00’
  read WALLCHOICE
  case $WALLCHOICE in
  ”” ) WALLTIME=’00:30:00’;;
  ”1” ) WALLTIME=’00:30:00’;;
  ”2” ) WALLTIME=’02:00:00’;;
  ”3” ) WALLTIME=’08:00:00’;;
  ”4” ) WALLTIME=’24:00:00’;;
  ”5” ) WALLTIME=’240:00:00’;;
  esac

  echo ’Perform USERDUMP using mgdraw.f? (leave blank for no)’
  read USERDUMP

### CREATES UNIQUE DIRECTORY NAME FOR RUN

  jobdir=${FLUKAINP}_‘date +%d%m%y‘_‘date +%H%M‘
```

```
### CALC NUMBER OF PARTICLES FOR EACH RUN

  NPS=$[ $TOTNPS/$[ $NODES*$CYCLES ] ]

### IF USERDUMP NOT REQUIRED, FINISH END OF INPUT FILE

  if [ -z $USERDUMP ]; then

cat >$ROOTDIR/.nps << EOF
START      ${NPS}.0
STOP
EOF

echo 'USERDUMP switched OFF'

### ELSE INSERT USERDUMP CARD INTO INPUT FILE

  else

cat >$ROOTDIR/.nps << EOF
START      ${NPS}.0
USERDUMP          100.        99.         2.         1.                        MGDRAWOU
STOP
EOF

echo 'USERDUMP switched ON'
  fi

echo 'Job started: ' `date`

echo 'Input file is ' $FLUKAINP '.inp'
echo 'Submitting ' $NPS ' particles per cycle per node on ' $NODES ' nodes...'
echo '--> Total of ' $TOTNPS ' particles'
echo 'Job outputted to directory ' $jobdir

mkdir $ROOTDIR/$jobdir
cd $ROOTDIR/$jobdir

### SAVES USER OPTIONS TO FILE FOR FUTURE REFERENCE

  echo $FLUKAINP $NODES $CYCLES $TOTNPS > .fluka

cat $ROOTDIR/$FLUKAINP.inp $ROOTDIR/.nps > run.tmp


### CREATES NEW RANDOM SEED FOR EACH RUN AND CREATES FINAL INPUT FILES

  i=1
  until [ $i -gt $NODES ]; do
     final_run=$[ $i*$CYCLES ]
     last_run=$[ $final_run-$CYCLES ]
     cat >.rndm <<EOF
s%RANDOMIZ          1.0%RANDOMIZ          1.0      $i.0%
EOF
     sed -f .rndm run.tmp > run${i}.inp

### JOB SUBMISSION COMMAND

     echo $FLUPRO/flutil/rfluka -e $FLUPRO/trkfluka -N0 -M$CYCLES run$i |
            qsub -A greensy01 -N fluka -l walltime=${WALLTIME} -l nodes=1:ppn=1 -j oe -d $ROOTDIR/$jobdir
     i=$[ $i+1 ]
  done

  echo 'Total of ' $NODES 'jobs sent'
  echo 'Send another? Leave blank or enter new input name'
  read FLUKAINP

done

rm run.tmp
rm .rndm
```

C.2 Combining FLUKA output files

```
#!/bin/sh

### COMBINES ALL OUTPUT FILES (DESIGNED FOR USRBIN DEPTH DOSES)

if [ -z $1 ]; then
      echo 'Output dir:'
      read jobdir
else
      jobdir=$1
fi

if [ -z $2 ]; then
      echo 'Fortran unit number:'
      read unit
else
      unit=$2
fi

cd $MYFLUKA/$jobdir

### MAKES USE OF .fluka FILE - USER OPTIONS CREATED DURING JOB SUBMISSION

read FLUKAINP NODES CYCLES TOTNPS < .fluka

until [ -z $unit ]; do

### RUNS FLUKA'S OWN ROUTINE FOR COMBINING OUTPUT

$FLUPRO/flutil/usbsuw << EOF
`find *.$unit`

comb.bin
EOF

### RUNS FLUKA'S BINARY->ASCII CONVERTER

$FLUPRO/flutil/usbrea << EOF
comb.bin
${FLUKAINP}.o${unit}
EOF

### RUNS IN-HOUSE ROUTINE TO PREPARE OUTPUT IN PREFERRED COLUMN BASED
### FORMAT FOR IMPORT INTO EXCEL/OTHER PLOTTING SOFTWARE

../fluka2cols << EOF
${FLUKAINP}
${unit}
EOF

echo 'Combine another unit? (enter unit or leave blank to exit)'
read unit

done

echo Clearing out the gumph...
if [ $PWD = $MYFLUKA/$jobdir ]; then
      rm ran*
      rm *.inp
      rm comb.bin
fi
echo Done
echo
```

APPENDIX D

SAMPLES OF MONTE CARLO INPUT AND SUPPLEMENTARY FILES

A large number of input files were used throughout this work, and are available upon request. In the interest of brevity, only one sample input file for 29 MeV protons will be included here for each code. In any case, the main aspects of importance are the geometry descriptions and physical options selected which generally remained the same throughout.

D.1 FLUKA

The modifications to the default *mgdraw*, *comscw* and *source* routines present in the *usermvax* subdirectory are included here as standalone segments of code. The rest of the code in these routines is left unchanged from the original source files that come with the FLUKA package, and comments are included here as to where these user-written segments of code were inserted.

D.1.1 Sample input file

```
* ..+....1....+....2....+....3....+....4....+....5....+....6....+....7....+....8
TITLE
29.15 MeV proton beam with 0.3% dp/p spread and 5 mrad divergence (5 mrad full width)
* ..+....1....+....2....+....3....+....4....+....5....+....6....+....7....+....8
BEAM       -29.15D-3  -.001663       5.0       0.0       0.0      -1.0PROTON
BEAMPOS          0.0       0.0    -405.0       0.0       0.0
GEOBEGIN                                                              COMBNAME
    0    0          Birmingham cyclotron geometry
RPP exvoid      -10.1 1000.0 -1000.0 1000.0 -1000.0 1000.0
RPP surrair     -10.0 10.0 -10.0 10.0 -410.0 10.0
RCC beamport    0.0 0.0 -408.0 0.0 0.0 406.3 2.5
RCC monitent    0.0 0.0 -1.1 0.0 0.0 0.01 5.0
RCC monitext    0.0 0.0 -0.21 0.0 0.0 0.01 5.0
RPP phantom     -4.25 4.25 -4.25 4.25 0.0 0.8
ZCC innerAl     0.0 0.0 1.0
ZCC innerTa     0.0 0.0 0.5
XYP window1     -5.1
XYP window2     -5.097
XYP coll1       -3.1
XYP coll2       -2.4
END
BH           3 +exvoid -surrair
VAC          3 +beamport +window1
ALLAIR       3 | +surrair -beamport -phantom -monitent -monitext | +innerTa -coll2
               +beamport | +beamport -coll1 +coll2 | +innerAl -window2 +coll1
HAVWIN       3 +innerAl -window1 +window2
ALUMSURR     3 +beamport -window1 +coll1 -innerAl
TANTCOLL     3 +beamport -coll2 -innerTa
MONITOR      3 | +monitent | +monitext
PMMA         3 +phantom
END
GEOEND
* ..+....1....+....2....+....3....+....4....+....5....+....6....+....7....+....8
MATERIAL         0.0       0.0      1.19      26.0                    PERSPEX
COMPOUND    0.333333    CARBON  0.133333    OXYGEN  0.533334  HYDROGENPERSPEX
MATERIAL         0.0       0.0      1.42      27.0                    POLYIMID
COMPOUND      0.5641    CARBON    0.1282    OXYGEN    0.2564  HYDROGENPOLYIMID
COMPOUND      0.0513  NITROGEN                                        POLYIMID
MATERIAL        24.0   51.9961      7.19      28.0                    CHROMIUM
MATERIAL        25.0 54.938045      7.21      29.0                    MANGANES
MATERIAL        27.0 58.933195       8.9      30.0                    COBALT
MATERIAL        42.0     95.96     10.28      31.0                    MOLYBDEN
MATERIAL         0.0       0.0       8.3      32.0                    HAVAR
COMPOUND    0.009648    CARBON  0.222858  CHROMIUM  0.016874  MANGANESHAVAR
COMPOUND    0.181139      IRON  0.417828    COBALT  0.128336    NICKELHAVAR
COMPOUND    0.014494  MOLYBDEN  0.008823  TUNGSTEN                    HAVAR
MATERIAL         0.0       0.0  0.001205      33.0                    DRYAIR
COMPOUND   0.0001502    CARBON 0.2107559    OXYGEN 0.7844227  NITROGENDRYAIR
COMPOUND   0.0046712     ARGON                                        DRYAIR
ASSIGNMA    BLCKHOLE        BH
ASSIGNMA      VACUUM       VAC
ASSIGNMA       HAVAR    HAVWIN
ASSIGNMA      DRYAIR    ALLAIR
ASSIGNMA     PERSPEX      PMMA
ASSIGNMA    POLYIMID   MONITOR
ASSIGNMA    TANTALUM  TANTCOLL
ASSIGNMA    ALUMINUM  ALUMSURR
*
* ..+....1....+....2....+....3....+....4....+....5....+....6....+....7....+....8
* electron transport low-energy cutoff in GeV
EMFCUT      -5.0D-06
*
* Multiple Coulomb scattering down to Moliere allowable energies
MCSTHRES         1.0       1.0
*
* Maximum fractional energy loss for hadrons/muons (0.15 & 0.012 defaults)
FLUKAFIX        0.07      0.15     0.012   PERSPEX
*
* score in each region energy deposition and stars produced by primaries
SCORE         ENERGY
*
* Energy loss fluctuations: hadrons / electrons / accuracy / materials
IONFLUCT         1.0       1.0       4.0   PERSPEX
*
```

```
* E threshold for delta ray production/ dp/dx bins / log interval / material
DELTARAY     1.0D-06       0.0      1.03   PERSPEX                        PRINT
*
* 1 keV cutoff for protons
PART-THR    -1.0D-06    PROTON    PROTON       1.0       0.0
USRBIN          11.0    ENERGY      -30.     0.265       0.0       0.8TOTALDEP
USRBIN           0.0       0.0       0.0       1.0       1.0     400.0&
RANDOMIZ         1.0
* Final cards inserted by job submission script
```

D.1.2 *mgdraw* modifications

```
**********************************************
*** CODE INSERTED INSIDE FIRST IF STATEMENT ***
**********************************************

            OPEN ( UNIT = 90, FILE = 'PDUMP', STATUS = 'NEW', FORM =
     &           'FORMATTED' )
            OPEN ( UNIT = 91, FILE = 'EDUMP', STATUS = 'NEW', FORM =
     &           'FORMATTED' )
         END IF

**************************************
*** Proton/Electron track info dump ***
**************************************

*** If particle is proton and is at position z > 0
         IF (JTRACK .EQ. 1 .AND. ZTRACK(1) .GT. ZERZER) THEN

*** If proton vertex withing Markus radius of central axis, write info
            IF (XTRACK(0)**2.0+YTRACK(0)**2.0 .LE. 7.0225D-02 .OR.
     &          XTRACK(1)**2.0+YTRACK(1)**2.0 .LE. 7.0225D-02) THEN

               WRITE (90,54) XTRACK(1),YTRACK(1),ZTRACK(1),ETRACK-AMPRTN

            ENDIF

*** If particle is electron and is at position z > 0
         ELSE IF (JTRACK .EQ. 3 .AND. ZTRACK(1) .GT. ZERZER) THEN

*** If electron vertex withing Markus radius of central axis, write info
            IF (XTRACK(0)**2.0+YTRACK(0)**2.0 .LE. 7.0225D-02 .OR.
     &          XTRACK(1)**2.0+YTRACK(1)**2.0 .LE. 7.0225D-02) THEN

               WRITE (91,54) XTRACK(1),YTRACK(1),ZTRACK(1),ETRACK-AMLECT

            ENDIF

         ENDIF


 54      format(2(1x,d11.5),1x,d13.7,1x,d9.4)
```

D.1.3 *comscw* modifications

```
*********************************************
*** CODE INSERTED AFTER FIRST IF STATEMENT ***
*********************************************

         IF ( ISCRNG .EQ. 1 ) THEN
            IF ( JTRACK .EQ. 1 ) THEN

               IF (TITUSB(JSCRNG).EQ.'MD55DOSE') THEN

* ===== MDV255 Weighted fit to Fluka RE

               RE0 = 0.505
               delRE = 0.45
               C = 4.3
               logEm = 0.56

         ELSE IF (TITUSB(JSCRNG).EQ.'EBTDOSE') THEN
```

```
* ===== EBT Weighted fit to Fluka RE

               RE0 = 0.49
               delRE = 0.51
               C = 3.3
               logEm = 0.23

        ELSE
          GOTO 100
        ENDIF


* =====  Find kinetic energy in MeV
             Ekin=REAL((ETRACK-0.9382723D+0)*1.0D+3)

             logEk=LOG10(Ekin)
             Elogs=logEk-logEm


* =====  0.5 MeV binning used for scoring BP library 0-15 MeV

            DO 100 i=1,30

* ===== Defines lower and upper energy bin values
               TUPPER=0.5D-3*DBLE(i)
               TLOWER=0.5D-3*DBLE(i-1)

               IF ( JSCRNG .EQ. i ) THEN
                  IF (TKSOEV(1).GT.TLOWER.AND.
     &               TKSOEV(1).LE.TUPPER) THEN

* =====  Use this line to simulate GafChromic film
                     COMSCW=DBLE(RE0+delRE/(1.0+EXP(-C*Elogs)))

* =====  Use this line for normal energy deposition
C                    COMSCW=ONEONE
                  ELSE
                     COMSCW=ZERZER
                 ENDIF
              ENDIF

100    CONTINUE

         ELSE

* ===== Prevents scoring of neutron dose (or any other particle!)
            COMSCW=ZERZER

         ENDIF
        ENDIF
```

D.1.4 *source* modifications

```
*************************************************
*** CODE INSERTED IN USER INITIALISATION AREA ***
*************************************************
          E_MIN  = WHASOU(1)
          E_MAX  = WHASOU(2)
          KT     = whasou(3)
C         radius = whasou(4)
C         ZBEAM  = whasou(5)
          divdeg = whasou(6)
          PI     = 3.141592654D0
          PI2    = 2.0D0*PI
          divrad = divdeg*PI/180.D0
          Ymin   = exp(-E_MAX/KT)
          Ymax   = exp(-E_MIN/KT)
*************************************
               ^
               |
[ EXISITING SOURCE.F CODE ]
               |
               v
```

```
****************************************************
*** CODE INSERTED JUST BEFORE MOMENTUM ASSIGMENT ***
****************************************************

*** Random sampling of proton energy (GeV) from exponential distribution

 33    pippo = FLRNDM(XXX)*Ymax-FLRNDM(YYY)*Ymin
       if(pippo.ge.Ymin)then
          ENERGY = -KT*log(pippo)
       else
          goto 33
       endif
       TKEFLK (NPFLKA) = ENERGY

*** Isotropic direction sampling within specified divergence

       blabla = FLRNDM(AAA)
       alpha  = (sqrt(blabla))*divrad
       beta   = FLRNDM(BBB)*PI2
       TXFLK  (NPFLKA)  = sin(alpha)*cos(beta)
       TYFLK  (NPFLKA)  = sin(alpha)*sin(beta)
       TZFLK  (NPFLKA)  = cos(alpha)
```

D.2 MCNPX

D.2.1 Sample input file

```
MESSAGE: datapath=/bb/phy/djk191/mcnpx250/lib outp=alta.o
runtpe=alta.r mdata=alta.m

c CELL CARDS
c BH
1  0  9
c VAC
2  0  -1 -10
c ALLAIR
3  2  -0.001205  -9 #2 #4 #5 #6 #7 #8
c HAVWIN
4  1  -8.3  -4 -11 10
c ALUMSURR
5  5  -2.7  -1 10 -2 4
c TANTCOLL
6  6  -16.65  -1 3 5
c MONITOR
7  3  -1.42  -7 : -6
c PMMA
8  4  -1.19  -8

c SURFACE CARDS
1     RCC      0.00  0.00  -408.00  0.00  0.00  406.30  2.50    $ BEAMPORT
2     PZ      -3.10   $ COLL1
3     PZ      -2.40   $ COLL2
4     CZ       1.0    $ INNERAL
5     CZ       0.5    $ INNERTA
6     RCC      0.00  0.00  -1.10  0.00  0.00  0.01  5.00   $ MONITOR1
7     RCC      0.00  0.00  -0.21  0.00  0.00  0.01  5.00   $ MONITOR2
8     RPP     -4.25  4.25  -4.25  4.25  0.0  0.8       $ PHANTOM
9     RPP     -10.0  10.0  -10.0  10.0  -410.0  10.0  $ SURRAIR
10    PZ      -5.10   $WINDOW1
11    PZ      -5.097  $WINDOW2

C     MODE CARD
MODE H
C
C      Cell proton importances
IMP:H 0 1 1 1 1 1 1 1
CUT:H J 0.001 0 0
C
C     SOURCE DEFINITION
C      Pencil beam 29.2 MeV protons - 0.3% sigma KE spread (not p!)
```

```
SDEF PAR=H POS=0.0 0.0 -405.0 ERG=D1 DIR=D2 VEC=0 0 1
SP1  -4 0.24779 29.2     $ a = FWHM/SQRT(ln 2)
SI2  0.9999875 1.0       $ 5 mrad divergence, uniform spread
SP2  0.0 1.0
C
C
C
C    MESH TALLY
TMESH
CMESH11:H pedep flux
CORA11 0 0.265
CORB11 0. 399i 0.8
CORC11 360
C
ENDMD
C
C
C
C    MATERIAL CARDS
M1   6000 0.009648 24000 0.222858 25000 0.016874 26000 0.181139 27000
     0.417828 28000 0.128336 42000 0.014494 74000 0.008823     $ Havar
M2   6000 0.0001502 8000 0.2107559 7000 0.7844227 18000 0.0046712 $ Air
M3   6000 0.5641 1000 0.2564 8000 0.1282 7000 0.0513  $ Polyimide
M4   6000 0.333333 8000 0.133333 1000 0.533334        $ Perspex
M5   13000 1.0   $ Al
M6   73000 1.0   $ Ta
C
C
C
C PRINT 85
C
C   NPS to be added
```

APPENDIX E

TECHNICAL DRAWINGS

E.1 Perspex jig

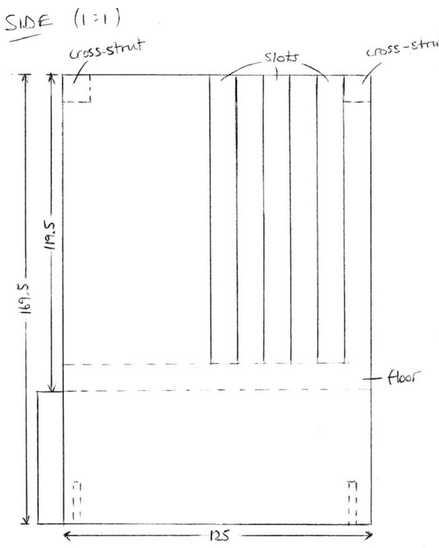

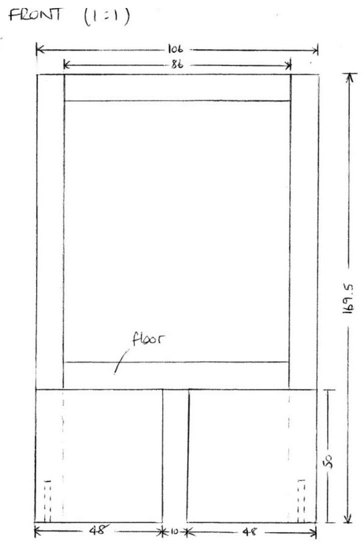

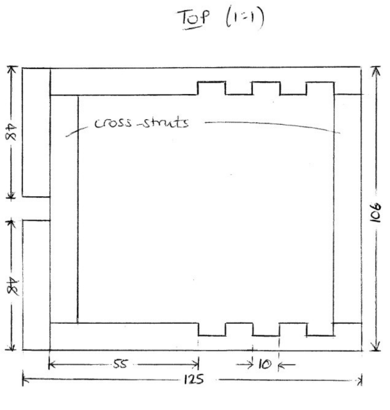

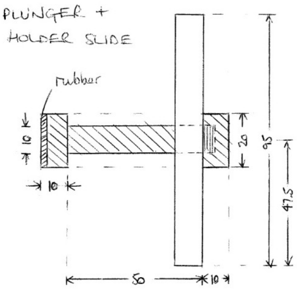

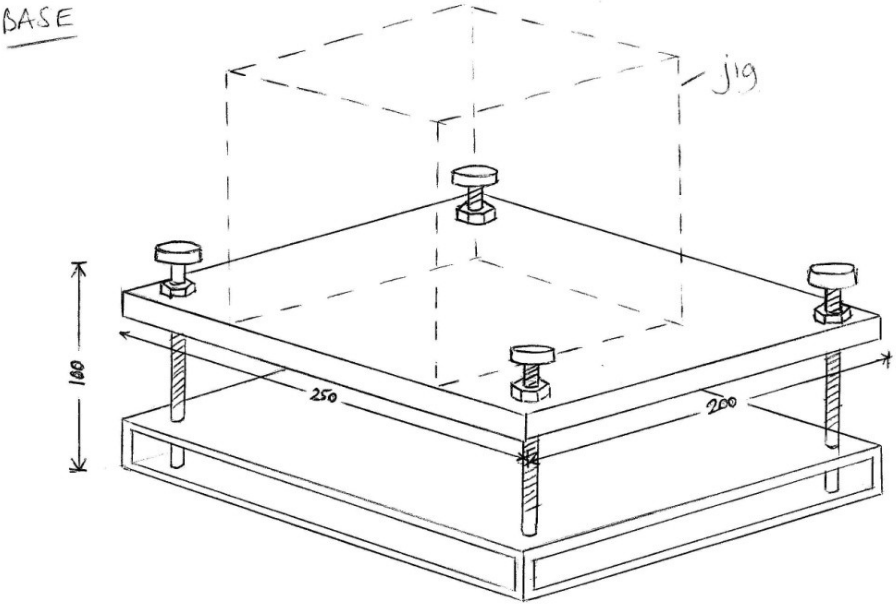
BASE
jig
180
250
200

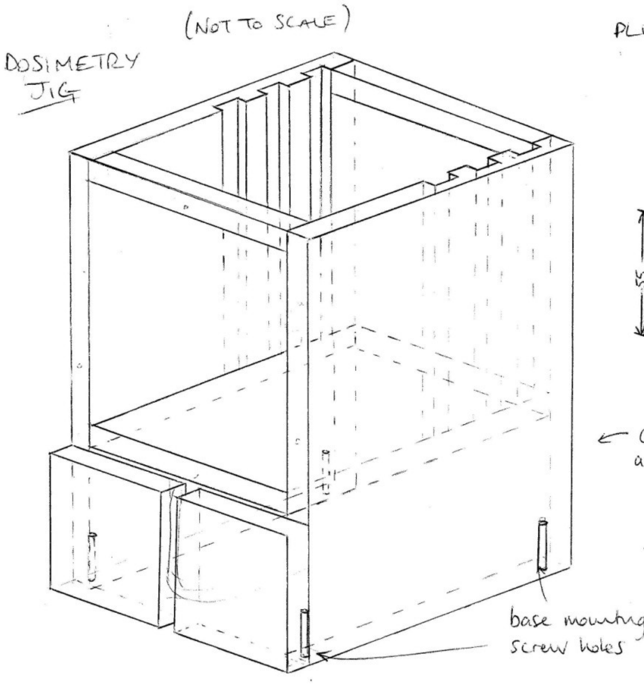
(NOT TO SCALE)
DOSIMETRY JIG
cable access
base mounting screw holes

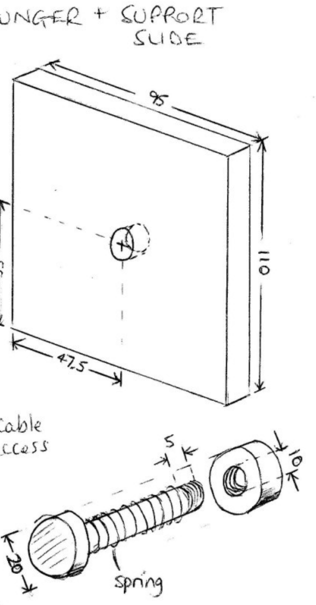
PLUNGER + SUPPORT SLIDE
8
55
110
47.5
5
10
20
spring

E.2 Monitor chamber

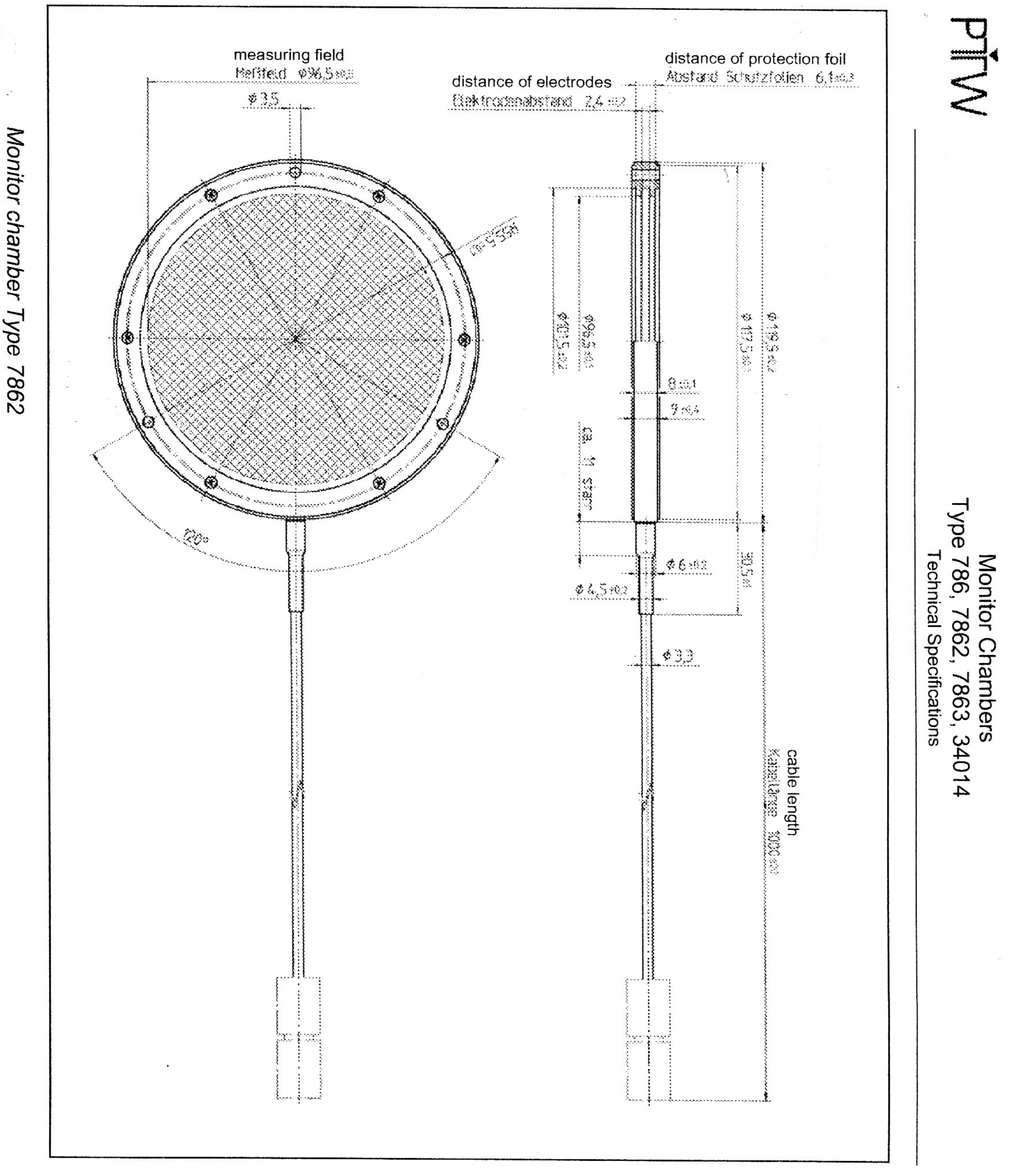

APPENDIX F

EBT IMAGES PRODUCED BY NSC 5000 AND 9000

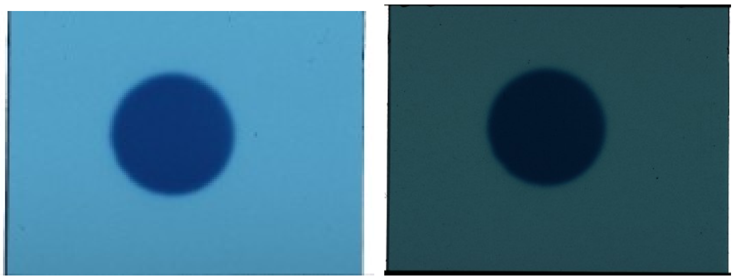

Figure F.1: On the left is a scan of an EBT film performed with the NSC 9000, and on the right is the same film scanned with the NSC 5000. The same scan parameters (apart from resolution) were selected in the Nikon Scan software, so the difference in image is hardware related.

APPENDIX G

DOSE UNCERTAINTIES

Table G.1: Estimated relative uncertainties in percent for D_w measured with the Markus ionisation chamber and for $d_w(net\mathrm{OD}, z)$ measured with GafChromic film. Ionisation chamber uncertainties are taken from TRS-398 and those for GafChromic film are estimates based on measurements in chapter 5 and in other literature.

Markus (plane-parallel) chamber	protons	α-particles
PSDL $N_{D,w}$ calibration of dosimeter	0.4	0.4
Long term stability of dosimeter	0.4	0.4
Establishment of reference conditions	0.4	0.6
Dosimeter reading M_Q relative to monitor	0.6	0.6
Correction for influence quantities (k_{TP}, k_{ion} ...)	0.5	0.5–1.1[a]
k_Q correction	2.1	2.9[b]
Combined uncertainty for Markus chamber	**2.3**	**3.1-3.3**
GafChromic film		
Scanning conditions:	HD-810/MD-V2-55	EBT/EBT2
– reproducibility	0.2	0.2
– temperature effects	1.2	1.2
– orientation	0.3	0.3
– difference in darkening time	1.0	0.6
– non-uniformity	2.0	1.5
Calibration:	6 MV X-rays	protons
– D_w delivered	2.0	2.3
– polynomial fit (mean absolute error)	0.6–1.7	
Combined uncertainty for GafChromic film	**2.9–4.4**	

[a] Variation linked to k_{ion} which depends on dose rate/depth of measurement.

[b] Less than TRS-398 value due to more accurate $s_{w,air}$.

APPENDIX H

MATRICES $\mathbf{M}$ AND $\mathbf{M}^{-1}$ FOR ALUMINIUM FOIL ENERGY LOSS CORRECTION

M =

0	0	0	0	0	0	0	0	0	0	0	0	0	0	0	0	0	0	0	0	0	0	0	0	0	0	0	0	0	0
0	0	0	0	0	0	0	0	0	0	0	0	0	0	0	0	0	0	0	0	0	0	0	0	0	0	0	0	0	0
0.431	0.087	0	0	0	0	0	0	0	0	0	0	0	0	0	0	0	0	0	0	0	0	0	0	0	0	0	0	0	0
0	0.523	0.482	0	0	0	0	0	0	0	0	0	0	0	0	0	0	0	0	0	0	0	0	0	0	0	0	0	0	0
0	0	0.264	0.74	2E-04	0	0	0	0	0	0	0	0	0	0	0	0	0	0	0	0	0	0	0	0	0	0	0	0	0
0	0	0	0.082	0.867	0.053	0	0	0	0	0	0	0	0	0	0	0	0	0	0	0	0	0	0	0	0	0	0	0	0
0	0	0	0	0.002	0.846	0.153	0	0	0	0	0	0	0	0	0	0	0	0	0	0	0	0	0	0	0	0	0	0	0
0	0	0	0	0	0	0.767	0.234	0	0	0	0	0	0	0	0	0	0	0	0	0	0	0	0	0	0	0	0	0	0
0	0	0	0	0	0	0	0.702	0.299	0	0	0	0	0	0	0	0	0	0	0	0	0	0	0	0	0	0	0	0	0
0	0	0	0	0	0	0	0	0.647	0.354	0	0	0	0	0	0	0	0	0	0	0	0	0	0	0	0	0	0	0	0
0	0	0	0	0	0	0	0	0	0.601	0.399	0	0	0	0	0	0	0	0	0	0	0	0	0	0	0	0	0	0	0
0	0	0	0	0	0	0	0	0	0	0.562	0.439	0	0	0	0	0	0	0	0	0	0	0	0	0	0	0	0	0	0
0	0	0	0	0	0	0	0	0	0	0	0.528	0.473	0	0	0	0	0	0	0	0	0	0	0	0	0	0	0	0	0
0	0	0	0	0	0	0	0	0	0	0	0	0.498	0.503	0	0	0	0	0	0	0	0	0	0	0	0	0	0	0	0
0	0	0	0	0	0	0	0	0	0	0	0	0	0.472	0.528	0	0	0	0	0	0	0	0	0	0	0	0	0	0	0
0	0	0	0	0	0	0	0	0	0	0	0	0	0	0.448	0.552	0	0	0	0	0	0	0	0	0	0	0	0	0	0
0	0	0	0	0	0	0	0	0	0	0	0	0	0	0	0.427	0.573	0	0	0	0	0	0	0	0	0	0	0	0	0
0	0	0	0	0	0	0	0	0	0	0	0	0	0	0	0	0.408	0.592	0	0	0	0	0	0	0	0	0	0	0	0
0	0	0	0	0	0	0	0	0	0	0	0	0	0	0	0	0	0.392	0.608	0	0	0	0	0	0	0	0	0	0	0
0	0	0	0	0	0	0	0	0	0	0	0	0	0	0	0	0	0	0.376	0.624	0	0	0	0	0	0	0	0	0	0
0	0	0	0	0	0	0	0	0	0	0	0	0	0	0	0	0	0	0	0.361	0.639	0	0	0	0	0	0	0	0	0
0	0	0	0	0	0	0	0	0	0	0	0	0	0	0	0	0	0	0	0	0.348	0.652	0	0	0	0	0	0	0	0
0	0	0	0	0	0	0	0	0	0	0	0	0	0	0	0	0	0	0	0	0	0.336	0.664	0	0	0	0	0	0	0
0	0	0	0	0	0	0	0	0	0	0	0	0	0	0	0	0	0	0	0	0	0	0.325	0.675	0	0	0	0	0	0
0	0	0	0	0	0	0	0	0	0	0	0	0	0	0	0	0	0	0	0	0	0	0	0.314	0.686	0	0	0	0	0
0	0	0	0	0	0	0	0	0	0	0	0	0	0	0	0	0	0	0	0	0	0	0	0	0.305	0.695	0	0	0	0
0	0	0	0	0	0	0	0	0	0	0	0	0	0	0	0	0	0	0	0	0	0	0	0	0	0.296	0.704	0	0	0
0	0	0	0	0	0	0	0	0	0	0	0	0	0	0	0	0	0	0	0	0	0	0	0	0	0	0.287	0.713	0	0
0	0	0	0	0	0	0	0	0	0	0	0	0	0	0	0	0	0	0	0	0	0	0	0	0	0	0	0.28	0.72	0
0	0	0	0	0	0	0	0	0	0	0	0	0	0	0	0	0	0	0	0	0	0	0	0	0	0	0	0	0.272	0.728

M^{-1} =

-4E-21	0	2.281	-0.217	0.045	-0.004	2E-04	-5E-05	2E-05	-7E-06	4E-06	-3E-06	2E-06	-1E-06	9E-07	-6E-07	4E-07	-2E-07	1E-07	-7E-08	4E-08	-2E-08	9E-09	-4E-09	2E-09	-8E-10	3E-10	-1E-10	5E-11	-2E-11
2E-19	0	0.198	1.072	-0.223	0.018	-0.001	2E-04	-8E-05	4E-05	-2E-05	1E-05	-9E-06	6E-06	-4E-06	3E-06	-2E-06	1E-06	-6E-07	4E-07	-2E-07	1E-07	-5E-08	2E-08	-9E-09	4E-09	-2E-09	6E-10	-2E-10	8E-11
3E-19	0	-0.215	0.912	0.242	-0.019	0.001	-3E-04	8E-05	-4E-05	2E-05	-1E-05	9E-06	-7E-06	5E-06	-3E-06	2E-06	-1E-06	7E-07	-4E-07	2E-07	-1E-07	5E-08	-2E-08	1E-08	-4E-09	2E-09	-7E-10	3E-10	-8E-11
3E-19	0	0.077	-0.325	1.266	0.007	-4E-04	9E-05	-3E-05	1E-05	-8E-06	5E-06	-3E-06	2E-06	-2E-06	1E-06	-7E-07	4E-07	-3E-07	1E-07	-7E-08	4E-08	-2E-08	8E-09	-4E-09	2E-09	-6E-10	2E-10	-9E-11	3E-11
1E-19	0	-0.007	0.031	-0.12	1.154	-0.072	0.014	-0.005	0.002	-0.001	8E-04	-5E-04	4E-04	-3E-04	2E-04	-1E-04	7E-05	-4E-05	2E-05	-1E-05	6E-06	-3E-06	1E-06	-6E-07	2E-07	-1E-07	4E-08	-1E-08	5E-09
5E-18	0	2E-05	-8E-05	3E-04	-0.003	1.182	-0.235	0.078	-0.036	0.02	-0.013	0.009	-0.006	0.004	-0.003	0.002	-0.001	7E-04	-4E-04	2E-04	-1E-04	5E-05	-2E-05	1E-05	-4E-06	2E-06	-7E-07	2E-07	-8E-08
-2E-17	0	2E-08	-7E-08	3E-07	-3E-06	4E-05	1.303	-0.433	0.198	-0.112	0.072	-0.049	0.034	-0.024	0.016	-0.01	0.006	-0.004	0.002	-0.001	5E-04	-3E-04	1E-04	-5E-05	2E-05	-9E-06	4E-06	-1E-06	4E-07
5E-17	0	-6E-08	2E-07	-9E-07	9E-06	-1E-04	9E-04	1.422	-0.65	0.367	-0.236	0.162	-0.113	0.078	-0.052	0.033	-0.021	0.012	-0.007	0.004	-0.002	9E-04	-4E-04	2E-04	-7E-05	3E-05	-1E-05	4E-06	-1E-06
-9E-17	0	1E-07	-6E-07	2E-06	-2E-05	3E-04	-0.002	0.008	1.524	-0.86	0.553	-0.38	0.265	-0.183	0.122	-0.079	0.048	-0.028	0.016	-0.008	0.004	-0.002	9E-04	-4E-04	2E-04	-7E-05	3E-05	-1E-05	3E-06
1E-16	0	-2E-07	1E-06	-4E-06	4E-05	-6E-04	0.004	-0.015	0.041	1.573	-1.01	0.694	-0.485	0.335	-0.224	0.144	-0.088	0.051	-0.029	0.015	-0.008	0.004	-0.002	8E-04	-3E-04	1E-04	-5E-05	2E-05	-6E-06
-2E-16	0	4E-07	-2E-06	6E-06	-6E-05	9E-04	-0.006	0.022	-0.062	0.137	1.52	-1.044	0.73	-0.504	0.337	-0.216	0.132	-0.077	0.043	-0.023	0.011	-0.006	0.003	-0.001	5E-04	-2E-04	8E-05	-3E-05	9E-06
1E-16	0	-5E-07	2E-06	-8E-06	7E-05	-0.001	0.007	-0.028	0.079	-0.176	0.333	1.335	-0.933	0.644	-0.43	0.276	-0.169	0.099	-0.055	0.029	-0.015	0.007	-0.003	0.001	-6E-04	3E-04	-1E-04	4E-05	-1E-05
-8E-17	0	5E-07	-2E-06	8E-06	-8E-05	0.001	-0.008	0.032	-0.088	0.196	-0.372	0.626	1.041	-0.718	0.48	-0.308	0.189	-0.111	0.061	-0.033	0.016	-0.008	0.004	-0.002	7E-04	-3E-04	1E-04	-4E-05	1E-05
-5E-18	0	-5E-07	2E-06	-8E-06	8E-05	-0.001	0.008	-0.031	0.087	-0.194	0.368	-0.619	0.959	0.711	-0.475	0.305	-0.187	0.109	-0.061	0.032	-0.016	0.008	-0.004	0.002	-7E-04	3E-04	-1E-04	4E-05	-1E-05
9E-17	0	5E-07	-2E-06	7E-06	-7E-05	0.001	-0.007	0.028	-0.078	0.173	-0.329	0.553	-0.856	1.257	0.424	-0.272	0.167	-0.098	0.054	-0.029	0.014	-0.007	0.003	-0.001	6E-04	-2E-04	1E-04	-4E-05	1E-05
-2E-16	0	-4E-07	2E-06	-6E-06	6E-05	-9E-04	0.006	-0.023	0.063	-0.141	0.267	-0.449	0.695	-1.021	1.467	0.221	-0.135	0.079	-0.044	0.023	-0.012	0.006	-0.003	0.001	-5E-04	2E-04	-8E-05	3E-05	-1E-05
2E-16	0	3E-07	-1E-06	5E-06	-4E-05	7E-04	-0.004	0.017	-0.047	0.105	-0.199	0.335	-0.518	0.761	-1.093	1.58	0.101	-0.059	0.033	-0.017	0.009	-0.004	0.002	-9E-04	4E-04	-1E-04	6E-05	-2E-05	7E-06
-2E-16	0	-2E-07	8E-07	-3E-06	3E-05	-5E-04	0.003	-0.012	0.032	-0.072	0.137	-0.23	0.357	-0.524	0.753	-1.088	1.619	0.041	-0.023	0.012	-0.006	0.003	-0.001	6E-04	-3E-04	1E-04	-4E-05	2E-05	-5E-06
2E-16	0	1E-07	-5E-07	2E-06	-2E-05	3E-04	-0.002	0.007	-0.021	0.046	-0.088	0.148	-0.23	0.337	-0.485	0.701	-1.042	1.617	0.015	-0.008	0.004	-0.002	9E-04	-4E-04	2E-04	-7E-05	3E-05	-1E-05	3E-06
-1E-16	0	-7E-08	3E-07	-1E-06	1E-05	-2E-04	0.001	-0.005	0.013	-0.028	0.053	-0.089	0.138	-0.203	0.292	-0.422	0.628	-0.975	1.594	0.005	-0.002	0.001	-5E-04	2E-04	-1E-04	4E-05	-2E-05	6E-06	-2E-06
9E-17	0	4E-08	-2E-07	7E-07	-7E-06	1E-04	-7E-04	0.003	-0.007	0.016	-0.03	0.051	-0.078	0.115	-0.165	0.239	-0.356	0.552	-0.903	1.564	0.001	-6E-04	3E-04	-1E-04	6E-05	-2E-05	9E-06	-3E-06	1E-06
-5E-17	0	-2E-08	9E-08	-4E-07	4E-06	-6E-05	4E-04	-0.001	0.004	-0.008	0.016	-0.027	0.042	-0.061	0.088	-0.128	0.19	-0.295	0.482	-0.834	1.533	3E-04	-2E-04	7E-05	-3E-05	1E-05	-5E-06	2E-06	-6E-07
3E-17	0	1E-08	-5E-08	2E-07	-2E-06	3E-05	-2E-04	7E-04	-0.002	0.004	-0.008	0.014	-0.021	0.031	-0.045	0.065	-0.096	0.149	-0.244	0.423	-0.777	1.506	8E-05	-4E-05	1E-05	-6E-06	2E-06	-9E-07	3E-07
-1E-17	0	-5E-09	2E-08	-9E-08	9E-07	-1E-05	9E-05	-3E-04	9E-04	-0.002	0.004	-0.007	0.01	-0.015	0.022	-0.031	0.046	-0.072	0.117	-0.203	0.374	-0.725	1.481	2E-05	-7E-06	3E-06	-1E-06	4E-07	-1E-07
3E-18	0	2E-09	-1E-08	4E-08	-4E-07	6E-06	-4E-05	2E-04	-4E-04	9E-04	-0.002	0.003	-0.005	0.007	-0.01	0.014	-0.021	0.033	-0.054	0.093	-0.171	0.332	-0.678	1.458	3E-06	-1E-06	5E-07	-2E-07	6E-08
3E-18	0	-1E-09	5E-09	-2E-08	2E-07	-3E-06	2E-05	-7E-05	2E-04	-4E-04	8E-04	-0.001	0.002	-0.003	0.004	-0.006	0.009	-0.014	0.024	-0.041	0.075	-0.145	0.297	-0.639	1.439	6E-07	-2E-07	9E-08	-3E-08
-4E-18	0	5E-10	-2E-09	8E-09	-7E-08	1E-06	-7E-06	3E-05	-8E-05	2E-04	-3E-04	6E-04	-9E-04	0.001	-0.002	0.003	-0.004	0.006	-0.01	0.017	-0.032	0.061	-0.125	0.269	-0.604	1.42	1E-07	-4E-08	1E-08
8E-19	0	-2E-10	8E-10	-3E-09	3E-08	-5E-07	3E-06	-1E-05	3E-05	-7E-05	1E-04	-2E-04	3E-04	-5E-04	7E-04	-0.001	0.002	-0.002	0.004	-0.007	0.013	-0.025	0.05	-0.108	0.244	-0.573	1.403	1E-08	-5E-09
-4E-18	0	7E-11	-3E-10	1E-09	-1E-08	2E-07	-1E-06	4E-06	-1E-05	3E-05	-5E-05	9E-05	-1E-04	2E-04	-3E-04	4E-04	-6E-04	9E-04	-0.002	0.003	-0.005	0.01	-0.02	0.042	-0.095	0.222	-0.545	1.388	2E-09
2E-18	0	-3E-11	1E-10	-4E-10	4E-09	-7E-08	4E-07	-2E-06	5E-06	-1E-05	2E-05	-3E-05	5E-05	-7E-05	1E-04	-2E-04	2E-04	-4E-04	6E-04	-0.001	0.002	-0.004	0.007	-0.016	0.035	-0.083	0.204	-0.519	1.374

APPENDIX I

PUBLICATIONS

Two full journal articles were published during the course of this work. The first was entitled “LET dependence of GafChromic films and an ion chamber in low-energy proton dosimetry” and was published in January 2010 in *Physics in Medicine and Biology*, vol. 55, p. 417–433. This contains most of the proton dosimetry work described in chapters 4 and 5. A second paper entitled “Radiochromic film spectroscopy of laser-accelerated proton beams using the FLUKA code and dosimetry traceable to primary standards” was published in June 2011 in *Laser and Particle Beams*, vol. 29, p. 231–239.